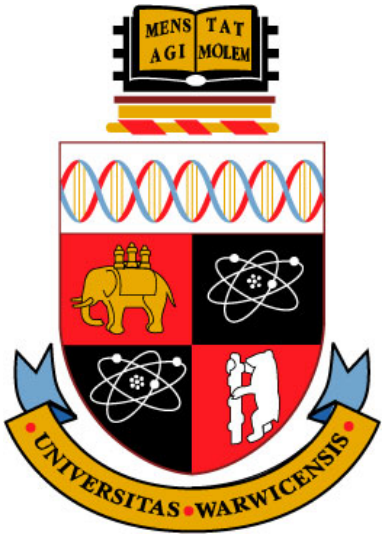

ELECTROANALYTICAL APPLICATIONS OF CARBON ELECTRODES

Anisha Naran Patel

A Thesis submitted for the degree of Doctor of Philosophy

THE UNIVERSITY OF WARWICK

September 2012

TABLE OF CONTENTS

ACKNOWLEDGEMENTS

I would like to express my deepest appreciation to my supervisors Prof. Patrick R. Unwin and Prof. Julie V. Macpherson. Without their guidance and support this thesis would not have been possible. Thank you for all your enthusiasm, optimism and encouragement, most importantly, for all your confidence in me throughout my PhD.

I owe a special thanks to the many members of the Electrochemistry and Interfaces Group. For all their help and support over the course of my PhD and, of course, for making my PhD a uniquely enjoyable experience.

Finally, to all my family and friends, thank you for all your love, patience and support.

DECLARATION

The work contained within this thesis is entirely original and my own work, except where acknowledged below.

In Chapter 3 the SECCM mapping with two redox mediators were done in conjunction with Dr. S. C. C. Lai. In Chapter 4, atomic force microscopy was carried out in conjunction with M. A. O'Connell. In Chapter 7, cyclic voltammetry measurements were carried out in conjunction with P. M. Kirkman. All SECCM imaging was performed using programming scripts written by K. M^{c}Kelvey.

Parts of this thesis have been published as detailed below:

S. C. C. Lai, A. N. Patel, K. M^{c}Kelvey, P. R. Unwin, *Definitive Evidence for Fast Electron Transfer at Pristine Basal Plane Graphite from High-Resolution Electrochemical Imaging*, *Angew. Chem. Int. Ed.,* **2012,** *51,* 5405-5408

A. N. Patel, M. Guille Collignon, M. A. O'Connell, W. O. Y. Hung, J. V. Macpherson, P. R. Unwin, *A New View of Electrochemistry at Highly Oriented Pyrolytic Graphite (HOPG)*, *J. Am. Chem. Soc*., **2012**, *134*, 20117–20130

A. N. Patel, K. McKelvey, P. R. Unwin, *Nanoscale Electrochemical Patterning Reveals the Active Sites for Catechol Oxidation at Graphite Surfaces, J. Am. Chem. Soc.,* **2012**, *134,* 20246–20249

Parts of this thesis is due to be published as detailed below:
A. N. Patel, J. V. Macpherson, P. R. Unwin, *Comparison and Re-Appraisal of Carbon Electrodes for the Voltammetric Detection of Dopamine: Optimal Trace Detection and Electrochemical Reversibility at Highly Orientated Pyrolytic Graphite (HOPG)*, [in preparation]

A. N. Patel, P. M. Kirkman, K. McKelvey, P. R. Unwin, *Macroscopic and Microscopic Electrochemistry of Anthraquinone-2,6-Disulfonate at Highly Ordered Pyrolytic Graphite: Basal Plane vs. Edge Plane Activity,* [in preparation]

A. N. Patel, P. R. Unwin, J. V. Macpherson, *Electrochemical detection and analysis of serotonin on polycrystalline boron doped diamond (pBDD),* [in preparation]

A. N. Patel, J. V. Macpherson, P. R. Unwin, *Ultra-thin Langmuir-Schaefer films of Nafion and glucose oxidase for the amperometric detection of glucose*, [in preparation]

Work carried out and not included within this thesis but published as detailed below:

L. Hutton, M. Vidotti, A. N. Patel, M. E. Newton, P. R. Unwin, J. V. Macpherson, *Electrodeposition of Nickel Hydroxide Nanoparticles on Boron-Doped Diamond Electrodes for Oxidative Electrocatalysis, J. Phys. Chem. C,* **2011**, *115*, 1649-1658

ABSTRACT

Carbon materials, such as graphite and conducting diamond, are highly popular for analytical and electrochemical applications, and fundamental knowledge of heterogeneous electron transfer is required to understand and optimise applications. In this thesis, the relationship between the structure of HOPG (Highly Oriented Pyrolytic Graphite) and its electrochemical behaviour has been thoroughly studied from the macroscale to the nanoscale. With the use of data collected from a wide range of techniques, spanning voltammetry, electrochemical imaging and high resolution microscopy, on 5 different grades of basal plane HOPG whose surfaces vary in defect density, the contribution of edge plane vs. basal plane on the electrochemical activity of HOPG has been re-examined. The significant body of work presented herein shows, without doubt, that the basal plane of HOPG is a very active electrode for $Ru(NH)_6^{3+/2+}$; $Fe(CN)_6^{4-/3-}$; the oxidation of the neurotransmitter, dopamine (DA), and quinones in aqueous solution. This overturns a well-established (textbook) model that the basal surface is inert, which researchers have assumed for two decades, with implications that carry over to related sp^2 carbon materials, such as graphene and carbon nanotubes. A second aspect has considered polycrystalline boron-doped diamond (pBDD) to study neurotransmitters, such as DA and serotonin (5-HT). The electrode surface was found to be resistive towards permanent surface blocking during the electrochemical oxidation of these neurotransmitters. The properties of the film formed by 5-HT oxidative products, was thoroughly investigated using voltammetry and high resolution microscopy. It is shown, for the first time, that electro-oxidation of 5-HT results in an electrically insulating, but charged and porous film, but procedures are demonstrated that allow the pBDD to be renewed in-situ for precise electroanalysis.

ABBREVIATIONS

LSV	Linear sweep voltammetry
CV	Cyclic voltammetry
ET	Electron transfer
ΔE_p	Peak potential difference between the anodic and the cathodic peaks
i_p	Peak current
GC	Glassy carbon
HOPG	Highly ordered pyrolytic graphite
CVD	Chemical vapour deposition
EPPG	Edge plane pyrolytic graphite
DOS	Density of states
CNT	Carbon nanotubes
BPPG	Basal plane pyrolytic graphite
NP	Nanoparticle
STM	Scanning tunnelling microscopy
2,6-AQDS	Anthraquinone-2,6-disulfonate
SFM	Scanning force microscopy
$_p$BDD	Boron doped diamond
FE-SEM	Field emission-scanning electron microscopy
SECM	Scanning electrochemical microscopy
SECCM	Scanning electrochemical cell microscopy
AFM	Atomic force microscopy
C-AFM	Conducting atomic force microscopy
DA	Dopamine
5-HT	Serotonin
LS	Langmuir-Schaefer
GOx	Glucose oxidase
GA	Glutaraldehyde
QRCE	quasi-reversible counter electrode
WE	Working electrode
Ag/AgCl	Silver/Silver chloride reference electrode
PBS	Phosphate buffered saline
L.O.D	Limit of detection
L.O.Q	Limit of quantification

LIST OF FIGURES

LIST OF TABLES

CHAPTER 1: INTRODUCTION

This thesis is concerned with the development and analysis of carbon electrodes for electroanalytical applications.

1.1 DYNAMIC ELECTROCHEMISTRY

Dynamic electrochemistry is the main experimental focus of this thesis, where a potential bias is applied to an electrode to drive the transfer of electrons between the electrode/electrolyte interface. When an electrode is placed into an electrolyte solution, an excess or deficiency of electrons develops at the electrode surface, and in order to maintain charge neutrality. A double layer develops at the electrode surface. Ions spontaneously redistribute creating a layer of oppositely charged species near the electrode surface. A common model often used to described the double layer is the Gouy-Chapman-Stern-Graham model,[1-3] shown schematically in Figure 1. 1. The region closest to the electrode/electrolyte interface is the inner Helmholtz plane (IHP), where species that have lost their hydration shell and solvent molecules are specifically adsorbed due to van der Waals interactions. Next to it is the outer Helmholtz plane (OHP), which consists of a layer of hydrated ions that have very strong long-range electrostatic interactions with the charged electrode. The diffuse layer accounts for a gradient of charge accumulation due to coulombic forces and disorder caused by random thermal motion. This ordering of charged species in the interfacial region means the electrode/electrolyte interface resembles a parallel plate capacitor, the effect of which can be seen as a charging process in transient electrochemical measurements.

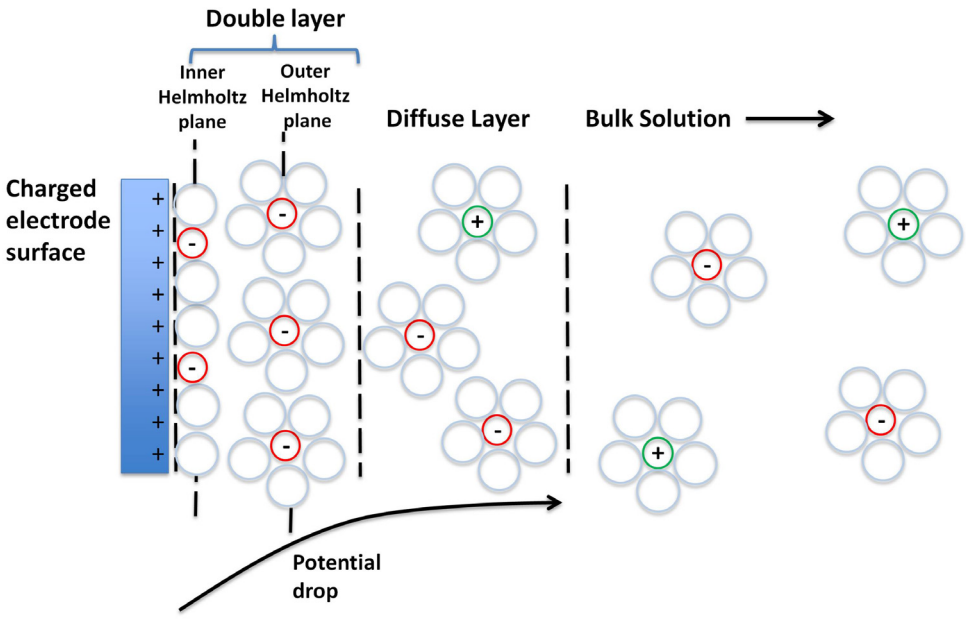

Figure 1. 1 Schematic diagram for the Gouy-Chapman-Stern-Graham model of the electrochemical double layer. The compact double layer consisting of densely arranged ions which maintain charge neutrality. In the inner Helmholtz plane are specifically adsorbed dehydrated species, the outer Helmholtz plane consists of hydrated counterions and the diffuse layer of ions due to coulombic and thermal forces which extends into the bulk solution.

Dependent on the potential applied, two different redox processes can take place: reduction or oxidation. In a reduction process, the electrode provides electrons to the species in solution and in an oxidation process, the electrode accepts electrons from species in solution. In linear-sweep voltammetry (LSV), a potential is applied to the working electrode with respect to a reference electrode. A counter or auxiliary electrode is required to pass the current when ohmic drop becomes an influencing factor in the electrochemical response. This is usually when the flowing currents are greater than 1 μA in aqueous solution.[2] The working electrode potential is swept from a value where no current flows, i.e. no electrochemical reaction takes place, to a potential where reduction/oxidation occurs beyond a diffusion-controlled rate. During the potential sweep, the current slowly increases and reaches a peak before dropping (Figure 1. 2). The peak in the current is due to a shift in the equilibrium of the redox species as the electrode potential is scanned to a potential favouring either the oxidation or reduction reaction. This observation can be explained by the Nernst equation[3] (Equation 1.1)

$$E = E^{O} - \frac{RT}{nF}\log\frac{[R]}{[O]} \qquad \textbf{Equation 1.1}$$

where E is the electrode potential, E^{O} is the standard electrode potential, n is the number of electron's transferred, F is Faraday's constant (96485 C mol^{-1}), R is the universal gas constant (8.314 J mol^{-1} K), T is the absolute temperature (K), [R] and [O] are the

concentrations of the redox species. The resulting effect of shifting the equilibrium is the depletion of species at the electrode-solution interface; the thickness of this diffusion layer increases with time for a planar electrode (1-dimension diffusion), and the rate at which redox takes place becomes dependant on the rate of mass transport for species from the bulk solution to the interfacial region. The size of the diffusion layer can be controlled by the potential scan rate; at slower scan rates the diffusion layer becomes larger (low mass transport), by increasing the scan rate the diffusion length is kept small (higher diffusive mass transport) and the peak current increases.[1]

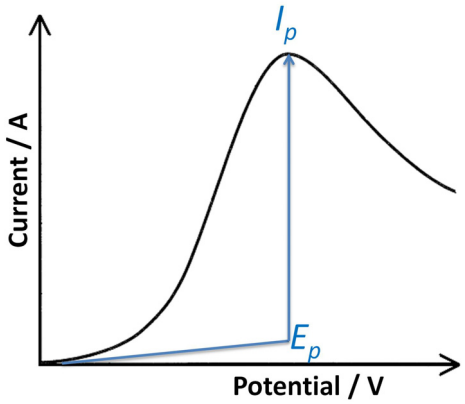

Figure 1. 2 An example of a reversible linear sweep voltammogram.

Fick's 1st law relates the rate of diffusion to concentration i.e. the flux, *j,* as given by Equation 1.2:

$$j = -D\frac{\partial[O]}{\partial x} \qquad \textbf{Equation 1. 2}$$

where *j* is the flux, *D* is the diffusion coefficient and *∂[O]/ ∂x* is the change in concentration of the electrode species, *O,* with respect to the distance from the electrode surface, *x*.[1-3]

In cyclic voltammetry (CV), the forward sweep produces the same response as in LSV. By reversing the potential applied, the reverse electrochemical reaction takes place. The shape of the resulting CV provides information on the electron transfer process for the electroactive species of interest. For a process controlled by diffusion alone where the electron transfer (ET) kinetics are deemed fast, the system is termed 'reversible'. The ratio of the two peak currents obtained is one, and as the position of the peak potentials does not change with scan rate. The potential difference between the cathodic and anodic current peaks (ΔE_p) is 59/n mV for a reversible n-electron system at 298 K.[2-3] In a reversible system, the peak current is dependent on the square root of the scan rate and the peak potential is independent of the scan rate (Equation 1.3).[2] For systems where electron transfer is slow compared to the diffusion rate, the CV changes shape. Notably, the peak current is lower

than the expected based on Equation 1.3, and the peak potentials are widely shifted due to an overpotential that has to be applied to promote heterogeneous electron transfer, i.e. the ΔE_p is greater than 59/n mV. These systems are described as quasi-reversible or irreversible. In these systems, the current is controlled by both the kinetics of charge transfer and mass transport.[1-3]

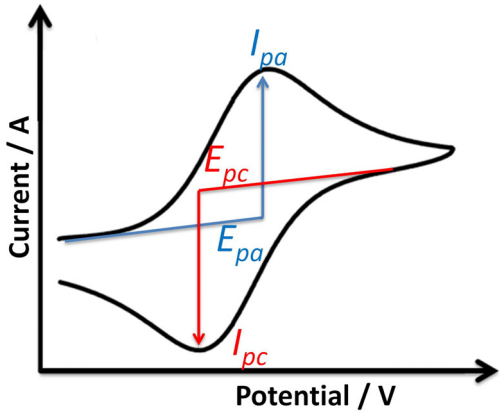

Figure 1. 3 An example of a cyclic voltammetry graph for a reversible one-electron transfer process.

Figure 1. 3 shows an example of a CV for a reversible electron transfer process, E_{pa} and E_{pc} are the peak potentials and the i_{pa} *and* i_{pc} are the peak currents. The peak current for an electrochemically reversible system is described by the Randles-Sevcik[1-3] (Equation 1.3):

$$i_p = 0.446nFA\left(\frac{nF}{RT}\right)^{\frac{1}{2}} D^{\frac{1}{2}}v^{\frac{1}{2}}[O] \qquad \textbf{Equation 1.3}$$

where i_p is the peak current (in A), [*O*] is the bulk concentration (mol cm^{-3}), *A* is the electrode area (cm^2) and *v* is the potential scan rate (V s^{-1}). A plot of i_p *vs.* $v^{1/2}$ has a gradient that can be used to determine the diffusion coefficient, when *n, A* and *c* are known or the concentration of species when *D, n* and *A* are known.[1-3]

Mass transport of species from the bulk to the surface of the electrode is evidently an important factor which affects electrochemical reaction rates and currents.[2] There are three forms of mass transport and contributions from all three are possible. Migration is the movement of charged species by electrostatic forces, which is due to the influence of a potential gradient; this gradient is formed when voltage difference is applied between two electrodes. Diffusion is the movement of species from a region of high concentration to a region of low concentration, which is the main form of mass transport in CV discussed above. The third form of mass transport is convection; this is the movement of species due to the movement of the solution due to external forces such as vibrations. To overcome these effects, electrochemical measurements are usually done in unstirred solutions with the

addition of a supporting electrolyte, which minimises the effects of migration and lowers the resistance of the solution.[1, 3] Hence, under conditions where electron transfer is very fast, the current is controlled by diffusion in solution.

1.2 ELECTRON TRANSFER AND THE ELECTRONIC STRUCTURE OF AN ELECTRODE

The thickness of the double layer affects the rate of an electrochemical reaction, as redox species must be in close enough proximity for electron tunnelling to take place between the electrode and solution species. Depending on the electrochemical process, electron transfer (ET) is maybe influenced by the electronic structure and chemical properties of the electrode material and the redox species of interest. The relationship between electronic structure and electrochemical activity can be described using the Marcus-Gerischer model (among other possibilities) and is based on the theory that ET takes place between occupied states and unoccupied states (on the electrode and solution species) when equal in energy.[1, 4]

The time-scale at which ET takes place is much faster than the time-scale for nuclear motions of a molecule to occur; therefore all nuclear changes and reorganisation of solvent shell must take place before and after ET, as stated by the Franck-Condon principle.[2-3] The energy of an electron during transfer does not change, therefore the Fermi level in the electrode must be the same as the does or acceptor states of the redox species in order for the electron to posses the same energy during a redox reaction, consistent with Marcus theory.[2-3] The density of states (DOS) associated with the oxidised state and reduced state of a redox species are defined by the lowest unoccupied molecular orbital (LUMO) and the highest occupied molecular orbital (HOMO) into which electrons can be accepted or donated from.[4] However, there is a distribution of such states due to the intramolecular energy changes and the solvent shell reorganisation, in the case of hydrated species, with the redox potential of the couple situated between the HOMO and LUMO as depicted in Figure 1. 4. The rate of ET varies between different redox species due to the requirement for the oxidised and reduced states of a redox species to share the same nuclear configuration immediately before and after ET. Hence, when the oxidised and reduced state are similar in structure the reorganisation energy is smaller and electrochemical reactions are faster. On the other hand, where large structural changes are required for the species to share the same nuclear energy, the slower the rate of ET.

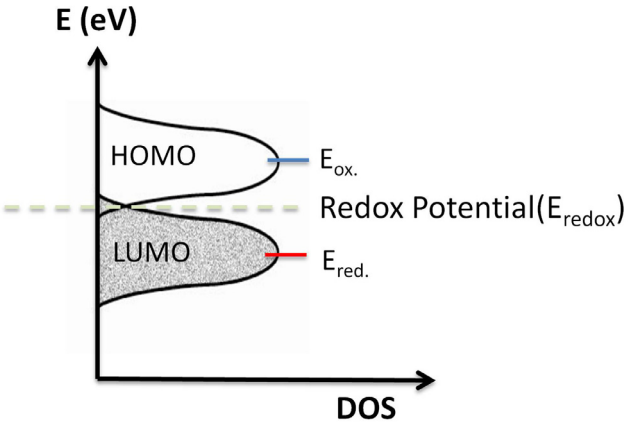

Figure 1. 4 Energy distribution of the density of states (DOS) in a hydrated redox couple showing a small overlap between the electronic energy for the reduced and oxidised states with the standard redox potential situated between the LUMO and HOMO.

For conduction of charge to take place in an electrode, electrons need to be excited from the valence band to the conduction band. The orbitals of atoms in a solid combine creating filled occupied (valence) and unoccupied (conduction) bands, VB and CB, respectively. The greater the separation of these bands the more energy is required in order to promote transfer from the VB to CB and therefore, the separation of the two bands characterises the electrical properties of materials. Metals have overlapping VB and CB: whereas in a semiconductor the two bands are separated (Figure 1. 5).

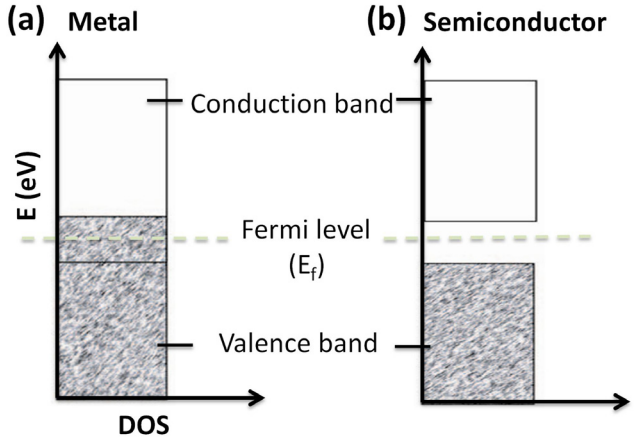

Figure 1. 5 Density of electronic states (DOS) band diagrams for (a) metal and (b) a semiconductor showing: the conduction band; the valence band; and the position of the Fermi level.

When an electrode is placed into an ionic solution, charge transfer takes place at the electrode-electrolyte interface to equilibrate the energy between the Femi level at the electrode surface and the redox potential of the electrolyte solution. For a metallic electrode,

the charges are located just below the surface, but for semiconductors, the carrier density is much smaller than in a metal electrode and so the charges can be distributed on a significant distance, 100- 10000 Å, below the interface into the bulk of the electrode.[5] This creates what is called a space charge region. Hence, whereas for a metal electrode the interface of interest is just the electrode/electrolyte double layer; for semiconductor electrochemistry, the interfaces of interest are the electrode/electrolyte double layer and the space charge double layer. Due to this space charge layer to attain equilibrium between the energy of the Femi level at the electrode surface and the redox potential of the electrolyte solution, there is a downward or upward bending of the band edges.[5] When the density of charge carriers is reduced in the space charge region due to this process it creates a depletion layer. By applying a potential to the semiconductor the density of charge carriers increases, creating an accumulation layer. Figure 1. 6 shows this effect for a p-type semiconductor. As with a metallic electrode, applying a potential to a semiconductor electrode changes the position of the Fermi level and shifts the energy of the band edge in the interior of the electrode, however, at the interface the energy of the band edges are not affected. Hence, the magnitude and direction of band bending from the interior of the semiconductor to the interface varies with the applied potential.

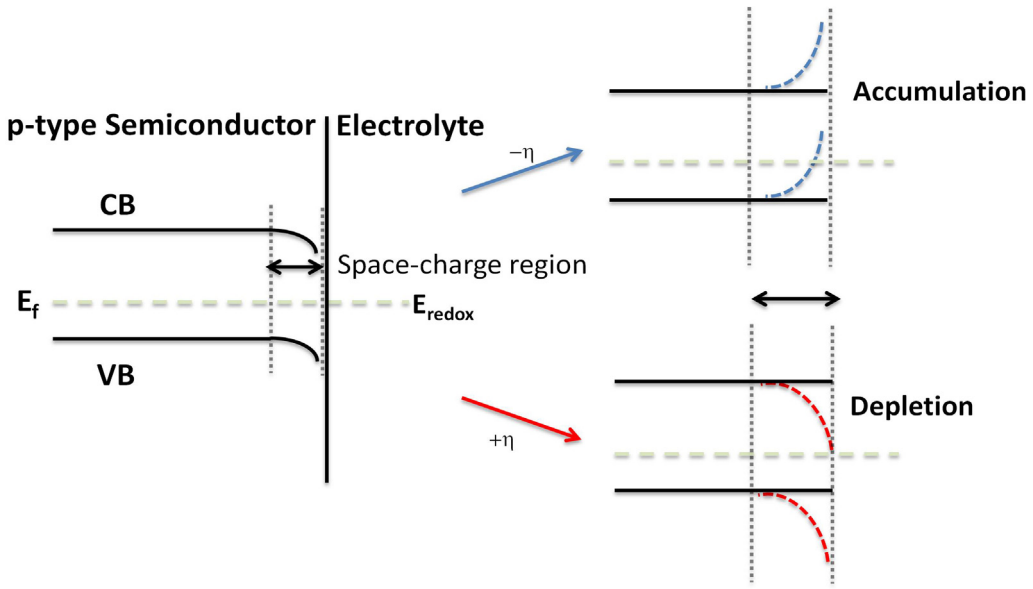

Figure 1. 6 Simplified diagram of band bending for a p-type semiconductor in equilibrium with an electrolyte. The upward and downward bending of the CB and VB due to the application of a negative or positive overpotential (η) increasing the size of the space-charge regions.

During an electrochemical process, ET takes place at the electrode/electrolyte interface where the transfer of electron to and from a redox species can proceed with the species maintaining its solvation shell (outer sphere) and therefore at the OHP, or without its salvation shell, due to adsorption on the electrode surface (inner sphere). As reversible redox

species are at equilibrium, to drive a reduction or oxidation process the position of the equilibrium must be perturbed, this is achieved by the application of a potential more negative or more positive than the standard equilibrium potential.[3-4] Applying a potential shifts the energy of the Fermi level in the electrode, altering the ratio between the occupied and unoccupied DOS of the redox species to favour either the reduction or oxidation reaction.[2, 4] The DOS in the electrode and in the redox species many influence the rate of ET. A metal electrode possesses a high DOS at its Fermi level and ET occurs readily at its Fermi level; whereas a semiconductor has no DOS at its Fermi level and ET takes place via the conduction band or the valence band. This difference in the DOS at the Fermi level causes a variation in the rate of ET to a given redox species, where the rate is generally faster at a metallic electrode compared to a semiconductor electrode. Figure 1. 7 summaries the effect on both types of electrodes.

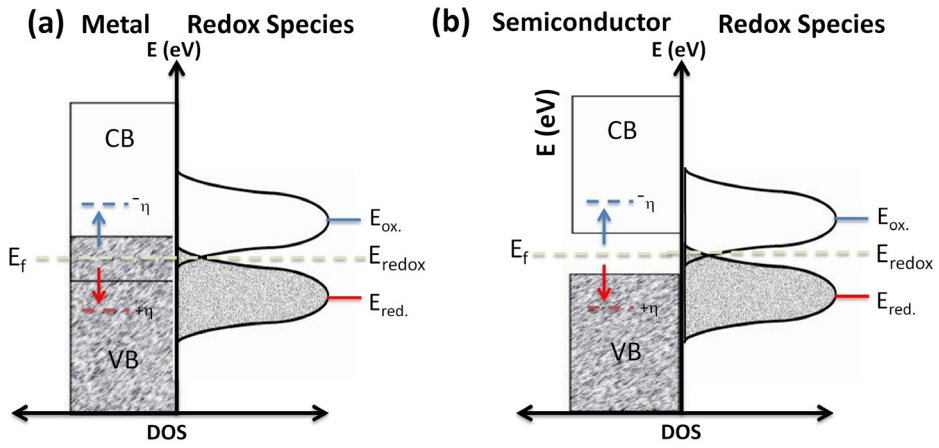

Figure 1. 7 Diagram showing (a) metal and (b) semiconductor electrodes in contact with a hydrated redox couple and the effect of applying negative or positive overpotentials on each material to perturb the redox equilibrium, favouring either the oxidation or reduction reaction. For a metal electrode the overlap in CB and VB means ET takes place readily at Fermi level, whereas for the semiconductor ET takes place via the CB or VB.

1.3 CARBON MATERIALS

Carbon is one of the most abundant elements available and naturally produced in several crystalline forms, from diamond to graphite. Often referred to as the building block of life; [6] of all the chemical elements, carbon has the greatest capacity to bond not only to itself but also to most other non-metallic elements. Fundamental innovations in the 1960s led to the start of a new era for carbon, with the development of new carbon allotropes: from carbon fibres (1960) to nanotubes (1991).[7] The use of carbon materials has become widely popular in analytical and industrial electrochemistry due to its superior electrochemical properties

compared to metal electrodes: low cost; biocompatibility; chemical inertness.[8-10] The chemical inertness of carbon materials means that surface processes such as the formation and reduction of surface oxides does not occur in a wide potential window, this results in lower background currents compared to conventional metal electrodes.

1.3.1 Glassy Carbon (GC)

Glassy carbon (GC) is a synthetic polymer carbon consisting of randomly disordered and tangled graphite-like ribbons and isotropic in structure.[10-11] Although early models for the structure of GC assumed a combination of sp^2 and sp^3 bonded atoms, it is now accepted that it consists purely of sp^2 bonded carbon[12] and possibly even has a fullerene-related structure.[13-15] Figure 1. 8 shows the structure for GC, where the stacked aromatic ribbons can be seen. These ribbons are believed to be 15-70 Å in diameter and height, with an interplanar spacing of 3.4-3.6 Å.[10, 14, 16-17] These ribbons are randomly orientated and tangled with pores that have been reported to range from 3.5 Å to 10 nm.[7, 18-19]

Although, GC is graphitic in structure, its electronic properties do not bare similarity to that of pyrolytic graphite.[7] Studies have found the band gap in GC to vary (1-4 eV) based on the structural disorder and population of oxygen groups;[15, 20-21] where the structure is more ordered, charge carriers have been found to have a higher mobility.[22] The composition of a GC rod will vary throughout the material due to the variation in the microstructure and possible small void spaces, which exist within the rod.[23]

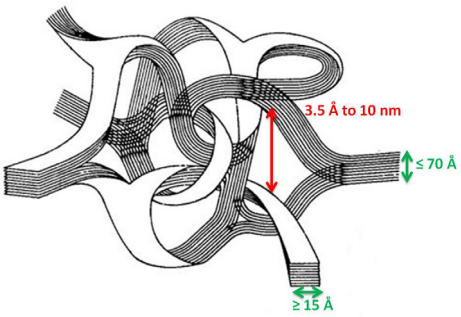

Figure 1. 8 Stacked aromatic ribbons randomly orientated and tangled forming the structure of GC.

1.3.1.1 GC as an Electrode Material

GC has been extensively studied since it was first produced in the mid 1960's, and is the most extensively employed carbon electrode due to its low density, high conductivity, chemical inertness, and impermeable to gas as well as wide availability and inexpensiveness.[13-14, 24-27] GC exhibits relatively low background currents and wide potential

window compared to conventional metal electrodes.[14] A major disadvantage of GC electrodes is its high sensitivity towards surface preparation, surface pre-treatment as well as electrode history; this leads to a variation in the observed electrochemistry.[10, 18, 28] The exposed graphitic edges and oxygen containing functional groups have been proposed to be the active sites on GC for certain reactions.[10, 14, 28]

This electrode material has been extensively employed to study the ET kinetics of a wide range of mediators; where the affect of surface termination (as well as surface pre-treatment) has been comprehensively studied.[29-31] The resistance of GC to corrosion and chemical inertness under a wide variety of conditions, has led to its use in extremely corrosive environments over a wide range of electrical potentials.[18] On the other hand, although GC is chemically inert, its sp^2 content and high density of oxygen containing functional groups leaves it vulnerable to the adsorption of molecules, especially biomolecules, via intermolecular forces.[10] This means the GC surface is highly susceptible to surface deactivation.

The rate of ET at the GC surface can be greatly improved via various activation techniques: electrochemical pre-treatment; [32-33] mechanical polishing;[34-35] laser treatment;[30, 36] plasma treatment;[37-38] and vacuum heat treatment[39-40] which lead to an adventitious change in either the surface termination or/and microstructure.[10, 18, 41] Mechanical polishing with alumina is the easiest method for revealing a clean, new, activated electrode surface, where oxygen containing functional groups are incorporated onto the surface. This is used most commonly.[10, 14, 41] However, this means the surface characteristics and/or area of the electrode may change over time, with each polishing of the electrode surface revealing a new layer of material, with potentially different properties.[32]

1.3.2 Highly Ordered Pyrolytic Graphite (HOPG)

HOPG consists of a lamellar like structure of sp^2 carbons arranged as six-membered rings, where a π system exists above and below the rings, formed by the unhybridised p-orbitals from each atom overlapping.[14, 42] Each graphene layer is arranged in an alternating ABAB stacking pattern (Figure 1. 9), over a short distance, and at random angular orientations, over longer a range.[7, 10, 14] Strong forces are present between the carbon atoms in lateral planes, whereas weaker (van der Waals) forces are present between the planes.[7, 10] The material is a chemically inert, thermal and electrically conducting, dense,[7, 17] and its atomically smooth basal surface over large areas make this material ideal for studying electrochemical reactions and molecular adsorption.[43-44]

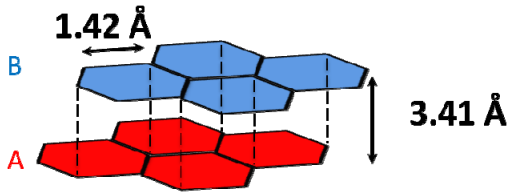

Figure 1. 9 Schematic diagram showing the AB arrangement of carbon atoms in graphite.

In each graphene layer the carbon atoms are sp^2 hybridised with a C-C spacing of 1.42 Å and each graphene layer is separated by approximately 3.35-3.41 Å, as shown in Figure 1. 9.[10, 45-46] HOPG offers two types of morphologies, basal-plane and edge-plane. For the case of basal-plane HOPG, the layers are orientated in parallel to the surface, as shown in Figure 1. 10. Surface defects can occur, such as stacking faults, micro-cracks and dislocations that arise from misalignments between domains.[45] Variation in growth conditions leads to samples that differ in quality (in terms of order). Analysis of the mosaic spread is often used to characterise the quality of basal plane HOPG enabling grading of samples. The mosaic spread of a sample is found using x-ray diffraction to assess the average angle of deviation of the grains in the perpendicular axis; hence, a low mosaic spread refers to a sample with a high degree of order.[47] Commercially, there are two major brands of basal-plane HOPG, both providing several grades of basal plane HOPG: ZYA; ZYB; ZYH grades, products of Advanced Ceramics, and SPI-1; SPI-2; SPI-3 grades, products of SPI Supplies.[48-50] These commercial samples possess mosaic spreads ranging between 0.4°, for the highest quality, to 3.5°, for the lowest quality; where the grain sizes can up as big as 10 mm for the highest quality, or as small as 30 nm for the lowest quality.

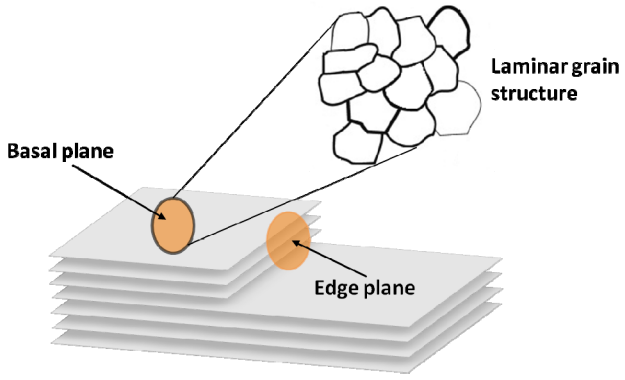

Figure 1. 10 Schematic showing the structure of HOPG.

The weaker forces between sheets, allow thin layers of the graphite to be removed on basal-plane HOPG, providing a fresh, new workable surface.[45] This can be achieved using scotch tape, pressing gently flat on the surface and pulling to remove the top few layers and

producing a freshly cleaved surface.[51-52] Mechanical cleaving using a razor blade is another method for preparing the basal plane of HOPG; the razor blade is inserted perpendicular to the basal plane, and in a gentle rocking motion slowly worked through the sample.[53-54] A small piece of HOPG, usually, spontaneously delaminates; producing a fresh surface to work on.

For the edge-plane pyrolytic graphite (EPPG), the surface comprises of an array of graphene layers, shown in Figure 1. 10. An active surface with this orientation has to be regenerated by abrasive polishing i.e. with alumina on emery paper.[55-56] The sites/defects introduced during this regenerative process are thought to result in faster ET as it results in the formation of oxygen-containing functional groups.[57]

The two morphologies of graphite are electronically anisotropic; the conjugated π-system allows electron conduction to occur across the plane enabling metallic conductivity, whereas conductance between the planes occurs through electron tunnelling allowing semiconducting to semi-metallic conductivity as well as chemically different.[46, 58-59] the basal plane is hydrophobic whereas the step edges/defect sites are hydrophilic and therefore exhibit different electrochemical properties.[45, 60] Pristine basal-plane HOPG is considered semi-metallic due to a very small overlap (0.03-0.04 eV) between the conduction band and valence band, Figure 1. 11, giving rise to a low density of states (DOS), 2.2 x 10^{-3} eV, at the Fermi level.[46, 61-62] Models show that an equal number of electrons and holes exist in the overlapping region, giving rise to a build up of excess charge in the electrode at the electrode surface creating a space charge region.[61, 63-65] The considerably low capacitance observed from basal-plane HOPG (0.6 μF cm^{-2}), compared to EPPG (60 μF cm^{-2}) or other traditional carbon electrodes such as GC (> 20 μF cm^{-2}),[66-67] is believed to be the result of a the small space charge region which dominates over double layer capacitance. The introduction of any step-edge defects introduces energy levels that increase the DOS,[68] hence highly defective basal-plane HOPG (or EPPG) displays a large capacitance and is, electronically, metallic.

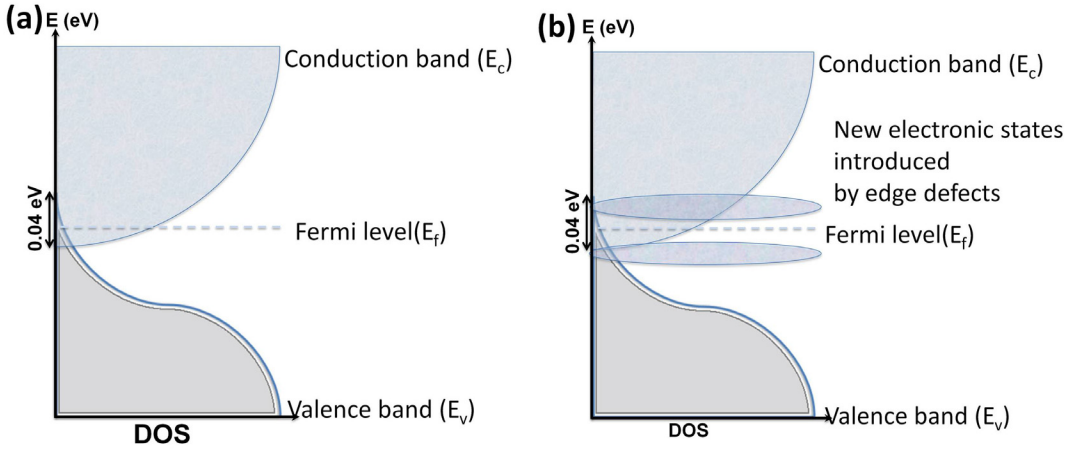

Figure 1. 11 Band structure for (a) pristine basal plane HOPG and (b) for basal plane HOPG with a large coverage of edge defects.

1.3.2.1 Electrode History and Related Properties of HOPG

Since the mid 1960's, graphite has been used extensively as an electrode material. The basal surface of HOPG has proven popular as an electrode support for the deposition of electroactive nanostructured materials, for a variety of applications, including fundamental studies of heterogeneous metal nucleation and electrodeposition,[69-76] for model studies of nanoparticle (NP) electrocatalysts,[77-81] and the creation of nanostructured interfaces for electrochemistry, sensing and biosensing.[82-89] Compared to classical carbon electrodes, e.g. carbon fibre and GC, basal-plane HOPG exhibits lower background currents and a wider potential window, as well as the many optimal properties demonstrated by carbon electrodes in general: highly chemically inert; biocompatible; electrically conductive; low cost. The current intense activity in electrochemical applications of novel sp^2 carbon materials, such as CNTs and graphene, has led to a resurgence of interest in the intrinsic electrochemical properties of basal-plane HOPG, to which these materials are often compared.

A large body of work has suggested that the basal surface of HOPG is characterised by very low[29] or even zero ET kinetics,[66] with the step edges intersecting the basal surface essentially providing all of the sites for electrochemistry,[60, 90-94] for a wide range of redox couples, including classical outer sphere and inner sphere couples.[92-95] This has been attributed to the fact that HOPG has a low density of states at the Fermi level.[61] There is also evidence opposing this proposition; variants of the technique scanning electrochemical microscopy have been used by several different groups to show the ET kinetics at the basal-plane of HOPG to be just as facile as on conventional metal electrodes.[52, 96-98]

In early work, CV measurements were carried out with the aim of ascertaining the electrochemical properties of basal-plane HOPG by determining the ET kinetics over extensive areas of the surface (typically > 0.1 cm^2), probing both the basal surface and step edges that emerge at the surface.[61, 66, 93-94] In studies carried out in the early 1990's, McCreery *et al* advocated the use of CV measurements with the $Fe(CN)_6^{4-/3-}$ couple as the main method for inferring the 'quality' of the basal surface, referred to as 'validation experiments'.[66, 92, 99] High quality surfaces, *i.e.* those assumed to have low defect density were defined as those demonstrating a peak-to-peak separation, ΔE_p, > 0.7 V (at 0.2 V s^{-1}) for $Fe(CN)_6^{4-/3}$, but this value could be as high as 1.2 V.[29] For surfaces showing this characteristic, the $Fe(CN)_6^{4-/3-}$ solution was removed and the surface used (without further treatment) with the addition of a new solution containing a redox couple of interest.[29] Surfaces exhibiting smaller ΔE_p, which could be as little as 58 mV (indicating essentially reversible behavior) were discarded, being considered too defective.[29]

More recently, Compton and co-workers carried out CV measurements on SPI-1 grade HOPG.[4] For the $Fe(CN)_6^{4-/3-}$ couple only one CV was reported in which a large peak separation was observed, ΔE_p ~ 1.2 V, [45, 60, 94] but a value as small as 350 mV was also reported in another CV in a different study on an apparently similarly freshly cleaved surface.[100] Attempts were made to fit the large ΔE_p CV to a model that assumed only steps were active for ET, with the basal-plane considered to have zero activity. However, to achieve a reasonable analysis, it had to be assumed that the step spacing was many orders of magnitude larger than evident experimentally.[94] On the other hand, the one CV reported by Compton *et al* for $Ru(NH_3)_6^{3+/2+}$ on SPI-1 grade HOPG was found to be reversible, contrasts with ΔE_p of 285 mV[61] found by McCreery. Yet, in both cases it was proposed that the basal surface was totally[100] or largely inert.[60, 94] Figure 1. 12 shows example voltammograms where for the same electrode (basal plane HOPG) and the same redox mediator (ferrocyanide), 3 very different observations have been reported.

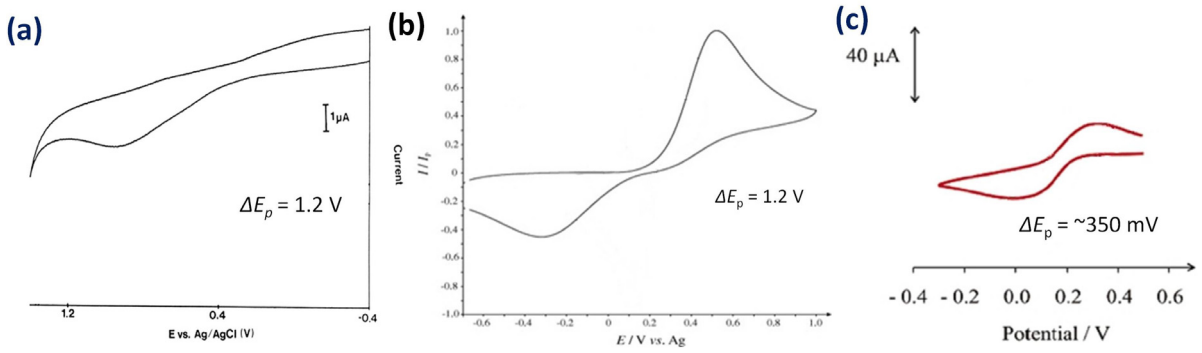

Figure 1. 12 Examples of CVs found within literature for the oxidation of ferrocyanide on basal plane HOPG. Taken from (a) R. J. Bowling, R. T Packard, R. L. McCreery, *J. Am. Chem. Soc., 111,* 1989, 1217, (b) T. J. Davies, R. R. Moore, C. E. Banks, R. G. Compton, *J. Electroanal Chem., 574,* 2004*, 123* and (c) X. Ji, C. E. Banks, W. Xi, S. J. Wilkins, R. G. Compton*, J. Phys. Chem. B, 110,* 2006, 22306.

Scanning tunneling microscopy (STM) of the basal surface of HOPG reveals step edge densities in the range of 1-10%,[54] with the step density depending on the source of HOPG and cleavage method.[11] For HOPG, "obtained as a gift from Dr. Arthur Moore, Union Carbide", which is hereafter referred to as HOPG (AM), the step density was *ca.* 1% of the HOPG basal surface.[11] Both ZYA and ZYH grade basal-plane HOPG were also investigated by STM and while step densities were not reported, it was noted that the step density was lower on ZYA grade HOPG.[101] If a simple partially-blocked electrode analysis is applied to the HOPG electrode structure (assuming the basal-plane is inert and only step edges are active) and planar diffusion to the electrode,[102] a difference in apparent (average) ET kinetics between the edge plane and basal plane of HOPG of no more than two orders of magnitude would be expected, even for the most extreme case where only adventitious steps, at 1% surface coverage, were on the basal surface, *i.e.* using the lowest value for step edge density and ignoring other possible defects.[92, 100] This contrasts with a much larger factor apparently seen,[92, 94, 100] and the question therefore arises as to why? Moreover, the range of ΔE_p values found for $Fe(CN)_6^{4-/3-}$ on the cleaved basal surface alone, i.e. 58 mV – 1.2 V, also spans effective standard heterogeneous ET rate constants of many orders of magnitude (under conditions of planar diffusion)[10, 60, 90-91, 102] and by implication, a similar change of magnitude in surface defect coverage from one cleave of HOPG to another would be needed for a defect-driven model of HOPG electrode activity to be applicable. This does not appear reasonable based on current knowledge of defect density of freshly cleaved HOPG.

As well as performing electrochemical measurements to study the activity of HOPG, capacitance measurements,[53, 66, 101] complementary microscopy and spectroscopy studies [11, 92, 101, 103] and 2,6-anthraquinone disulfonate (2,6-AQDS) adsorption studies have been carried

out.[53] Claims about the inactivity of basal plane HOPG have been extended to speculate the sites of ET on CNTs[60,93] and graphene.[104] Based on the model for HOPG, it has been proposed that interfacial ET only occurs at edge-plane like sites in multi-walled CNTs and at the open ends of single-walled and multi-walled CNTs,[60, 93-94,105-106] or at the graphene edge.[104] However, as in the case for basal-plane HOPG, fast (often reversible) electrochemistry has been found on studies of pristine, well-characterized single walled carbon nanotubes (SWNTs) grown by chemical vapor deposition,[107-117] and at mechanically exfoliated graphene,[118] which suggests that ET occurs readily at the interface between sp^2 carbon and electrolyte solution.

1.3.3 Boron-Doped Diamond (BDD)

Diamond is an allotrope of carbon, where the sp^3 carbon atoms are tetrahedrally bonded and packed in a face-centred cubic lattice, as shown in Figure 1. 13(a).[119] Its unique properties: optical, thermal, electronic, chemical and electrochemical[119-125] has made it possible to work in conditions and detect species never before possible due the physical and chemical limitations of conventional electrodes.

The carbon atoms in diamond are tetrahedrally bonded and packed in a face-centred cubic lattice. Dependant on the seed used to drive the growth process, e.g. single crystal diamond or polycrystalline silicon substrate, synthetic diamond can be grown as a single crystal or in polycrystalline form. [146]

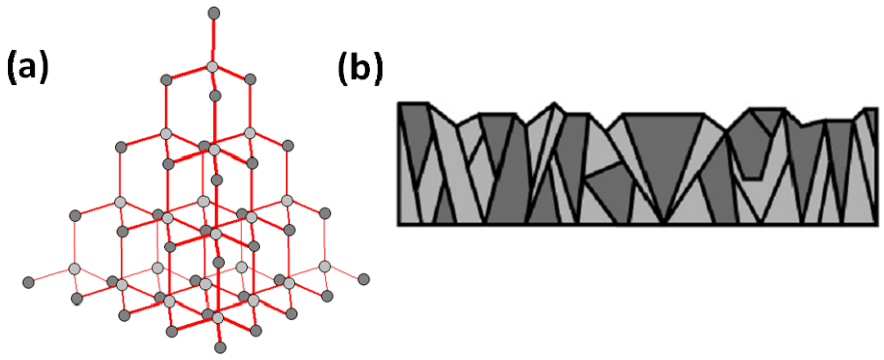

Figure 1. 13 Schematics showing (a) the arrangement of carbon atoms in diamond and (b) the grain structure of polycrystalline diamond.

Intrinsic diamond is naturally an electrical insulator, with a wide band-gap of 5.47 eV (at 300 K) and, therefore, unsuitable as an electrode material.[119, 126] However, through doping during its growth process conductive properties can be incorporated into the material. There are two types of doping: n-type, where the addition of group V ions, e.g. nitrogen, creates a donor level 1.6 eV below the conduction band; and p-type, where the addition of group III ions, e.g.

boron (from B_2H_6), creates an acceptor level 0.36-0.37 eV above the valence band, see Figure 1. 14.[119, 127-128] BDD is commonly the diamond material of choice within the electrochemical community. A boron doping density of at least ~ 10^{17} cm^{-3} is required in order for the minimum number of charge carriers to have enough mobility that enables current to flow.[129] Therefore, this material can exhibit the characteristics of an extrinsic semiconductor, with boron concentration of ~10^{18} cm^{-3} producing a resistance of ~ 10^4 Ω, to a semimetal, with boron concentration 10^{20} cm^{-3} producing a resistance of 10^{-2} Ω within the material.[119, 129-130] As the doping level increases, the mechanism by which conduction takes place changes: from valence band conduction for lowly doped (*ca.* < 10^{18} cm^{-3}) to metallic conduction for highly doped (*ca.* > 10^{20} cm^{-3}) with hopping conduction for BDD with concentrations in between.[131-132] The level of doping can be determined using secondary ion mass spectrometry (SIMS).[133-134]

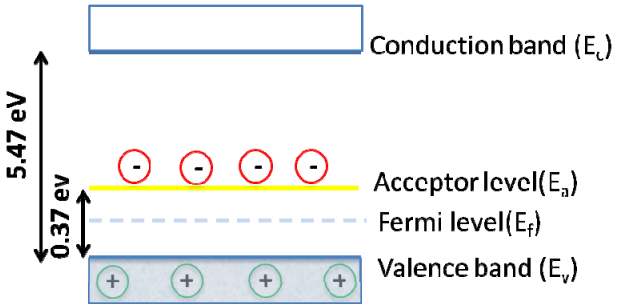

Figure 1. 14 Band structure for p-type semiconducting BDD

In the case of polycrystalline boron doped diamond (pBDD), the different crystal facets have a different rate of growth and boron uptake;[127, 129, 135] this leads to a heterogeneous surface comprised of various crystal facets which vary in grain sizes as well as boron concentration (Figure 1. 13b).[135-137]

1.3.3.1 Conducting Diamond as an Electrode Material

Since the first attempt at using diamond as an electrode in 1983 by Iwaki and Sakairi, conducting diamond has been employed for a wide range of electroanalytical applications: from heavy metal detection to *in-vivo* neurotransmitter detection.[138-139] Compared to that of common metal electrodes: e.g. gold and platinum; and common carbon electrodes: e.g. glassy carbon and carbon fibre; diamond electrodes have an extremely wide potential window; lower background currents; higher chemical and mechanical stability; resistance to fouling; and controllable surface termination.[128, 140-142]

The electrochemical properties of pBDD can be influenced by surface termination.[129, 143] As grown, CVD diamonds posses a non-polar hydrogen terminated surface due to the presence of hydrogen gas during the cooling stage at the end of the CVD growth process.[140, 143] This

surface termination is unstable and can change during anodic polarisation to contain a range of oxygen functional groups: hydroxyl, ether and carbonyl.[144-146] Oxygen-terminated surfaces display greater stability under potential control and have been found to provide a wider potential window and lower background currents than hydrogen terminated diamond.[147-149] The surface termination can also be modified to be completely oxygen terminated via several methods, including subjecting the material to oxygen plasma or boiling in acid.[148, 150-152]

The surface of diamond is relatively inert compared to other carbon electrodes, particularly with regard to the adsorption of species. Therefore, electrode reactions that require the adsorption of species/intermediates are strongly inhibited on diamond and require high overpotentials in order to drive the electrochemical reaction.[153-155] On the other hand, the inability of electroactive species to adsorb gives rise to a resistance of an electrode towards surface deactivation from fouling by adsorbed species; especially biological species such as dopamine, making it an ideal material for the detection of biomolecules.[141, 156-159] The electrolysis of water is an inner-sphere reaction, requiring the adsorption of intermediates in order for the evolution of oxygen (water oxidation) and hydrogen (water reduction) to take place.[154, 160-161] The inhibited (dissociative) adsorption at pBDD means the reaction is inhibited; hence, the requirement of large over-potentials to drive hydrogen and oxygen evolution.[154, 162] The wider potential window enables the detection of a greater range of electroactive species, previously impossible to measure due to the limitations of commonly used electrodes.[163-164] Diamond electrodes have been found to produce potential windows of 3-4 V in aqueous solution.[128-129, 143, 165-166]

Low background currents are another example of a superior characteristic demonstrated by pBDD electrodes. Low capacitance is due to the low DOS near the Fermi level.[167] This results in the capacitative currents being dominated by a space charge layer; where electrons move from the electrolyte solution to the electrode in order to achieve equilibrium, creating a depletion layer of holes at the surface.[168-169] The chemical inertness of the electrode surface also contributes to the low background currents; surface processes (surface oxide formation and reduction) that would contribute to background currents are negligible.[165] The result is in an improved electroanalytical sensitivity compared to conventional electrodes.

These remarkable chemical and physical properties depend greatly on the quality of the diamond; the presence of any sp^2 carbon both diminishes the potential window as well as making the electrode more reactive and less resistant towards surface blocking.[143, 170] sp^2 hybridised carbon is more electro-reactive towards oxygen and water and also allows the

adsorption of species via a range of intermolecular forces.[10] Lower quality pBDD, containing a significant amount of graphitic carbon thus has a potential window similar to that of GC and HOPG. The presence of graphitic carbon can be determined with Raman spectroscopy, which can also give an indication of the level of boron doping.[171-172]

The surface of pBDD has been studied using a wide range of techniques where it has been shown that the heterogeneous uptake of boron results in heterogeneous electrochemical and electrical properties. For example it has been found that the (111) crystal face may incorporate up to 10 times more boron than the (100) face during synthesis.[135-137] Using cathodoluminescence, field emission scanning electrochemical microscopy (FE-SEM) and Fluorescence Laser Scanning Confocal Microscopy studies have shown that different crystal facet orientations incorporate boron at different rates (Figure 1. 15).[173-176] Conducting atomic force microscopy (C-AFM) has been used to study the local resistivity of the pBDD surface and electrochemical imaging techniques such as scanning electrochemical microscopy (SECM) and scanning electrochemical cell microscopy (SECCM) have been employed to study the local electrochemical properties of pBDD (Figure 1. 15).[173, 176] These studies have shown that crystals of different orientations, and hence different boron concentration, which impacts on ET kinetics, more importantly these studies have shown that electrochemical activity occurs over an entire grain and is not limited to grain boundaries.[173-176]

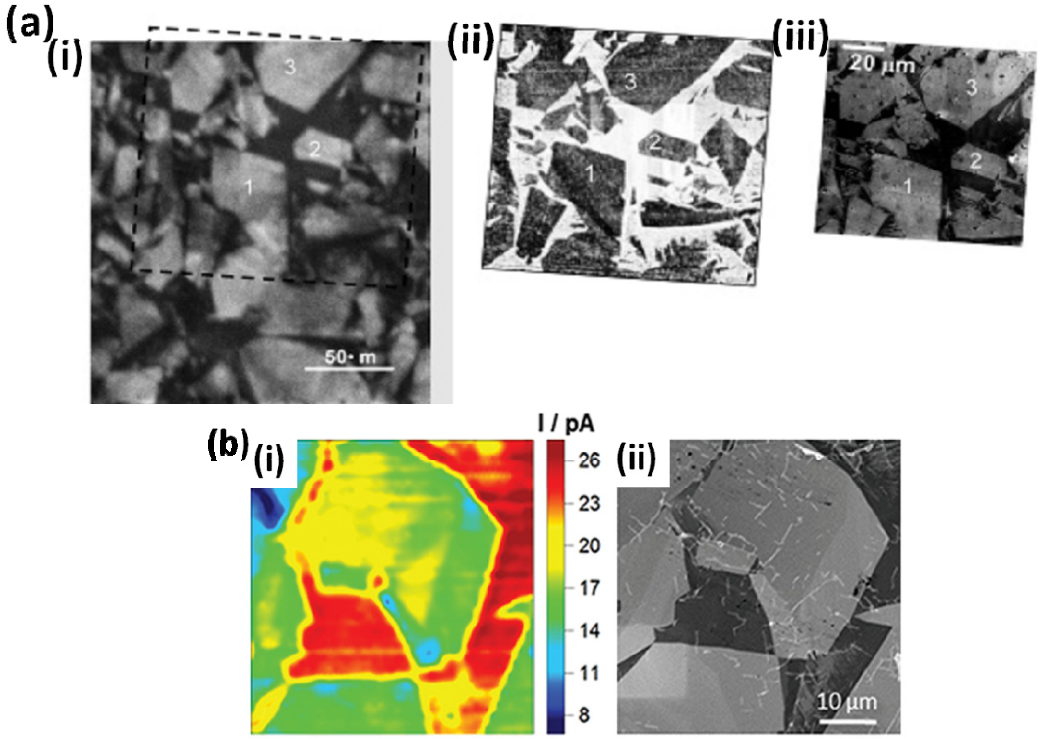

Figure 1. 15 (a) (i) Cathodoluminescence mapping; (ii) C-AFM image and (iii) FE-SEM image of a pBDD surface. Adapted from reference 173. (b) (ii) SECCM and FE-SEM image of a pBDD surface. Adapted from reference 176.

1.4 PROJECT AIM

It is evident from the overview that carbon electrodes have key attributes for use in electrochemical sensing and analysis, yet fundamental aspects of their behaviour are unclear. It is the hypothesis of this work that an improved understanding of carbon electrodes would aid in the design and optimisation of carbon electrodes particularly for electroanalysis.

Chapters 3 and 4 are concerned with understanding the electrochemical properties and surface effects of pyrolytic graphite.

Chapter 5 explores the reactivity of the neurotransmitter, DA, on the basal plane of HOPG and how it compares to GC, pBDD, BPPG and EPPG is examined in Chapter 6.

Chapter 7 investigates the relationship between the adsorption of 2,6-AQDS to step defect density of graphite surfaces in order to determine whether it is an appropriate measure for determining the quality of a carbon surfaces.

Chapter 8 explores the use of pBDD to study the neurotransmitter, 5-HT, and Chapter 9 studies its suitability for the development of a glucose sensor.

1.5 REFERENCES

1. Fisher, A. C., *Electrode Dynamics*. Oxford University Press: 2006.
2. Brett, C. M. A.,A. M. O. Brett, *Electrochemistry: Principles, Methods and Applications*. Oxford University Press: 2005.
3. Bard, A. J.,L. R. Faulkner, *Electrochemical methods : fundamentals and applications*. 2nd ed.; John Wiley & Sons: 2001.
4. Sato, N., *Electrochemistry at Metal and Semiconductor Electrodes*. Elsevier Science Ltd: Amsterdam, 2003.
5. Memming, R., *Semiconductor Electrochemistry*. John Wiley & Sons: Weinheim, 2008.
6. Ingber, D., *Sci. Am.,* **1998,** *278,* 48-57.
7. Inagaki, M., *New Carbons - Control of Structure and Functions*. ELSEVIER: Oxford, 2000.
8. Crespi, F.,K. Martin,C. Marsden, *Neuroscience,* **1988,** *27,* 885-896.
9. Bertrand, P. P., *Neurogastroent. Motil.,* **2004,** *16,* 511-514.
10. McCreery, R. L., *Chem. Rev,* **2008,** *108,* 2646-2687.
11. McDermott, M. T.,R. L. McCreery, *Langmuir,* **1994,** *10,* 4307-4314.
12. McCreery, R. L., *Electroanalytical Chemistry: A Series of Advance*. Marcel Dekker: New York, 1990; Vol. 17.
13. Harris, P. J. F., *Crit. Rev. Solid State Mater. Sci.,* **2005,** *30,* 235-253.
14. Zoski, C. G., *Handbook of Electrochemistry*. Elsevier: Amsterdam, 2007.
15. Robertson, J.,E. O'Reilly, *Phys. Rev. B.,* **1987,** *35,* 2946-2957.
16. Jenkins, G. M.,K. Kawamura, *Nature,* **1971,** *231,* 175-176.
17. McKee, D. W., *Annu. Rev. Mater. Sci.,* **1973,** *3,* 195-231.
18. Van der Linden, W. E.,J. W. Dieker, *Anal. Chim. Acta,* **1980,** *119,* 1-24.
19. Burket, C. L.,R. Rajagopalan,A. P. Marencic,K. Dronvajjala,H. C. Foley, *Carbon,* **2006,** *44,* 2957-2963.
20. Baker, D. F., *J. Non-Cryst. Solids,* **1983,** *58,* 57-69.
21. O'Reilly, E. P., *J. Non-Cryst. Solids,* **1987,** *97,* 1095-1102.
22. Lentz, C. M.,B. A. Samuel,H. C. Foley,M. A. Haque, *J Nanomater,* **2011**.
23. Schueller, O. J. A.,S. T. Brittain,C. Marzolin,G. M. Whitesides, *Chem. Mater.,* **1997,** *9,* 1399-1406.
24. Zittel, H. E.,F. J. Miller, *Anal. Chem.,* **1965,** *37,* 200-203.
25. Shigemitsu, T.,G. Matsumoto,S. Tsukahara, *Med Biol Eng Comput,* **1979,** *17,* 465-470.
26. Walker, P. L., *Carbon,* **1972,** *10,* ii-382.
27. Yamada, S.,H. Sato, *Nature,* **1962,** *193,* 261.
28. Chen, P. H.,R. L. McCreery, *Anal. Chem.,* **1996,** *68,* 3958-3965.
29. Kneten, K. R.,R. L. McCreery, *Anal. Chem.,* **1992,** *64,* 2518-2524.
30. Rice, R. J.,N. M. Pontikos,R. L. McCreery, *J. Am. Chem. Soc.,* **1990,** *112,* 4617-4622.
31. Chen, Q. Y.,G. M. Swain, *Langmuir,* **1998,** *14,* 7017-7026.
32. Engstrom, R. C., *Anal. Chem.,* **1982,** *54,* 2310-2314.
33. Alsmeyer, Y. W.,R. L. McCreery, *Langmuir,* **1991,** *7,* 2370-2375.
34. Hu, I.-F.,D. H. Karweik,T. Kuwana, *J. Electroanal. Chem.,* **1985,** *188,* 59-72.
35. Kamau, G. N.,W. S. Willis,J. F. Rusling, *Anal Chem,* **1985,** *57,* 545-551.
36. Pontikos, N. M.,R. L. McCreery, *J. Electroanal. Chem.,* **1992,** *324,* 229-242.
37. Kusano, Y.,H. Mortensen,B. Stenum,S. Goutianos,S. Mitra,A. Ghanbari-Siahkali,P. Kingshott,B. F. Sørensen,H. Bindslev, *Int. J. Adhes. Adhes.,* **2007,** *27,* 402-408.
38. Miller, C. W.,D. H. Karweik,T. Kuwana, *Anal. Chem.,* **1981,** *53,* 2319-2323.
39. Fagan, D. T.,I. F. Hu,T. Kuwana, *Anal. Chem.,* **1985,** *57,* 2759-2763.
40. Stutts, K. J.,P. M. Kovach,W. G. Kuhr,R. M. Wightman, *Anal. Chem.,* **1983,** *55,* 1632-1634.

41. Kamanu, G. N., *Anal. Chim. Acta,* **1988,** *207,* 1-16.
42. Pierson, H. O., *Handbook of chemical vapour deposition: Principles, Technology, and Applications*. 2nd ed.; Noyes Publications: New York, 1999.
43. Smith, D. P. E.,J. K. H. Horber,G. Binnig,H. Nejoh, *Nature,* **1990,** *344,* 641-644.
44. Ahlund, J.,J. Schnadt,K. Nilson,E. Gothelid,J. Schiessling,F. Besenbacher,N. Martensson,C. Puglia, *Surf. Sci.,* **2007,** *601,* 3661-3667.
45. Banks, C. E.,R. G. Compton, *The Analyst,* **2006,** *131,* 15-21.
46. Chung, D. D. L., *J. Mater. Sci.,* **2002,** *37,* 1475-1489.
47. Tuffanelli, A.,M. Sanchez del Rio,G. Pareschi,M. Gambaccini,A. Taibi,A. Fantini,M. Ohler, *Proc. SPIE,* **1999,** *3773,* 192-198.
48. No Title. www.ktechnano.com (accessed 31-05-2012).
49. www.ntmdt-tips.com. www.ntmdt-tips.com (accessed 31-05-2012).
50. http://www.2spi.com/catalog/new/hopgsub.php.
51. Xu, J.,Q. Chen,G. M. Swain, *Anal. Chem.,* **1998,** *70,* 3146-3154.
52. Edwards, M. A.,P. Bertoncello,P. R. Unwin, *J. Phys. Chem. C,* **2009,** *113,* 9218-9223.
53. McDermott, M. T.,K. Kneten,R. L. McCreery, *J. Phys. Chem.,* **1992,** *96,* 3124-3130.
54. Chang, H.,A. J. Bard, *Langmuir,* **1991,** *7,* 1143-1153.
55. Banks, C. E.,R. R. Moore,T. J. Davies,R. G. Compton, *Chem. Commun.,* **2004,** 1804-1805.
56. Banks, C. E.,R. G. Compton, *Anal. Sci.,* **2005,** *21,* 1263-1268.
57. Banks, C. E.,R. G. Compton, *The Analyst,* **2005,** *130,* 1232-1239.
58. Cooper, J. D.,J. Woore,D. A. Young, *Nature,* **1970,** *225,* 721-722.
59. I. L. Spain,A. R. U. and,D. A. Young, *Phil. Trans. R. Soc. ,* **1967,** *262,* 345-386
60. Banks, C. E.,T. J. Davies,G. G. Wildgoose,R. G. Compton, *Chem. Commun.,* **2005,** 829-841.
61. Cline, K. K.,M. T. Mcdermott,R. L. McCreery, *J. Phys. Chem.,* **1994,** *98,* 5314-5319.
62. Gerischer, H.,R. McIntyre,D. Scherson,W. Storck, *J. Phys. Chem.,* **1987,** *91,* 1930.
63. Morcos, I.,E. Yeager, *Electrochim. Acta,* **1975,** *15,* 257.
64. Gerischer, H., *J. Phys. Chem.,* **1985,** *89,* 4249-4251.
65. Hahn, M.,M. Baertschi,O. Barbieri,J. C. Sauter,R. Kotz,R. Gallay, *Electrochem Solid St,* **2004,** *7,* A33-A36.
66. Rice, R. J.,R. L. McCreery, *Anal. Chem.,* **1989,** *61,* 1637-1641.
67. Rice, R. J.,N. M. Pontikos,Rl, *Journal of the American,* **1990**.
68. Koivusaari, K. J.,T. T. Rantala,S. Leppävuori, *Diamond Relat. Mater.,* **2000,** *9,* 736-740.
69. Liu, H.,F. Favier,K. Ng,M. P. Zach,R. M. Penner, *Electrochim. Acta,* **2001,** *47,* 671-677.
70. Menke, E. J.,Q. Li,R. M. Penner, *Nano Lett.,* **2004,** *4,* 2009-2014.
71. Penner, R. M., *J. Phys. Chem. B,* **2002,** *106,* 3339-3353.
72. Zoval, J. V.,R. M. Stiger,P. R. Biernacki,R. M. Penner, *J. Phys. Chem.,* **1996,** *100,* 837-844.
73. Boxley, C. J.,H. S. White,T. E. Lister,P. J. Pinhero, *J. Phys. Chem. B,* **2003,** *107,* 451-458.
74. Gloaguen, F.,J. M. Leger,C. Lamy,A. Marmann,U. Stimming,R. Vogel, *Electrochim. Acta,* **1999,** *44,* 1805-1816.
75. Zubimendi, J. L.,L. Vazquez,P. Ocon,J. M. Vara,W. E. Triaca,R. C. Salvarezza,A. J. Arvia, *J. Phys. Chem.,* **1993,** *97,* 5095-5102.
76. Hendricks, S. A.,Y.-T. Kim,A. J. Bard, *J. Electrochem. Soc.,* **1992,** *139,* 2818-2824.
77. González Orive, A.,D. Grumelli,C. Vericat,J. M. Ramallo-López,L. Giovanetti,G. Benitez,J. C. Azcárate,G. Corthey,M. H. Fonticelli,F. G. Requejo,A. Hernández Creus,R. C. Salvarezza, *Nanoscale,* **2011,** *3,* 1708-1716.

78. Brülle, T.,U. Stimming, *J. Electroanal. Chem.,* **2009,** *636,* 10-17.
79. Peruffo, M.,P. Contreras-Carballada,P. Bertoncello,R. M. Williams,L. D. Cola,P. R. Unwin, *Electrochem. Commun.,* **2009,** *11,* 1885-1887.
80. Rodríguez-Nieto, F. J.,T. Y. Morante-Catacora,C. R. Cabrera, *J. Electroanal. Chem.,* **2004,** *571,* 15-26.
81. Cherstiouk, O. V.,P. A. Simonov,E. R. Savinova, *Electrochim. Acta,* **2003,** *48,* 3851-3860.
82. Armstrong, F. A.,A. M. Bond,H. A. O. Hill,B. N. Oliver,I. S. M. Psalti, *J. Am. Chem. Soc.,* **1989,** *111,* 9185-9189.
83. Armstrong, F. A.,A. M. Bond,H. A. O. Hill,I. S. M. Psalti,C. G. Zoski, *J. Phys. Chem.,* **1989,** *93,* 6485-6493.
84. Gorodetsky, A. A.,J. K. Barton, *J. Am. Chem. Soc.,* **2007,** *129,* 6074-6075.
85. Gorodetsky, A. A.,J. K. Barton, *Langmuir,* **2006,** *22,* 7917-7922.
86. Hui, F.,J.-M. Noël,P. Poizot,P. Hapiot,J. Simonet, *Langmuir,* **2011,** *27,* 5119-5125.
87. Bradbury, C. R.,L. Kuster,D. J. Fermín, *J. Electroanal. Chem.,* **2010,** *646,* 114-123.
88. Wang, M.,S. Bugarski,U. Stimming, *J. Phys. Chem. C,* **2008,** *112,* 5165-5173.
89. Ventosa, E.,J. L. Palacios,P. R. Unwin, *Electrochem. Commun.,* **2008,** *10,* 1752-1755.
90. Dumitrescu, I.,P. R. Unwin,J. V. Macpherson, *Chem. Commun.,* **2009,** *7345,* 6886-6901.
91. Pumera, M., *Chem. Soc. Rev.,* **2010,** *39,* 4146-4157.
92. Bowling, R. J.,R. T. Packard,R. L. McCreery, *J. Am. Chem. Soc.,* **1989,** *111,* 1217-1223.
93. Ji, X.,C. E. Banks,A. Crossley,R. G. Compton, *ChemPhysChem,* **2006,** *7,* 1337-1344.
94. Davies, T. J.,R. R. Moore,C. E. Banks,R. G. Compton, *J. Electroanal. Chem.,* **2004,** *574,* 123-152.
95. Lee, C.-Y.,S.-X. Guo,A. M. Bond,K. B. Oldham, *J. Electroanal. Chem.,* **2008,** *615,* 1-11.
96. Anne, A.,E. Cambril,A. Chovin,C. Demaille,C. Goyer, *ACS Nano,* **2009,** *3,* 2927-2940.
97. Williams, C. G.,M. A. Edwards,A. L. Colley,J. V. Macpherson,P. R. Unwin, *Anal. Chem.,* **2009,** *81,* 2486-2495.
98. Frederix, P. L.,P. D. Bosshart,T. Akiyama,M. Chami,M. R. Gullo,J. J. Blackstock,K. Dooleweerdt,N. F. de Rooij,U. Staufer,A. Engel, *Nanotechnology,* **2008,** *19,* 384004.
99. McCreery, R. L.,K. K. Cline,C. A. McDermott,M. T. McDermott, *Colloids Surf., A,* **1994,** *93,* 211-219.
100. Davies, T. J.,M. E. Hyde,R. G. Compton, *Angew. Chem.,* **2005,** *44,* 5121-5126.
101. Robinson, R. S.,K. Sternitzke,M. T. Mcdermott,R. L. McCreery, *J. Electrochem. Soc.,* **1991,** *138,* 2412-2418.
102. Amatore, C.,J. M. Savéant,D. Tessier, *J. Electroanal. Chem.,* **1983,** *147,* 39-51.
103. Ray, K.,R. L. McCreery, *Anal. Chem.,* **1997,** *69,* 4680-4687.
104. Banks, C. E.,P. M. Hallam, *Electrochem. Commun.,* **2011,** *13,* 8-11.
105. Chou, A.,T. Bocking,N. K. Singh,J. J. Gooding, *Chem. Commun.,* **2005,** 842-844.
106. Gong, K.,S. Chakrabarti,L. Dai, *Angew. Chem. Int. Ed.,* **2008,** *47,* 5446-5450.
107. Bertoncello, P.,J. P. Edgeworth,J. V. Macpherson,P. R. Unwin, *J. Am. Chem. Soc.,* **2007,** *129,* 10982-10983.
108. Day, T. M.,P. R. Unwin,J. V. Macpherson, *Nano Lett.,* **2007,** *7,* 51-57.
109. Day, T. M.,P. R. Unwin,N. R. Wilson,J. V. Macpherson, *J. Am. Chem. Soc.,* **2005,** *127,* 10639-10647.
110. Dudin, P. V.,P. R. Unwin,J. V. Macpherson, *J. Phys. Chem. C,* **2010,** *114,* 13241-13248.
111. Dumitrescu, I.,P. V. Dudin,J. P. Edgeworth,J. V. Macpherson,P. R. Unwin, *J. Phys. Chem. C,* **2010,** *114,* 2633-2639.

112. Dumitrescu, I.,P. R. Unwin,N. R. Wilson,J. V. Macpherson, *Anal. Chem.,* **2008,** *80,* 3598-3605.
113. Snowden, M. E.,P. R. Unwin,J. V. Macpherson, *Electrochem. Commun.,* **2011,** *13,* 186-189.
114. Wilson, N. R.,M. Guille,I. Dumitrescu,V. R. Fernandez,N. C. Rudd,C. G. Williams,P. R. Unwin,J. V. Macpherson, *Anal. Chem.,* **2006,** *78,* 7006-7015.
115. Heller, I.,J. Kong,H. A. Heering,K. A. Williams,S. G. Lemay,C. Dekker, *Nano Lett.,* **2005,** *5,* 137-142.
116. Heller, I.,J. Kong,K. A. Williams,C. Dekker,S. G. Lemay, *J. Am. Chem. Soc.,* **2006,** *128,* 7353-7359.
117. Kim, J.,H. Xiong,M. Hofmann,J. Kong,S. Amemiya, *Anal. Chem.,* **2010,** *82,* 1605-1607.
118. Li, W.,C. Tan,M. A. Lowe,H. D. Abruña,D. C. Ralph, *ACS Nano,* **2011,** *5,* 2264-2270.
119. Luong, J. H.,K. B. Male,J. D. Glennon, *Analyst,* **2009,** *134,* 1965-1979.
120. Yao, Y.,Y. Kubota,T. Murakami,T. Ochiai,H. Ishiguro,K. Nakata,A. Fujishima, *J Water Health,* **2011,** *9,* 534-543.
121. Granger, M. C.,M. Witek,J. Xu,J. Wang,M. Hupert,A. Hanks,M. D. Koppang,J. E. Butler,G. Lucazeau,M. Mermoux,J. W. Strojek,G. M. Swain, *Anal Chem,* **2000,** *72,* 3793-3804.
122. Spataru, N.,B. V. Sarada,E. Popa,D. A. Tryk,A. Fujishima, *Anal. Chem.,* **2001,** *73,* 514-519.
123. Xu, J.,M. C. Granger,Q. Chen,J. W. Strojek,T. E. Lister,G. M. Swain, *Anal. Chem.,* **1997,** *69,* 591A-597A.
124. Xu, J. Z.,G. M. Swain, *Anal. Chem.,* **1998,** *70,* 1502-1510.
125. Saterlay, A. J.,J. S. Foord,R. G. Compton, *Analyst,* **1999,** *124,* 1791-1796.
126. Kubovic, M.,M. Kasu, *Appl Phys Express,* **2009,** *2*.
127. Kawarada, H., *Surf. Sci. Rep.,* **1996,** *26,* 205-206.
128. Pleskov, Y. V., *Russ. J. Electrochem.,* **2002,** *38,* 1275-1291.
129. Ristein, J., *Structural and electronic properties of diamond surfaces*. Elsevier B. V.: Amsterdam, 2004; Vol. 2.
130. Fryda, M.,T. Matthee,S. Mulcahy,A. Hampel,L. Schafer,I. Troster, *Diamond Relat. Mater.,* **2003,** *12,* 1950-1956.
131. Lagrange, J. P.,A. Deneuville,E. Gheeraert, *Diamond Relat. Mater.,* **1998,** *7,* 1390-1393.
132. Ye, H.,N. Tumilty,M. Bevilacqua,S. Curat,M. Nesladek,B. Bazin,P. Bergonzo,R. B. Jackman, *J. Appl. Phys.,* **2008,** *103*.
133. Spicka, H.,M. Griesser,H. Hutter,M. Grasserbauer,S. Bohr,R. Haubner,B. Lux, *Diamond Relat. Mater.,* **1996,** *5,* 383-387.
134. Shiomi, H.,Y. Nishibayashi,N. Fujimori, *Japanese Journal of Applied Physics,* **1991,** *30,* 1363-1366.
135. Janssen, G.,W. J. P. Vanenckevort,W. Vollenberg,L. J. Giling, *Diamond Relat. Mater.,* **1992,** *1,* 789-800.
136. Samlenski, R.,C. Haug,R. Brenn,C. Wild,R. Locher,P. Koidl, *Diamond Relat. Mater.,* **1996,** *5,* 947.
137. Spitsyn, B. V.,L. L. Bouilov,B. V. Derjaguin, *J. Cryst. Growth,* **1981,** *52,* 219.
138. Manivannan, A.,D. A. Tryk,A. Fujishima, *Electrochem Solid St,* **1999,** *2,* 455-456.
139. Suzuki, A.,T. A. Ivandini,K. Yoshimi,A. Fujishima,G. Oyama,T. Nakazato,N. Hattori,S. Kitazawa,Y. Einaga, *Anal Chem,* **2007,** *79,* 8608-8615.
140. Xu, J.,Q. Chen,G. M. Swain, *Anal Chem,* **1998,** *70,* 3146-3154.
141. Fujishima, A.,D. Shin,D. A. Tryk,A. Merkoci,J. Wang, *Electroanal.,* **2005,** *17,* 305-311.
142. Compton, R. G.,J. S. Foord,F. Marken, *Electroanal.,* **2003,** *15,* 1349-1363.

143. Angus, J. C.,Y. V. Pleskov,S. C. Eaton, *Electrochemistry of diamond*. Elsevier B. V.: Amsterdam, 2004; Vol. 2.
144. Girard, H. A.,N. Simon,D. Ballutaud,E. de La Rochefoucauld,A. Etcheberry, *Diamond Relat. Mater.,* **2007,** *16,* 888-891.
145. Rao, T. N.,D. A. Tryk,K. Hashimoto,A. Fujishima, *J. Electrochem. Soc.,* **1999,** *146,* 680-684.
146. Shirafuji, J.,Y. Sakamoto,A. Furukawa,H. Shigeta,T. Sugino, *Diamond Relat. Mater.,* **1995,** *4,* 984-988.
147. Yano, T.,D. A. Tryk,K. Hashimoto,A. Fujishima, *J. Electrochem. Soc.,* **1998,** *145,* 1870-1876.
148. Yagi, I.,H. Notsu,T. Kondo,D. A. Tryk,A. Fujishima, *J. Electroanal. Chem.,* **1999,** *473,* 173-178.
149. Yano, T.,E. Popa,D. A. Tryk,K. Hashimoto,A. Fujishima, *J. Electrochem. Soc.,* **1999,** *146,* 1081-1087.
150. Pehrsson, P. E.,J. P. Long,M. J. Marchywka,J. E. Butler, *Appl. Phys. Lett.,* **1995,** *67,* 3414-3416.
151. Liu, F. B.,J. D. Wang,B. Liu,X. M. Li,D. R. Chen, *Diamond Relat. Mater.,* **2007,** *16,* 454-460.
152. Salvadori, M. C.,W. W. R. Araujo,F. S. Teixeira,M. Cattani,A. Pasquarelli,E. M. Oks,I. G. Brown, *Diamond Relat. Mater.,* **2010,** *19,* 324-328.
153. Canizares, P.,C. Saez,J. Lobato,M. A. Rodrigo, *Afinidad,* **2006,** *63,* 121-129.
154. Panizza, M.,G. Cerisola, *Electrochim. Acta,* **2005,** *51,* 191-199.
155. Ivandini, T. A.,B. V. Sarada,C. Terashima,T. N. Rao,D. A. Tryk,H. Ishiguro,Y. Kubota,A. Fujishima, *J. Electroanal. Chem.,* **2002,** *521,* 117-126.
156. Wei, M.,Y. Zhou,J. Zhi,D. Fu,Y. Einaga,A. Fujishima,X. Wang,Z. Gu, *Electroanal.,* **2008,** *20,* 137-143.
157. Rao, T. N.,A. Fujishima, *Diamond Relat. Mater.,* **2000,** *9,* 384-389.
158. Swain, G. M.,M. Hupert,A. Muck,R. Wang,J. Stotter,Z. Cvackova,S. Haymond,Y. Show, *Diamond Relat. Mater.,* **2003,** *12,* 1940-1949.
159. Trouillon, R.,D. O'Hare, *Electrochim. Acta,* **2010,** *55,* 6586-6595.
160. Conway, B. E.,M. Salomon, *Electrochim. Acta,* **1964,** *9,* 1599 -1615.
161. Rossmeisl, J.,A. Logadottir,J. K. Norskov, *Chem. Phys.,* **2005,** *319,* 178-184.
162. Yoshimura, M.,K. Honda,T. Kondo,R. Uchikado,Y. Einaga,T. N. Rao,D. A. Tryk,A. Fujishima, *Diamond Relat. Mater.,* **2002,** *11,* 67-74.
163. Fujishima, A.,T. N. Rao,D. A. Tryk, *Electrochim. Acta,* **2000,** *45,* 4683-4690.
164. Granger, M. C.,J. Xu,J. W. Strojek,G. M. Swain, *Anal. Chim. Acta,* **1999,** *397,* 145-161.
165. Kraft, A., *Int J Electrochem Sc,* **2007,** *2,* 355-385.
166. May, P. W., *Philos T Roy Soc A,* **2000,** *358,* 473-495.
167. Swain, G. M.,R. Ramesham, *Anal. Chem.,* **1993,** *65,* 345-351.
168. Bott, A. W., *Current Separations,* **1998,** *17,* 87-91.
169. Pleskov, Y. V., *Electrochemistry of Diamond: Semiconductor and Structural Aspects*. Elsevier B. V: Amsterdam, 2005.
170. Foord, J.,J. P. Hu, *Phys Status Solidi A,* **2006,** *203,* 3121-3127.
171. Ferrari, A. C.,J. Robertson, *Philosophical transactions. Series A, Mathematical, physical, and engineering sciences,* **2004,** *362,* 2477-2512.
172. Filik, J., *Spectrosc. Eur.,* **2005,** *17,* 16-17.
173. Wilson, N. R.,S. L. Clewes,M. E. Newton,P. R. Unwin,J. V. Macpherson, *J. Phys. Chem. B,* **2006,** *110,* 5639-5646.
174. Wang, S.,G. M. Swain, *J. Phys. Chem. C,* **2007,** *111,* 3986-3995.
175. Colley, A. L.,C. G. Williams,U. D'Haenens Johansson,M. E. Newton,P. R. Unwin,N. R. Wilson,J. V. Macpherson, *Anal. Chem.,* **2006,** *78,* 2539-2548.

176. Patten, H. V.,S. C. Lai,J. V. Macpherson,P. R. Unwin, *Anal Chem,* **2012,** *84,* 5427-5432.

CHAPTER 2: EXPERIMENTAL

This section details the instrumentation, methodologies, reagents and apparatus used in the experiments described in this thesis.

2.1 CHEMICALS AND MATERIALS

2.1.1 Chemicals

All chemicals were used as received and all solutions were prepared with high purity Milli-Q reagent water (Millipore Corp.) with a resistivity of *ca.* 18.2 MΩ cm at 25°C. Chemicals were weighed using a four decimal place analytical balance (Sartorius A2008) and pH of solutions measured using a pH meter (PHM201 Portable pH meter, Radiometer, Copenhagen). Table 2.1 lists all the chemicals used in this thesis.

Table 2.1 Chemicals and materials used within this thesis including supplier

Chemicals	Commercial source
Potassium ferrocyanide trihydrate ($K_4Fe(CN)_6 \cdot 3H_2O$) 99.99%	Sigma-Aldrich
Potassium ferrocyanide trihydrate ($K_4Fe(CN)_6 \cdot 3H_2O$) 99.0%	Fisher Scientific
Potassium chloride (KCl) 99.99%	Fisher Scientific
Hexaammineruthenium(III) chloride ($Ru(NH_3)_6Cl_3$) 99.00%	Strem Chemicals
0.1 M phosphate buffer saline (pH 7.2)	Sigma-Aldrich
Silver nitrate ($AgNO_3$) 99.99%	Sigma-Aldrich
Potassium nitrate (KNO_3) 99.99%	Sigma-Aldrich
Sulphuric acid (H_2SO_4) 99.9%	Sigma-Aldrich
Acheson Electrodag (1415M)	Agar Scientific
Serotonin hydrochloride >98%	Sigma-Aldrich
4-(2-hydroxyethyl)-1-piperazineethanesulfonic acid (HEPES, BioUltra grade)	Sigma-Aldrich
Ferrocenemethanol ($Fe(CH_3OH)$) 97%	Sigma-Aldrich
Dopamine hydrochloride (98%)	Sigma-Aldrich
L (+)-Ascorbic acid sodium > 98%	Sigma-Aldrich
Disodium anthraquinone-2,6-disulfonate (2,6-AQDS)	Acros organics
Perchloric acid (70%)	Acros organics
Glucose oxidase type II-S (GOx, EC 1.1.3.4; Aspergillus niger, 50K units/g)	Sigma-Aldrich
Glutaraldehyde grade I, 25% in water (GA)	Sigma-Aldrich

Bovine serum albumin (BSA, fraction V, 99%)	Sigma-Aldrich
Nafion 117 solution (5 wt% in lower aliphatic solutions),	Sigma-Aldrich
Methanol (Analytical grade)	Sigma-Aldrich
Sodium chloride (NaCl, 99.9%)	Sigma-Aldrich
$_D$-(+)-Glucose (99.9%)	Sigma-Aldrich
Silver loaded epoxy	RS components
Alumina slurry (0.005 micron suspension)	Buehler
Microcloth pad	Buehler
Carbimat paper	Buehler
GC electrode	CH Instruments
BPPG and EPPG	Mersen
HOPG samples (grades SPI-1, SPI-2, ZYA and ZYH)	SPI Supplies
HOPG (AM) kindly provided by Prof. R. L. McCreery (University of Alberta, Canada). This originated from Dr. A. Moore, Union Carbide (now GE Advanced Ceramics).	GE Advanced Ceramics
pBDD samples	Element Six
Potentiostat (models CH1040A and CH600b)	CH Instruments

2.2 CARBON ELECTRODES

GC electrodes were bought ready to use. All graphite samples were mounted on silicon wafers, which had been sputtered with ~20 nm titanium followed by a ~400 nm of gold using an Edwards E306 sputter/evaporator. An electrical connection was made between the graphite sample and coated silicon wafer by using Acheson Electrodag (Agar Scientific, 1415M) to mount the samples. An external electrical contact was created by lowering a metal pin on to the gold surface using a probe micro-positioner; this method also enabled the samples to be secured for AFM. A schematic is shown Figure 2. 1.

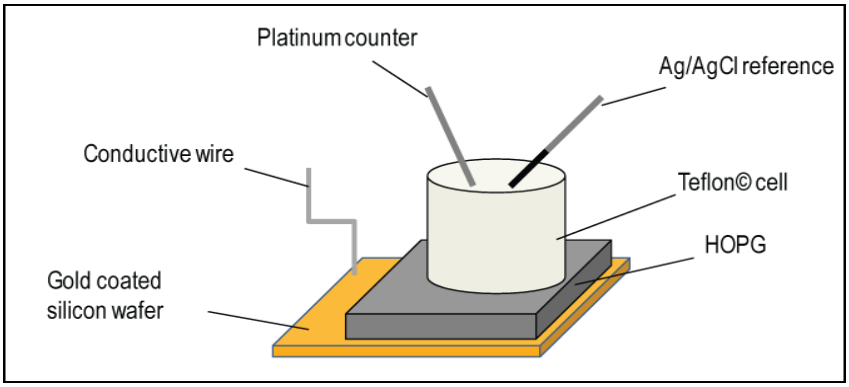

Figure 2. 1 Schematic of the electrochemical set-up employed for graphite electrodes.

The surface of each electrode was cleaned and renewed before any experiment was performed. For BPPG, a fresh surface was prepared by abrasively polishing on fine silicon carbide paper (Carbimat paper, Buehler Ltd) and then using scotch tape to remove the top layers by gently pressing down and then lifting off the tape, as described by Compton *et al;*[1-2] this was repeated at least three times. For EPPG, a fresh surface was prepared by polishing in alumina on emery pad, rinsing and then polishing on wet microcloth pad to ensure the removal of alumina.

The following two methods were found to provide reproducible freshly exposed surfaces, on the commercially available grades of HOPG: ZYA, ZYH, SPI-1 and SPI-2. In the first method, single-sided scotch tape was gently pressed onto the HOPG surface and then pulled off to remove the top layers. Alternatively, a second glass slide bearing double-sided adhesive tape was gently contacted to the HOPG basal surface and pulled vertically away from the substrate to reveal a freshly created surface. It was found that both cleaving methods produced similar surface topography and indistinguishable voltammetric response, as verified by AFM (Chapter 4) and FE-SEM (Chapter 4), and complementary capacitance measurements (Chapter 4). Consequently, the former was used for all studies in this thesis (unless otherwise stated), as it removes fewer basal plane layers per cleave, therefore allowing more experiments with each HOPG sample.

All HOPG (AM) samples were cleaved using a razor blade, as directed by Professor Richard McCreery in private correspondence. A fresh razor blade was gently inserted perpendicular to the basal plane and by gentle rocking of the blade through the sample, spontaneous cleavage of a piece of HOPG was encouraged. This cleaving method yielded HOPG pieces for which the cleaved area varied; only samples at least 1 x 1 cm. Initial capacitance measurements and voltammetric experiments were carried out with a droplet before using the Teflon cell. Both approaches yielded indistinguishable behaviour.

The pBDD samples were received as large wafers, approximately 500 μm thick with a roughness of 1-3 nm μm^{-2}. The average boron doping level of the pBDD material was *ca.* 5×10^{20} atoms cm^{-3}, as determined by secondary ion mass spectroscopy.[3] Preparation of pBDD into an electrode is described below. Firstly, small discs, approximately 1 mm in diameter, were cut from the large wafer using a laser micromachining (E-355H-3-ATHI-O system, Oxford Lasers). The cut pBDD samples were cleaned in acid to remove any sp^2 carbon left behind from the lasering. This cleaning process involved gently boiling in concentrated sulphuric acid (98%) saturated with KNO_3. The samples were left to boil until the fumes released went from brown to white, indicated the exhaustion of the nitrate. After the solution had cooled, the sample was removed, rinsed, and left to dry.

Next, an electrical contact was made by sputtering titanium and gold on the pBDD samples. A Ti/Au back contact layer has been found to provide a low resistance ohmic contact when annealed to pBDD.[4] A ~20 nm layer of titanium followed by a ~400 nm layer of gold was sputtered on all the diamond samples using an Edwards E306 sputter/evaporator. The samples were then left to anneal in an in a tube furnace (MTF 12/25/400, Carbolite, UK) at 500°c for 4 hours.

Finally, the pBDD was sealed in a pulled glass capillary (o.d. 2 mm, i.d. 1.16 mm, Harvard Apparatus Ltd, Kent, UK), which had been pulled using a micropipette puller (*PB-7* , Narishige), using a hot filament to melt the glass around the side of the diamond. An electrical contact was made with the pBDD sample using a tinned copper wire, by loading the capillary with silver epoxy resin and then pushing the wire through, as shown in Figure 2. 2. The capillary was then polished back with using carbimet grit paper discs (Buehler, Germany), to reveal the surface of the pBDD.

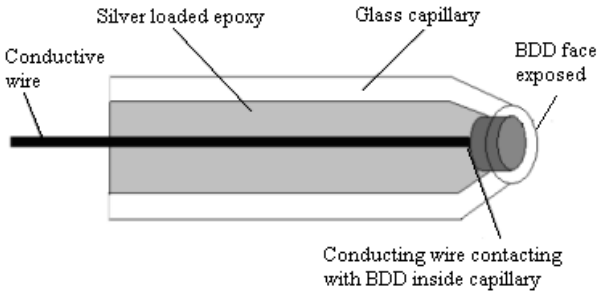

Figure 2. 2 A schematic highlighting the in-house fabrication of a pBDD electrode.

Before use, the electrode was polished on alumina on a microcloth pad, rinsed and polished again on a wet microcloth pad. The electrode was tested by running a voltammogram in 0.1 KNO_3 and then in $Ru(NH_3)_6^{3+}$ to check the resistance, the capacitance and the potential window.

2.3 VOLTAMMETRIC MEASUREMENTS

CV measurements were recorded using a potentiostat (see Table 2.1 for details). For pBDD and GC, before each experiment the electrode surface was cleaned and renewed by polishing in alumina on microcloth pad, rinsing and then polishing on wet microcloth pad to ensure the removal of alumina. The clean electrode was immersed in a solution of *ca.* 10 mL, with a platinum gauze electrode as the counter electrode or a commercial saturated calomel electrode and a commercial Ag/AgCl electrode or a commercial saturate calomel electrode employed as the reference electrode.

For all graphite samples electrochemical measurements were performed in a droplet arrangement or in a Teflon cell arrangement (Figure 2. 1 and further described below), where a Pt wire served as the counter electrode and a chloridised silver wire served as the reference electrode.

2.4 ELECTROCHEMICAL SETUP

2.4.1 Droplet arrangement

The droplet arrangement requires a humidified cell in order to minimize solution evaporation. The HOPG electrode was placed on a small Perspex block which, in turn, sat on a larger Teflon base. A larger glass cell body containing a small outlet hole was pushed over the Teflon base to create a tight seal. The cell was filled with water to a level slightly lower than the height of the Perspex block and deaerated with nitrogen or argon for 15 minutes. The freshly cleaved HOPG sample was then placed in the cell and a droplet of the solution of interest (either 10 µl, with a diameter of ~3 mm, or 20 µl, with a diameter ~ 5 mm) was gently placed on the surface of the HOPG in an area that by eye, appeared to be the most "shiny" and hence comprised the highest degree of the pristine basal surface as confirmed by FE-SEM and AFM. The droplet was typically placed on the HOPG surface within 1 min of sample cleaving, and the reference electrode and auxiliary electrode added. The cell was sealed using parafilm, and humidified by gently passing nitrogen gas through the droplet cell. A schematic is shown in Figure 2. 3(a).

2.4.2 Teflon cell arrangement

The Teflon cell arrangement utilized a cell with outer cylindrical dimensions of 8 mm diameter by 6 mm height, machined internally to a cylindrical diameter of 6 mm (4 mm in height), which decreased to a diameter of 3 mm (2 mm in height at the part closest to the substrate). A schematic is shown in Figure 2. 3(b). The bottom of the cell *was very* lightly greased with Apeizon wax, with any excess removed with tissue, and then positioned gently on the HOPG surface. The cell was filled with ca. 100 µl of solution into which the auxiliary and reference electrodes were placed. Using this arrangement the electrode contact area was defined as a 3 mm diameter disc and it was possible to deaerate solution directly in contact with the HOPG surface (using nitrogen). However, similar results were obtained with and without deaeration of the solution and, consequently, most experiments were conducted without deaeration of the solution.

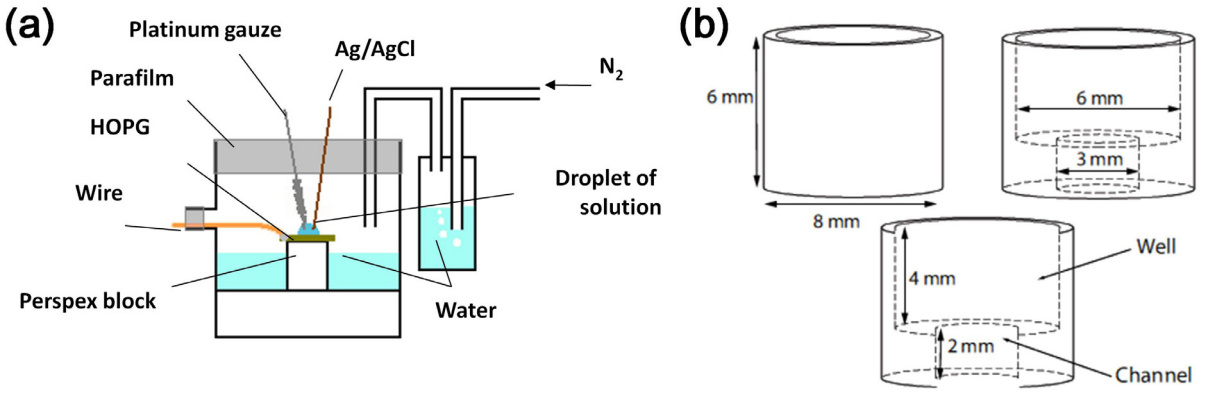

Figure 2. 3 (a) Schematic of the humidity cell used for some CV measurements on HOPG. Not to scale. (b) Schematic of the Teflon cell used to hold solution on HOPG with a defined contact area.

2.5 ATOMIC FORCE MICROSCOPY (AFM)

Tapping mode (TM) AFM imaging provides topographical mapping of a surface at nanometre resolution, without damaging the substrate, by measuring the force between a tip mounted on a cantilever and the surface under investigation. Changes in the force interaction between the tip and substrate are used to maintain a constant tip-to-sample separation using positional feedback. The cantilever is mounted on a holder and connected to a piezoelectric scanner which is then used to drive the tip to oscillate at a frequency close to resonance. The deflection of a laser from the backside of the cantilever onto a split photodiode detector, via a mirror, is used to measure the force between the tip and the substrate. When the tip encounters the surface, there is an interaction which causes a shift in the resonance frequency and decreases the oscillation amplitude which is detected by the deflection of the laser. Using a lock-in amplifier with feedback positioning, the amplitude of the oscillation is used as a set-point to maintain a constant tip-to-sample separation whilst scanning the surface in a raster fashion.[5] TM-AFM provides information on not only topography but also adhesion, friction and viscoelasticity.[6] Various modes of AFM enable a wider range of information to be collected under various conditions.

In this thesis in air TM-AFM imaging was performed using a Bruker Nano Multimode V AFM with Nanoscope V controller, using RFESP (Veeco) tips. Topographical, amplitude and phase data were obtained simultaneously.

In-situ AFM experiments were carried out using a Veeco Bioscope catalyst AFM, operated in Tapping Mode™ and imaging was performed using standard silicon nitride tips (NP-type). Topographical, amplitude and phase imaging of the sample was obtained simultaneously. *In-situ* electrochemical measurements were carried out using CH instruments model 800B

potentiostat (Austin, Texas). A chloridised silver wire electrode served as the quasi-reference electrode and a Pt wire was used as the counter electrode. Figure 2. 4 shows a schematic for the modification of in-air tapping mode AFM to this method of imaging.

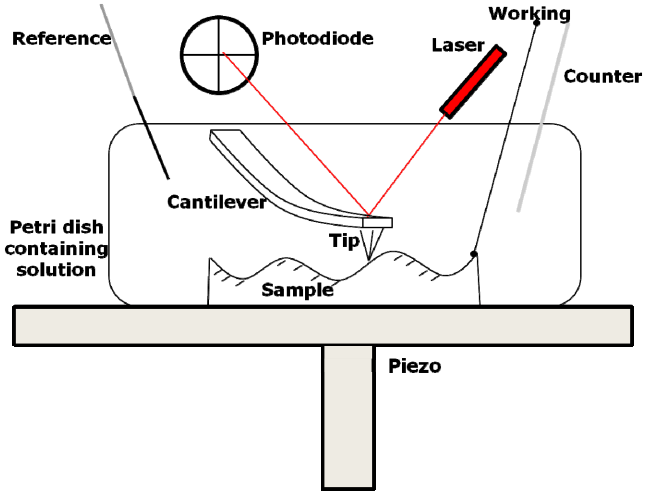

Figure 2. 4 Schematic diagram for *in-situ* AFM. The sample under investigation was secured in a petri dish and filled with the electrolyte solution containing the redox species. A reference electrode and counter electrode were placed into the electrolyte solution and the substrate was connected as the working electrode. Electrochemistry was externally driven using a CH potentiostat.

C-AFM images were obtained using a Veeco Multimode V AFM with a conducting module and Nanoscope V controller. In imaging mode, a bias of 20 mV was typically applied to a Pt−Ir coated Si probe (SCM-PIC, Bruker, quoted nominal radius of curvature ~20 nm) using the controller, with a current-limiting resistor of 1 MΩ in series with the grounded sample; the current output was detected by the controller. Topographical, deflection error and conductivity imaging of the sample was carried out simultaneously. Figure 2. 5 shows a schematic for the modification of in-air contact mode AFM to this method of imaging. Experiments were also made where the tip was held stationary in an area of interest and conductance current-voltage (*i*-V) curves recorded. After measurements, the integrity of all conducting tips was checked by replacing the sample with a new piece of freshly cleaved HOPG.

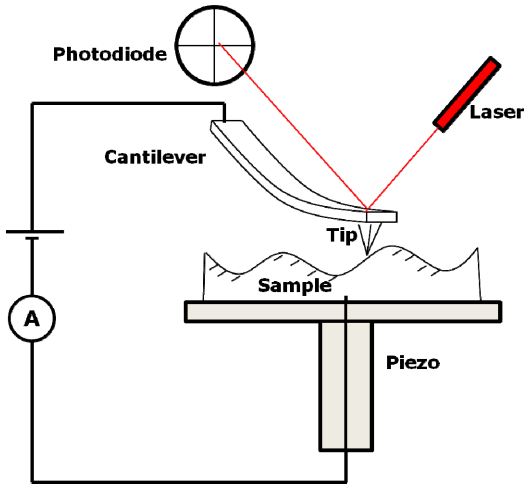

Figure 2. 5 Schematic diagram for C-AFM set-up. The conductive substrate under investigation was held at ground, and a bias was applied to a conducting tip. The current flowing between the tip and substrate was measured.

2.6 FIELD EMISSION SCANNING ELECTRON MICROSCOPY (FE-SEM)

Depending on the type of detector used during imaging, different information can be collected on the samples of interest. The secondary electron emission detector provides high-resolution images informing of surface morphology; whilst the in-lens detector informs of elemental composition as well as the topography of the sample. FE-SEM imaging was performed under vacuum using a Zeiss SUPRA 55 VP field emission SEM with an in-lens detector and a secondary electron emission detector was used to obtain images.

2.7 LANGMUIR-BLODGETT AND LANGMUIR-SCHAEFER FILMS

The Langmuir-Schaefer (LS) techniques are interesting methods for creating modified surfaces.[7-9] The LS method was used in this work to create an enzyme immobilised electrode, as it allowed for the transfer of ultra-thin films in which the thickness of the film, density and the orientation of the molecules could controlled.[10-11] The basis of the technique is the formation of a monolayer at the liquid/air interface of a suitable sub-phase solvent; Figure 2. 6 outlines the basic concept. Amphiphilic molecules are trapped at the interface where they self-assemble.

The following describes how thin films of immobilised glucose oxidase (GOx) were made. A solution containing 10 mg/mL of glucose oxidase (GOx) in phosphate buffered saline (PBS), which was cross-linked with 35 mg of bovine serum albumin (BSA) and 1 mL glutaraldehyde (GA). The enzyme was then copolymerised in 400 µl of Nafion (diluted to 2.5% using methanol). This solution was then allowed to sit for ~30 min in order to allow the Nafion/GA/BSA/GOx mixture to homogenise.

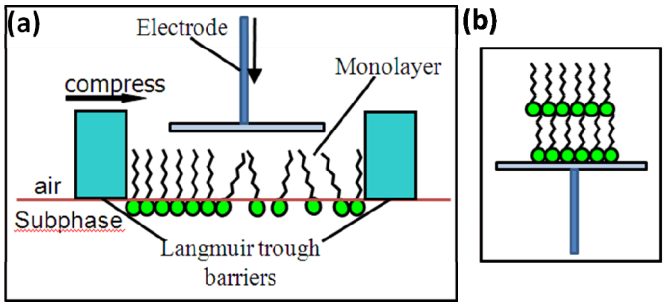

Figure 2. 6 Outline of (a) monolayer formation on a Langmuir trough and (b) electrode surface after two monolayer transfers.

The sub-phase for the Langmuir trough was prepared 0.1 M aqueous KNO_3. Using a Wilhemy balance, the surface pressure was measured within an accuracy of ± 0.1 mN m^{-1}. After 5 minutes of having added the Nafion/GA/BSA/GOx mixture onto the sub-phase, compression of the floating films began. Based on the obtained Langmuir isotherm (Chapter 9), a surface pressure of 25 mN m^{-1} was established and maintained. A layer of the film was transferred onto the electrodes surface by binging the electrode surface down towards the film until contact was made. The electrode was removed vertically and allowed to dry before the addition of another. Once a desired number of layers had been transferred, the electrode was stored in a solution of 0.1 mM $FcTMA^+$ (0.1 M PBS, pH 7.2) for at least 24 hours at room temperature (*ca.* 20-25°C).

2.8 ELLIPSOMETRY

Ellipsometry is a spectroscopic technique in which a polarised light is reflected off a sample. The change in polarisation is detected and using mathematical modelling used to extract a series of information. The technique can provide information on the a variety of sample properties, including morphology, crystal quality, chemical composition, or electrical conductivity.[12] It is commonly used to characterise film thickness and has a resolution of a few angstroms or tenths of a nanometer to several micrometers.[12]

Ellipsometry (UVISEL spectroscopic ellipsometer, Horiba Jobin-Yvon, UK) operating with DeltaPsi2 v2.0.8 software was used in order to determine the thickness of LS films on pBDD substrate. The angle of incidence was set to 70˚. The wavelength range for the incident light was 250-800 nm. The spot size used covered approximately 2 mm^2 of the sample. Calculation of the mean film thicknesses was performed for each measurement, based on a three-phase ambient/film/counter surface model, in which the film was assumed to be isotropic and modelled using a simple classical layer model, with an initial thickness that was varied using a multivariate iterative calculation procedure.

2.9 SCANNING ELECTROCHEMICAL CELL MICROSCOPY (SECCM)

SECCM utilises a liquid meniscus that forms at the end of a dual-channel pipette as a positionable and mobile nanoelectrochemical cell once in contact with a working electrode surface.[13-15] The idea of using a droplet cell was first proposed in the mid 1990's for high resolution corrosion studies[16-17] but was significantly advanced to enable the simultaneous study of topography, surface electroacitivity and conductivity in the 2010.[13] As with TM-AFM, a positional feedback loop is employed to maintain a contant tip-to-substrate seperation during scanning, but unlike in TM-AFM where the force interaction between the tip and the substrate surafce is used to maintain the seperation, in SECCM it is a component of the ion conductance current (see below). The technique is capable of delivering high mass transport rates, and allows for the analysis of ET at an electrode surface, the study of ion transfer, and enables the control of mass transport via the potential bias between the two barrels. This technique has an advantage over conventional microscopy techniques, such as SECM, as it utilises a confined droplet to probe the surface of interest, collecting fresh measurements on a fresh surface. In SECM the surface of interest is often immersed in electrolyte solution under potential control for long time periods (e.g. 1-2 hours), during which changes in the properties of the surface and the probe can change. Another disadvantage of SECM is restrictions in being able to maintain a contant tip-to-substrate seperation and resolution.

A dual-channel glass pipette (o.d. 1.5 mm, i.d. 0.17 mm, TGC150-10, Harvard Apparatus) was pulled to a sharp taper using a CO_2-laser puller (P-2000, Sutter Instruments). The dimensions of the tapered opening were measured accurately with FE-SEM for each experiment. The resulting pipettes were silanised[18] to ensure a hydrophobic outer wall. Each channel was filled with the solution of interest and a freshly chloridised silver wire (99.9%, Mateck) was inserted into each channel; these wires served as quasi-reference counter electrodes (QRCEs). The pipette was mounted on a high-dynamic *z*-piezoelectric positioner (P-753.3CD LISA, Physik Instrumente), the substrate of interest was mounted on a *xy*-piezoelectric stage (P-622.2CL PIHera, Physik Instrumente). A potential bias was applied between the two QRCEs which resulted in the generation of a conductance current (direct component (DC)) across the meniscus. A sinusoidal oscillation (20 nm peak amplitude, 233.3 Hz) was imposed on the *z*-position of the tip, generated by lock-in amplifier (SR830, Stanford Research Instruments). The pipette was then translated towards the surface until contact was made between the meniscus of the pipette and the electrode surface to form the positionable and mobile electrochemical cell. The set-up is highlighted schematically in Figure 2. 7(a).

Upon contact, three changes are detected: there is the development of a surface current; an increase in the DC conductance current between the two channels; and the development of an alternating current (AC) component of the conductance current. The development of a surface current provides conformation of surface activity and the formation of the electrochemical cell. An increase in the DC conductance current is due to the wetting of the liquid meniscus on the substrate surface upon contact, which causes an increase in the droplet size and a decrease in the local resistance. The conductance current is a measure of the flow of ions across the two barrels and, hence, is directly related to the droplet size, therefore, an increase in the meniscus due to wetting size leads to an increase in the DC conductance current between the barrels. Hence, during a scan, small disturbances in the AC conductance current and DC conductance current can be indicative of small changes in the droplet size and/or surface properties. The development of the AC component for the conductance current upon contact, is due to the oscillation imposed on the pipette using the *z*-piezoelectric positioner. This causes a periodic deformation of the liquid meniscus, which in turn modulates the droplet resistance, hence the AC conductance current is also related to

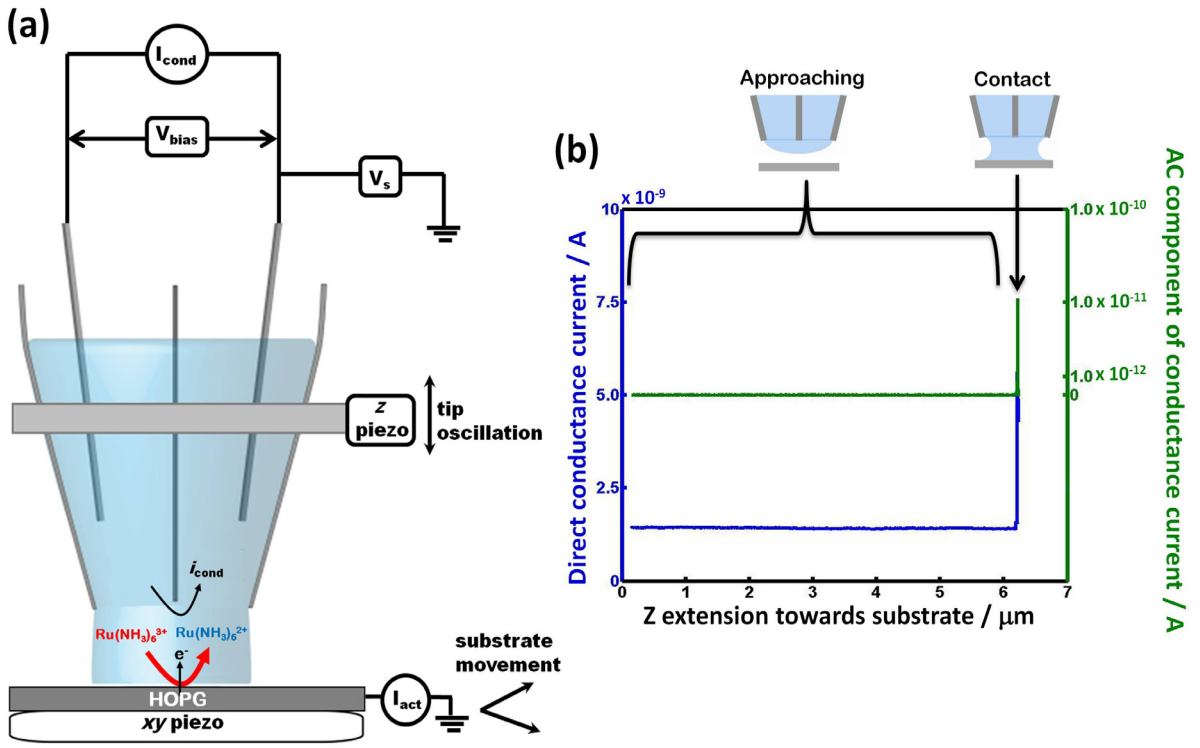

Figure 2. 7 (a) Schematic of the set up for SECCM. Each channel of the pipette contains the solution of interest and a QRCE. Both the substrate and the pipette are mounted on piezoelectric positioners to enable modulation and displacement of the pipette towards the sample, and of the substrate for lateral scanning. (b) A typical SECCM approach curve showing : (i)the change in DC conductance current; and (ii) the AC conductance current, as the pipette approaches and makes contact with the substrate surface.

the meniscus size.[14, 19] The lock-in amplifier was used to identify the AC component of the conductance current and used as a set-point during scanning to maintain a constant tip to surface separation. Figure 2. 7b shows a representative approach curve for a typical SECCM experiment in which the change in the direct conductance current and the AC component of the conductance current from approach to contact can be seen (note the log scale on the AC magnitude plot).

During each SECCM experiment, the conductance current between the QRCEs and the current at the substrate were recorded simultaneously, along with the *xy* and *z* position of the pipette and the conductance current (both DC and AC components). Data acquisition was achieved using an FPGA card (PCIe-7852R) with a LabView 2011 interface. SECCM imaging was carried out in two modes: raster scanning and line patterning Figure 2. 8). In raster scanning, a constant tip-to-substrate height separation was maintained using the AC set-point, whilst moving the electrode substrate over a 10 μm × 10 μm (or 10 μm × 5 μm) area in the *xy* direction in a raster fashion (Figure 2. 8(a)). The SECCM pipette was typically scanned at a speed of 0.3 μm s^{-1}, scanning 3 lines per μm and recording a data point every 30.1 ms. This resulted in the acquisition of *ca.* 1100 points per line and over 30,000 (or 15,000) individual measurements in most images. To carry out line-patterning, a constant tip-to-substrate height separation was maintained whilst moving the electrode substrate in the *xy* direction to create a square-spiral pattern (Figure 2. 8(b)). Reactive patterning was carried out to create a line-pattern that covered 560 μm of the HOPG surface at 1 μm s^{-1}, with 78 points recorded per second (an average of 512 samples per point) resulting in *ca.* > 40,000 individual measurements.

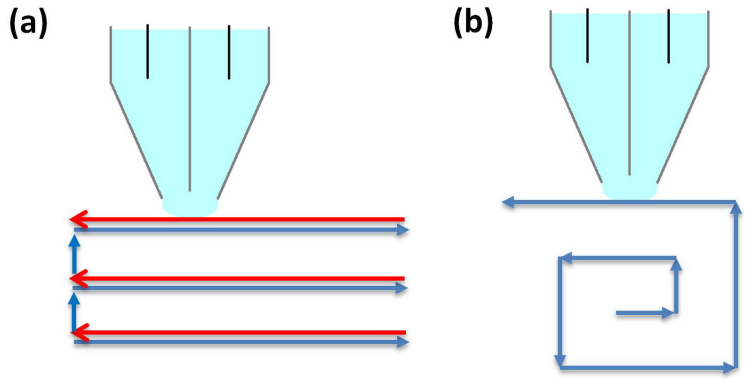

Figure 2. 8 SECCM imaging modes: (a) raster scanning and (b) square-spiral line patterning where the blue arrows indicate the direction of scanning on a fresh surface and the red arrow indicate a reverse scan over the same area.

When a large potential bias is applied between the two QRCEs a large electric field forms across the two barrels, and this may influence the local mass transport of redox-active

species down the two barrels differently. This is evident in some of the studies shown in Chapter 7 where enhanced deposition of 2,6-$AQDS^{2-}$ is seen under the more negative barrel.

2.10 REFERENCES

1. Kneten, K. R.,R. L. McCreery, *Anal. Chem.,* **1992,** *64,* 2518-2524.
2. Ji, X.,C. E. Banks,A. Crossley,R. G. Compton, *ChemPhysChem,* **2006,** *7,* 1337-1344.
3. Wilson, N. R.,S. L. Clewes,M. E. Newton,P. R. Unwin,J. V. Macpherson, *J. Phys. Chem. B,* **2006,** *110,* 5639-5646.
4. Zhen, C. M.,X. Q. Liu,Z. J. Yan,H. X. Gong,Y. Y. Wang, *Surf. Interface Anal.,* **2001,** *32,* 106-109.
5. Baro, A. M.,R. G. Reifenberger, *Atomic Force Microscopy in Liquid: Biological Applications*. Wiley-VCH: Singapore, 2012.
6. Tamayo, J.,R. Garcia, *Langmuir,* **1996,** *12,* 4430-4435.
7. Bertoncello, P.,M. K. Ram,A. Notargiacomo,P. Ugo,C. Nicolini, *Phys. Chem. Chem. Phys.,* **2002,** *2,* 4036-4043.
8. Zhang, L.,Q. Lu,M. Liu, *J. Phys. Chem. B,* **2003,** *107,* 2565-2569.
9. Bertoncello, P.,I. Ciani,F. Li,P. R. Unwin, *Langmuir,* **2006,** *22,* 10380-10388.
10. Yasuzawa, M.,M. Hashimoto,S. Fujii,A. Kunugi,T. Nakaya, *Sensor. Actuat. B,* **2000,** *65,* 241-243.
11. Sun, S.,P. Ho-Si,J. Harrison, *Langmuir,* **1991,** *4,* 727.
12. Fujiwara, H., *Spectroscopic ellipsometry: principles and applications*. Wiley: West Sussex 2007.
13. Ebejer, N.,M. Schnippering,A. W. Colburn,M. A. Edwards,P. R. Unwin, *Anal. Chem.,* **2010,** *82,* 9141-9145.
14. Snowden, M. E.,A. G. Güell,S. C. S. Lai,K. McKelvey,N. Ebejer,M. A. O'Connell,A. W. Colburn,P. R. Unwin, *Anal. Chem.,* **2012,** *84,* 2483-2491.
15. Lai, S. C. S.,P. V. Dudin,J. V. Macpherson,P. R. Unwin, *J. Am. Chem. Soc.,* **2011,** *133,* 10744-10747.
16. Suter, T.,H. Bohni, *Electrochim. Acta,* **1997,** *42,* 3275-3280.
17. Hassel, A. W.,M. M. Lohrengel, *Electrochim. Acta,* **1997,** *42,* 3327-3333.
18. Shao, Y. H.,M. V. Mirkin, *Anal. Chem.,* **1998,** *70,* 3155-3161.
19. Rodolfa, K. T.,A. Bruckbauer,D. Zhou,Y. E. Korchev,D. Klenerman, *Angew. Chem. Int. Ed.,* **2005,** *44,* 6854-6859.

CHAPTER 3: DEFINITIVE EVIDENCE FOR FAST ELECTRON TRANSFER AT PRISTINE BASAL PLANE GRAPHITE FROM HIGH RESOLUTION ELECTROCHEMICAL IMAGING

More than 2 decades of research on electrochemistry at highly oriented pyrolytic graphite (HOPG) has led to an apparent consensus that the basal plane of HOPG is largely, or completely, inert for a wide range of heterogeneous electron transfer (ET) processes, with step edges which intersect the surface providing most or all of the ET activity. It is shown herein that this model – derived from macroscopic measurements – is incorrect for the two most studied redox couples, $Ru(NH)_6^{3+/2+}$ and $Fe(CN)_6^{4-/3-}$ in aqueous solution. Using high resolution scanning electrochemical cell microscopy (SECCM) the redox activity of high quality HOPG is mapped, with a spatial resolution much smaller than the step spacing and report unequivocal evidence for high and essentially uniform ET activity at basal plane HOPG free from any influence of step edges. The work presented within this chapter indicates that a new view of electrochemical processes at HOPG is required, with implications that carry over to related sp^2 carbon materials, such as graphene and carbon nanotubes.

3.1 INTRODUCTION

The recent interest in the electrochemical properties of novel sp^2 carbon materials, such as carbon nanotubes[1-4] and graphene,[5-12] has led to a resurgence of interest in the intrinsic electrochemical properties of highly oriented pyrolytic graphite (HOPG). The traditional consensus, deduced mostly from macroscopic cyclic voltammetry measurements (typically on areas > 0.1 cm^2) is that the electron transfer (ET) activity of HOPG is dominated by the step edges,[1-4, 13-16] with the basal plane showing very low[17] to no[18-19] electroactivity. However, the scale of these measurement necessarily means HOPG basal planes and step edges are probed simultaneously,[13, 17, 20-22] making it difficult to separate their individual reactivity. Furthermore, there are significant variations in reported HOPG electroactivity,[3, 13-15, 17-29] which has been attributed to each HOPG cleaved surface showing different quality (primarily step edge density), and various methods have consequently been proposed to determine the step or defect density of cleaved HOPG.[13, 17, 20-22, 26, 30-32] However, the methods used hitherto are either microscopic and can only access a tiny fraction of the surface that is probed by macroscopic electrochemistry,[25-26, 31-32] or are indirect measurements of surface quality,[17, 21-22, 26] making it difficult to correlate HOPG surface structure and ET activity.

In this chapter scanning electrochemical cell microscopy (SECCM), [33-34] which provides spatially resolved electrochemical imaging on a scale where the HOPG basal plane can be studied directly in isolation from step edges, is used with atomic force microscope (AFM) to image over the same area, showing unambiguously that the HOPG basal plane supports fast ET activity.

3.2 BASAL PLANE HOPG SAMPLE PREPARATION AND CHARACTERISATION

A fresh surface was revealed by cleaving with scotch tape, as for the majority of studies carried out on HOPG[3, 13, 15, 20, 22, 35-40] including key studies in which significant conclusions have been drawn relating to the activity of basal plane HOPG.[3, 13, 15, 26, 36, 38, 41-43] From AFM analysis of 20 images taken over areas of 3 – 10 μm on 3 different ZYA grade HOPG samples (Table 3. 1), the step heights in terms of the number of graphite layers was determined and is shown in Figure 3. 1, which shows that ZYA grade HOPG exhibits predominantly monolayer and bilayer steps, and very low step coverage - among the lowest reported - providing the optimum basal surface on which the density of step edges is minimized. The step density is the length of step per unit area of the surface, while data for step edge coverage takes account of different step heights and represents the total amount of edge plane area within a unit area of the basal surface of HOPG.

Table 3. 1 Characterisation of step edges on basal plane HOPG (ZYA)

Step density range (μm μm^{-2}) from AFM	0.02 – 0.7
Mean step density (μm μm^{-2}) from AFM	0.29 ± 0.2 (*N* = 20)
Step edge coverage on basal plane	Average 0.26% (range 0.03-1%)

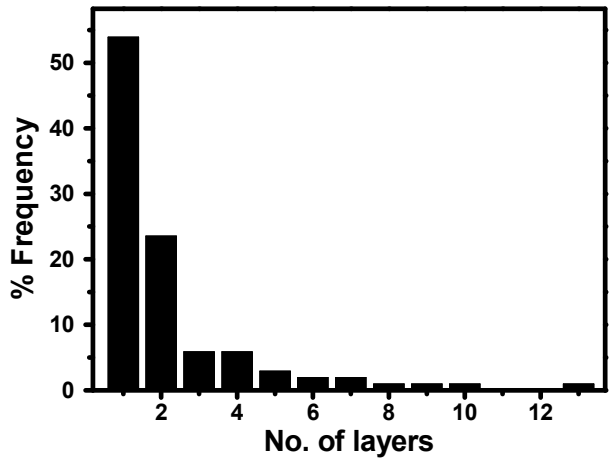

Figure 3. 1 Histogram of step edge heights on freshly cleaved ZYA grade HOPG

Capacitance values were extracted from macroscopic CV measurements in 1 M KCl at 0.1 V s^{-1} on a freshly cleaved surface. The capacitance was extracted as the current amplitude at 0.02 V, from 10 runs values ranging between 1.7 – 2.3 μF cm^{-2} were obtained. This is consistent with values obtained for HOPG prepared by scotchtape and described as being anomalously low, 2 - 3 μF cm^{-2}, [21, 44] on which very slow kinetics were found.

3.3 SECCM: CONTACT AREA DETERMINATION

The spatial resolution of SECCM is ultimately determined by the contact area of the meniscus and the substrate, which, in turn, is determined by the tip diameter and local wetting properties. To quantify the contact area, SECCM was employed to electropolymerize aniline in a line-pattern on HOPG, as the width of the line would be a direct measure of the meniscus diameter during the scan. In this case a 400 nm tip was filled with 1 mM aniline in 100 mM KCl and the substrate potential was held at 750 mV relative to the Ag/AgCl QRCE. A tapping mode-atomic force microscope (TM-AFM) image of part of the pattern is shown on a scale comparable to the step spacing on HOPG in Figure 3. 2. The deposited polyaniline is clearly visible and has a uniform width, indicating that the variation in meniscus contact area is minimal as the tip is moved along the surface. From cross-sections of the line, Figure 3. 2(c), the contact diameter can be determined to be 220 and 320 nm, depending on the relative orientation of the capillary. This is an order of magnitude smaller than the typical step spacing on basal surface HOPG, providing confidence that electrochemical measurements can be made unambiguously on the basal plane, free from the influence of steps.

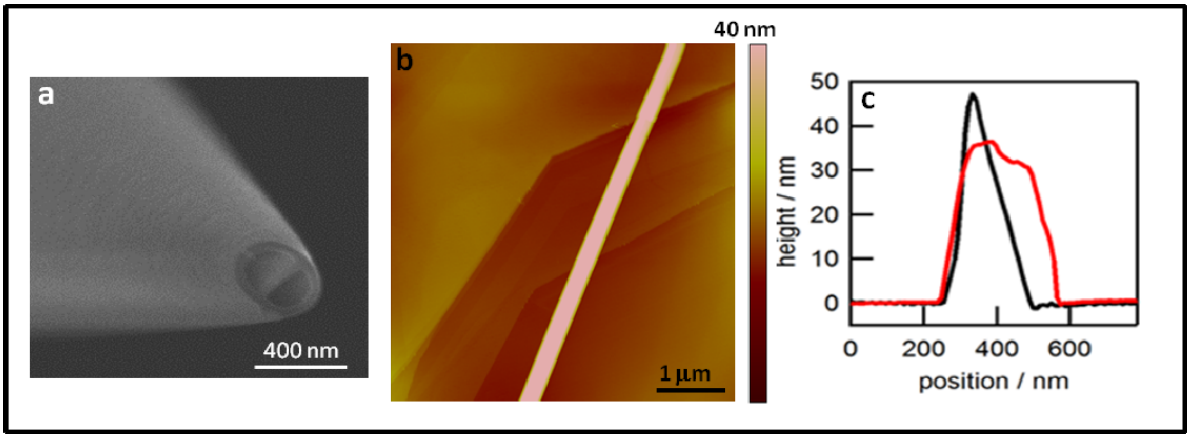

Figure 3. 2 Contact area determination of SECCM (a) FE-SEM image of the end of a pipette used. (b)Tapping mode - atomic force microscope image of polyaniline deposited using SECCM. (c) Cross-sections of deposited polyaniline (PAN) formed by scanning parallel (red) and perpendicular (black) to the septum in the capillary.

3.4 SECCM: MAPPING

SECCM mapping for the one-electron reduction of $Ru(NH_3)_6^{3+}$ (0.1 M KCl) was carried out on freshly cleaved ZYA grade HOPG, Figure 2. The topographical map of the surface (Figure 3. 3a) clearly shows parallel steps (also evident from AFM, Figure 3. 3e) across the surface, highlighting the outstanding ability of the technique to accurately track the surface and resolve nanoscale topographical features, despite a slight tilt (~1.5º) on the sample. The steps are especially pronounced in Figure 3. 3b, which shows the AC component of the conductance current (used as the feedback parameter). The sharp lines on this 'error' map indicate a transient change in the feedback as the liquid meniscus comes into contact with a step, which is attributed to different wetting properties of the basal plane and the step edge (*vide infra*).

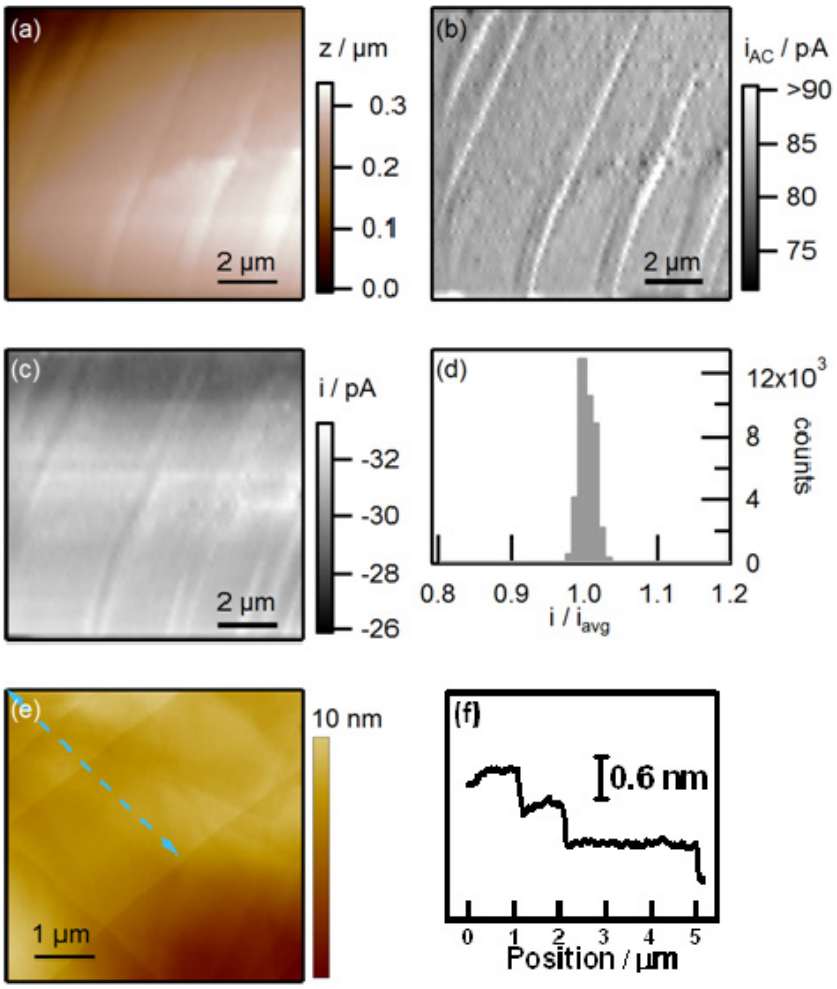

Figure 3. 3 Reduction of 2 mM $Ru(NH_3)_6^{3+}$ at HOPG. SECCM maps of (a) topography (z-piezo response), (b) the AC component of the conductance current, (c) surface redox activity recorded at -0.25 V. (d) Normalized activity histogram (see text). (e) AFM image of the area of interest. (f) Line scan along the arrow of the AFM image.

A simultaneously recorded map of the surface redox activity at the reversible half-wave (formal) potential (-0.25 V *vs.* Ag/AgCl/0.1M KCl), as determined by SECCM voltammetry (Figure 3. 4), shows the currents over the entire surface to be essentially constant at 30.9 ± 1.1 pA (1 σ) (Figure 3. 3c). The step sites show slightly higher currents (2-3%), but this is not necessarily an indicator of higher intrinsic activity, i.e. current density (*vide infra*). Most importantly, in the regions between the steps (where the electrolyte solution is only in contact with the basal surface), the current is at a constant (high) value. Based on the observed current, an estimate of the standard ET rate constant can be made. The reversible voltammogram for $Ru(NH_3)_6^{3+}$ reduction shows a diffusion limited current of 16 pA (Figure 3. 4).

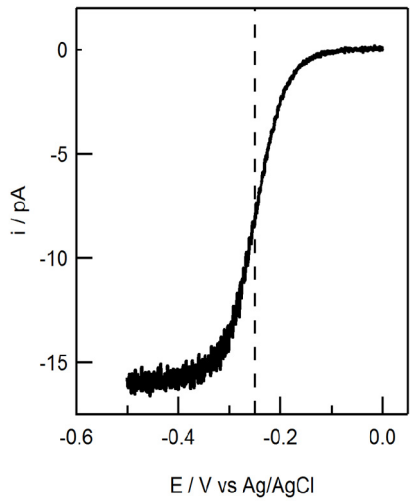

Figure 3. 4 Linear sweep voltammogram (LSV) obtained with the SECCM set-up in the absence of a potential bias between the QRCEs for the reduction of 2 mM $Ru(NH_3)_6^{3+}$ (0.1 M KCl) run at 100 mV s^{-1}. The potential is with respect to Ag/AgCl/(0.1 M KCl).

By applying a potential bias of 0.5 V between the two QRCEs the limiting current increased by a factor of 4-5 due to migration. A full discussion on the mass transport of reactant and product species within the SECCM set-up has recently been reported elsewhere.[45] In brief, in the absence of potential bias between the two QRCEs in the barrels of the pipette, mass transport of reactant (product) species is governed by diffusion down the pipette to the liquid meniscus. This is similar to the scanning micropipet contact method,[46] and because of the small pipette aperture and slight taper of the walls, steady-state difussion is readily attained. Thus, in this case, driving the reaction to the mass transport limited regime in voltammetric measurements leads to a steady limiting current at moderate scan rates (Figure 3. 4). In the presence of a potential bias between the two QRCEs (in the case of imaging experiments), the potential bias gives rise to a conductance current (ion flow) between the two QRCEs. The conductance current is related to an ion flux (both ions from the supporting electrolyte as well as reactant/product ions) from one barrel of the pipette across the meniscus to the other barrel. Consequently, mass transport of (charged) reactant to the working electrode substrate is not only governed by diffusion, but also has a migration component. The enhanced mass transport due to migration (due to the potential bias applied between the two QRCEs) compared to the diffusion-only case (without a potential applied between the QRCEs) is dependent on a number of factors, including the magnitude of the potential bias, pipette geometry, electrolyte concentration and the charge on the product and reactant species. These facts can be accounted for fully[45] and under the conditions employed in this chapter, the mass-transport was found to be enhanced by a factor 4-5.

The data indicates a high mass transport coefficient of ~ 0.5 cm s^{-1}, based on a 300 nm contact diameter. As the currents measured in the SECCM maps at the formal potential are *ca.* 50% of the transport-limited values, it is evident that the surface redox process measured during imaging is fast, and close to reversible, and a conservative lower estimate on the standard ET rate constant of > 0.5 cm s^{-1} can be put for $Ru(NH_3)_6^{3+}$ oxidation on basal plane HOPG. That is to say, the process at HOPG would be entirely reversible to essentially all macroscopic electrochemical techniques, including past CV measurements, purely based on the activity of the basal surface, without needing to consider any activity of the step edges. This is in sharp contrast with the previously reported 'negligible' activity of the basal surface.[3, 47-48] These findings are further validated by the other maps obtained simultaneously during imaging, most notably the consistency between all recorded trace and retrace images (Figure 3. 5). A slight increase can be seen in the retrace compared to trace for the DC, AC and activity current maps, for example in the surface activity maps the retrace shows activity 1-2 pA greater than the trace across the entire image. The subtle increase can be attributed to two possible factors, firstly, during the trace same solution may be left behind that increases the conductance on the retrace. Secondly, the wetting of the meniscus could be slightly different based on whether it is being scanned into a step or off a step, thereby changing the dimensions of the electrochemical cell. Any change related to the wetting and meniscus size will be reflected in all three DC, AC and surface activity current maps. As the increase is negligible on the current scale it is considered inconsequential to the interpretation of the data which aims to address activity of the basal surface.

The spread in redox activity over the image can be evaluated quantitatively (normalized for each line to minimize time effects), as shown by the histogram in Figure 2d. It can clearly be seen that the total spread in surface currents (*ca.* 30,000 data points), is less than 5%, indicating a very homogeneously active surface. After performing SECCM measurements, the imaged area was characterized by AFM (Figure 3. 3) showing a step spacing ranging between 500 nm to 3 μm (Figure 3. 3f), with mainly monolayer steps present. As the lateral contact of SECCM is an order of magnitude smaller than the (average) step spacing, it is without doubt that during the electrochemical mapping the surface in contact with the electrolyte solution would mostly consist of only the HOPG basal plane. Thus, the data provides unambiguous evidence for the very high ET activity of the basal surface.

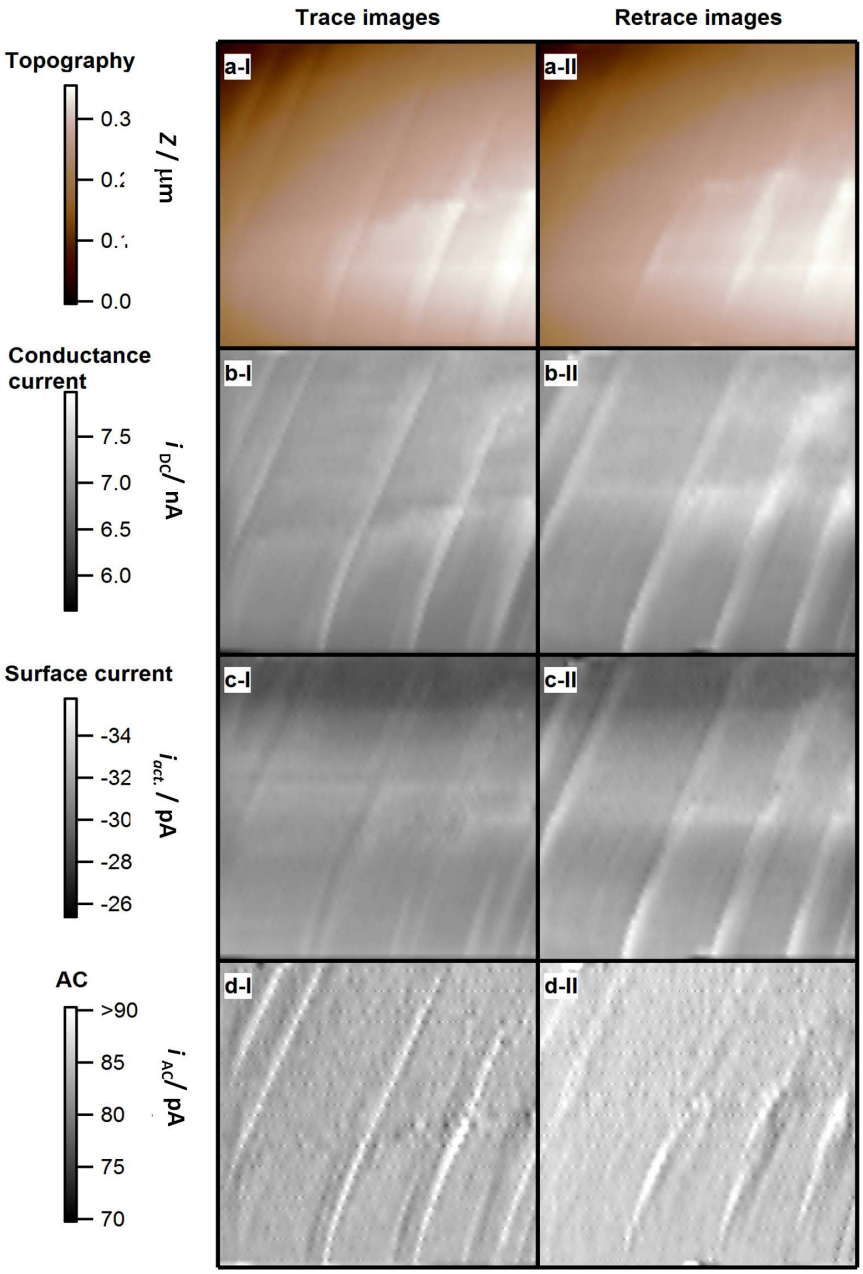

Figure 3. 5 Set of SECCM *xy*-maps for the reduction of $Ru(NH_3)_6^{3+}$ obtained during a single experiment. (a) Surface topography. (b) Conductance current between the two QRCEs in the pipette tip. (c) Surface activity current recorded on the HOPG substrate. (d) Alternating current component of the conductance current, used as a feedback parameter. Images sub-labelled I (left column) refer to forward going (trace) sweeps, recorded from left to right. Images sub-labelled II (right column) refer to backward going (retrace) sweeps, recorded from right to left. The consistency between trace and retrace images is indicative of the stability of the liquid meniscus scanning in different directions and provides further confidence in the data obtained. All images are constructed from 31 line scans from bottom to top, with each line comprising ~1100 recorded data points.

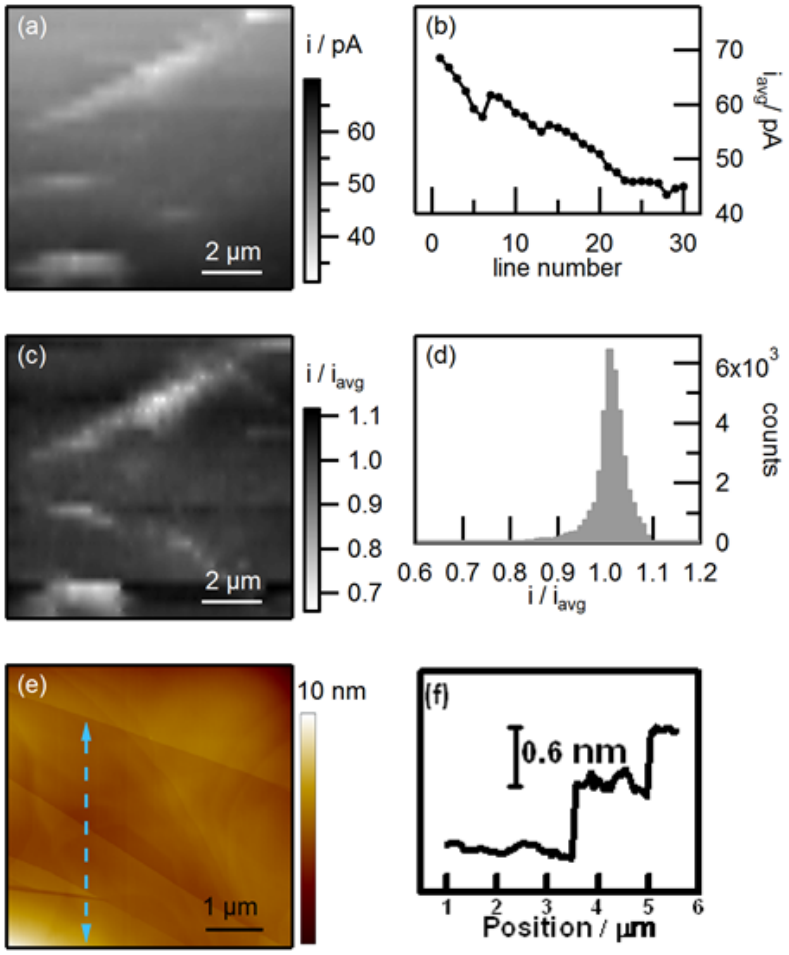

Figure 3. 6 Oxidation of 2 mM $Fe(CN)_6^{4-}$ at HOPG. (a) SECCM surface redox activity map recorded at 0.25 V. (b) Average current of each line scan. (c) Normalized SECCM surface redox activity map (see text). (d) Normalized activity histogram (see text). (e) AFM image of the area of interest. (f) Line scan along the arrow of the AFM image.

The electrochemical activity of $Fe(CN)_6^{4-/3-}$ was also considered, a common benchmark redox system often used to study the electrochemical properties of HOPG,[1-4, 13-14, 17-18, 20, 28] and related sp^2 carbon materials[3, 12, 14] and originally employed to draw conclusions regarding the relative electroactivity of the basal plane and step sites. SECCM results for the oxidation of 2 mM $Fe(CN)_6^{4-}$ (0.1 M KCl) on HOPG at 0.25 V (*vs.* Ag/AgCl/0.1 M KCl) are shown in Figure 3. 6. The potential was chosen based on voltammograms recorded on freshly cleaved HOPG and on HOPG after exposure to air for ~1 hour, being the timescale of a SECCM measurement (Figure 3. 7). The limiting current in the absence of migration was 15 pA and 4 – 5 times larger with the applied potential between the QRCEs.

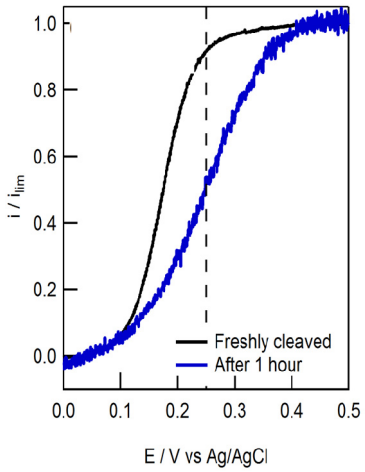

Figure 3. 7 Normalized LSVs for the oxidation of 2 mM $Fe(CN)_6^{4-}$ (0.1 M KCl) run at 100 mV s^{-1} on freshly cleaved HOPG (black line) and HOPG after one hour exposure to air (blue line). The potential is with respect to Ag/AgCl/(0.1 M KCl).The LSVs are normalized for comparison as they were obtained with 2 different pipettes with different sizes.

The resulting electroactivity map (Figure 3. 6a) shows a clear side-on 'V-shaped' feature consistent with the step sites on the HOPG surfaces (see AFM data, Figure 3. 6e and f). Interestingly, in contrast to the reduction of $Ru(NH_3)_6^{3+}$, these steps display lower currents than the basal plane. Furthermore, a clear deactivation of the overall surface is seen during the timescale of the image (from bottom to top). This decrease is especially clear from the average current of each line (Figure 3. 6b), which dropped by 35% over the course of the image from 69 pA (where the reaction is rapid and close to reversible) to 45 pA. It should again be emphasized that the other simultaneously obtained maps (Figure 3. 8) indicate a stable meniscus contact, and that the meniscus is moved during the scan to areas which have not been exposed to the electrolyte solution. This deterioration has been observed in extensive related experiments and is due a combination of issues which is expanded on briefly below. For this study, to probe the relative reactivity of basal and step sites in isolation of time effects, a current distribution was obtained by normalizing each line with the average current of that line (Figure 3. 6c and d). Most of the sites display similar activity (within 10%), although a slight tailing towards lower activity can be seen. Looking at the normalized current SECCM map, the regions of below average current are assigned to the step sites. Furthermore, the difference between the step site and basal plane reactivity appears to increase with time, giving rise to the broad distribution of activity in Figure 3. 7d between 0.7 and 1. This increasing difference could be indicative of a preferential deactivation of step sites over basal plane sites with time, similar to metal electrodes.[49-50]

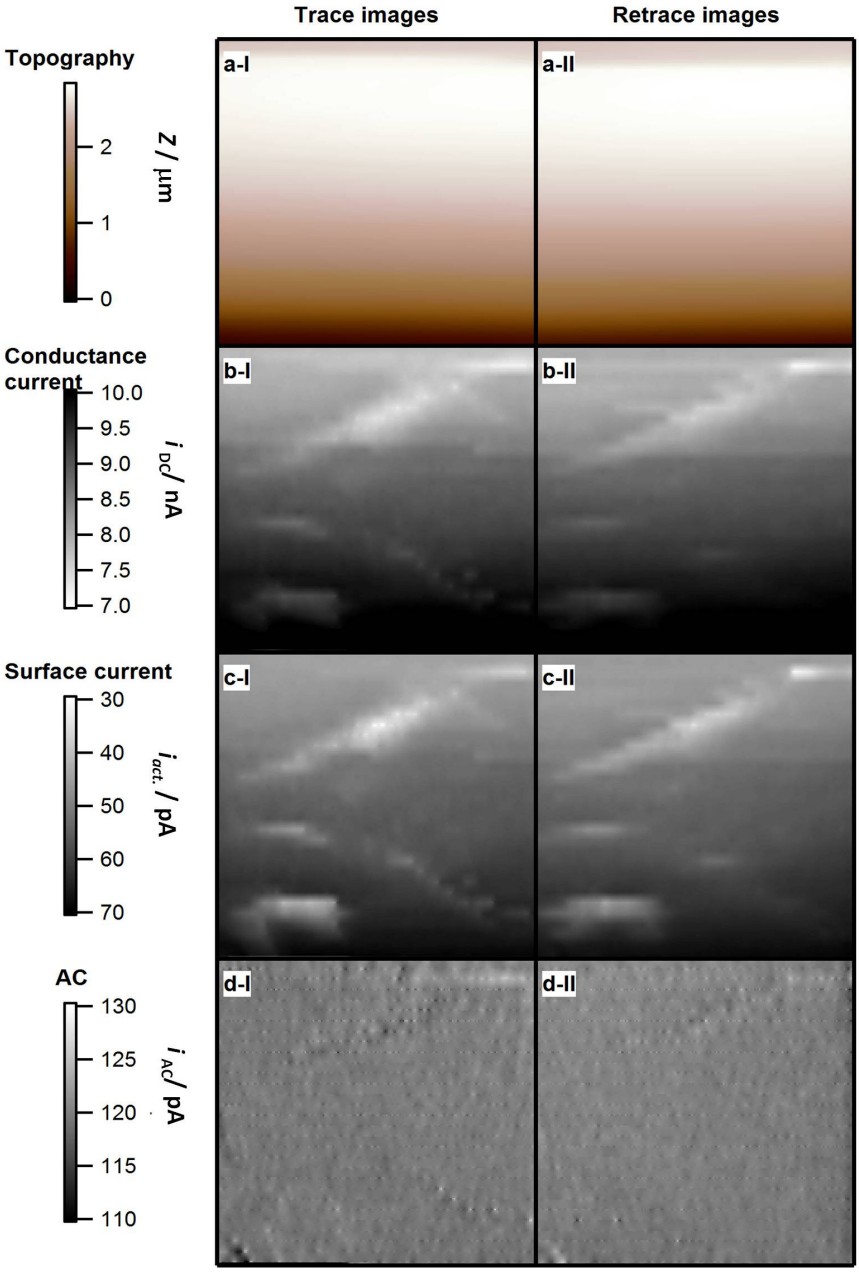

Figure 3. 8 Set of SECCM xy-maps for the reduction of $Fe(CN)_6^{4-}$ obtained during a single experiment. (a) Surface topography. (b) Conductance current between the two QRCEs in the capillary. (c) Surface current recorded on the HOPG substrate (d). Alternating current component of the conductance current, used as a feedback parameter. Images sub-labelled I (left column) refer to forward going (trace) sweeps, recorded from left to right. Images sub-labelled I (right column) refer to backward going (retrace) sweeps, recorded from right to left. The consistency between trace and retrace images is indicative of the stability of the liquid meniscus scanning in different directions and provides further confidence to the data obtained. All images are constructed from 31 line scans from bottom to top, which each line comprising ~1100 recorded data points.

Based on these data, it can only conclude that the HOPG basal plane is highly active for the $Fe(CN)_6^{4-/3-}$ benchmark system, being close to reversible initially, albeit with some

complications. This contrasts markedly with previous reports, and it should be noted that previously reported ET standard rate constants (10^{-5} – 10^{-9} cm s^{-1}, averaged for the surface[13, 21-22] or 10^{-9} cm s^{-1}, extrapolated for the basal surface[3, 15]) would have yielded negligible (close to zero) currents at the potential of high mass transport rate studies. Furthermore, it should be noted that the ET rate constants reported here are consistent with predictions from Marcus theory (> 1 cm s^{-1}).[51]

Although SECCM clearly illustrates the HOPG basal plane to be highly active, the different currents obtained when imaging directly over step sites is interesting and merits some discussion. This effect is likely to be due to the heterogeneous properties of the basal surface versus step edges, resulting in different (nanoscale) wetting and adsorption processes: the excess negative charge on the HOPG step edges[52] could draw in the positively charged $Ru(NH_3)_6^{3+}$ through electrostatic interaction, causing a slight spreading of the meniscus, thereby increasing the contact area. This finding is supported by an increase in conductance current (Figure 3. 5), which is a good indicator for variances in meniscus size, and the transient surges in the AC (Figure 3. 3b). Due to the increased contact area, the surface current increases, even if the intrinsic activity remains unchanged going over a step edge. In contrast, for the negatively charged $Fe(CN)_6^{4-}$ species, the conductance current decreases, suggesting that the meniscus slightly contracts when going over a step site (Figure 3. 8). These data highlight the high information content of SECCM for structure-function imaging of surfaces and interfaces.

3.5 CONCLUSION

In this chapter it has been shown that the (freshly exposed) basal plane of HOPG display considerable electroactivity, while many previous studies have come to the opposite conclusion. [1-4, 13-16] In this respect, it should be noted that reversible (fast) ET for $Fe(CN)_6^{4-/3-}$ and $Ru(NH_3)_6^{3+/2+}$ on freshly cleaved HOPG has been reported by others for HOPG,[29, 53] but often discarded as ‘very defective’ based on the current models without further surface characterisation. Furthermore, the surface of HOPG is known to be very sensitive to pre-treatment: for example, exposure of HOPG to organic solvents, can lead to significant alteration of its surface properties.[53] In addition, as shown herein, exposure to air for less than an hour after cleaving leads to a decrease in ET-rates. As for many electroanalytical applications, the HOPG surface needs to be modified before use, significant deterioration might already have occurred in the time between exposing a fresh HOPG surface and the moment it is used. The results presented herein clearly represent the intrinsic electrochemical properties of (pristine) HOPG.

In summary, SECCM has allowed us to study ET at basal plane HOPG under conditions of very high mass transport and high spatial resolution, and where the liquid probe makes a series of fresh measurements across the surface. It has been able to isolate the response of the pristine basal plane (directly after cleaving, reflecting the intrinsic material properties), and show unambiguously that ET is fast (close to reversible) for the 2 most studied redox couples. This new view – which overturns more than 2 decades of past research[1-4, 13-17, 20-22, 26, 30-32] - not only impacts the understanding of the electroactivity of HOPG, but potentially the properties of related sp^2 materials, such as carbon nanotubes and graphene, illustrating the importance of these findings. The studies also demonstrate the significant potential of SECCM as a new nanoscale probe of electrochemical and interfacial processes.

3.6 REFERENCES

1. Dumitrescu, I.,P. R. Unwin,J. V. Macpherson, *Chem. Commun.,* **2009,** 6886-6901.
2. McCreery, R. L., *Chem. Rev.,* **2008,** *108,* 2646-2687.
3. Banks, C. E.,T. J. Davies,G. G. Wildgoose,R. G. Compton, *Chem. Commun.,* **2005,** 829-841.
4. Pumera, M., *Chem. Soc. Rev.,* **2010,** *39,* 4146-4157.
5. Zhou, M.,Y. M. Zhai,S. J. Dong, *Anal. Chem.,* **2009,** *81,* 5603-5613.
6. Wang, Y.,Z. Q. Shi,Y. Huang,Y. F. Ma,C. Y. Wang,M. M. Chen,Y. S. Chen, *J. Phys. Chem. C,* **2009,** *113,* 13103-13107.
7. Tang, L. H.,Y. Wang,Y. M. Li,H. B. Feng,J. Lu,J. H. Li, *Adv. Funct. Mater.,* **2009,** *19,* 2782-2789.
8. Shan, C. S.,H. F. Yang,J. F. Song,D. X. Han,A. Ivaska,L. Niu, *Anal. Chem.,* **2009,** *81,* 2378-2382.
9. Chen, F.,Q. Qing,J. L. Xia,J. H. Li,N. J. Tao, *J. Am. Chem. Soc.,* **2009,** *131,* 9908-+.
10. Alwarappan, S.,A. Erdem,C. Liu,C. Z. Li, *J. Phys. Chem. C,* **2009,** *113,* 8853-8857.
11. Li, W.,C. Tan,M. A. Lowe,H. D. Abruna,D. C. Ralph, *ACS Nano,* **2011,** *5,* 2264-2270.
12. Valota, A. T.,I. A. Kinloch,K. S. Novoselov,C. Casiraghi,A. Eckmann,E. W. Hill,R. A. W. Dryfe, *ACS Nano,* **2011,** *5,* 8809-8815.
13. Bowling, R. J.,R. T. Packard,R. L. McCreery, *J. Am. Chem. Soc.,* **1989,** *111,* 1217-1223.
14. Ji, X. B.,C. E. Banks,A. Crossley,R. G. Compton, *ChemPhysChem,* **2006,** *7,* 1337-1344.
15. Davies, T. J.,R. R. Moore,C. E. Banks,R. G. Compton, *J. Electroanal. Chem.,* **2004,** *574,* 123-152.
16. Lee, C. Y.,A. M. Bond, *Anal. Chem.,* **2009,** *81,* 584-594.
17. Kneten, K. R.,R. L. McCreery, *Anal. Chem.,* **1992,** *64,* 2518-2524.
18. Banks, C. E.,R. R. Moore,T. J. Davies,R. G. Compton, *Chem. Commun.,* **2004,** 1804-1805.
19. Davies, T. J.,M. E. Hyde,R. G. Compton, *Angew. Chem.-Int. Edit.,* **2005,** *44,* 5121-5126.
20. Cline, K. K.,M. T. Mcdermott,R. L. McCreery, *J. Phys. Chem.,* **1994,** *98,* 5314-5319.
21. Rice, R. J.,R. L. McCreery, *Anal. Chem.,* **1989,** *61,* 1637-1641.
22. McDermott, M. T.,K. Kneten,R. L. McCreery, *J. Phys. Chem.,* **1992,** *96,* 3124-3130.
23. Bowling, R. J.,R. L. McCreery,C. M. Pharr,R. C. Engstrom, *Anal. Chem.,* **1989,** *61,* 2763-2766.
24. Chen, P. H.,M. A. Fryling,R. L. McCreery, *Anal. Chem.,* **1995,** *67,* 3115-3122.
25. McDermott, M. T.,R. L. McCreery, *Langmuir,* **1994,** *10,* 4307-4314.
26. Robinson, R. S.,K. Sternitzke,M. T. Mcdermott,R. L. McCreery, *J. Electrochem. Soc.,* **1991,** *138,* 2412-2418.
27. Moore, R. R.,C. E. Banks,R. G. Compton, *Anal. Chem.,* **2004,** *76,* 2677-2682.
28. Lee, C.-Y.,S.-X. Guo,A. M. Bond,K. B. Oldham, *J. Electroanal. Chem.,* **2008,** *615,* 1-11.
29. Kariuki, J. K.,M. T. McDermott, *Langmuir,* **1999,** *15,* 6534-6540.
30. McCreery, R. L.,K. K. Cline,C. A. McDermott,M. T. McDermott, *Colloid Surf. A-Physicochem. Eng. Asp.,* **1994,** *93,* 211-219.
31. Ray, K.,R. L. McCreery, *Anal. Chem.,* **1997,** *69,* 4680-4687.
32. Chang, H.,A. J. Bard, *Langmuir,* **1991,** *7,* 1143-1153.
33. Lai, S. C. S.,P. V. Dudin,J. V. Macpherson,P. R. Unwin, *J. Am. Chem. Soc.,* **2011,** *133,* 10744-10747.
34. Ebejer, N.,M. Schnippering,A. W. Colburn,M. A. Edwards,P. R. Unwin, *Anal. Chem.,* **2010,** *82,* 9141-9145.

35. Dumitrescu, I.,P. R. Unwin,J. V. Macpherson, *Chem. Commun.,* **2009,** *7345,* 6886-6901.
36. Rice, R. J.,R. L. McCreery, *Anal. Chem.,* **1989,** *61,* 1637-1641.
37. Kneten, K. R.,R. L. McCreery, *Anal. Chem.,* **1992,** *64,* 2518-2524.
38. Ji, X.,C. E. Banks,A. Crossley,R. G. Compton, *ChemPhysChem,* **2006,** *7,* 1337-1344.
39. Liu, H.,F. Favier,K. Ng,M. P. Zach,R. M. Penner, *Electrochim. Acta,* **2001,** *47,* 671-677.
40. Xu, J.,Q. Chen,G. M. Swain, *Anal. Chem.,* **1998,** *70,* 3146-3154.
41. Bowling, R.,R. T. Packard,R. L. McCreery, *Langmuir,* **1989,** *5,* 683-688.
42. Bowling, R. J.,R. L. McCreery,C. M. Pharr,R. C. Engstrom, *Anal. Chem.,* **1989,** *61,* 2763-2766.
43. Alsmeyer, Y. W.,R. L. McCreery, *Langmuir,* **1991,** *7,* 2370-2375.
44. Sternitzke, K. D.,R. L. McCreery, *Anal. Chem.,* **1990,** *62,* 1339-1344.
45. Snowden, M. E.,A. G. Güell,S. C. S. Lai,K. McKelvey,N. Ebejer,M. A. O'Connell,A. W. Colburn,P. R. Unwin, *Anal. Chem.,* **2012,** *84,* 2483-2491.
46. Williams, C. G.,M. A. Edwards,A. L. Colley,J. V. Macpherson,P. R. Unwin, *Anal. Chem.,* **2009,** *81,* 2486-2495.
47. Banks, C. E.,R. R. Moore,T. J. Davies,R. G. Compton, *Chem. Commun.,* **2004,** 1804-1805.
48. Davies, T. J.,M. E. Hyde,R. G. Compton, *Angew. Chem.,* **2005,** *44,* 5121-5126.
49. Feibelman, P. J.,S. Esch,T. Michely, *Phys. Rev. Lett.,* **1996,** *77,* 2257-2260.
50. Zambelli, T.,J. Wintterlin,J. Trost,G. Ertl, *Science,* **1996,** *273,* 1688-1690.
51. Pumera, M., *Chem. Soc. Rev.,* **2010,** *39,* 4146-4157.
52. Koestner, R.,Y. Roiter,I. Kozhinova,S. Minko, *J. Phys. Chem. C,* **2011,** *115,* 16019-16026.
53. Liu, Y.,M. S. Freund, *Langmuir,* **2000,** *16,* 283-286.

CHAPTER 4: A NEW VIEW OF ELECTROCHEMISTRY AT HIGHLY ORIENTED PYROLYTIC GRAPHITE (HOPG)

Knowledge of the fundamental electrochemical properties of graphitic materials is important for the design and optimization of electrochemical technologies from sensing to energy conversion and storage. In this Chapter, new insights on the electrochemistry at graphite are reported through extensive investigations of two well studied redox couples, $Fe(CN)_6^{4-/3-}$ and $Ru(NH_3)_6^{3+/2+}$, on 5 different grades of highly orientated pyrolytic graphite (HOPG) which vary in step edge density, surface height ranges and general surface quality. Significantly, cyclic voltammetry (CV) characteristic of reversible electrochemical behavior is observed consistently on pristine basal plane HOPG, independent of step-edge density, for both redox couples. This contrasts with previous macroscopic measurements, and the current textbook view, that considers the basal surface to be largely (or completely) inert with the activity dominated (or completely determined) by step edges emerging at the basal surface. However, repeated potential cycling and electrochemistry over long time scales leads to a deterioration of electron transfer (ET) kinetics, notably for the $Fe(CN)_6^{4-/3-}$ couple. *In-situ* AFM reveals that the change in apparent ET kinetics over time is coupled with the deposition of material on the HOPG electrode. Conducting-AFM also highlights that, after cleaving, the local surface conductivity of HOPG deteriorates significantly with time, which impacts the electrochemical response. These observations offer an explanation for the differences reported herein and some earlier studies. High spatial resolution (several hundred nm) electrochemical imaging with scanning electrochemical cell microscopy (SECCM) on the highest quality mechanically cleaved HOPG is able to probe electrochemistry at the basal surface, free from the influence of step edges, and demonstrates definitively that the pristine basal surface exhibits fast and highly uniform activity consistent with other microscopic studies.

4.1 INTRODUCTION

There are significant differences between the results obtained from microscale and nanoscale electrochemical measurements, on the one hand, and macroscale investigations, on the other hand. Moreover, at the macroscale, significant differences are evident in electrochemical behavior of apparently similar HOPG.[1-5] Further surprising is that studies purporting to show that the basal surface of HOPG supports only sluggish or no ET,[1-5] have been obtained on HOPG with very different surface quality (*vide infra*), and might have been expected to show very different behavior within the framework of a defect-driven activity model. Given the importance of HOPG as an electrode material, as highlighted herein, and

its recent prominence as a comparator for graphene studies,[6-9] the studies in this chapter aim to resolve and explain the issues highlighted. The investigations presented herein have been carried out intermittently for a period of at least 4 years, on more than 25 HOPG samples, with cleavage of the surface and voltammetry carried out independently by 4 different people. Ambient conditions have been considered, since these have been used in all previous electrochemical studies. Initially, the focus was on the oxidation of $Fe(CN)_6^{4-}$ (CV measurements on > 300 freshly cleaved surfaces), as most previous studies have been carried out with this electrode reaction, but included further studies of $Ru(NH)_3^{3+}$ reduction (measurements on > 100 freshly cleaved surfaces), given the discrepancies in ET kinetics alluded to above.[3c,6b,25] Four commercially available HOPG samples are examined: ZYA; ZYH; SPI-1; and SPI-2 (all from SPI supplies, Aztech Trading, UK), the first 3 of which have been employed in previous electrochemical studies. It was also possible to study high quality unclassified HOPG (kindly donated by Prof. R M. McCreery, University of Alberta, Canada, and originally sourced from Dr. A. Moore, Advanced Ceramics, formerly Union Carbide).

Within this chapter it is shown unequivocally that freshly cleaved pristine HOPG is much more electrochemically active than previously considered; however, the HOPG basal surface is shown to readily passivate in a number of ways. A particularly important observation is that the $Fe(CN)_6^{4-/3-}$ couple blocks and modifies the surface of HOPG during voltammetry, making this couple unsuitable for 'validation experiments',[3,19,20] and for the assessment of electrode kinetics.[3-4] Consistent behavior is observed at both the macroscale and nanoscale, and studies presented herein provide a self-consistent and new view of HOPG electrochemistry, with significant implications for studying and understanding electrochemistry at related sp^2 materials.

4.2 HOPG SURFACE TOPOGRAPHY AND STEP DENSITY

In order to understand the relationship between the voltammetric behaviour of HOPG and surface structure it was important to fully characterise sample topography, particularly since the overwhelming majority of all previous voltammetric studies (see Introduction) have suggested that HOPG electroactivity is dominated, or controlled entirely, by step edges (edge planes) with the basal plane providing little or no contribution. Given its use as a flat substrate for imaging nanostructures and biomaterials, [10-12] there are many AFM images of HOPG in the literature, but relatively only a few studies[13,2,14] have examined HOPG surfaces of different grades in any detail. Here, the surface topography of four major types of commercially available HOPG and HOPG (AM) are examined in more detail than in any previous study to obtain clear bounds on the step density, which is essential to examine the validity (or otherwise) of the step-active models.[3, 14-27] Typical TM-AFM images are shown in

Figure 4. 1 and a summary of the data obtained is detailed in Table 4. 1. HOPG samples SPI-2 and AM represent the two extremes in terms of step densities, and for both samples three AFM images are shown in different areas of the a cleaved surface and with different scan sizes to show how heterogeneous the surface is for these two grades.

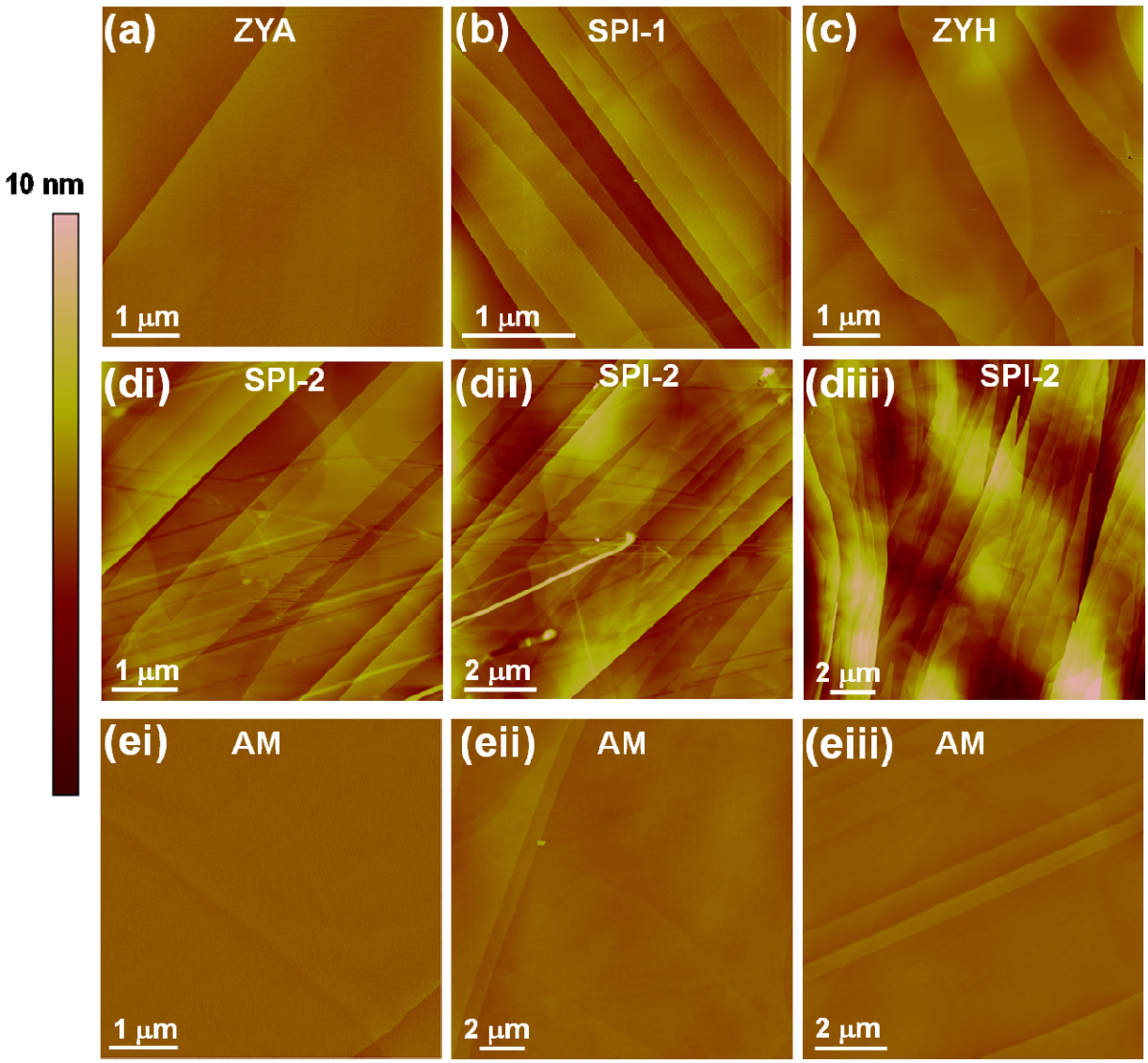

Figure 4. 1 TM-AFM topography images of freshly cleaved HOPG: (a) ZYA, (b) SPI-1, (c) ZYH, (d) SPI-2 grades, and (e) AM.

Figure 4. 1 and Table 4. 1 show clearly that mechanically cleaved HOPG (AM), closely followed by scotch tape cleaved ZYA grade HOPG, provide by far the most superior surfaces in terms of low step density. The other grades of HOPG show increasing step densities in the order ZYH, SPI-1 and SPI-2. Notably, SPI-1 grade, which has been used extensively for CV measurements,[1c,4a,6b-d,32] shows a much higher step density than ZYA grade HOPG, even though ZYA and SPI-1 HOPG exhibit a similar mosaic spread. Surprisingly, although ZYH

grade appeared to be roughest 'to the eye', the cleaved surface was found to have a reasonably low step density.

Table 4. 1 Characterisation of HOPG properties and topography

	ZYA	SPI-1	ZYH	SPI-2	AM†††
Mosaic spread†	0.4° ± 0.1°	0.4° ± 0.1°	3.5° ± 1.5°	0.8° ± 0.2°	n/a
Step density range (μm μm^{-2})	0.1 – 0.7	0.3 - 3.6	0.5 - 2.3	1 - 3.5	0.003-0.12
Mean step density (μm μm^{-2})	0.5 ± 0.1 (*N* = 15)	1.5 ± 0.21 (*N* = 14)	1.2 ± 0.6 (*N* = 10)	2.1 ± 0.9 (*N* = 10)	0.02 ± 0.02 (*N* = 20)
Step edge coverage on basal plane	Average 0.3% (range 0.03 - 1%)	Average 1.8% (range 0.5 - 3.4%)	Average 0.8% (range 0.2 - 2.1%)	Average 2.2% (range 0.6 - 6.7%)	Average 0.09% (range 0.006 - 0.48%)
Size (mm)	12 × 12 × 2	10 × 10 × 2	12 × 12 × 2	10 × 10 × 2	varied
Capacitance (μF cm^{-2})††	2.0 ± 0.3 (range 1.7 - 2.8) (*N* = 10)	2.9 ± 1.2 (range 2.0 - 3.8) (*N* = 10)	-	-	2.4 ± 1.5 (range 0.7 – 7.4) (*N* = 20)

† From www.spi2.com. The mosaic spread describes how ordered a sample is by providing the average angle of deviation of grains from the perpendicular axis.
†† Measured at 0.05 V vs. Ag/AgCl (1.0 M KCl).
††† AM was mechanically cleaved and other samples were cleaved using scotch tape.
For image analysis and capacitance measurements, *N* refers to the number of cleaved surfaces investigated. Errors are 1 standard deviation.

Given that the layer separation in HOPG is 0.335 nm,[19,23] the AFM images were used to deduce step heights in terms of the number of graphite layers. From AFM analysis of 69 images taken on ZYA, SPI-1, SPI-2, ZYH grade HOPG (scotch tape cleaved), and HOPG (AM) (mechanically cleaved), the step heights in terms of the number of graphite layers was calculated, producing the histograms shown in Figure 4. 2 and summarized in Table 4. 1. The data shows that ZYA, SPI-1 AM grades exhibit predominantly monolayer and bilayer steps, with AM, followed closely by ZYA grade, providing the optimum surface on which the density of step edges is minimized (Table 4. 1). Using the AFM images, the fraction of the basal surface occupied by edge plane-like sites was calculated. These data are summarized in Table 4. 1. It can be seen that the average step edge coverage varies significantly across the different grades, and also that within a grade, the range (from image to image on a particular surface) can vary by an order of magnitude. Thus, while the HOPG samples used

herein provide a set of basal surfaces with different edge plane densities to test the premise that edge planes alone are responsible for the electroactivity of HOPG, the detailed analysis immediately raises questions about the validity of the step-edge active model for two significant reasons.

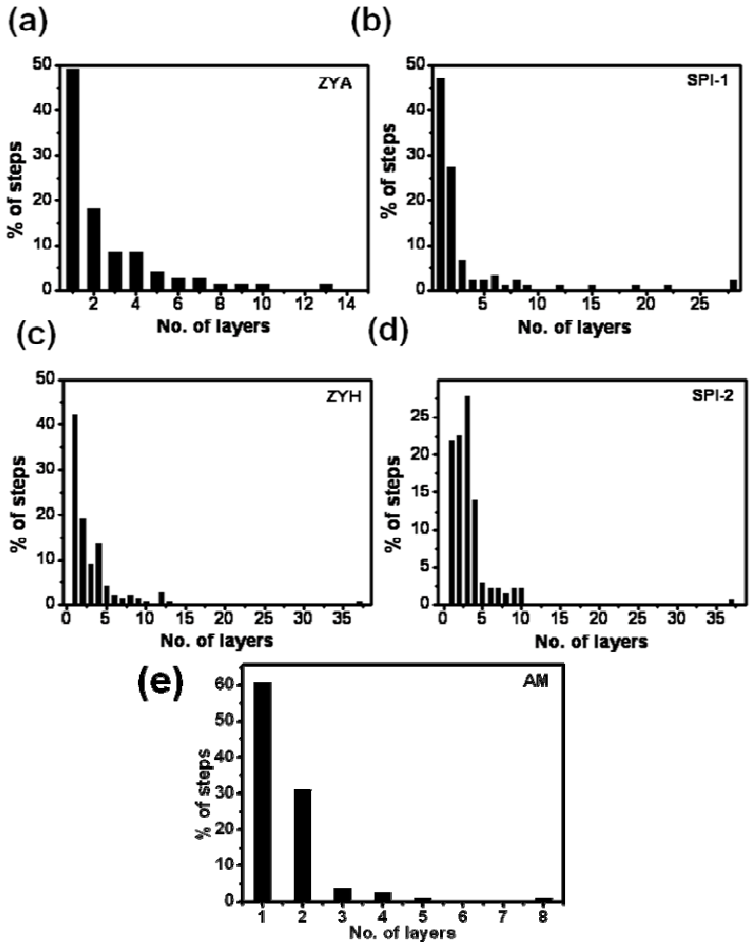

Figure 4. 2 Histograms of step edge heights on different grades of freshly cleaved HOPG: (a) ZYA, (b) SPI-1, (c) ZYH, (d) SPI-2 grades and (e) AM.

First, previous work[2, 19-23] - highlighted in the introduction - has found that the standard rate constants of the $Fe(CN)_6^{4-/3-}$ couple, spans a factor of *ca.* 10^8 (manifested in ΔE_p values of 59 mV to 1.5 V (scan rate 1 V s^{-1})), yet step densities,[2, 13-14, 28] including herein, only span a maximum range of 10^2. Second, while studies of different grades of HOPG in one laboratory apparently show different ET kinetics,[13, 23] investigations of different HOPG grades (evidently of widely variable quality based on the data herein) in different laboratories show similar slow ET kinetics. This appears contradictory for a step edge model of HOPG activity.

For the commercial samples, cleaved by scotch tape, it was found that as a particular (new) HOPG sample was cleaved, the step density and step heights tended, very gradually, to

become larger. This was consistent with technical information which recommends that the last 1 mm of a sample (i.e. half the initial sample) is discarded, since it comprises of the 'base layer' in which the mosaic spread is much higher than the 'top working layer'.[29-30] This advice was followed for the electrochemical measurements reported.

The AFM analysis of surface quality was supported by capacitance measurements of SPI-1, ZYA and HOPG (AM) (Figure 4. 1 and Table 4. 1). Capacitance values were extracted from simple CV measurements in 1 M KCl at 0.1 V s^{-1}. Figure 4. 3 shows data for three types of HOPG: (a) SPI-1, (b) ZYA and (c) AM, where freshly exposed surfaces for the first two were produced by cleaving with scotch tape and the latter by mechanical cleavage. Each cycle shown is the initial CV for a freshly cleaved surface, which – in every case - was representative of subsequent cycles (up to 10 runs), within ± 2%. The capacitance was extracted as the current amplitude at 0.05 V. For SPI-1 grade the capacitance was 2.9 ± 1.2 μF cm^{-2} (range 2.0 - 3.8 μF cm^{-2}). For ZYA grade, consistent values were obtained of 2.0 ± 0.3 μF cm^{-2} (range 1.7 – 2.8 μF cm^{-2}). The lowest values are consistent with the best reported in the early literature where very slow kinetics for $Fe(CN)_6^{4-/3-}$ was proposed.[13] For AM samples the values obtained were 2.4 ± 1.5 μF cm^{-2}, however a histogram of the values obtained (Figure 4. 3(d)) clearly shows that the majority of the values cluster between 0.7 μF cm^{-2} and 2.2 μF cm^{-2} with a few significant outliers which skews the overall data. Note that the lower values of 0.7 μF cm^{-2} and 1.1 μF cm^{-2} are close to the lowest observed value for this grade of HOPG cleaved mechanically.[23]

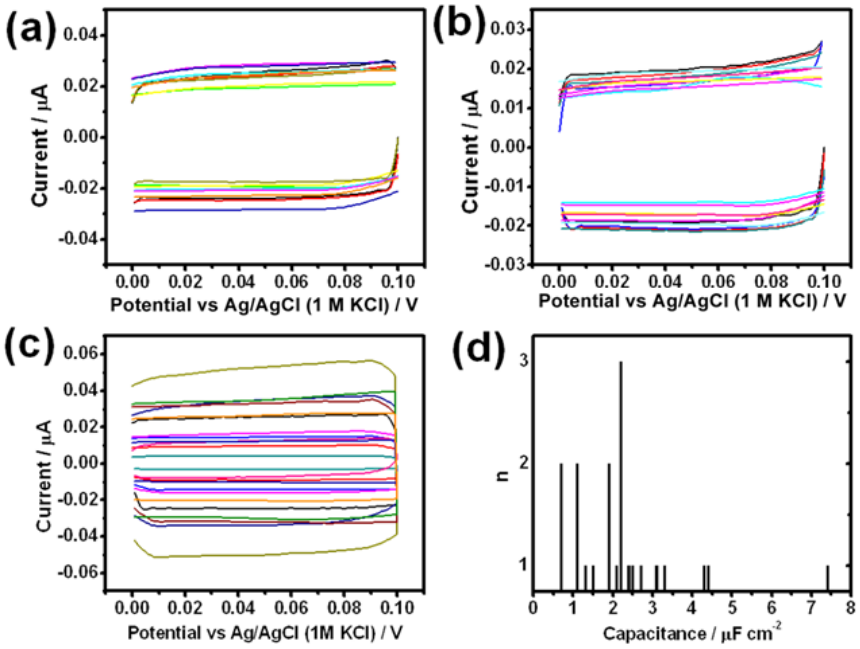

Figure 4. 3 CVs showing the background currents for 1 M KCl at 0.1 V s^{-1}. Each cycle was run on freshly cleaved HOPG: (a) SPI-1, (b) ZYA and (c) AM, using the Teflon cell arrangement. (d) A histogram of capacitance values extracted from (c).

ZYA consistently yielded a capacitance value of 2.0 ± 0.3 µF cm^{-2} (ranging between 1.7 to 2.8 µF cm^{-2}) consistent with the measurements of McCreery *et al.* on this material.[13, 23] Moreover, the lower capacitance values measured on ZYA grade HOPG are close to the lowest reported for low defect HOPG in early work (1.9 µF cm^{-2})[20] for which very large ΔE_p (>700 mV at 0.2 V s^{-1}) was seen for $Fe(CN)_6^{4-/3-}$. On the other hand, SPI-1 HOPG showed a slightly higher mean value and more variation, *i.e.* 2.9 ± 1.2 µF cm^{-2}, but this is still a reasonably low value in the context of some values reported.[20, 22, 31-33] For example, these values are far superior (lower) compared to those of ZYH grade HOPG recently reported by Bond and co-workers,[34] which varied between 3.4 to 7.1 µF cm^{-2} (suggesting surfaces with more defects).[13, 20] Yet, very large ΔE_p (slow kinetics) were still obtained for $Fe(CN)_6^{4-/3-}$ CVs in that work. It can thus be concluded that the samples used are of low step (and defect) density; at least as good as the best reported (for scotch tape cleaved material), and in many cases better. Mechanically cleaved HOPG (AM) provided the lowest capacitance values (0.7 µF cm^{-2}) – which essentially matched the very lowest ever reported for $HOPG^{23}$- but also occasionally much larger values (7.4 µF cm^{-2}) were seen, leading to an average of 2.4 ± 1.5 µF cm^{-2} (1 σ). This is again consistent with the wide range of values also observed by McCreery for HOPG (AM), where values between 0.6 and 6.5 µF cm^{-2} were reported.[23]

For HOPG (AM), cleaved mechanically, CVs of 1 mM $Fe(CN)_6^{4-/3-}$ in 1 M KCl at 0.1 V s^{-1} were run after measuring capacitance by quickly replacing the KCl solution with the mediator, in

order to explore any possible correlations between capacitance and ET kinetics. A plot of the capacitance vs. ΔE_p for $Fe(CN)_6^{4-/3-}$ redox is shown in Figure 4. 4. For 10 different measurements carried out on freshly prepared surfaces, ΔE_p is essentially independent of capacitance. Ten further measurements were performed on freshly cleaved AM HOPG, without first running capacitance. Statistically a significant fraction of these studies would be expected to be of high quality, and again the ΔE_p was found to range from 59 to 69 mV.

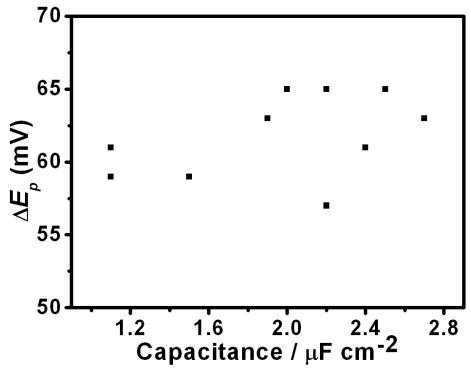

Figure 4. 4 Capacitance vs. ΔEp for 1 mM $Fe(CN)_6^{4-}$ oxidation in 0.1 M KCl at 0.1 V s^{-1} on the same surfaces.

FE-SEM was employed to visualize further the step density on ZYA and SPI-1 grade HOPG over much wider areas, since these were used for most voltammetric studies. This analysis also confirmed that the step density was much lower on ZYA grade HOPG than SPI-1 grade. Ag was electrodeposited from a solution containing 1 mM $AgNO_3$ in 1 M KNO_3. A 3-electrode arrangement was employed and electrodeposition was promoted by closing the circuit at a potential of -0.4 V vs. chloridised silver wire for 0.5 s. Figure 4. 5 shows representative images of: (a) SPI-1 grade HOPG and (b) ZYA grade HOPG after electrodeposition, from which it can be seen that the density of step edges is clearly much lower on ZYA grade HOPG than for SPI-1, consistent with the AFM data reported in Figure 4. 1 and Table 4. 1. However, it can also be seen that both surfaces exhibit some spatial heterogeneity in step separation. The average separation between two step edges ranges from approximately ~ hundreds of nm for SPI-1 grade to a few micrometers for ZYA grade, the latter in agreement with metal electrodeposition measurements on HOPG (AM) and ZYA grade HOPG samples.[35-39]

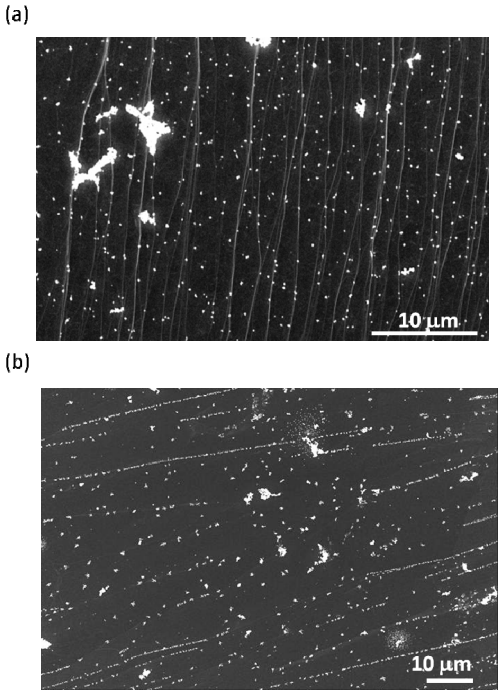

Figure 4. 5 FE-SEM images of initially freshly cleaved HOPG: (a) SPI-1 and (b) ZYA, after Ag electrodeposition.

4.3 CV CHARACTERISTICS

4.3.1 Voltammetry on freshly cleaved surfaces.

CV measurements are first considered as a function of scan rate for SPI-1 and ZYA grade HOPG. For the plots shown in Figure 4. 6, each CV was run on a freshly cleaved surface. For Figure 4. 6(a) and (b), 1 mM $Fe(CN)_6^{4-/3-}$ (purity 99.99%) in 1 M aqueous KCl was used. Similar data were obtained with 99% purity $Fe(CN)_6^{4-/3-}$. The data shown are entirely representative of measurements carried out on > 300 freshly cleaved surfaces with the $Fe(CN)_6^{4-/3-}$ couple, independently by 4 different people. These measurements show near reversible behaviour of the $Fe(CN)_6^{4-/3-}$ couple, for which ΔE_p would be *ca.* 59 mV[40] (Figure 4. 6(aii) and (bii)).

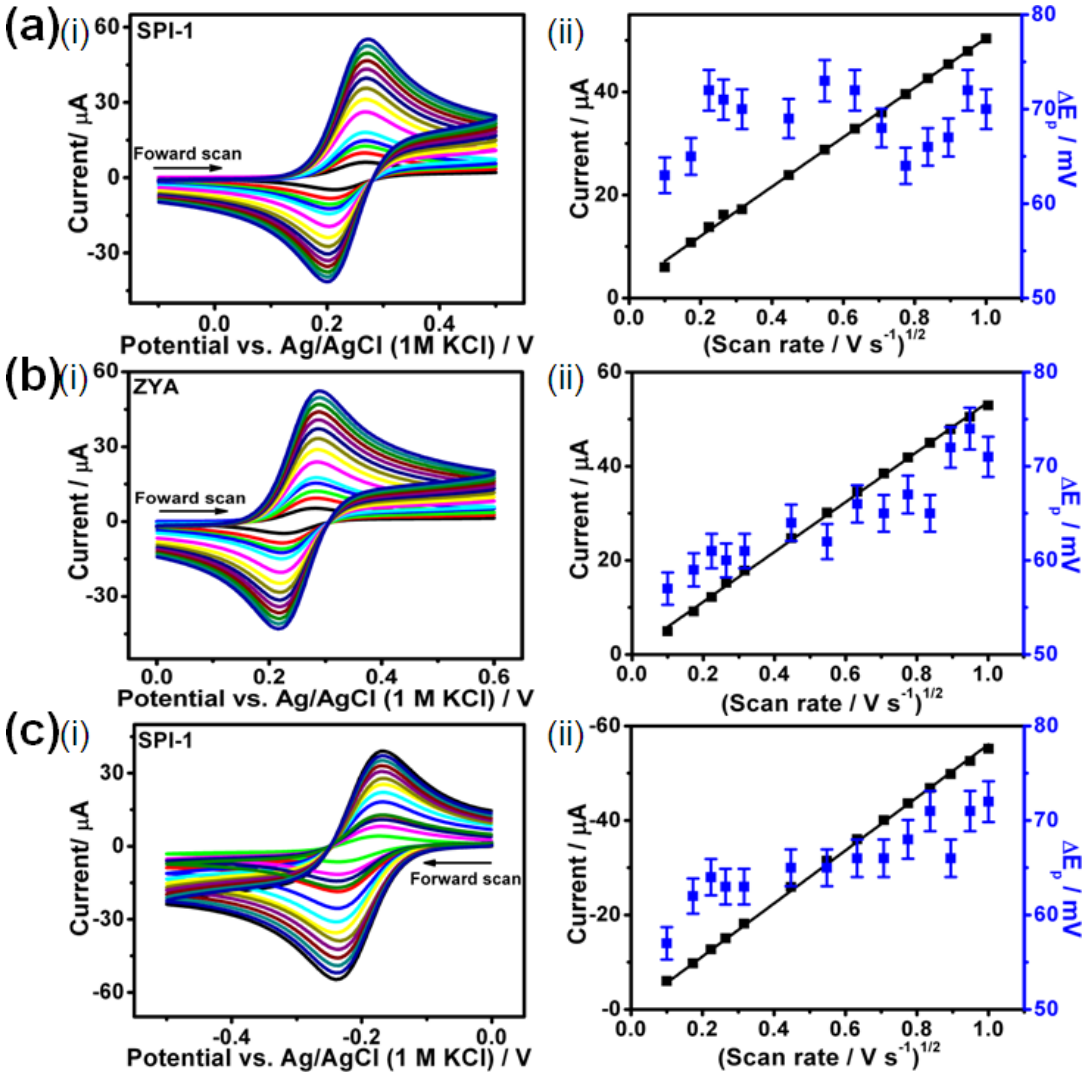

Figure 4. 6 CVs at a range of scan rates for the oxidation of 1 mM $Fe(CN)_6^{4-}$ (99.99%) in 1 M KCl on (a) SPI-1 and (b) ZYA HOPG. (c) CVs for the reduction of 1 mM $Ru(NH_3)_6^{3+}$ in 0.5 M KCl on HOPG (SPI-1). In all figures labelled (i) the scan rates are follows: 0.01, 0.03, 0.05, 0.07, 0.1, 0.2, 0.3, 0.4, 0.5, 0.6, 0.7, 0.8, 0.9, 1 V s^{-1}. The corresponding analyses of peak current (i_p) and peak-to-peak separation (ΔE_p) as a function of (scan rate)$^{1/2}$ are shown in (ii). Each CV shown was run on a freshly cleaved surface.

Although, in principle, one could attempt to analyze the CVs to obtain kinetic information, the ΔE_p values are too close to the reversible limit for this to be meaningful. Furthermore, as shown below, the HOPG surface and the $Fe(CN)_6^{4-/3-}$ couple is complicated by time-dependent heterogeneous surface effects, making a kinetic analysis - that would assume a uniform surface and simple electrochemical process -less than ideal. Evidently, the ΔE_p values are very similar for both types of HOPG despite the very large difference in characteristic step spacing and step coverage (Table 4. 1). The data in Figure 4. 6(aii) and (bii) also clearly show that the (forward) peak current is linear with the square root of scan rate and yielded a diffusion coefficient of 7.3 (± 0.3) × 10^{-6} cm^2 s^{-1} for $Fe(CN)_6^{4-}$, which is in agreement with literature.[41-42] The data is in sharp contrast with that reported (*vide supra*) in

the past, where values as high as 1.5 V have been observed on samples with low defect density,[3, 17, 21, 23, 43] but smaller values have also been reported, ranging from ~ 350 mV[44] to 58 mV[21] (indicating essentially reversible behaviour). In the past, such surfaces that exhibited reversible behaviour, were discarded as being too defective without further characterisation to confirm surface quality and cleaved again.[20-21] The analysis suggests this is an incorrect interpretation of the voltammetric characteristics. As outlined above, CV measurements on 20 freshly mechanically cleaved surfaces of HOPG (AM), half of which had capacitance run first, also yielded responses that were close to reversible.

Figure 4. 6(c) shows the CV behaviour and analysis of a freshly cleaved HOPG electrode (SPI-1 grade) for the reduction of 1 mM $Ru(NH_3)_6^{3+}$ in 1 M aqueous KCl, over the scan rate range 0.01 V s^{-1} to 1 V s^{-1}. The redox process is again close to reversible and the diffusion coefficient for $Ru(NH_3)_6^{3+}$ is calculated as 8.7 (± 0.3) × 10^{-6} cm^2 s^{-1}, which is in agreement with literature.[45-46] The data, again, contrasts markedly with previous studies where large ΔE_p have been observed for the $Ru(NH_3)_6^{3+/2+}$ couple ~ 200 mV.[21-22, 47] Reversible behaviour has been reported once before[24] but it was still concluded that the basal surface was totally[44] or largely inert.[1c,4b] The reversible behaviour observed for both $Ru(NH_3)_6^{3+/2+}$ and $Fe(CN)_6^{4-/3-}$ is consistent with data presented in Chapter 3 and recent microscale studies which evidenced fast ET at the basal surface.[48-51]

4.2.2 Time-dependent effects.

Due to the contrast between the CV behaviour seen herein, in earlier work and in light of microscale measurements reported recently as well as nanoscale data (Chapter 3),[52,] time-dependent effects wee next investigated on the macroscale to ascertain any possible complications associated with voltammetry at HOPG. CVs were typically recorded at 0.1 V s^{-1} every 5 minutes in the same solution for up to two hours. These studies were carried out with commercially available HOPG cleaved by scotch tape, as this is the cleavage procedure used by researchers in the field in all recent studies, [1, 3-5] and many early studies.[19-20, 53-54] Figure 4. 7 shows data for 1 mM $Fe(CN)_6^{4-}$ (purity 99.99%) in 1 M aqueous KCl on initially freshly cleaved HOPG: (a) ZYA; (b) SPI-1; (c) ZYH; (d) SPI-2. For all four grades, the ΔE_p value was seen to increase monotonically, with a dramatic change in wave shape and decrease in the magnitude of the current. This behaviour is indicative of a systematic diminution in the effective rate of ET as the electrode undergoes repetitive CV. Notably, there is very little difference in the behaviour of any of the grades of HOPG even though they have very different step quality (Table 4. 1).

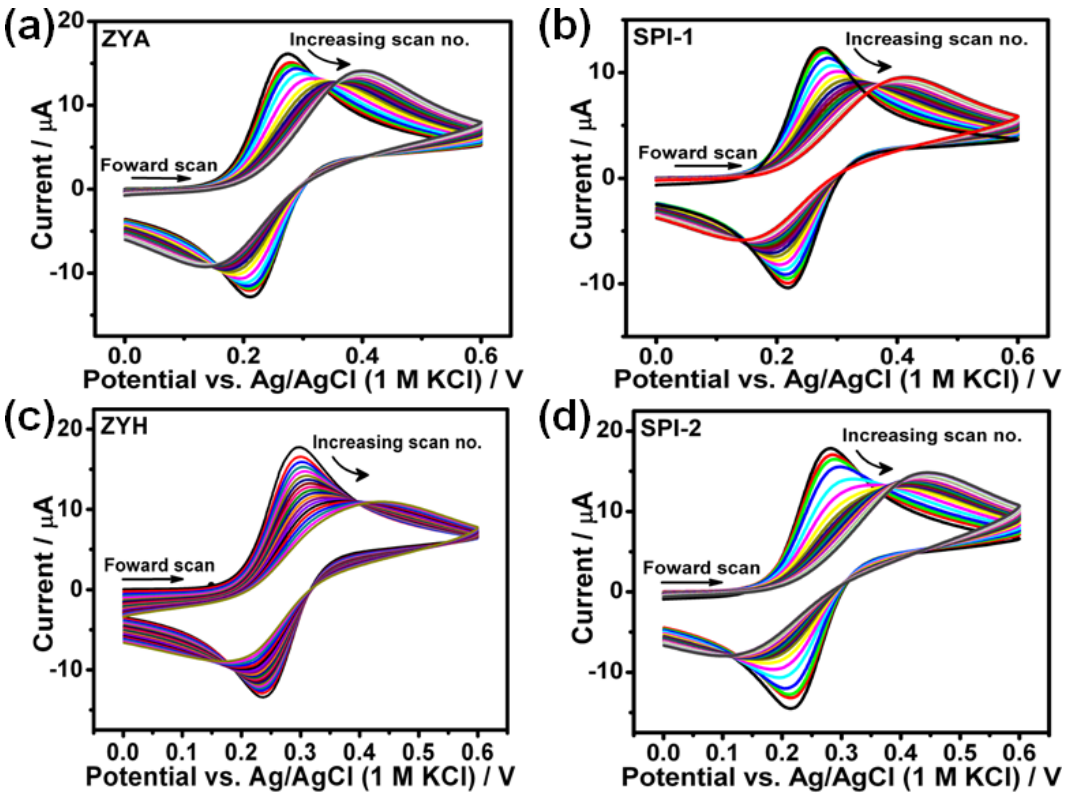

Figure 4. 7 Repeat CVs for the oxidation of 1 mM $Fe(CN)_6^{4-}$ (1 M KCl), run at 0.1 V s^{-1} on (a) ZYA, (b) SPI-1, (c) ZYH, (d) SPI-2 HOPG. Each cycle was run at 5 minute intervals; total of 20 cycles in each case.

By comparison, for the reduction of 1 mM $Ru(NH_3)_6^{3+}$ in 0.5 M KCl (0.1 V s^{-1}) at freshly cleaved HOPG (SPI-1 grade) recorded in the same manner, as a function of time, only a small systematic change in the ΔE_p was seen, Figure 4. 8, which ranged between ~64 mV (first scan) to 77 mV (last scan). In this case there is very little variation in the ΔE_p, which ranged between ~64 mV (first scan) to 77 mV (last scan). The origins of these effects and the differences in the two systems are discussed in the next sections.

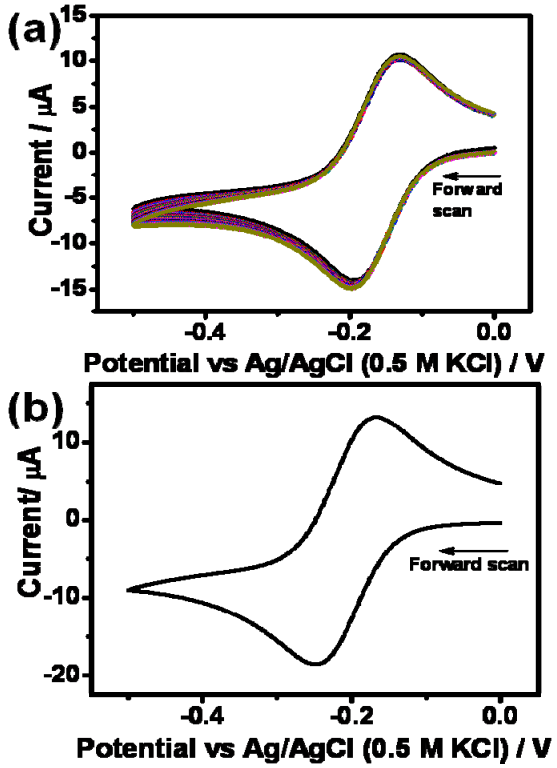

Figure 4. 8 (a) Repeat CVs for the reduction of 1 mM $Ru(NH_3)_6^{3+}$ in 0.5 M KCl, at 0.1 V s^{-1}, on HOPG (SPI-1) with each CV run at 5 min intervals (total of 20 cycles). (b) CV for the reduction of 1 mM $Ru(NH_3)_6^{3+}$ in 0.5 M KCl, at 0.1 V s^{-1}, run on a surface that had first been subjected to 20 cycles of 1 mM $Fe(CN)_6^{4-}$ in 1 M KCl, at 5 minute intervals on HOPG (SPI-1).

An important consideration for these measurements is the possibility that the composition in the cell changes, due to the finite volume, and that this impacts the subsequent voltammetric response. For a typical sweep rate of 0.1 V s^{-1}, as used above, and in the remaining studies reported herein, the charge passed in the forward wave for $Fe(CN)_6^{4-}$ oxidation was typically 4×10^{-6} C, representing ~0.05 % of the total redox active material in the cell. Furthermore, in the reverse scan most of the electrogenerated $Fe(CN)_6^{3-}$ is converted back to $Fe(CN)_6^{4-}$. Thus, even though a small volume is employed, voltammetry has negligible effect on the bulk solution composition.

Studies at a range of concentrations are valuable as a means of probing surface adsorption and passivation effects. Yet, surprisingly, previous studies of redox processes at HOPG (highlighted in the Introduction) were typically carried out at just one concentration (1 mM). It was found that the time-dependent CV response for $Fe(CN)_6^{4-/3-}$ showed a strong concentration effect. Figure 4. 9 shows a plot of ΔE_p against cycle number (5 minutes between scans) for concentrations of $Fe(CN)_6^{4-/3-}$ between 1 and 10 mM in 1 M KCl. Increasing the concentration of the redox species (and hence flux to the electrode surface) evidently leads to more rapid and more extensive passivation of the electrode surface with a

tendency towards a limiting ΔE_p value of *ca.* 500 mV on this time scale. The concentration dependence is a clear suggests that the observed passivation of the HOPG electrode is due to the electrolysis of the $Fe(CN)_6^{4-/3-}$ couple.

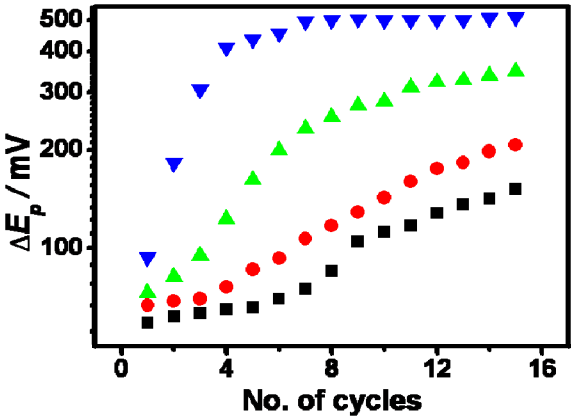

Figure 4. 9 ΔE_p against CV cycle number for concentrations of 1 mM (■), 2 mM (●), 5 mM(▲) and 10 mM (▼) $Fe(CN)_6^{4-}$ in 1 M KCl, run at 0.1 V s^{-1} on SPI-1 grade HOPG.

To determine whether the surface passivation could involve just the solution (without voltammetry), experiments were carried out where the solution (1 mM $Fe(CN)_6^{4-}$ (99.99%) in 1 M aqueous KCl), was left for: 0 mins (black); 1 hr (red) and 3 hrs (green) (at open circuit) on freshly cleaved HOPG before running a CV at 0.1 V s^{-1}. Typical data obtained on SPI-1 HOPG are shown in

Figure 4. 10(a). It can be seen that the ΔE_p value increases significantly with the time of HOPG surface exposure to solution. This is again evidence of a significant decrease in the effective ET kinetics. Thus, although the oxidation of $Fe(CN)_6^{4-}$ and subsequent reduction of $Fe(CN)_6^{3-}$ 'passivates' the HOPG surface, so does simply leaving the $Fe(CN)_6^{4-}$ solution in contact with the surface. It has been reported that for both HOPG[21] and a related material, BPPG,[3] simply leaving the surface in air for short periods of time, just a few minutes, resulted in an increase in the ΔE_p value for $Fe(CN)_6^{4-/3-}$.

As evident from Figure 5(b), a similar deterioration was also observed in the CV response at HOPG for 1 mM $Fe(CN)_6^{4-}$ in 1 M KCl (0.1 V s^{-1}) by comparing: immediately after cleaving (black); 1 hr wait time before adding the solution (red) and 3 hr wait time before adding the solution (green). Interestingly, when the same procedures were carried out for 1 mM $Ru(NH_3)_6^{3+}$ in 0.5 M KCl, no significant change in the ΔE_p value was observed;

Figure 4. 10(c) and 5(d).

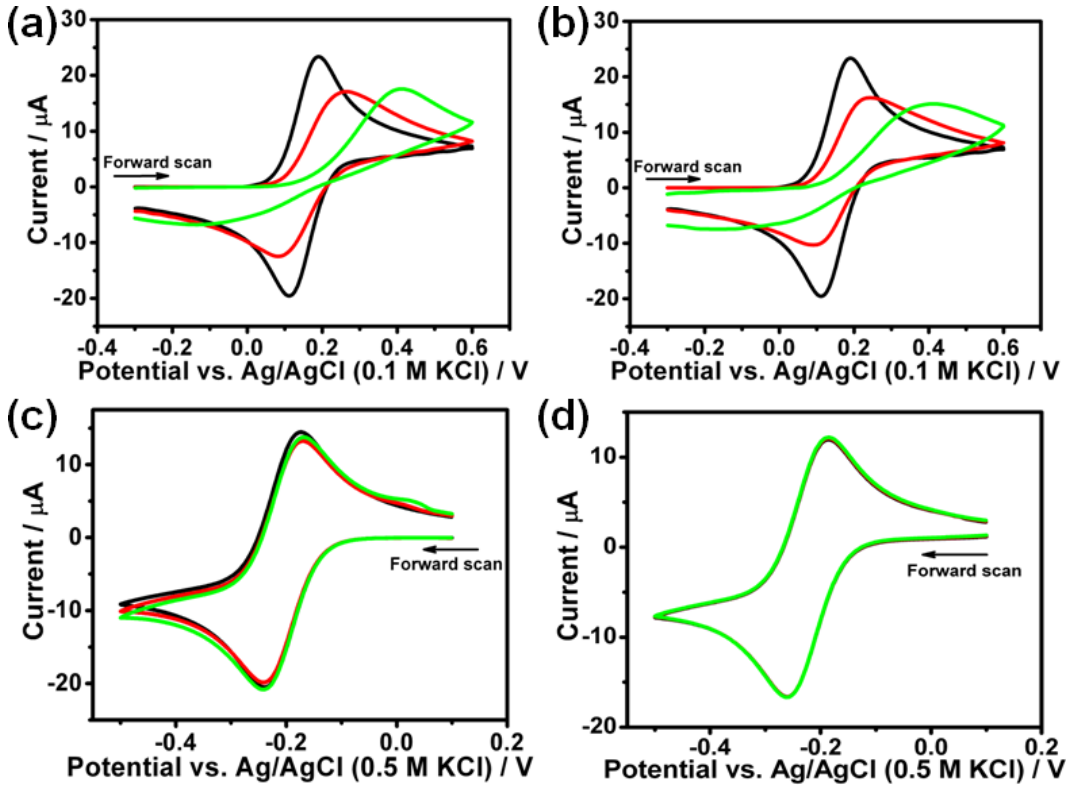

Figure 4. 10 CVs for the oxidation of 1 mM $Fe(CN)_6^{4-}$ in 0.1M KCl, at 0.1 V s^{-1}: (a) after leaving the solution in contact with the HOPG (SPI-1) for 0 minutes (black), 1 hour (red) and 3 hours (green); (b) after a freshly cleaved HOPG (SPI-1) surface was left for 0 minutes (black), 1 hour (red) and 3 hours (green). CVs for the reduction of 1 mM $Ru(NH_3)_6^{3+}$ in 0.5M KCl at 0.1 V s^{-1}: (c) after leaving the solution in contact with the HOPG for 0 minutes (black), 1 hour (red) and 3 hours (green); (d) after a freshly cleaved HOPG (SPI-1) surface was left for 0 minutes (black), 1 hour (red) and 3 hours (green). All CVs run on HOPG (SPI-1).

Further data for SPI-1 grade HOPG, Figure 4. 11, show the effect of cleaving HOPG and leaving the surface in air for 24 hours before running CV measurements of: (a) 1 mM $Fe(CN)_6^{4-}$ in 1 M KCl at 0.1 V s^{-1}; and (b) 1 mM $Ru(NH_3)_6^{3+}$ in 0.5 M KCl. Voltammetry for $Fe(CN)_6^{4-/3-}$ is now very irreversible (ΔE_p > 1 V), and for $Ru(NH_3)_6^{3+/2+}$ the behaviour is affected (ΔE_p ~ 115 mV) but much less.

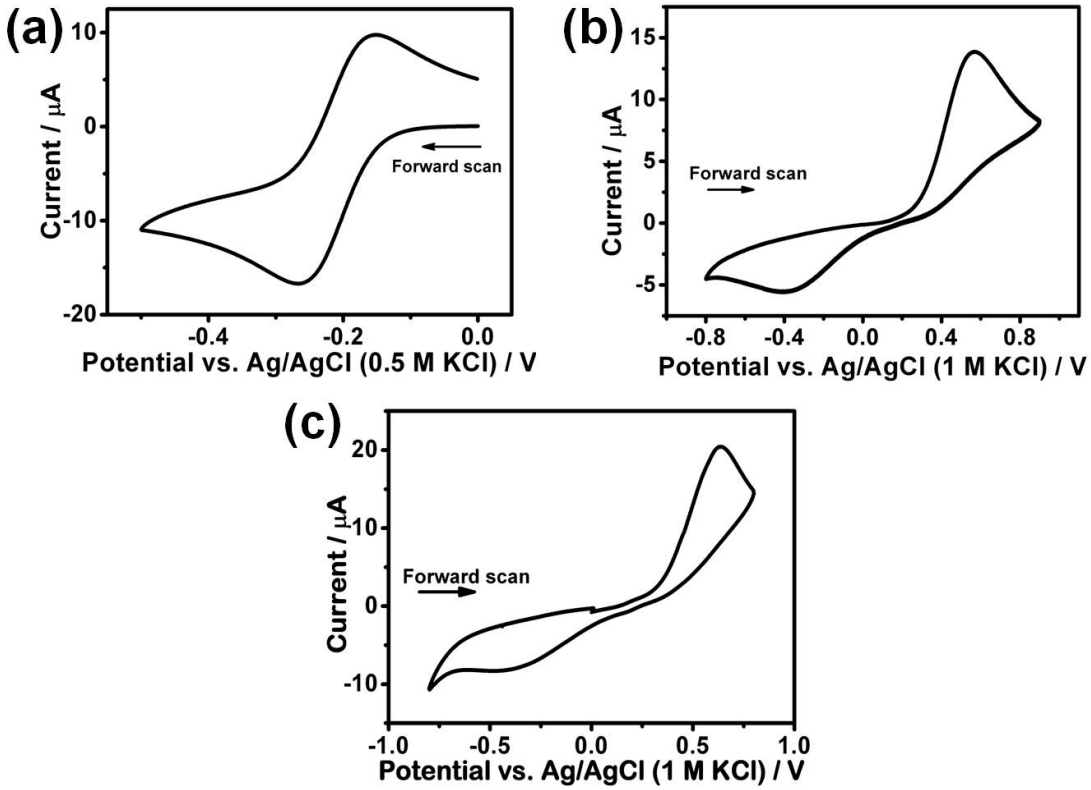

Figure 4. 11 CVs (0.1 V s^{-1}) for (a) the oxidation of 1 mM $Fe(CN)_6^{4-}$ in 1M KCl and (b) the reduction of 1 mM $Ru(NH_3)_6^{3+}$ in 0.5 M KCl. Each CV was run after the surface of the HOPG (SPI-1) was cleaved and left in air for 24 hours. (c) the CV for the oxidation of freshly made 1 mM $Fe(CN)_6^{4-}$ in 1 M KCl when the sample had been in Fe(CN)64- solution and cycled between 0 to 0.8 V for over 2 hours then gently cleaved once to remove the minimum number of layers but ensuring that the entire surface had been cleaved.

The origin of these various effects are considered in the next section. Importantly, all of these macroscale observations are entirely consistent with SECCM data presented in Chapter 3 and recent SMCM studies.[49] During SECCM imaging with $Fe(CN)_6^{4-/3-}$, on ZYA HOPG, the response was found to deteriorate during the course of a single scan (duration ~ 30 min), immediately after cleaving the HOPG surface, but for $Ru(NH_3)_6^{3+/2+}$ the response was more consistent, with only a small deterioration over time. The passivation of HOPG by $Fe(CN)_6^{4-/3-}$ voltammetry was found to not only affect the exposed surface but also occasionally the sub-surface, most likely via penetration at step edges, as found for other anions.[55-57] This is illustrated by Figure 4. 11(c), which shows the CV of freshly prepared HOPG (SPI-1 grade) with 1 mM $Fe(CN)_6^{4-}$ in 1 M KCl, after the sample had been fully immersed in solution and cycled at 5 minute intervals 20 times between -0.4 and 0.6 V, and then cleaved gently once. The CV shows a very irreversible response (ΔE_p of ~1.2 V).

4.3 HOPG SURFACE EFFECTS

Blocking of the electrode surface would be a plausible reason for the change in ET kinetics for $Fe(CN)_6^{4-/3-}$ with time reported above, and it was thus investigated whether such effects occurred via *in-situ* TM-AFM experiments. Images of HOPG electrode surfaces (SPI-1 grade) were recorded in solution, before and after the electrode was cycled up to 20 times at 5 minute intervals at 0.1 V s^{-1} between 0.0 V and 0.6 V, in a solution of 1 mM $Fe(CN)_6^{4-}$ (purity 99.99%) in 1 M KCl. This grade of HOPG was chosen because of its use for prominent voltammetric studies,[1, 17, 44, 58] and also because the relatively high density of steps (Table 4. 1) allows us to compare step-edge vs. basal regions of the cleaved HOPG surface.

TM-AFM provides simultaneous topographical (height) and phase images. The AFM phase image informs on any changes in energy dissipation during the tip-sample interaction due to changes in topography, tip-sample molecular interactions and deformation at the tip-sample contact, among other factors.[59] Although difficult to interpret quantitatively, the phase angle is sensitive to changes in the local material properties and can thus provide enhanced contrast. This aspect of TM-AFM is evident in data obtained for HOPG after 1 hour in solution (before any voltammetry), where the topography image appears to show a relatively clean surface (Figure 4. 12(ai)), while the phase image highlights considerable surface heterogeneity, notably around step edges but also on the basal terrace. This morphological change of the surface links directly to the slower kinetics seen after leaving $Fe(CN)_6^{4-}$ solution in contact with the surface.

After potential cycling, the topography - recorded in the same area as for Figure 4. 12(ai) - still appears to indicate a clean surface, but the corresponding phase image evidences further significant local changes in the surface at many locations, which could be indicative of adsorbed material. The images in Figure 4. 12(b) in fact represent the cleanest surface observed of eight substrates that were potential cycled in separate AFM experiments. For example, Figure 4. 12(c) shows other behaviour, where - after potential cycling - adsorbed material can be seen as discrete topographical features of *ca.* 5-10 nm in height, which also give rise to significant contrast in the corresponding phase image. Note that during the recording of this image the tip is likely to have picked up material from the surface, as indicated by the sudden change in the phase image part of the way through the scan and the repetition of features in both the topography and phase image ("multiple tip imaging"). Since Figure 4. 12(bii), (ci) and (cii) show evidence that material is deposited over the basal surface as well as at the step edges, in agreement with the voltammetric data above, it is deduced that blocking of the basal surface of HOPG leads (at least in part) to a diminution in electrode activity for the $Fe(CN)_6^{4-/3-}$ couple.

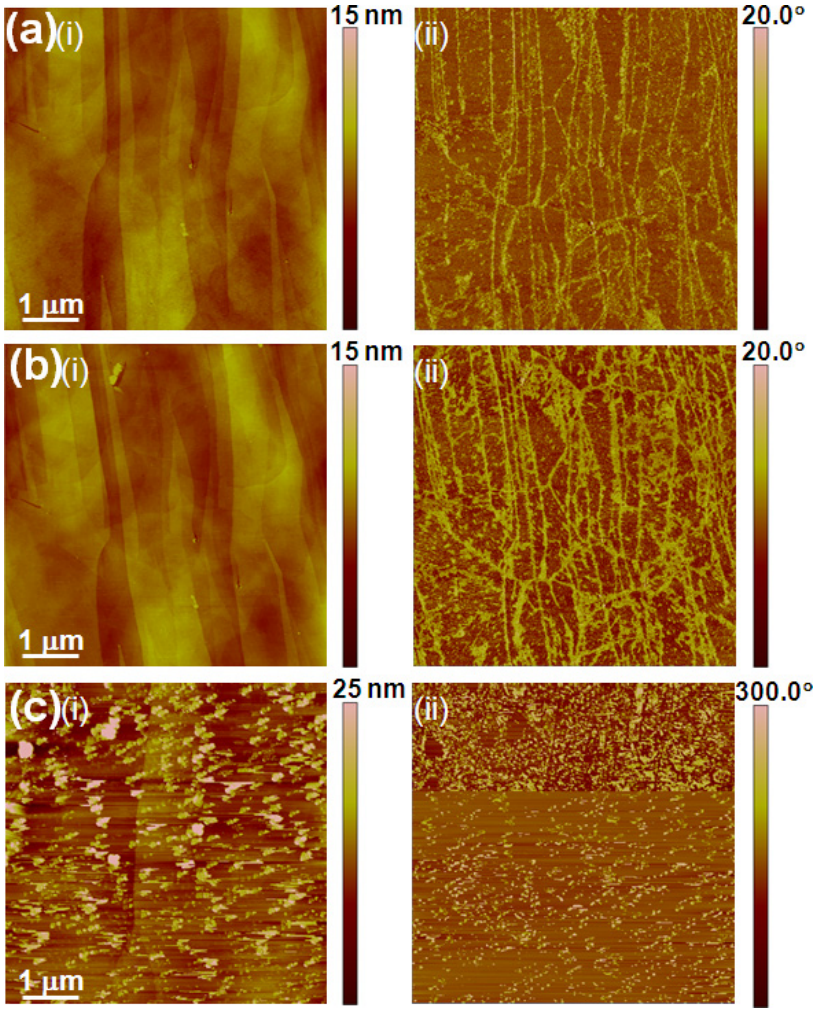

Figure 4. 12 *In-situ* TM-AFM height (i) and phase (ii) images taken on HOPG (SPI-1) during CV measurements run at 0.1 V s^{-1} in 1 mM $Fe(CN)_6^{4-}$ (purity 99.99%) in 1 M aqueous KCl: (a) before the first CV was run; (b) in the same area as (a) after 20 cycles; and (c) a different sample to (a) and (b) after 20 cycles were run.

Additional (control) *in-situ* TM-AFM studies were carried out using the same time procedure, but with 1 mM $Ru(NH_3)_6^{3+}$ in 0.5 M KCl, with the HOPG cycled between 0 V and -0.8 V, and with just supporting electrolyte (1M KCl), with the working electrode potential cycled between 0 V and 0.6 V. No changes in the topography or in the phase images were seen in either of these cases, even after cycling for up to 2 hours. Thus, it is clear that the observed deterioration in electrode kinetics for the $Fe(CN)_6^{4-/3-}$ couple on HOPG is specific to this couple. High resolution imaging and spectroscopic studies[60-61] for other electrode materials has clearly shown that side-products are involved in the $Fe(CN)_6^{3-/4-}$ voltammetric process, leading to the formation of insoluble Prussian Blue-like materials.[60] It is entirely reasonable to assume that similar processes operate for $Fe(CN)_6^{4-/3-}$ on HOPG.

It has been shown for other carbon-based electrodes that maps of the local electroactivity of the surface correspond well to the local intrinsic conductivity of the electrode, as determined

by C-AFM.[62-63] The local conductivity of HOPG can be assessed using C-AFM in air, focusing again on SPI-1 grade material, using the protocol outlined in the experimental section. Figure 4. 13(a) and (b) show typical (i) height and (ii) conductivity images (5 × 5 μm) recorded simultaneously, at 0.5 Hz, of (a) a freshly cleaved surface and (b) an initially freshly cleaved surface that was left in air for 24 hours before imaging. Note that slight "streaking" seen, also evident in previous C-AFM images of HOPG,[64-66] is likely due to variations in the tip to surface contact, as the tip scans the surface, but does not impact the capability to identify the general surface conductivity properties of HOPG.

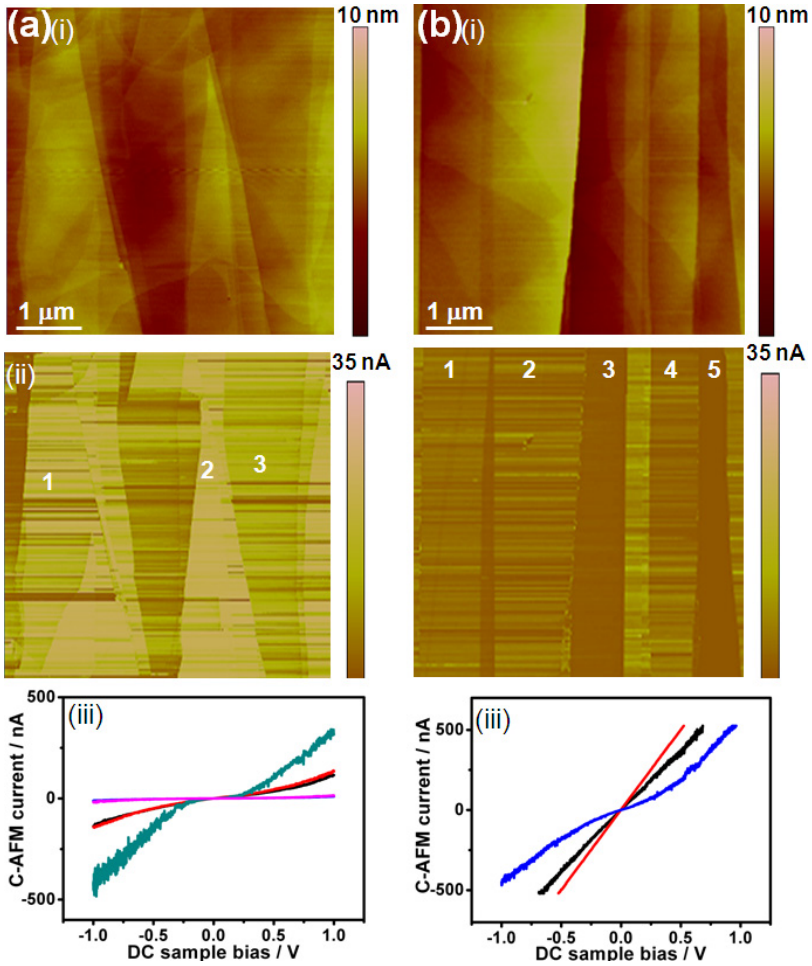

Figure 4. 13 Simultaneously recorded height (i) and conductivity (ii) images (5 × 5 μm) on HOPG (SPI-1) immediately after cleavage (a) and 24 hours after cleavage (b). (iii) C-AFM *i*-V curves recorded in terrace locations 1, 2 and 3 marked on (aii) and terrace locations 1, 2, 3, 4 and 5 marked on b(ii).

It is evident that although the surface is conducting, the current varies from terrace to terrace. To provide further information on the local conductivity of the HOPG surface, C-AFM (*i*-V) curves were recorded in distinct regions of the basal surface, which showed different current levels in the C-AFM map. Three such curves are shown in Figure 4. 13(aiii), recorded in the vicinity of the terrace regions labeled 1 (black), 2 (red) and 3 (blue) in Figure 4. 13(aii). In all

cases the *i*-V curves recorded repeatedly in the same spot overlapped (n = 5). For these three different characteristic *i*-V curves, local resistance (R) values were extracted in the low bias region *i.e.* -100 mV to +100 mV yielding R = 1.3 MΩ (terrace 1), R = 1 MΩ (terrace 2) and R = 3.7 MΩ (terrace 3). Note that these values include the 1MΩ resistor placed in series in the experimental measurements to limit the current flowing and possible damage to the metal-coated tip.

It is evident from Figure 4. 13(b) that the conductivity of the surface, after 24 hrs exposure to the atmosphere, is dramatically altered compared to the freshly cleaved case (Figure 8(a)), with some domains essentially inert at the applied potential bias and others showing greatly reduced conductivity. By recording *i*-V curves in the vicinity of the 5 different terraces labeled in Figure 4. 13(biii), R values were extracted in the region of low bias: R = 13 MΩ (terrace 1), R = 13 MΩ (terrace 2), R = 268 MΩ (terrace 3), R = 26 MΩ (terrace 4) and R = 267 MΩ (terrace 5), with a 1 MΩ resistor in series. These raw values are one to two orders of magnitude higher than the R values recorded on the freshly cleaved surface, and indicate a change in either tip-surface contact resistance or the local resistance of the HOPG surface layers of at least 3 orders of magnitude in some locations (taking into account the current-limiting resistor). The *i*-V curves all show a non-linear increase in the current at high bias.

The C-AFM data clearly show that long time exposure of HOPG to ambient conditions results in a significant increase in the local resistance of the surface compared to a freshly cleaved surface. In fact the deterioration in basal plane conductivity occurs on a fairly rapid time scale. Figure 4. 14 shows topography (i) and simultaneous C-AFM (ii) images for SPI-1 grade HOPG recorded immediately after cleaving (a) and 2 hours later (b). It can be seen that there is a significant decrease in conductivity over the surface, and that the changes are heterogeneous, as reported for more extensive times in the main text.

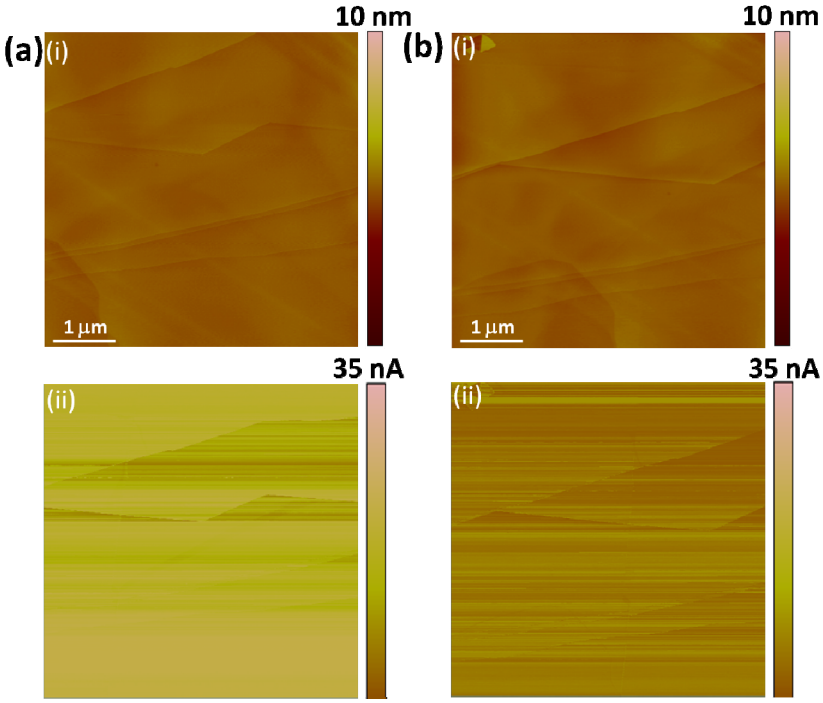

Figure 4. 14 Topography (i) and simultaneous C-AFM (ii) images for SPI-1 grade HOPG recorded immediately after cleaving (a) and 2 hours later (b).

It has been reported[24] that polished and cleaved BPPG exposed to air for up to 2 hrs, resulted in increasing kinetic effects for $Fe(CN)_6^{4-/3-}$. This was attributed purely to the oxygenation of edge planes. The data clearly indicates that, although this effect may occur, gross changes in the conductivity of much of the exposed basal surface must also be considered in the case of HOPG (and, by extension, to BPPG as well). It is well known that HOPG voltammetry is notoriously sensitive to deliberate treatment of the surface with organic impurities.[67] Naturally, extended periods, under ambient conditions, enhances the chance of the surface becoming contaminated, which would result in a greater contact resistance and tunneling barrier between the C-AFM tip and the HOPG surface. Such a barrier layer would naturally also influence voltammetric behaviour, and links convincingly to the electrochemical studies presented above. It is also possible that the top layer(s) of the HOPG could spontaneously delaminate leading to poor electrical contact. Evidently, the C-AFM studies highlight new issues connected with HOPG surface properties which may impact the analysis of earlier work,[3, 6-7, 9, 22, 24, 44, 53-54, 68] and need to be taken into account in the design and analysis of future studies of HOPG and mechanically exfoliated graphene.

4.4 NANOSCALE VISUALIZATION OF ELECTROCHEMICAL ACTIVITY WITH SECCM

SECCM is a powerful imaging technique for the simultaneous study of topography, surface electroactivity and conductivity, where the meniscus at the end of a pipette is used as a

positionable and moveable nanoelectrochemical cell once contacted with a electrode surface.[69-73] As described in the experimental section, and in full elsewhere,[72] I_{AC} is used as a set-point for imaging during which the surface electrochemical current, I_{act}, at an effective bias of V_s + ½ V_{bias}, with respect to the QRCEs in the pipette, is recorded. This technique used to visualize electrochemistry at cleaved ZYA grade HOPG (Chapter 3) where an electrochemical cell, an order in magnitude smaller than the step spacings, conclusively showed essentially uniform and fast electrochemical activity for the reduction of $Ru(NH_3)_6^{3+}$.

As highlighted above (Figure 4. 1 and Table 4. 1), the step spacing on mechanically cleaved HOPG (AM) is even larger than scotch tape cleaved ZYA grade HOPG, and as this has been proposed as the key material and cleavage procedure[74] it was considered worthwhile to map the local electrochemical activity of this material. As there are major complications involved in using the $Fe(CN)_6^{4-/3-}$ couple, as evidenced in Chapter 3 and previous imaging studies[49] and the macroscopic measurements reported herein, the focus of the following studies is on the $Ru(NH_3)_6^{3+/2+}$ couple.

Figure 4. 15 shows SECCM maps of: (a) quasi-topography, (b) surface current and (c) conductance current recorded between the barrels of the SECCM tip obtained for the reduction of 1 mM $Ru(NH_3)_6^{3+}$ in 0.1 M KCl at a potential close to the reversible quarter-wave potential, as determined by SECCM voltammetry, on mechanically cleaved AM HOPG. Parallel steps running across the surface with a basal region spanning up to 5 μm in length is clearly evident in the quasi-topography (a) and SECCM conductance (b) maps. The surface activity can be seen to be essentially constant at approximately 12.7 ± 1.0 pA (1 σ). For this tip the mass transport limited current was *ca.*80 pA and so the surface redox process measured is close to reversible across the basal surface of HOPG (AM).

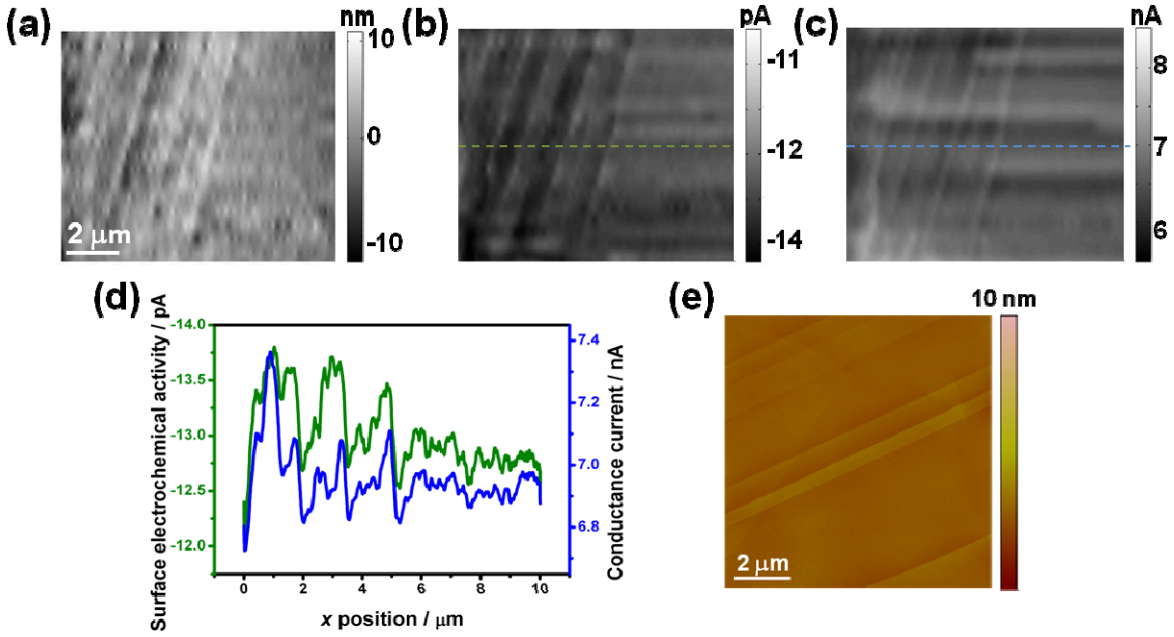

Figure 4. 15 SECCM maps of (a) quasi-topography, (b) surface current and (c) conductance current (DC component) recorded at -0.25 V for the reduction of 1 mM $Ru(NH_3)_6^{3+}$ at HOPG (AM) mechanically cleaved obtained with a ~350 nm pipette. (d) Example line section of surface electrochemical activity (green) and conductance current (blue) from marked region in (b) and (c). (e) AFM image representative of surface.

As in the study of ZYA grade HOPG presented in Chapter 3, a small increase in surface electrochemical current (Figure 4. 15(b)) is observed at the step sites, but there is also an increase in the conductance current between the barrels of the SECCM tip at the same locations (Figure 4. 15(d)). The conductance current is sensitive to variations in the meniscus size, and the increase is attributed to the meniscus increasing due to spreading as it passes over (hydrophilic) step edges, as discussed in Chapter 3.[52] A representative AFM image of mechanically cleaved HOPG (AM) in an area close to the SECCM measurements shows that there are step separations greater than 5 μm in this region of the surface (Figure 10(e)). The nanoscopic SECCM visualization studies are thus entirely consistent with the macroscopic measurements. Furthermore, the SECCM images on mechanically cleaved HOPG (AM) are consistent with the SECCM study presented in Chapter 3 on scotch tape cleaved ZYA grade HOPG. Both methods of cleaving produce wide basal terraces which display fast ET.

4.5 CONCLUSION

The classical voltammetry at the basal surface of HOPG has been reappraised, a material of intrinsic importance, but also one that is gaining increasing prominence as a 'standard' to which new sp^2 carbon materials, such as CNTs and graphene, are compared. Making extensive use of high resolution microscopy to understand the surface characteristics of

HOPG, the studies reported herein provide a new and self-consistent view of the electroactivity, tying together macroscale, microscale and nanoscale measurements. The results presented within this chapter show unequivocally that the pristine HOPG surface, which has been variously described as supporting only sluggish ET behavior,[2, 13, 19-23, 26, 53-54, 75-77] or even as being completely inert,[1, 3, 24, 43-44, 68, 78-82] has, in fact, considerable ET activity.

The freshly cleaved basal surfaces of five different grades of HOPG, cleaved by scotch tape or a mechanical procedure, show essentially reversible voltammetry for both $Fe(CN)_6^{4-/3-}$ and $Ru(NH_3)_6^{3+/2+}$ on the CV timescale. The general quality and step edge density of these surfaces has been fully characterized by AFM. For ZYA and SPI-1 material cleaved by scotch tape and HOPG (AM) cleaved mechanically, the quality of the surfaces has been further confirmed by capacitance measurements, as recommended in the early literature.[20-22] These HOPG samples provide a range of step-edge densities on the basal surface and, in the context of ZYA grade and AM material, particularly low step-edge densities (among the lowest reported) and a basal surface of high quality. This range of surfaces has enabled the significance of steps edges, in the HOPG electrode response, to be explored and identified.

Significantly, the new view of the macroscopic electrochemical response agrees entirely with recent direct microscale and nanoscale studies of basal surface HOPG,[48-52] and further SECCM studies reported herein. It is important to point out that the basal surface itself will contain point (atom-scale) defects that may have different ET activity to the basal terrace surface or indeed control it, but this has not, hitherto, been considered as an issue needed to explain the voltammetric response of HOPG. Determining the significance, if any, of such sites would require further improvement of nanoscale electrochemical imaging methods, which could eventually have sufficiently high resolution to address this issue directly.[71-72, 83]

The CV measurements on freshly cleaved surfaces conflict with many other high profile studies in the literature,[18, 84-88,8] which are frequently cited extensively as evidence that the basal surfaces of sp^2 carbon materials are essentially inert in terms of ET.[3-4, 17, 19-24, 43, 47, 76] Extensive studies reported in this chapter, exploring HOPG surface and time effects were aimed at rationalizing and explaining the data in the context of this past work. A significant finding is that $Fe(CN)_6^{4-}$ solution and voltammetry leads to the surface-adsorption of material which greatly impedes subsequent ET for the $Fe(CN)_6^{4-/3-}$ couple. Likewise, after cleaving, there are major time-dependant changes in the surface conductance properties of HOPG, probably by adsorbed impurities or other changes in the HOPG surface layer, which correlates with a measured deterioration in the $Fe(CN)_6^{4-/3-}$ voltammetric response. Even

freshly cleaved HOPG shows heterogeneous surface conductivity which may impact the voltammetric response.

On the other hand, the surface effects observed (blocking of the HOPG electrode and changes in the surface conductivity) have much less influence on $Ru(NH_3)_6^{3+/2+}$ voltammetry at the macroscale. Of course, microscale and nanoscale effects on surface activity may occur but are not manifest significantly in the macroscale response. In light of the work herein, it is unfortunate that $Fe(CN)_6^{4-/3-}$ voltammetry was selected as a means for 'surface validation'[19-23] of HOPG and that it has been used extensively as a redox probe to assess ET activity at the basal surface of HOPG. [3, 17, 24, 44, 78, 81]

The surface effects observed occur on a short time scale and become more prevalent over longer timescales (typically a few CVs, or a timescale of an hour or more). In some instances, the CV morphologies that result are then similar to some of those in the past literature. For example, the CVs for $Fe(CN)_6^{4-/3-}$ after extensive cycling (Figure 4. 7) and after deploying a wait time of a few hours before cycling (
Figure 4. 10(a) and (c)) resemble those shown by Compton *et al*).[24, 44] Similarly, the very distorted voltammograms evident after leaving HOPG for a long period before running voltammetry (Figure 4. 11(a)) and cleaving after extensively cycling (Figure 4. 11(c)) resemble the morphology of those reported previously.[3-4, 17, 19, 22, 43, 47] Some of these past studies provide little information on the precise time frame of the measurements,[3-4, 17, 43, 47] and the results herein thus potentially provide an explanation of this past work, particularly as work has been carried out with identical HOPG material from the same supplier, and cleaved in the same way. On the other hand, in the oldest body of past work measurements were apparently made immediately after cleaving HOPG.[20-21] In view of this, it is difficult to explain the difference in initial CV behavior seen herein and these past studies, but if impurity adsorption (and other surface effects) were responsible for the dramatic deterioration has been observed in HOPG surface conductivity, and concomitant changes in the $Fe(CN)_6^{4-/3-}$ voltammetric response, one might reasonably expect different timescales for such processes in different laboratories/environments and, of course, in different eras.

It is important to point out that the reversible (or fast ET) reported herein for $Fe(CN)_6^{4-/3-}$ on freshly cleaved HOPG has been seen by others for HOPG, [86,67, 77] but in light of the earlier recommendations about the $Fe(CN)_6^{4-/3-}$ couple being diagnostic of surface quality,[**19-23, 26**] it was assumed that the HOPG surfaces used must have been very defective, although no other corroboratory evidence was provided. The studies presented within this chapter clearly establish that the pristine basal surface of a wide range of HOPG (AM, ZYA, ZYH, SPI-1 and

SPI-2) provides an active electrode material for ET, as evident from studies of both $Fe(CN)_6^{4-/3-}$ and $Ru(NH_3)_6^{3+/2+}$. Finally, this new view of the electroactivity of the HOPG basal surface – and the important issues concerning the use of $Fe(CN)_6^{4-/3-}$ and the timescale of measurements, are expected to be valuable for rationalizing different viewpoints on other sp^2 materials, notably nanotubes and graphene. In particular, $Fe(CN)_6^{4-/3-}$ has been used in recent studies of the electrochemical properties of monolayer and multilayer graphene,[6, 8-9] and comparisons have generally been made between graphene and HOPG.[8-9] It is evident from these studies that $Fe(CN)_6^{4-/3-}$ should be used with caution for such studies in the future, if at all. Moreover, studies of exfoliated graphene need careful control and identification of the measurements time after exfoliation.

4.6 REFERENCES

1. Bowler, R.,T. J. Davies,M. E. Hyde,R. G. Compton, *Anal. Chem.,* **2005,** *77,* 1916-1919.
2. McDermott, M. T.,R. L. McCreery, *Langmuir,* **1994,** *10,* 4307-4314.
3. Davies, T. J.,R. R. Moore,C. E. Banks,R. G. Compton, *J. Electroanal. Chem.,* **2004,** *574,* 123-152.
4. Lee, C.-Y.,S.-X. Guo,A. M. Bond,K. B. Oldham, *J. Electroanal. Chem.,* **2008,** *615,* 1-11.
5. Bradbury, C. R.,L. Kuster,D. J. Fermín, *J. Electroanal. Chem.,* **2010,** *646,* 114-123.
6. Rodriguez-Lopez, J.,N. L. Ritzert,J. A. Mann,C. Tan,W. R. Dichtel,H. D. Abruna, *J Am Chem Soc,* **2012,** *134,* 6224-6236.
7. Li, W.,C. Tan,M. A. Lowe,H. D. Abruña,D. C. Ralph, *ACS Nano,* **2011,** *5,* 2264-2270.
8. Tan, C.,J. Rodriguez-Lopez,J. J. Parks,N. L. Ritzert,D. C. Ralph,H. D. Abruna, *ACS Nano,* **2012,** *6,* 3070-3079.
9. Valota, A. T.,I. A. Kinloch,K. S. Novoselov,C. Casiraghi,A. Eckmann,E. W. Hill,R. A. W. Dryfe, *ACS Nano,* **2011,** *5,* 8809-8815.
10. Jandt, K., *Surf. Sci.,* **2001,** *491,* 303-332.
11. Carswell, A. D. W.,E. A. O'Rear,B. P. Grady, *J. Am. Chem. Soc.,* **2003,** *125,* 14793-14800.
12. Ta, T. C.,M. T. Sykes,M. T. McDermott, *Langmuir,* **1998,** *14,* 2435-2443.
13. Robinson, R. S.,K. Sternitzke,M. T. Mcdermott,R. L. McCreery, *J. Electrochem. Soc.,* **1991,** *138,* 2412-2418.
14. Chang, H.,A. J. Bard, *Langmuir,* **1991,** *7,* 1143-1153.
15. Dumitrescu, I.,P. R. Unwin,J. V. Macpherson, *Chem. Commun.,* **2009,** *7345,* 6886-6901.
16. McCreery, R. L., *Chem. Rev,* **2008,** *108,* 2646-2687.
17. Banks, C. E.,T. J. Davies,G. G. Wildgoose,R. G. Compton, *Chem. Commun.,* **2005,** 829-841.
18. Liu, H.,F. Favier,K. Ng,M. P. Zach,R. M. Penner, *Electrochim. Acta,* **2001,** *47,* 671-677.
19. Bowling, R. J.,R. T. Packard,R. L. McCreery, *J. Am. Chem. Soc.,* **1989,** *111,* 1217-1223.
20. Rice, R. J.,R. L. McCreery, *Anal. Chem.,* **1989,** *61,* 1637-1641.
21. Kneten, K. R.,R. L. McCreery, *Anal. Chem.,* **1992,** *64,* 2518-2524.
22. Cline, K. K.,M. T. Mcdermott,R. L. McCreery, *J. Phys. Chem.,* **1994,** *98,* 5314-5319.
23. McDermott, M. T.,K. Kneten,R. L. McCreery, *J. Phys. Chem.,* **1992,** *96,* 3124-3130.
24. Ji, X.,C. E. Banks,A. Crossley,R. G. Compton, *ChemPhysChem,* **2006,** *7,* 1337-1344.
25. Xu, J.,Q. Chen,G. M. Swain, *Anal. Chem.,* **1998,** *70,* 3146-3154.
26. McCreery, R. L.,K. K. Cline,C. A. McDermott,M. T. McDermott, *Colloids Surf., A,* **1994,** *93,* 211-219.
27. Hathcock, K. W.,J. C. Brumfield,C. A. Goss,E. A. Irene,R. W. Murray, *Anal. Chem.,* **1995,** *67,* 2201-2206.
28. Hendricks, S. A.,Y.-T. Kim,A. J. Bard, *J. Electrochem. Soc.,* **1992,** *139,* 2818-2824.
29. No Title. www.ktechnano.com (accessed 31-05-2012).
30. www.ntmdt-tips.com. www.ntmdt-tips.com (accessed 31-05-2012).
31. Randin, J. P.,E. Yeager, *J. Elechochem. Soc.,* **1971,** *778,* 711-714.
32. Randin, J. P.,E. J. Yeager, *Electroanal. Chem.,* **1972,** *36,* 257-276.
33. Randln, J. P.,E. Yeager, *J. Electroanal. Chem.,* **1975,** *56*.
34. Lee, C. Y.,A. M. Bond, *Analytical Chemistry,* **2009,** *81,* 584-594.
35. Atashbar, M. Z.,V. Bliznyuk,D. Banerji,S. Singamaneni, *J. Alloys Compd.,* **2004,** *372,* 107-110.

36. Walter, E. C.,F. Favier,R. M. Penner, *Anal. Chem.,* **2002,** *74,* 1546-1553.
37. Zach, M. P.,K. Inazu,K. H. Ng,J. C. Hemminger,R. M. Penner, *Chem. Mater.,* **2002,** *14,* 3206-3216.
38. Stabel, A.,K. Eichhorst-Gerner,J. P. Rabe,A. R. Gonzalez-Elipe, *Langmuir,* **1998,** *14,* 7324-7326.
39. Hu, J.,R. W. Carpick,M. Salmeron,X. D. Xiao, *J Vac Sci Technol B,* **1996,** *14,* 1341-1343.
40. Bard, A. J.,L. R. Faulkner, *Electrochemical methods : fundamentals and applications*. 2nd ed.; John Wiley & Sons: 2001.
41. Konopka, S. J.,B. McDuffie, *Anal. Chem.,* **1970,** *42,* 1741-1746.
42. Aoki, K.,K. Akimoto,K. Tokuda,H. Matsuda,J. Osteryoung, *J. Electroanal. Chem.,* **1984,** *171,* 219-230.
43. Banks, C. E.,R. G. Compton, *The Analyst,* **2006,** *131,* 15-21.
44. Davies, T. J.,M. E. Hyde,R. G. Compton, *Angew. Chem.,* **2005,** *44,* 5121-5126.
45. Birkin, P. R.,S. SilvaMartinez, *J. Electroanal. Chem.,* **1996,** *416,* 127-138.
46. Macpherson, J. V.,D. O'Hare,P. R. Unwin,C. P. Winlove, *Biophys. J.,* **1997,** *73,* 2771-2781.
47. Lee, C.-Y.,A. M. Bond, *Anal. Chem.,* **2009,** *81,* 584-594.
48. Frederix, P. L.,P. D. Bosshart,T. Akiyama,M. Chami,M. R. Gullo,J. J. Blackstock,K. Dooleweerdt,N. F. de Rooij,U. Staufer,A. Engel, *Nanotechnology,* **2008,** *19,* 384004.
49. Williams, C. G.,M. A. Edwards,A. L. Colley,J. V. Macpherson,P. R. Unwin, *Anal. Chem.,* **2009,** *81,* 2486-2495.
50. Edwards, M. A.,P. Bertoncello,P. R. Unwin, *J. Phys. Chem. C,* **2009,** *113,* 9218-9223.
51. Anne, A.,E. Cambril,A. Chovin,C. Demaille,C. Goyer, *ACS Nano,* **2009,** *3,* 2927-2940.
52. Lai, S. C. S.,A. N. Patel,K. McKelvey,P. R. Unwin, *Angew. Chem. Int. Ed.,* **2012,** *51,* 5405-5408.
53. Bowling, R.,R. T. Packard,R. L. McCreery, *Langmuir,* **1989,** *5,* 683-688.
54. Bowling, R. J.,R. L. McCreery,C. M. Pharr,R. C. Engstrom, *Anal. Chem.,* **1989,** *61,* 2763-2766.
55. Hathcock, K. W.,J. C. Brumfield,C. A. Goss,E. A. Irene,R. W. Murray, *Anal. Chem.,* **1995,** *67,* 2201-2206.
56. Alsmeyer, D. C.,R. L. McCreery, *Anal. Chem.,* **1992,** *64,* 1528-1533.
57. Alliata, D.,P. Häring,O. Haas,R. Kötz,H. Siegenthaler, *Electrochem. Commun.,* **1999,** *1,* 5-9.
58. Banks, C. E.,R. R. Moore,T. J. Davies,Rg, *Chem. Commun.,* **2004**.
59. Tamayo, J.,R. Garcia, *Langmuir,* **1996,** *12,* 4430-4435.
60. López-Palacios, J.,A. Heras,A. Colina,V. Ruiz, *Electrochim. Acta,* **2004,** *49,* 1027-1033.
61. Pharr, C. M.,P. R. Griffiths, *Anal. Chem.,* **1997,** *69,* 4673-4679.
62. Colley, A. L.,C. G. Williams,U. D'Haenens Johansson,M. E. Newton,P. R. Unwin,N. R. Wilson,J. V. Macpherson, *Anal. Chem.,* **2006,** *78,* 2539-2548.
63. Wilson, N. R.,S. L. Clewes,M. E. Newton,P. R. Unwin,J. V. Macpherson, *J. Phys. Chem. B,* **2006,** *110,* 5639-5646.
64. Banerjee, S.,M. Sardar,N. Gayathri,A. K. Tyagi,B. Raj, *Phys. Rev. B.,* **2005,** *72,* 075418-075424.
65. Lu, Y.,M. Muñoz,C. Steplecaru,C. Hao,M. Bai,N. Garcia,K. Schindler,P. Esquinazi, *Phys. Rev. Lett.,* **2006,** *97,* 076805.
66. Shvets, V. V.,O. V. Sinitsyna,G. B. Meshkov,I. V. Yaminsky, *Mosc U Phys B+,* **2010,** *65,* 501-505.
67. Liu, Y.,M. S. Freund, *Langmuir,* **2000,** *16,* 283-286.
68. Moore, R. R.,C. E. Banks,R. G. Compton, *Analyst,* **2004,** *129,* 755-758.

69. Güell, A. G.,N. Ebejer,M. E. Snowden,J. V. Macpherson,P. R. Unwin, *J. Am. Chem. Soc.,* **2012,** *134,* 7258-7261.
70. Patten, H. V.,S. C. Lai,J. V. Macpherson,P. R. Unwin, *Anal Chem,* **2012,** *84,* 5427-5432.
71. Lai, S. C. S.,P. V. Dudin,J. V. Macpherson,P. R. Unwin, *J. Am. Chem. Soc.,* **2011,** *133,* 10744-10747.
72. Snowden, M. E.,A. G. Güell,S. C. S. Lai,K. McKelvey,N. Ebejer,M. A. O'Connell,A. W. Colburn,P. R. Unwin, *Anal. Chem.,* **2012,** *84,* 2483-2491.
73. Guell, A. G.,N. Ebejer,M. E. Snowden,K. McKelvey,J. V. Macpherson,P. R. Unwin, *Proc. Natl. Acad. Sci. U S A,* **2012,** *109,* 11487-11492.
74. McCreery, R. L.,M. T. McDermott, *Anal Chem,* **2012,** *84,* 2602-2605.
75. Ray, K.,R. L. McCreery, *Anal. Chem.,* **1997,** *69,* 4680-4687.
76. McCreery, R. L., *Electroanalytical Chemistry*. Dekker: NY, 1991; Vol. 17, p 221-374.
77. McDermott, M. T.,J. K. Kariuki, *Langmuir,* **1999,** *15,* 6534-6540.
78. Banks, C. E.,R. R. Moore,T. J. Davies,R. G. Compton, *Chem. Commun.,* **2004,** 1804-1805.
79. Hyde, M. E.,T. J. Davies,R. G. Compton, *Angew. Chem. Int. Ed.,* **2005,** *44,* 6491-6496.
80. Ji, X. B.,M. C. Buzzeo,C. E. Banks,R. G. Compton, *Electroanal.,* **2006,** *18,* 44-52.
81. Moore, R. R.,C. E. Banks,R. G. Compton, *Anal. Chem.,* **2004,** *76,* 2677-2682.
82. Banks, C. E.,R. G. Compton, *Anal. Sci.,* **2005,** *21,* 1263-1268.
83. Ebejer, N.,M. Schnippering,A. W. Colburn,M. A. Edwards,P. R. Unwin, *Anal. Chem.,* **2010,** *82,* 9141-9145.
84. González Orive, A.,D. Grumelli,C. Vericat,J. M. Ramallo-López,L. Giovanetti,G. Benitez,J. C. Azcárate,G. Corthey,M. H. Fonticelli,F. G. Requejo,A. Hernández Creus,R. C. Salvarezza, *Nanoscale,* **2011,** *3,* 1708-1716.
85. Brülle, T.,U. Stimming, *J. Electroanal. Chem.,* **2009,** *636,* 10-17.
86. Peruffo, M.,P. Contreras-Carballada,P. Bertoncello,R. M. Williams,L. D. Cola,P. R. Unwin, *Electrochem. Commun.,* **2009,** *11,* 1885-1887.
87. Rodríguez-Nieto, F. J.,T. Y. Morante-Catacora,C. R. Cabrera, *J. Electroanal. Chem.,* **2004,** *571,* 15-26.
88. Cherstiouk, O. V.,P. A. Simonov,E. R. Savinova, *Electrochim. Acta,* **2003,** *48,* 3851-3860.

CHAPTER 5: NANOELECTROCHEMICAL REACTIVE PATTERNING REVEALS THE ACTIVE SITES FOR DOPAMINE OXIDATION AT GRAPHITE SURFACES

Graphitic electrodes are widely used to bio-electroanalysis, particularly for the detection of neurotransmitters in a wide range of situations, and consequently there has been considerable effort to optimize and understand the intrinsic behavior of such electrode materials. Scanning electrochemical cell microscopy (SECCM) is used herein to directly examine the long-held view that the basal surface of graphite is inert for the electrochemical oxidation of the neurotransmitter dopamine (DA) and that the activity is confined to step edges. SECCM allows the analysis of individual electrochemical (EC) current measurements to be made across a surface, and because DA oxidation produces a polymeric product, which deposits on the electrode surface, it is possible to directly correlate EC currents with the surface location of measurement. The studies herein demonstrate unambiguously that DA oxidation occurs readily at pristine highly orientated pyrolytic graphite (HOPG) and that step edges are not needed to catalyse the reaction. These results have implications for understanding the response of related sp^2 carbon materials, such as nanotubes and graphene, and for the design of carbon-based electrodes for bio-electroanalysis.

5.1 INTRODUCTION

The detection of dopamine (DA) is currently a subject of significant interest. DA is a neurotransmitter that plays an essential role in the function of the central nervous, renal, hormonal and cardiovascular systems[1-3] and deficiencies or excess of DA has been linked to neurological diseases such as Parkinson's disease, schizophrenia, autism, and attention deficit hyperactivity disorder (ADHD).[3-6] The ability to monitor DA levels is highly desirable as a diagnostic tool to treat a wide range of physical and mental health conditions. As neurotransmitters are relatively easy to oxidise/reduce, electrochemical techniques have been extensively investigated as a means of detection and have provided both qualitative and quantitative information on DA levels.[7-11] Major issues in the use of electrochemistry are the reversibility of the process and the fouling of the electrode surface due to the accumulation of adsorbed oxidized products. This can lead to poor sensitivity, selectivity and deterioration in detection response over time.[12-13] Another major issue in the electrochemical detection of DA is interference from competing coexisting electrochemically active species, such as ascorbic acid (AA) and uric acid, which have a similar oxidation potential and are

present at concentrations greater than 0.1 mM[14-16] whereas DA is present in neural extracellular fluid at concentrations ranging between 0.01-1 μM.[17-19]

The oxidation of DA is widely believed to occur via a complex 2-electron 2-proton transfer oxidation process as outlined in Figure 5. 1,[5, 20-21] in which the initial electrode product, dopaminequinone, can undergo side reactions leading to the formation of leucodopaminechrome.[22-26] Ultimately, melanin-like compounds are formed, which are considered to inhibit electron transfer (ET) and suppress sensitivity.[23-24, 27] It has also been strongly suggested that DA electro-oxidation is 'self-catalyses' by adsorbed DA itself, or other adsorbed quinone-like products of the oxidation process.[28-32] Melanin have been shown to form a permselective film on carbon, which excludes negatively charged species, such as AA, and in some cases has been shown to enhance the electrochemical response for positively charged species, such as DA and serotonin.[33-35]

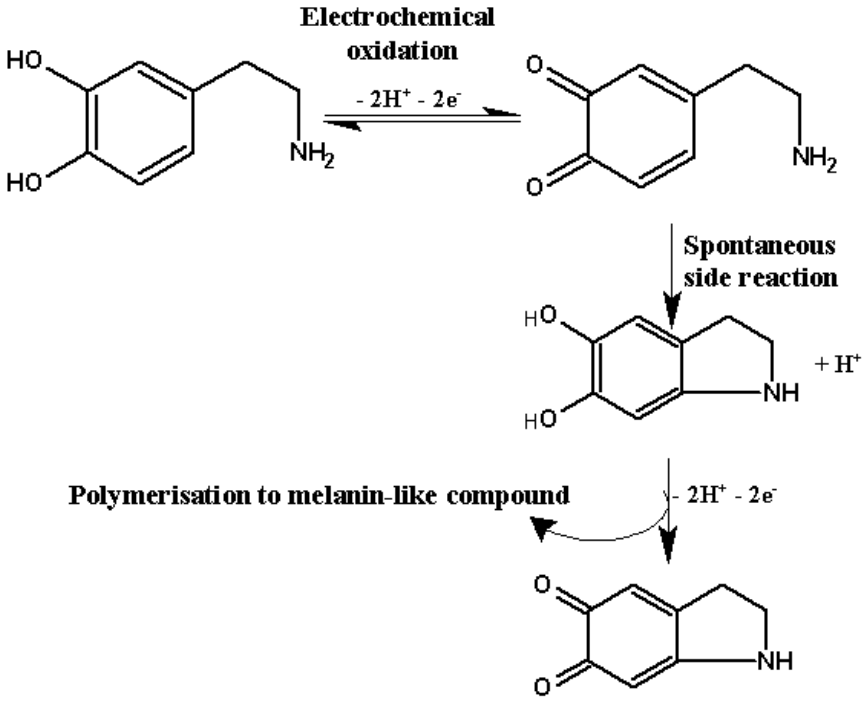

Figure 5. 1 Oxidation/reduction scheme for DA at neutral pH showing the side reactions believed to occur that ultimately lead to surface fouling.

Carbon electrodes, from graphite[36-40] to conducting diamond,[41-44] constitute interesting platforms for sensing and electrocatalysis due to low background currents, wide potential windows, chemical inertness, sensitivity, biocompatibility, low cost and ready availability.[29, 45-47] As such, they have found particularly wide application for bioelectrochemical analysis.[48-54] The introduction of graphene and carbon nanotubes (CNTs) expanded the range of carbon based electrode materials, and has greatly led to a need for an improved understanding of the electrochemical properties of carbon materials. A wealth of past research on graphite

materials has suggested the basal graphite surface is characterized by extremely slow or no ET kinetics, with the step edges at the surface providing the sites for ET.[55-59] This model has been applied to a wide range of electrochemical processes from outer-sphere[60] to more complex multi-stage reactions.[61-62] However, this model - largely derived from macro-scale electrochemical measurements – has been demonstrated to be incorrect for outer-sphere processes, these processes undergo rapid ET. This model has been extended to carbon nanotubes and graphene, implying that ET also mainly takes place at the ends and on defect sites.[63-64]

In this chapter it will be demonstrated that this model is also incorrect for complex multi-step reactions as exemplified by the model system of dopamine (DA) oxidation. As for the electrochemical detection of many neurotransmitters, and related molecules, the apparently slow kinetics observed by techniques such as CV has led to such processes being assigned as inner-sphere and catalyzed by step edges.[55, 65-67] This has further led to carbon electrodes used in neuroscience and on biosensing platforms being designed to maximize step edges.[58, 68-70] The studies herein show that this analysis is incorrect in the case of DA. Rather, the electrochemical reaction is rapid at the basal surface of HOPG, but rapidly poisoned by reaction products of the electro-oxidation process which block the electrode. It is possible to take advantage of this in SECCM,[40, 71-72] by designing experiments such that the reaction is measured essentially on a pristine surface but as the SECCM probe moves onto a new location it leaves behind the blocking products as a place marker of the locations of the electrochemical reaction that can be found by complementary miscopy imaging so that the electrochemical response can be related unambiguously to the location on the carbon electrode surface.

5.2 RESULTS AND DISCUSSION

The oxidation of DA with macroscopic electrochemistry was first investigated. Using a Teflon cell that provides a well defined 3 mm working area, ten consecutive CVs were recorded at 5 second intervals for DA in 0.15 M phosphate buffered saline (PBS) solution (150 mM NaCl), pH 7.2, at 0.1 V s^{-1} on freshly cleaved high quality, but ungraded, HOPG (AM) sample. HOPG (AM) was mechanically cleaved using a razor blade, as described in early work by McCreery *et al*.[56] As shown herein and outlined in past work, this provides a very high quality surface with a low step density and extensive terraces. **Error! Reference source not ound.**

Figure 5. 2 shows the CVs of (a) 1 mM and (b) 50 μM DA on basal plane. In the case of 1 mM DA, the initial CV shows a quasi-reversible electrochemical response with a peak to peak separation of 68 mV (c.f. *ca.* 30 mV for a reversible $2e^-$, $2H^+$ transfer process) [5, 20-21]

that rapidly deteriorates over the course of cycling. The fouling of the basal surface is evident from the decrease in peak current by 80% and increase in peak-to-peak separation to > 280 mV after 10 cycles. When the concentration was decreased to 50 μM not only does the electrochemistry show close ideal reversibility in the first scan (peak-to-peak separation of *ca.* 30 mV) but also the extent to which the signal decays is significantly reduced and a 10 mV increase in peak-to-peak separation over 10 cycles.

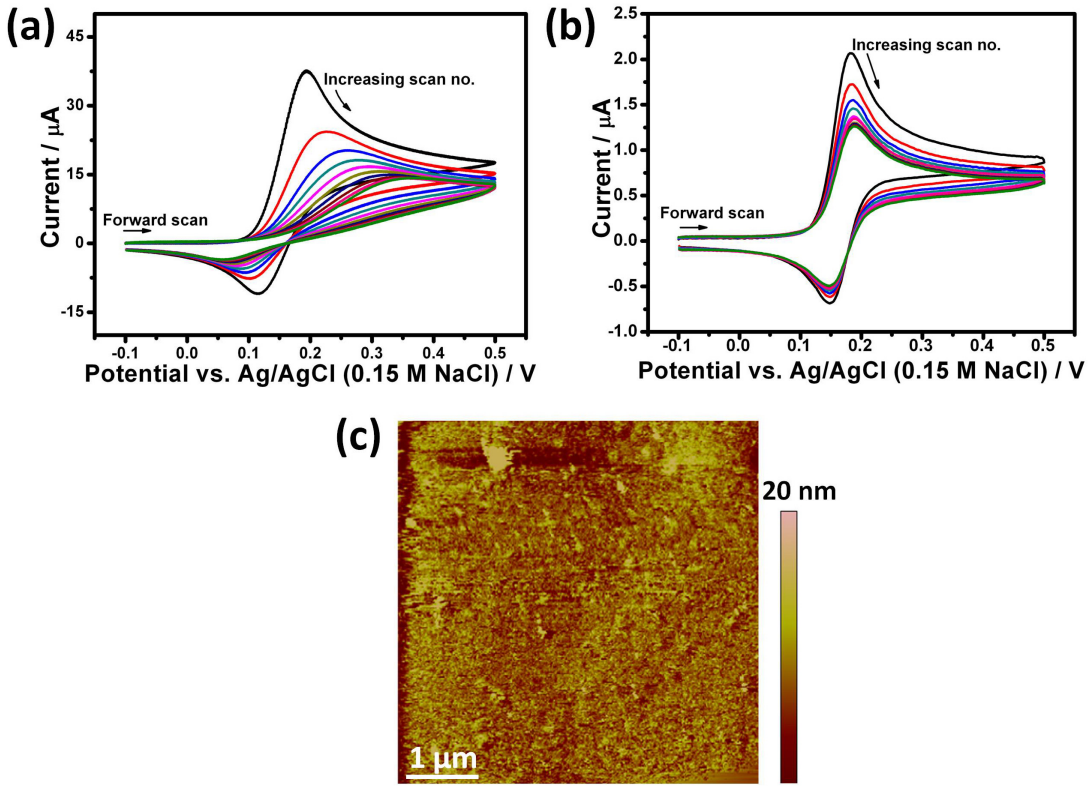

Figure 5. 2 CVs for the oxidation of (a) 1 mM and (b) 50 μM DA (0.15 M PBS, pH 7.2) at 0.1 V s^{-1} on basal plane HOPG (AM). (c) A 5 x 5 μm in-situ AFM image of 100 μm DA (0.15 M PBS, pH 7.2) after performing one CV between 0 and 0.45 V at 0.1 V s^{-1} on ZYA grade basal plane HOPG.

In-situ AFM, carried out whilst performing voltammetry, highlighted that significant blocking of the HOPG electrode occurred. Figure 5. 2d shows a typical image of the surface of ZYA grade HOPG in 50 μM DA (0.15 PBS, pH 7.2) after having performed just one CV between the potential limits of 0 V (start and end potential) and 0.9 V (reverse potential) at 0.1 V s^{-1}. The image shows complete coverage of the electrodes surface takes place indicating that the DA oxidation products are highly reactive and the polymerization[12, 22-23, 27] of these products takes place quickly and extensively.

To investigate the effect of surface structure on DA electro-oxidation, studies were carried out using SECCM to image an area of the HOPG with a distinctive line-pattern.[40, 71] SECCM electrode activity data could subsequently be compared with AFM and SEM measurements

of the same area to allow direct correlation of HOPG structure and electroactivity. A dual channel glass tip, pulled to a ~1 μm tapered end, was filled with 100 μM DA in 0.15 M PBS, pH 7.2, a liquid meniscus forms at the end of the tip and Ag/AgCl quasi-reference counter electrodes (QRCEs) are inserted into both channels. The HOPG sample was mounted on a high-precision *xy*-piezoelectric stage and connected as the working electrode (WE). When the tip was lowered using a *z*-piezoelectric positioner so that the meniscus at end made contact with the WE, the electrochemical cell was formed. Using the SECCM setup, a CV was run before patterning experiments; a typical example being shown in Figure 5. 3a. The wave is sigmoidal, as expected of the SECCM format with a tapered pipette,[71] reaching a limiting current of *ca.* 8 pA at ~0.2 V. The separation between the ¼ and ¾ wave potentials is *ca*. 60 mV.

SECCM line patterning was first carried out at a substrate potential of 0.25 V *vs.* Ag/AgCl resulting in a current just below the maximum diffusion-limited value, as determined by the CV obtained before carrying out the patterning (Figure 5. 3a). A small oscillation (20 nm peak amplitude, 233.6 Hz herein) is applied to the tip, this gives rise to a conductance current across the meniscus with an alternating current (AC) component due to periodic changes in the meniscus height. Using the AC as a set-point for feedback, the tip was kept at constant tip-to-substrate separation and whilst moving the WE in the *xy* direction to create a square-spiral pattern. The pattern covers 560 μm in total length and was scanned at a rate of 1 μm s^{-1}, collecting an average of 78 data points recorded every second, resulting in *ca.* > 40,000 individual measurements.

The SECCM surface activity (Figure 5. 3b) shows the surface currents are continuous and essentially constant around 6.3 ± 0.5 pA (1 σ) over the probed area. Spikes in the activity map can be seen along the *y* axis, which corresponds to multilayer steps as confirmed by AFM images. There are some small features along the *y* axis scan in the surface activity map that coincides with the conductance current (Figure 5. 3c) and the feedback current (Figure 5. 3d), which corresponds to positions where the droplet encounters the multilayer steps as confirmed by AFM imaging. These spikes are also seen in both of these are a good indicator for changes in the meniscus especially with regards to its size. The data shows the meniscus increases in size as the tip intersects large steps, the increase in contact area is reflected in the increase in the surface currents. This effect was also observed in Chapter 3 and 4. A small decrease in surface activity (~0.2 pA) and conductance current (< 0.1 nA) occurs when scanning along the *x* axis compared to the *y* axis, this is due to the asymmetry in the tips dimension, and has been observed and discussed previous chapters. The SECCM

conductance map (Figure 5. 3c) also shows the stability of the setup during imaging; the current remains constant around 3.45 ± 0.1 nA (1 σ) throughout the experiment.

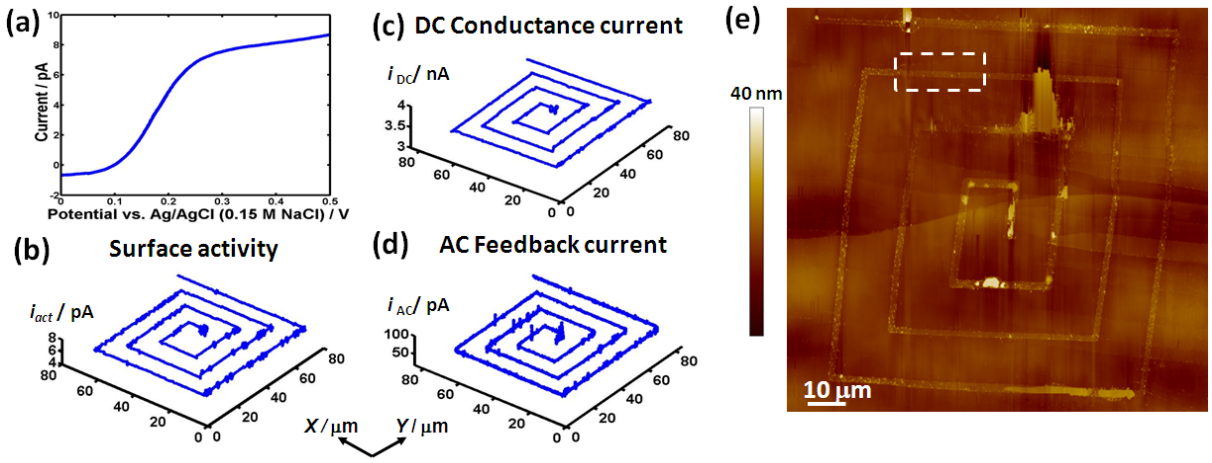

Figure 5. 3 (a) LSV for the oxidation of 100 μM DA (0.15M PBS) at 0.1 V s^{-1}, acquired using the SECCM setup run before the deposition patterning using the same ~ 1 μm diameter pipette. SECCM maps for the (b) surface activity, (c) DC component of conductance current and (d) AC component of the conductance current used as the feedback for the DA oxidation deposition patterning obtained with a 0.25 V bias. (e) An 80 × 80 μm AFM image of HOPG (AM) surface showing the deposited pattern.

As highlighted earlier, a key feature of the approach described is that the electro-oxidation of DA leads to the deposition of material which can then be identified with subsequent measurements to enable the activity from SECCM to be linked unambiguously to the site on the electrode. The AFM image in Figure 5. 3e confirms that continuous deposition of the DA oxidative products occurred throughout the SECCM measurements. Note that the streaking in a couple of areas of the deposited film (where it consequently appears higher) is due to the AFM tip sticking and dragging the film. This is not true topography and is not seen in SEM image (Figure 5. 4a). It has been suggested that the electronic structure of HOPG is perturbed near step edges, which extends on to the basal surface by a factor of 8 of the step height.[73] The AFM data show that the starting point of the deposition patterning (see Figure 5. 4b) for a magnified view of this region) confirms the deposition was initiated on a basal plane region which is at least 2 μm away from the nearest step edge. Moreover, this region in the centre of the spiral, had high electrochemical activity indicating that the patterning and corresponding electroactivity did not require a step defect but was solely due the electrochemical oxidation of DA on the basal plane.

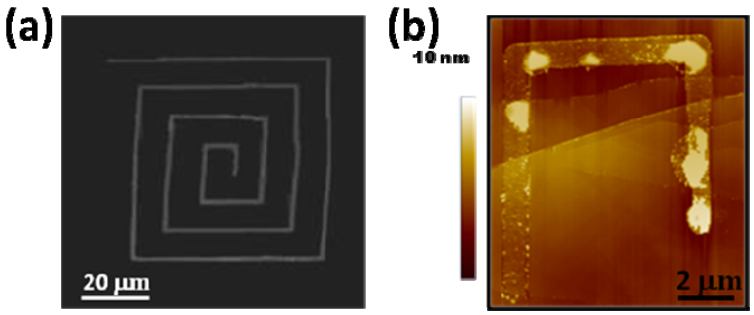

Figure 5. 4 (a) A 85 × 85 μm FE-SEM image showing DA SECCM patterning and (b) A 12 × 15 μm AFM image showing the starting point for DA patterning.

More detailed AFM analysis on sections of the pattern was carried out on a smaller scale and at higher resolution, to allow for a clearer distinction to be made between the basal terraces and the step edges and thus enabling a correlation between activity and HOPG site. Figure 5. 6a shows a 20 x 3 μm AFM image for a section of the deposited pattern in the *y* axis along with the corresponding (b) surface activity, (c) DC component of the conductance current, (d) AFM cross-section, and (e) the AC component of the conductance current which was used as the feedback. The AFM image clearly shows the line intersecting several steps but the deposition remaining consistent and relatively uniform. The surface activity during the first 10 μm remains can be seen to be constant around 6.7 pA until around 101 μm (in the *y* axis) when the meniscus intersects a step, several nm in height, creating a large spike in the DC conductance current which is reflected in both the surface activity and topography. A small increase in the DC conductance current is also observed around 96 μm in the *y* axis, but a corresponding change in surface activity is not seen, indicating the change is too small to be reflected in the surface activity and further suggesting that the sharp increases observed in surface activity are solely due to large changes in meniscus size and not a result of greater intrinsic activity at the step defects.

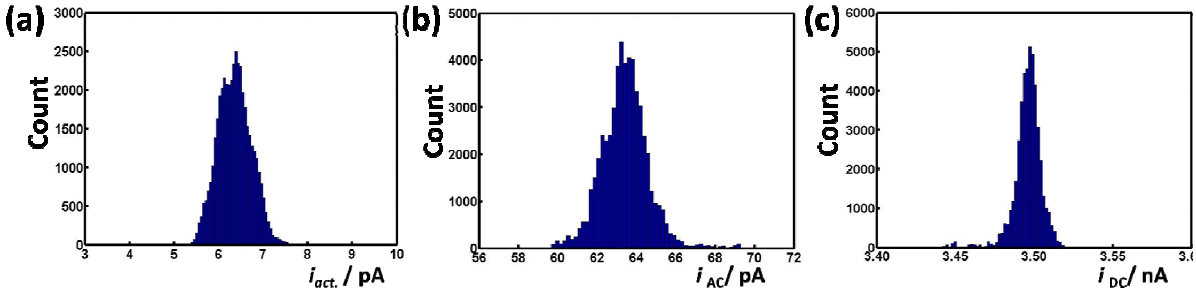

Figure 5. 5 Histograms showing the spread of current for SECCM line patterning carried out at the near the limiting current potential: (a) surface activity; (b) AC component of conductance current (feedback current) and (b) DC component of the conductance current.

The distribution of current for the surface activity, the feedback current and the conductance current are shown in histograms in Figure 5. 5 for data presented in Figure 5. 4b-d. The histograms show a small spread of surface activity, evidencing the probed area to be completely and uniformly active for the oxidation of DA. The fairly constant feedback current and conductance current shows the stability of the SECCM during imaging in maintaining a fixed sample-tip separation and a constant mass transport.

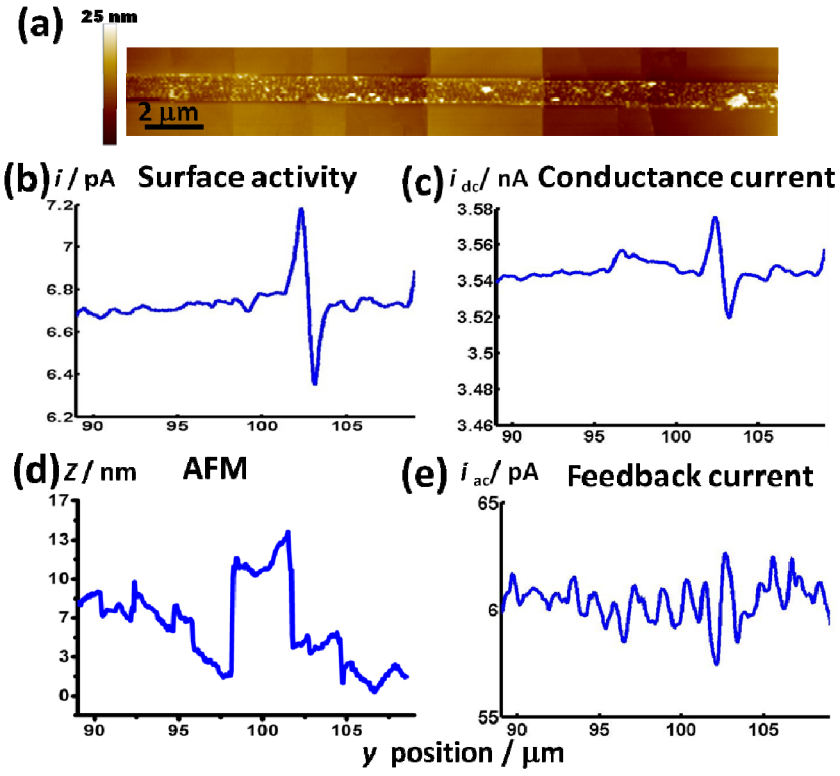

Figure 5. 6(a) 20 x 3 µm AFM image showing a section of the pattern, along with the corresponding (b) surface activity, (c) DC component of the conductance current, (d) AFM cross-section, and (e) the AC component of the conductance current used as feedback.

A 20 x 5 μm AFM image (Figure 5. 7a) shows a section of the deposited line in the *x* axis along with the corresponding (b) surface activity, (c) DC component of the conductance current, (d) AFM cross-section, and (e) the AC component of the conductance current used as feedback. The AFM image shows the deposited line travelling exclusively on a basal terrace. The corresponding SECCM data shows uniform surface activity that remains fairly constant around 6.6 pA.

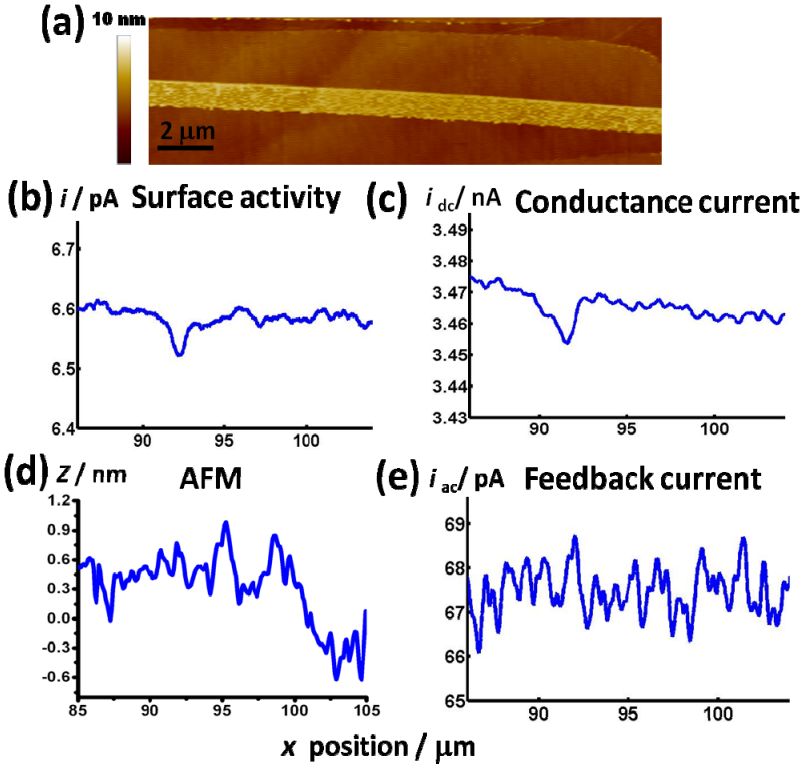

Figure 5. 7 (a) 20 x 5 μm AFM image showing a section of the pattern, along with the corresponding (b) surface activity, (c) DC component of the conductance current, (d) AFM cross-section, and (e) the AC component of the conductance current used as feedback.

SECCM imaging line patterning was also carried out at the half-wave potential of *ca.* 0.15 V to highlight further any heterogeneity in the ET kinetics of the basal plane vs. edge plane for the oxidation of DA. Imaging was successful with 100 μM DA, but the diminished reaction rate meant that the electrodeposited surface was not sufficiently thick to analyze by AFM. The concentration was thus increased to 300μM. A 20 × 6 μm AFM image (Figure 5. 8a) shows a uniform line of DA was deposited which travels along a large basal surface as well as intersects with several steps, ranging between 0.3 to 2 nm (see AFM cross-section Figure 5. 8a).

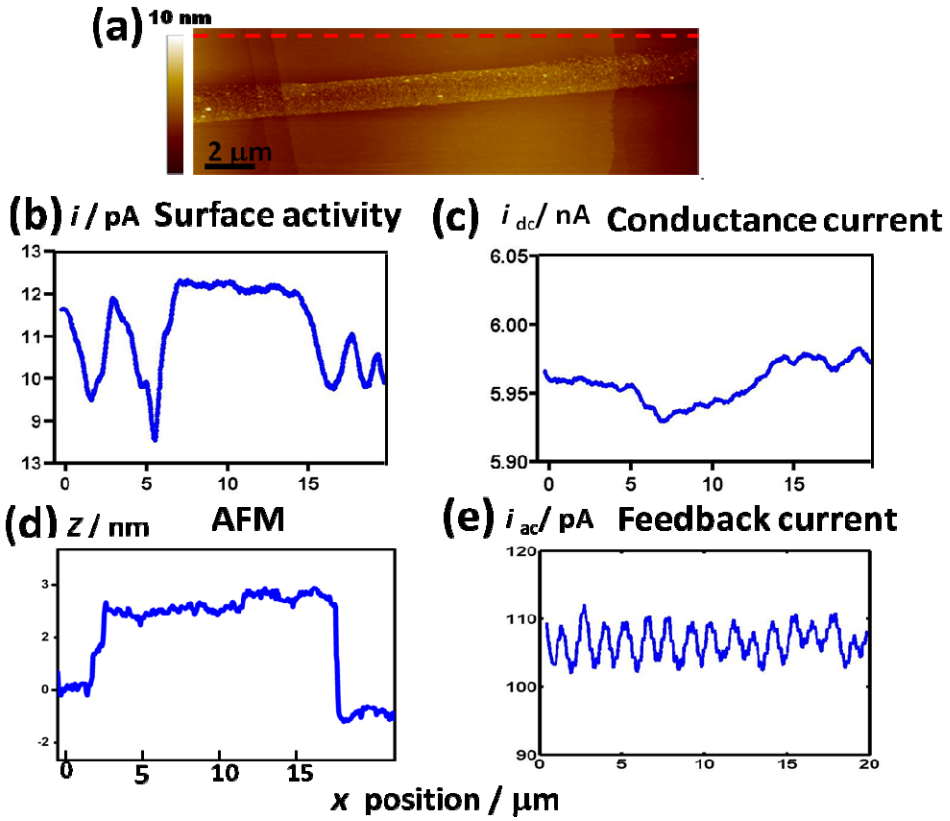

Figure 5. 8 (a) 20 × 6 μm AFM image showing a section the line patterning carried out at the half-wave potential of ~0.15 V with 300 μM DA (0.15M PBS), along with the corresponding (b) surface activity, (c) DC component of the conductance current, (d) AFM cross-section, and (e) the AC component of the conductance current used as feedback.

By correlating the AFM image with the DC component of the conductance current (bi) and the surface activity (bii) it can be seen that as the meniscus travels along a large basal terrace (approximately 9 μm) the surface activity remains constant around 11 ± 1 pA. Histograms for the distribution of current of the surface activity, the feedback current and the conductance current for SECCM line patterning carried out at the half-wave potential, are shown in Figure 5. 9.

As the oxidation was carried out at a potential where the reaction is not driven, if electrochemical oxidation of DA took place solely or preferentially at the step edges it would be expected that greater deposition of DA would be observed at (and around) the step edges and no deposition (or very little compared to the steps edges) would be observed on the basal terraces. This data presented herein shows that the freshly prepared and unmodified surface of basal plane HOPG provides fast electron transfer for the oxidation of DA.

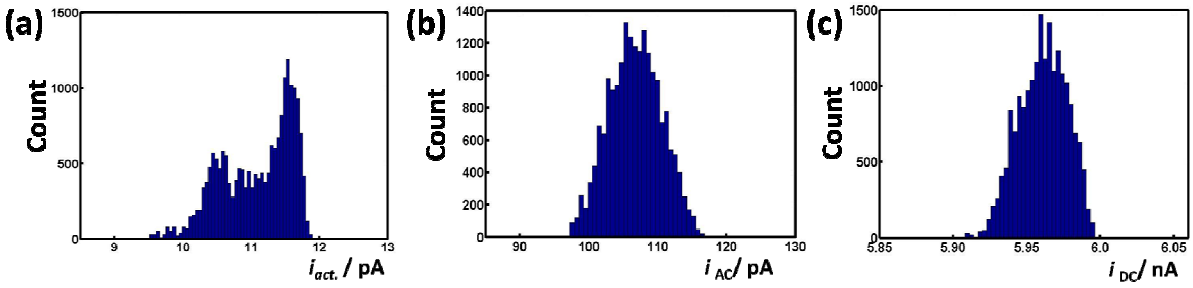

Figure 5. 9 Histograms showing the spread of current for SECCM line patterning carried out at the half-wave potential: (a) surface activity; (b) AC component of conductance current (feedback current) and (b) DC component of the conductance current.

5.3 CONCLUSION

It has been shown for the first time reversible electro-oxidation for the oxidation of DA on pristine basal plane HOPG with simple voltammetry. Using SECCM, a high resolution electrochemical imaging technique, the electrochemical oxidation of DA was studied under conditions of high mass transport, in which thousands of fresh measurements were made. This technique enabled an exact correlation to be made between the surface activity and the site under investigation. The data presented provides unequivocal evidence that the oxidation of DA is fast at the basal surface of HOPG can electrochemically catalyse DA and the difference in activity between the basal plane and step edges is negligible. This new view, which overturns more than 2 decades of past research[55-57, 74-86] is supported by the SECCM study presented in Chapter 3, in which it was shown that the basal plane provides fast ET kinetics for two outer-sphere redox couples, $Fe(CN)_6^{4-/3-}$ and $Ru(NH)_6^{3+/2+}$.

5.4. REFERENCES

1. Weng, J.,J. M. Xue,J. Wang,J. S. Ye,H. F. Cui,F. S. Sheu,Q. Q. Zhang, *Adv. Func. Mat.,* **2005,** *15,* 639-647.
2. Barras, A.,J. Lyskawa,S. Szunerits,P. Woisel,R. Boukherroub, *Langmuir,* **2011,** *27,* 12451-12457.
3. Shepherd, G. M., *Neurobiology*. 2nd ed.; Oxford University Press: Oxford, 1988.
4. Venton, B. J.,R. M. Wightman, *Anal. Chem.,* **2003,** *75,* 414a-421a.
5. Wu, K.,J. Fei,S. Hu, *Anal Biochem,* **2003,** *318,* 100-106.
6. Andersen, S. L.,M. H. Teicher, *Neurosci Biobehav R,* **2000,** *24,* 137-141.
7. Colliver, T. L.,A. G. Ewing, *Electrochemical detection of Neurotransmitters, Encyclopedia of Analytical Chemistry*. John Wiley & Sons Ltd.: UK, 2006; Vol. 11, p 9958-9983.
8. Berduque, A.,R. Zazpe,D. W. Arrigan, *Anal Chim Acta,* **2008,** *611,* 156-162.
9. Makos, M. A.,Y. C. Kim,K. A. Han,M. L. Heien,A. G. Ewing, *Anal. Chem.,* **2009,** *81,* 1848-1854.
10. Park, J.,V. Quaiserova-Mocko,B. A. Patel,M. Novotny,A. Liu,X. Bian,J. J. Galligan,G. M. Swain, *Analyst,* **2008,** *133,* 17-24.
11. Gerhardt, G.,R. N. Adams, *Anal. Chem.,* **1982,** *54,* 2618-2620.
12. Lin, X. Q.,L. Zhang, *Anal. Lett.,* **2001,** *34,* 1585-1601.
13. Raj, C. R.,T. Okajima,T. Ohsaka, *J. Electroanal. Chem.,* **2003,** *543,* 127-133.
14. Sun, C. L.,H. H. Lee,J. M. Yang,C. C. Wu, *Biosens. Bioelectron.,* **2011,** *26,* 3450-3455.
15. Liu, Q.,X. Zhu,Z. Huo,X. He,Y. Liang,M. Xu, *Talanta,* **2012**.
16. Behpour, M.,S. M. Ghoreishi,E. Honarmand,M. Salavati-Niasari, *Analyst,* **2011,** *136,* 1979-1986.
17. Zen, J. M.,I. L. Chen, *Electroanal.,* **1997,** *9,* 537-540.
18. Hou, S. F.,M. L. Kasner,S. J. Su,K. Patel,R. Cuellari, *J. Phys. Chem. C,* **2010,** *114,* 14915-14921.
19. Popa, E.,H. Notsu,T. Miwa,D. A. Tryk,A. Fujishima, *Electrochem Solid St,* **1999,** *2,* 49-51.
20. Zhao, Y.,Y. Gao,D. Zhan,H. Liu,Q. Zhao,Y. Kou,Y. Shao,M. Li,Q. Zhuang,Z. Zhu, *Talanta,* **2005,** *66,* 51-57.
21. Chen, S.-M.,K.-T. Peng, *J. Electroanal. Chem.,* **2003,** *547,* 179-189.
22. Zhao, H.,Y. Z. Zhang,Z. B. Yuan, *Analyst,* **2001,** *126,* 358-360.
23. Hou, S.,N. Zheng,H. Feng,X. Li,Z. Yuan, *Anal. Biochem.,* **2008,** *381,* 179-184.
24. Bernsmann, F.,V. Ball,F. Addiego,A. Ponche,M. Michel,J. J. Gracio,V. Toniazzo,D. Ruch, *Langmuir,* **2011**.
25. Hawley, M. D.,S. V. Tatawawadi,S. Piekarski,R. N. Adams, *J. Am. Chem. Soc.,* **1967,** *89,* 447-450.
26. Lane, R. F.,A. T. Hubbard, *Anal. Chem.,* **1976,** *48,* 1287-1293.
27. Alwarappan, S.,K. S. A. Butcher,D. K. Y. Wong, *Sensor. Actuat. B,* **2007,** *128,* 299-305.
28. DuVall, S. H.,R. L. McCreery, *J. Am. Chem. Soc.,* **2000,** *122,* 6759-6764.
29. McCreery, R. L., *Chem. Rev,* **2008,** *108,* 2646-2687.
30. Bath, B. D.,H. B. Martin,R. M. Wightman,M. R. Anderson, *Langmuir,* **2001,** *17,* 7032-7039.
31. Bath, B. D.,D. J. Michael,B. J. Trafton,J. D. Joseph,P. L. Runnels,R. M. Wightman, *Anal. Chem.,* **2000,** *72,* 5994-6002.
32. DuVall, S. H.,R. L. McCreery, *Anal. Chem.,* **1999,** *71,* 4594-4602.
33. Rubianes, M. D.,A. S. Arribas,E. Bermejo,M. Chicharro,A. Zapardiel,G. Rivas, *Sensor. Actuat. B,* **2010,** *144,* 274-279.

34. Rubianes, M. D.,G. A. Rivas, *Anal. Chim. Acta,* **2001,** *440,* 99-108.
35. Li, Y.,M. Liu,C. Xiang,Q. Xie,S. Yao, *Thin Solid Films,* **2006,** *497,* 270-278.
36. Surendranath, Y.,D. A. Lutterman,Y. Liu,D. G. Nocera, *J. Am. Chem. Soc.,* **2012,** *134,* 6326-6336.
37. Etacheri, V.,U. Geiger,Y. Gofer,G. A. Roberts,I. C. Stefan,R. Fasching,D. Aurbach, *Langmuir,* **2012,** *28,* 6175-6184.
38. Xue, Y.,M. B. Zimmt, *J Am Chem Soc,* **2012,** *134,* 4513-4516.
39. Bhattacharjya, D.,I. Mukhopadhyay, *Langmuir,* **2012,** *28,* 5893-5899.
40. Lai, S. C. S.,P. V. Dudin,J. V. Macpherson,P. R. Unwin, *J. Am. Chem. Soc.,* **2011,** *133,* 10744-10747.
41. Hutton, L.,M. E. Newton,P. R. Unwin,J. V. Macpherson, *Anal. Chem.,* **2009,** *81,* 1023-1032.
42. Hutton, L. A.,M. Vidotti,A. N. Patel,M. E. Newton,P. R. Unwin,J. V. Macpherson, *J. Phys. Chem. C,* **2011,** *115,* 1649-1658.
43. Fierro, S.,N. Mitani,C. Comninellis,Y. Einaga, *Phys. Chem. Chem. Phys.,* **2011,** *13,* 16795-16799.
44. Zhong, Y. L.,A. Midya,Z. Ng,Z. K. Chen,M. Daenen,M. Nesladek,K. P. Loh, *J Am Chem Soc,* **2008,** *130,* 17218-17219.
45. Jacobs, C. B.,M. J. Peairs,B. J. Venton, *Anal Chim Acta,* **2010,** *662,* 105-127.
46. Dumitrescu, I.,P. R. Unwin,J. V. Macpherson, *Chem. Commun.,* **2009,** *7345,* 6886-6901.
47. Zachek, M. K.,A. Hermans,R. M. Wightman,G. S. McCarty, *J. Electroanal. Chem.,* **2008,** *614,* 113-120.
48. Rodriguez-Lopez, J.,N. L. Ritzert,J. A. Mann,C. Tan,W. R. Dichtel,H. D. Abruna, *J Am Chem Soc,* **2012,** *134,* 6224-6236.
49. Yu, X.,Q. Wang,Y. Lin,J. Zhao,C. Zhao,J. Zheng, *Langmuir,* **2012,** *28,* 6595–6605.
50. Khatayevich, D.,C. R. So,Y. Hayamizu,C. Gresswell,M. Sarikaya, *Langmuir,* **2012,** *28,* 8589-8593.
51. Zafar, M. N.,X. Wang,C. Sygmund,R. Ludwig,D. Leech,L. Gorton, *Anal Chem,* **2012,** *84,* 334-341.
52. Güell, A. G.,K. E. Meadows,P. R. Unwin,J. V. Macpherson, *Phys. Chem. Chem. Phys.,* **2010,** *12,* 10108-10114.
53. Singh, Y. S.,L. E. Sawarynski,H. M. Michael,R. E. Ferrell,M. A. Murphey-Corb,G. M. Swain,B. A. Patel,A. M. Andrews, *ACS Chem. Neurosci.,* **2010,** *1,* 49-64.
54. Zhao, H.,X. C. Bian,J. J. Galligan,G. M. Swain, *Diamond Relat. Mater.,* **2010,** *19,* 182-185.
55. Bowling, R. J.,R. T. Packard,R. L. McCreery, *J. Am. Chem. Soc.,* **1989,** *111,* 1217-1223.
56. McDermott, M. T.,K. Kneten,R. L. McCreery, *J. Phys. Chem.,* **1992,** *96,* 3124-3130.
57. Cline, K. K.,M. T. Mcdermott,R. L. McCreery, *J. Phys. Chem.,* **1994,** *98,* 5314-5319.
58. Banks, C. E.,R. R. Moore,T. J. Davies,R. G. Compton, *Chem. Commun.,* **2004,** 1804-1805.
59. Davies, T. J.,M. E. Hyde,R. G. Compton, *Angew. Chem.,* **2005,** *44,* 5121-5126.
60. Lee, C.-Y.,S.-X. Guo,A. M. Bond,K. B. Oldham, *J. Electroanal. Chem.,* **2008,** *615,* 1-11.
61. Kachoosangi, R. T.,R. G. Compton, *Anal. Bioanal. Chem.,* **2007,** *387,* 2793-2800.
62. Neumann, C. C.,C. Batchelor-McAuley,C. Downing,R. G. Compton, *Chemistry,* **2011,** *17,* 7320-7326.
63. Pumera, M.,A. Ambrosi,A. Bonanni,E. L. K. Chng,H. L. Poh, *TrAC, Trends Anal. Chem.,* **2010,** *29,* 954-965.
64. Kampouris, D. K.,C. E. Banks, *Chem Commun (Camb),* **2010,** *46,* 8986-8988.

65. Kneten, K. R.,R. L. McCreery, *Anal. Chem.,* **1992,** *64,* 2518-2524.
66. McCreery, R. L.,M. T. McDermott, *Anal Chem,* **2012,** *84,* 2602-2605.
67. Kachoosangi, R. T.,C. E. Banks,R. G. Compton, *Electroanal.,* **2006**.
68. Banks, C. E.,R. G. Compton, *The Analyst,* **2005,** *130,* 1232-1239.
69. Sudhakara Prasad, K.,G. Muthuraman,J.-M. Zen, *Electrochem. Commun.,* **2008,** *10,* 559-563.
70. Lim, C. X.,H. Y. Hoh,P. K. Ang,K. P. Loh, *Anal Chem,* **2010,** *82,* 7387-7393.
71. Snowden, M. E.,A. G. Güell,S. C. S. Lai,K. McKelvey,N. Ebejer,M. A. O'Connell,A. W. Colburn,P. R. Unwin, *Anal. Chem.,* **2012,** *84,* 2483-2491.
72. Ebejer, N.,M. Schnippering,A. W. Colburn,M. A. Edwards,P. R. Unwin, *Anal. Chem.,* **2010,** *82,* 9141-9145.
73. McDermott, M. T.,R. L. McCreery, *Langmuir,* **1994,** *10,* 4307-4314.
74. Dumitrescu, I.,P. R. Unwin,J. V. Macpherson, *Chem. Commun.,* **2009,** 6886-6901.
75. McCreery, R. L., *Chem. Rev.,* **2008,** *108,* 2646-2687.
76. Banks, C. E.,T. J. Davies,G. G. Wildgoose,R. G. Compton, *Chem. Commun.,* **2005,** 829-841.
77. Pumera, M., *Chem. Soc. Rev.,* **2010,** *39,* 4146-4157.
78. Ji, X. B.,C. E. Banks,A. Crossley,R. G. Compton, *ChemPhysChem,* **2006,** *7,* 1337-1344.
79. Davies, T. J.,R. R. Moore,C. E. Banks,R. G. Compton, *J. Electroanal. Chem.,* **2004,** *574,* 123-152.
80. Lee, C. Y.,A. M. Bond, *Anal. Chem.,* **2009,** *81,* 584-594.
81. Rice, R. J.,R. L. McCreery, *Anal. Chem.,* **1989,** *61,* 1637-1641.
82. Kneten, K. R.,R. L. McCreery, *Anal. Chem.,* **1992,** *64,* 2518-2524.
83. McCreery, R. L.,K. K. Cline,C. A. McDermott,M. T. McDermott, *Colloid Surf. A-Physicochem. Eng. Asp.,* **1994,** *93,* 211-219.
84. Robinson, R. S.,K. Sternitzke,M. T. Mcdermott,R. L. McCreery, *J. Electrochem. Soc.,* **1991,** *138,* 2412-2418.
85. Ray, K.,R. L. McCreery, *Anal. Chem.,* **1997,** *69,* 4680-4687.
86. Chang, H.,A. J. Bard, *Langmuir,* **1991,** *7,* 1143-1153.

CHAPTER 6: COMPARISON AND RE-APPRAISAL OF CARBON ELECTRODES FOR THE VOLTAMMETRIC DETECTION OF DOPAMINE: OPTIMAL TRACE DETECTION AND ELECTROCHEMICAL REVERSIBILITY AT HIGHLY ORIENTATED PYROLYTIC GRAPHITE (HOPG)

In this chapter cyclic voltammetry (CV) is used to re-examine the electro-oxidation of the neurotransmitter dopamine (DA) on the unmodified surfaces of 5 different carbon electrode surfaces: glassy carbon (GC), oxygen-terminated polycrystalline boron-doped diamond (pBDD), edge plane pyrolytic graphite (EPPG), basal plane pyrolytic graphite (BPPG) and three grades of basal plane of highly oriented pyrolytic graphite (HOPG). The unmodified surface of pBDD showed the least susceptibility to surface fouling but it was the unmodified surface of pristine ZYA grade basal plane HOPG that demonstrated reversible electrochemistry for the oxidation of DA (ΔE_p ~ 30 mV) at concentrations ≤ 0.1 mM in 0.15 M PBS, pH 7.2, as well as providing the lowest detection limit (0.09 μM) compared to the GC (90 μM), pBDD (85 μM) and EPPG (1.1 μM). The extent to which the basal plane HOPG electrode response diminished as a result of fouling from DA oxidation products was found to have a minimal effect towards the current response as well as the electrochemical reversibility for concentrations ≤ 0.1 mM. *In-situ* AFM images and CV data show DA products rapidly adsorb indiscriminately onto the basal plane. As the electrochemical oxidation of DA is widely reported as requiring adsorption of the reactive species, the data presented shows the basal plane promotes the electro-oxidation of DA. The electrochemical oxidation response of DA in the presence of a common interference, namely ascorbic acid (AA), showed not only the signals for the two species to be clearly and easily resolved. Most surprisingly, CV and *in-situ* AFM data found that through the effect of performing repeated voltammetry, AA species adsorbed onto the surface forming a permselective film, which supports the reversible electrochemical oxidation of DA whilst excluding the electrochemical response of AA itself.

6.1 INTRODUCTION

The oxidation of DA is widely believed to occur via a complex 2-electron 2-proton transfer process (Figure 5. 1),[1-3] in which the initial electrode product, dopaminequinone, can undergo side reactions leading to the formation of leucodopaminechrome.[4-8] Ultimately, melanin-like

compounds are formed, which are considered to inhibit electron transfer (ET) and suppress sensitivity.[5-6, 9] It has also been strongly suggested that DA electro-oxidation is 'self-catalyses' by adsorbed DA itself, or other adsorbed quinone-like products of the oxidation process.[10-14] Melanin have been shown to form a permselective film on carbon, which excludes negatively charged species, such as AA, and in some cases has been shown to enhance the electrochemical response for positively charged species, such as DA and serotonin.[15-17]

Most research on the voltammetric detection of DA has focused on the use of carbon-based electrode materials due to their range of desirable properties namely biocompatibility, chemical inertness, and (sometimes) low background currents (providing better detection limits).[11, 18-21] However, most carbon electrodes are highly susceptible to fouling (as alluded to above).[12-13] The extent and rate of electrode fouling is dependent on the material: GC has been shown to foul relatively quickly, while pBDD and EPPG have been reported as being relatively resistant to fouling.[19, 22-26] Many surface modifications have been investigated in an attempt to overcome the problem of surface fouling and to improve detection limits, for example, thorough with the use of metal nanoparticles,[27-28] nanotubes, [29-30] self-assembled monolayers, [31-32] adsorption-medium exchange methods,[33-34] covalent modification,[4, 35] polymer films[36-37] and composites. [2, 38]

The goal of this chapter is to re-examine and compare the activity of various carbon electrodes towards the oxidation of DA. A comparison is made between GC, pBDD, basal plane of HOPG and two orientations of pyrolytic graphite (basal and edge). The traditional consensus has been that the basal plane of HOPG is electrochemically inert, characterised by slow ET kinetics, whereas the edge plane has been widely considered to be electrochemically active, providing fast ET kinetics.[39-42] The step edges have be reported as being able to promote adsorption and provide fast ET for DA oxidation, whilst the basal plane is supposedly inert towards adsorption, therefore providing slow ET towards DA oxidation.[13, 43-44] This is a general consensus that extends to other apparently inner sphere processes that are only electrocatalyzed by step edges. For the voltammetry (CV) analysis of DA on cleaved HOPG, very high overpotentials have been reported and, in some cases, the forward to reverse peak-to-peak separation (ΔE_p) value is as high as 1.2 V.[44]

In Chapter 3 and 4 it has been demonstrated definitively that, in fact, the basal plane supports fast ET kinetics as exemplified by the electrochemical response mapped for the redox of two mediators, $Fe(CN)_6^{4-/3-}$ and $Ru(NH_3)_6^{3+/2+}$ which were found to be close to reversible.[45] In Chapter 4, surface preparation, treatment and history were identified as

playing a key role in the quality of electrochemical behaviour observed from the electrode. It was also shown that the ratio of edge plane sites to basal plane has no noticeable effect on the observed electrochemical response, indicating that both morphologies are highly suitable as electrodes as far as ET kinetics are concerned. However, for more complex electrochemical mechanisms, which may require one or several coordination steps (such as the oxidation of DA), HOPG surface morphology might still play a role. In light of these recent findings the electrochemistry of DA on unmodified HOPG (basal plane) is re-examined and compared with that of bare GC, pBDD and pyrolytic graphite (basal and edge plane).

6.2 INFLUENCE OF REPETITIVE CYCLING.

It is widely appreciated that DA electro-oxidation leads to rapid fouling and contamination of the working electrodes surface, as highlighted above. Since the voltammetric response can be at least partly diagnostic of the structure of the electrode surface, the extent to which the different carbon electrodes fouled during DA electro-oxidation was first studied by recording consecutive CVs (typically 10) with 5 second intervals between each CV for each electrode. Figure 6. 1 shows the CVs for repetitive cycling in 1 mM DA (0.15 M PBS, pH 7.2) at 100 mV s^{-1}, using the following carbon electrodes: (a) GC; (b) pBDD; (c) basal plane HOPG (ZYA grade); (d) BPPG; and (e) EPPG. Only data for ZYA grade HOPG is shown in Figure 6. 1 as it was found to be typically representative of the electrochemical behaviour observed for SPI-1 and ZYH grade HOPG, although the extent of fouling of the different HOPG materials varied subtly, as discussed further within this chapter. It can be seen that the initial CV for each carbon electrode shows apparent quasi-reversible voltammetry and a significant change in electrochemical response is observable immediately after the first cycle. It is interesting to note, however, that freshly cleaved ZYA grade HOPG which would certainly be expected to be the least defective surface actually shows the fastest apparent kinetics with initial ΔE_p value of 68 mV. This point is picked up again below. With each successive cycle the peak current (I_p) decreases and ΔE_p increases, which is characteristic behaviour of the electrode response deteriorating, most likely by blocking (or fouling).

Using the Randles-Sevcik equation provided in the Chapter 1 (Equation 1.3) the theoretical peak current density was calculated, using a diffusion coefficient of 6 x 10^{-6} cm s^{-1} at room temperature for 1 mM DA concentrations, to be approximately 0.58 mA cm^{-2}. The data presented in Figure 6.2 therefore shows that the HOPG and BPPG electrode materials provide near to ideal current density for the 2 electron redox process but the GC, pBDD and EPPG show far from ideal currents. As DA is believed to a complex inner-sphere redox mediator, the deviation of ideal voltammetry could be due to surface chemistry where there

are fewer adsorption sites (or lack of sites to promote strong adsorption) to favour the oxidation/reduction process.

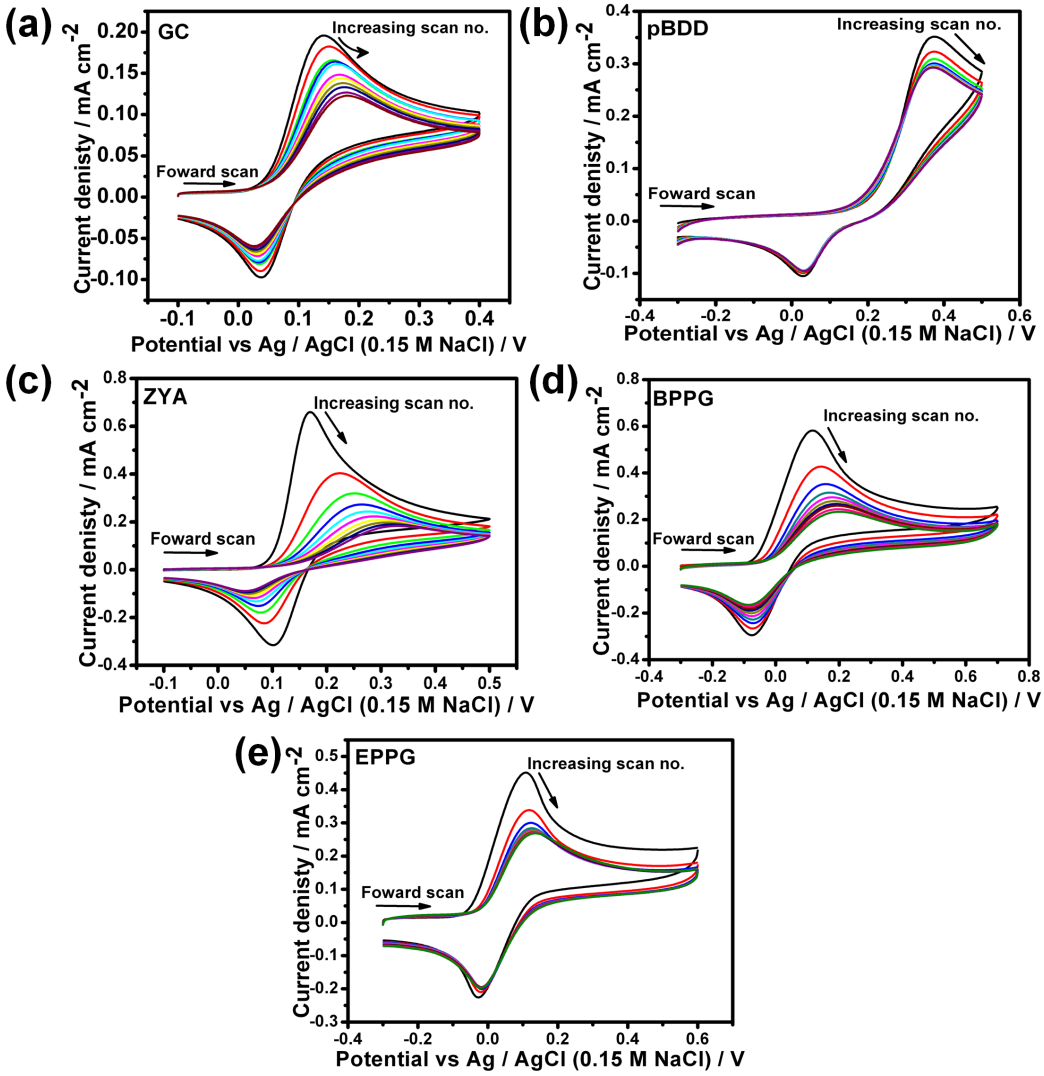

Figure 6. 1 Repetitive cycling for the oxidation of 1 mM DA in 0.15 M PBS, pH 7.2, at 0.1 V s^{-1} with: (a) GC; (b) BDD; (c) SPI-1 grade basal plane HOPG; (d) BPPG; (e) EPPG, where scans are run at 5 s intervals.

The extent to which the carbon electrodes are fouled by dopaminergic compounds formed in the electro-oxidation process varies greatly between the materials. A plot of ΔE_p and $I_{p(n)}/I_{p(initial)}$ against number of cycles, n, (Figure 6. 2) allows for an easy comparison of the different electrodes. The plots show that PBDD is the least affected by fouling since after 10 cycles the ΔE_p shows a minimal increase of ~ 5 mV and the I_p decreases after the first four cycles by 20% but then provides a stable response. The EPPG electrode also shows some level of resistance to fouling, the ΔE_p increases by 20 mV over the course of 10 cycles and the I_p decreases by ~ 50% over the course of the first 4 CVs but then stabilising. The GC electrode also shows some resistance towards surface deactivation but not the same extent as pBDD and EPPG, the ΔE_p increases by ~ 60 mV over the course of 10 cycles and the I_p

decreases to ~60% of the initial value, Figure 6. 2 shows these decrease occur steadily throughout the cycling without reaching a stable response as seen for pBDD and EPPG. The basal plane of HOPG (ZYA grade) was found to show the highest susceptibility to fouling with a significant decrease in I_p observed immediately after the first scan, with an I_p that was 60% of the initial value on second scan, and 20% of the initial value after 10 cycles. The ΔE_p increases from 68 mV to 283 mV after 10 cycles. The data shows the extent to which surface blocking occurs is limited for pBDD, EPPG and, to some degree, on GC. Although reversible voltammetry is not observed on any of the electrodes at this concentration, pBDD and EPPG electrode show the highest stability in for the oxidation of DA. The data also suggests that the dopaminergic compounds may have a stronger adsorption affinity to the basal plane compared to EPPG, and as GC posses both edge-like and basal-like structures, it is expected that the material would a response intermediate of the basal plane and EPPG electrodes.

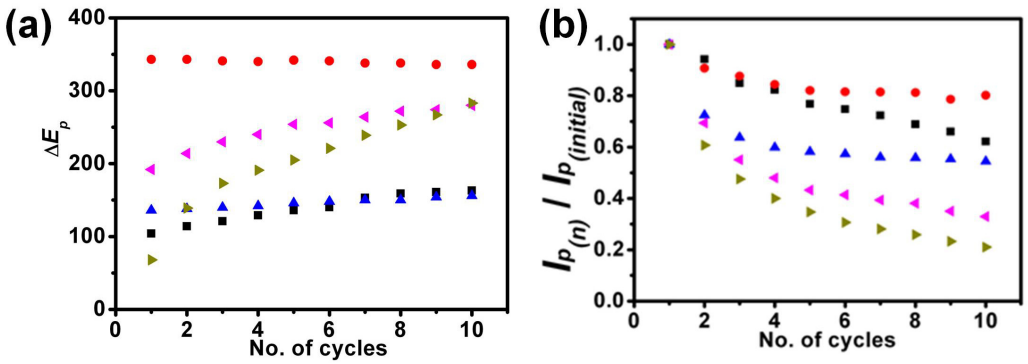

Figure 6. 2(a) plot of ΔE_p vs. no of cycles and (b) $i_{p(actual)}/i_{p(initial)}$ vs. no of cycles for: BDD (red); GC (black); EPPG (blue); BPPG (pink); ZYA (green).

6.3 DETECTION LIMITS AND CONCENTRATION EFFECTS

Although many voltammetric studies of DA CVs of DA electro-oxidation tend to focus on mM levels,[9, 30, 37, 44] trace level detection is much more relevant to neuroscience applications and the CVs for DA oxidation was measured at different concentrations on freshly prepared surfaces of all electrode materials. The data are summarised in Table 6. 1 which shows current density at 1 mM and the corresponding ΔE_p value as a function of decade changes in concentration. Strikingly, it can be seen that all electrodes have varying sensitivity. All electrodes were able to detect down to DA concentrations of 0.01 mM (Figure 6. 3 and Table 6. 1). The basal plane HOPG electrodes show the greatest sensitivity with SPI-1 and ZYH grades being able to detect down to ~ 1 μM and ZYA grade detecting down to ~ 0.1 μM. The basal plane is able to provide a superior electrochemical response in terms of reversibility of electrochemical behaviour and lowest detection limits. The BPPG shows similar voltammetric

behaviour to EPPG, which may be due to the high density of step edges present in BPPG created by the abrasive polishing.

Table 6. 1 Peak current density and peak-to-peak separations extracted from CVs for the oxidation of DA at varying concentrations in 0.15 M PBS, pH 7.2, at 100 mV s^{-1}, for: ZYA, SPI-1 and ZYH grade HOPG, GC, BDD, BPPG and EPPG.

		ZYA		SPI-1		ZYH		GC		BDD		BPPG		EPPG	
		ΔE_p (mV)	i_p	ΔE_p (mV)	i_p	ΔE_p (mV)	i_p	ΔE_p (mV	i_p	ΔE_p (mV)	i_p	ΔE_p (mV)	i_p	ΔE_p (mV)	i_p
DA Concentration (mm)	1	68	6.56×10^{-4}	70	6.79×10^{-4}	63	6.06×10^{-4}	98	3.37×10^{-4}	317	2.60×10^{-4}	192	5.57×10^{-4}	136	4.30×10^{-4}
	0.1	28	6.23×10^{-5}	38	4.47×10^{-5}	29	5.36×10^{-5}	61	3.60×10^{-5}	360	2.89×10^{-5}	66	1.66×10^{-5}	66	1.07×10^{-4}
	0.01	29	4.47×10^{-6}	30	5.5×10^{-6}	38	4.99×10^{-6}	60	9.51×10^{-6}	390	2.27×10^{-5}	38	1.25×10^{-6}	62	5.26×10^{-5}
	1×10^{-3}	31	4.27×10^{-7}	22	5.19×10^{-7}	35	4.77×10^{-7}	-	-	-	-	-	-	-	-
	1×10^{-4}	26	1.76×10^{-8}	-	-	-	-	-	-	-	-	-	-	-	-
Detection limits (μM)		0.09		0.98		0.85		90		85		1.8		1.1	

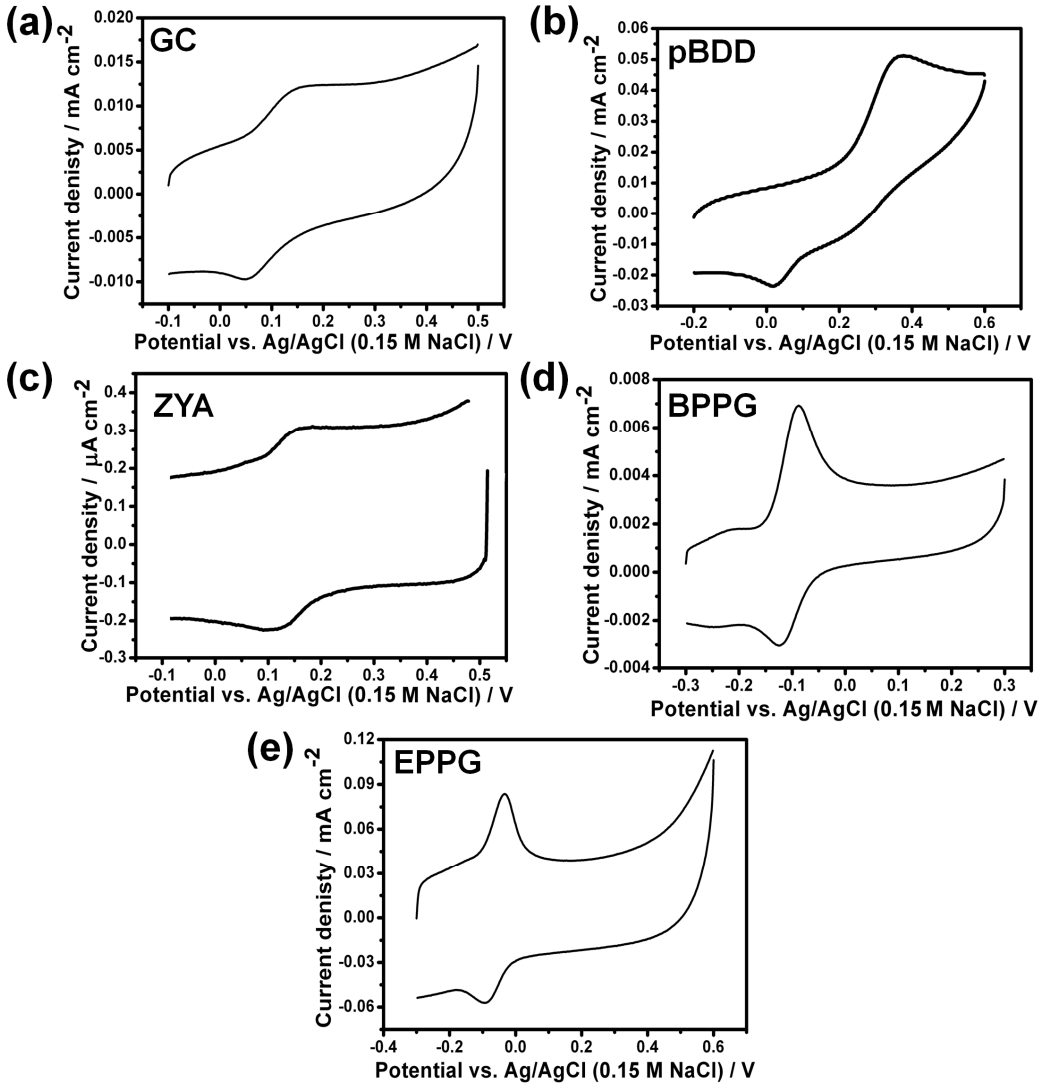

Figure 6. 3 CVs for the oxidation of 0.01 mM DA in 0.15 M PBS, pH 7.2, at 0.1 V s^{-1} at : (a) GC; (b) BDD; (c) SPI-1 grade basal plane HOPG; (d) BPPG; (e) EPPG.

The difference in detection limits between the basal plane grades is most likely due to the varying background currents and step density (discussed in Chapter 4). The ZYA grade has a slightly lower capacitance (2.0 ± 0.3 µF cm^{-2}) compared to the SPI-1 grade (2.9 ± 1.2 µF cm^{-2}) and lower step density (0.5 ± 0.1 µm $µm^{-2}$) compared to the ZYH and SPI-1 grades (1.2 ± 0.6 µm $µm^{-2}$ and 1.5 ± 0.21 µm $µm^{-2}$, respectively).

As the concentration is lowered, the reversibility of DA voltammetry was found to improve on BPPG and HOPG samples. Table 6. 1 shows that close to ideal reversibility was obtained, *i.e.* ΔE_p ~ 30 mV, at DA concentrations of 0.1 mM and less for all basal plane HOPG samples and at ~ 10 µM DA for BPPG. DA is known to be unstable in the presence of light, heat and oxygen, in all cases, undergoing spontaneous oxidation to form polymeric compounds, which would adsorb onto the electrode surface.[46-50] All experiments were carried out in a faraday cage and in the absence of light, however, not in the absence of oxygen. At

lower concentrations fewer spontaneous oxidation reactions would take place and fewer polymerisation reactions can take place due to oxygen, therefore the electrode surface cannot spontaneously foul as much before an initial CV can be performed.

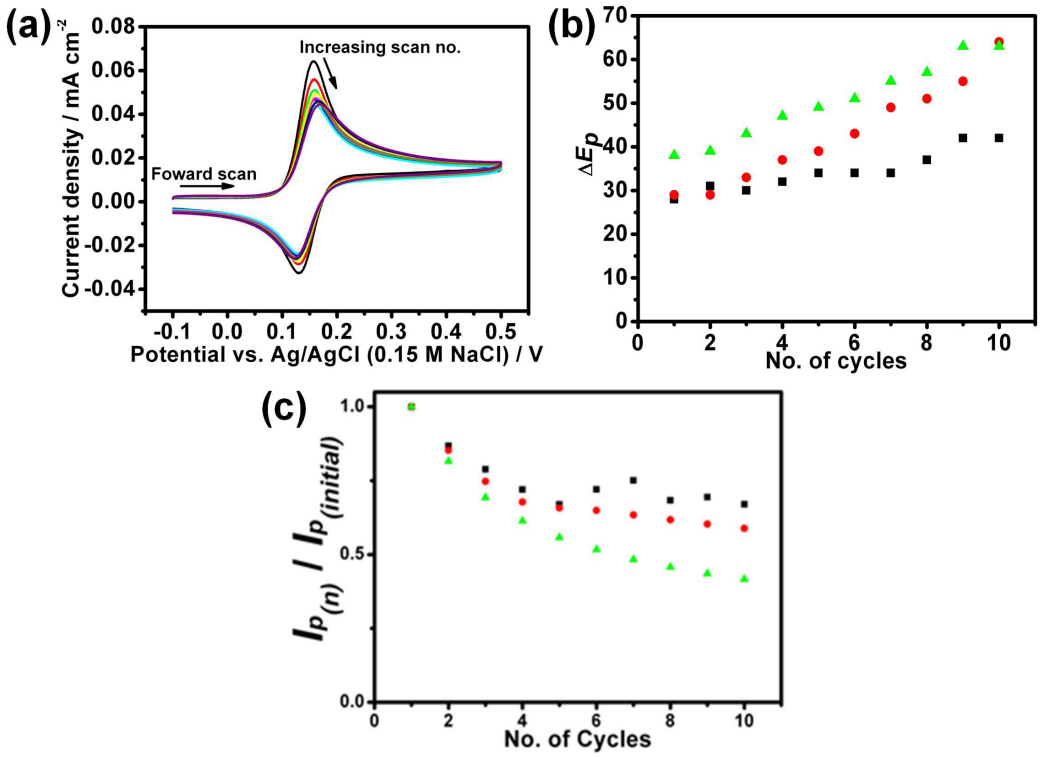

Figure 6. 4 (a) CVs of the repetitive cycling for the oxidation of 0.1 mM DA in 0.15 M PBS, pH 7.2, at 0.1 V s^{-1} on ZYA grade basal plane HOPG. (b) A plot comparing the change in peak-to-peak separation for each successive cycle for the different grade of HOPG, ZYA (black), ZYH (red) and SPI-1 (green). (c) A plot comparing the change in peak current for each successive cycle for the different grade of HOPG, ZYA (black), ZYH (red) and SPI-1 (green).

The extent to which the electrode fouls when the DA concentration was decreased to 0.1 mM and 10 μM was also studied on basal plane HOPG samples, which have shown the best electrochemistry in terms of reversible voltammetry. Figure 6.4shows 10 consecutive CV's at 5 s intervals in 0.1 mM DA with ZYA, ZYH and SPI-1 grade HOPG at 0.1 V s-1. From Figure 6.4(a) it can be seen that the second CV shows very little variation and after 10 CVs ΔEp shows a ~ 10 mV increase. Also the Ip decreases by ~ 30%, contrasting markedly with data for 1 mM DA on ZYA grade HOPG shown in Figure 6. 1 and Figure 6. 2.

Figure 6.4(b) and Figure 6. 3(c) show a plot of the ΔEp or Ip(actual)/Ip(initial) vs. number of cycles in which the fouling effect on the three grades of basal plane HOPG can be compared for 0.1 mM DA. The SPI-1 grade HOPG fouls to a greater extent compared to the ZYA grade. This contrasts with data above which indicates fouling takes place preferentially at the basal

plane, it maybe that the step edges promote nucleation but the basal plane promotes adsorption.

When the concentration is reduced further to 10 μM, very little change in ΔEp is observed over 10 cycles (Figure 6. 5). A change in ΔEp of ca. 5-8 mV for all grades is observed, indicating a minimal amount of fouling to the surface, but a noticeable decrease in Ip was seen for all grades similar to that seen for in Figure 6.4 for fouling with 0.1 mM DA.

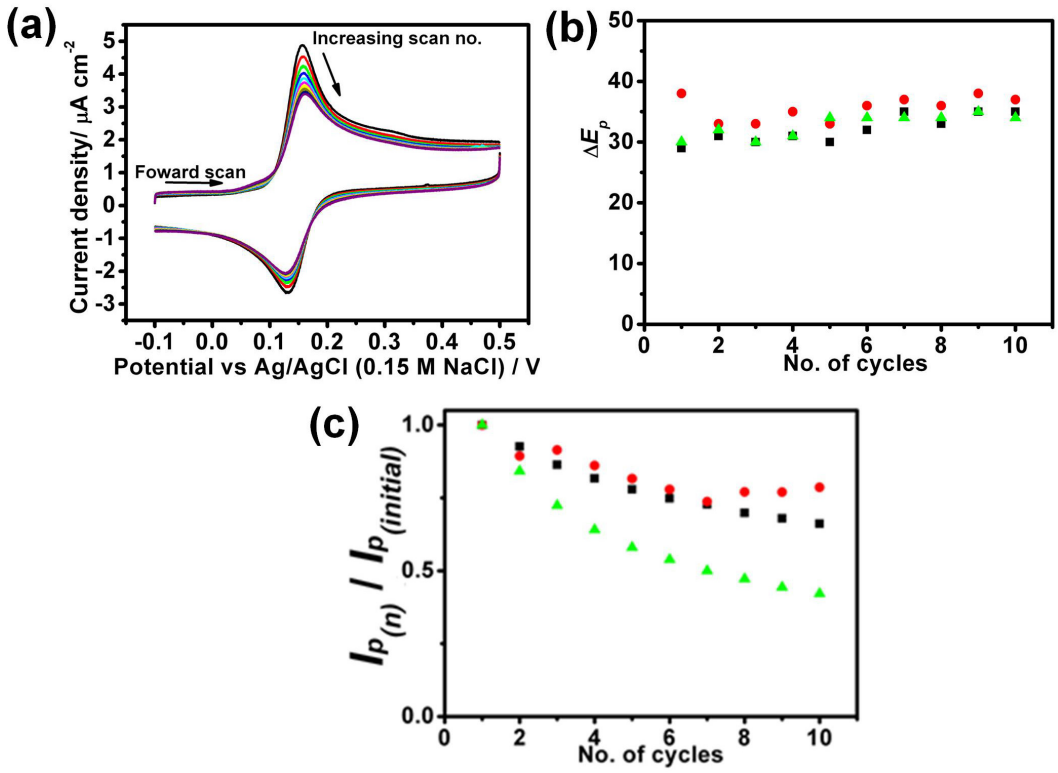

Figure 6. 5 (a) CVs of the repetitive cycling for the oxidation of 10 μM DA in 0.15 M PBS, pH 7.2, at 0.1 V s^{-1} on ZYA grade basal plane HOPG. (b) A plot comparing the change in peak-to-peak separation for each successive cycle for the different grade of HOPG, ZYA (black), ZYH (red) and SPI-1 (green). (c) A plot comparing the change in peak current for each successive cycle for the different grade of HOPG, ZYA (black), ZYH (red) and SPI-1 (green).

The decrease in surface fouling at lower DA concentrations suggests that fewer side reactions take place during electrochemistry, allowing most of the oxidised products to be reduced back to its original state. However, the presence of oxygen will still lead to a separate and spontaneous oxidation reaction. As these reactions take place randomly in the bulk solution, the products do not block the electrodes surface significantly enough to inhibit electron transfer. It is also possible that at lower concentrations the film is thinner and able to form in a more ordered fashion or may even contain pin holes, therefore instead of inhibiting ET promotes adsorption and ET to DA in solution.

6.4 TIME DEPENDENT AFFECTS

To explore the effects of the spontaneous fouling, 'time effect' experiments were carried out in which the HOPG basal plane surfaces had been left in contact with the solution for (a) 0 minutes and (b) 30 minutes with 1 mM DA before measuring a CV. Figure 6. 6(a) shows that the longer the solution is left, the poorer the electrochemistry becomes. When the solution was left for 30 minutes the I_p increases, from 55.8 μA to 79.6 μA, and the ΔE_p increases, from 85 mV to 156 mV. This experiment shows that there is a critical time frame in which voltammetry must take place under these conditions. These observations could be due to one or both of the following points, firstly, spontaneous oxidation of DA occurs in which polymeric compounds are formed that block the surface; secondly, the basal plane of HOPG deactivates over time, as discovered in Chapters 3 and 4. The deactivation was seen to impede the ET kinetics of some, but not all, redox species that occurred over a period of 2 hours.

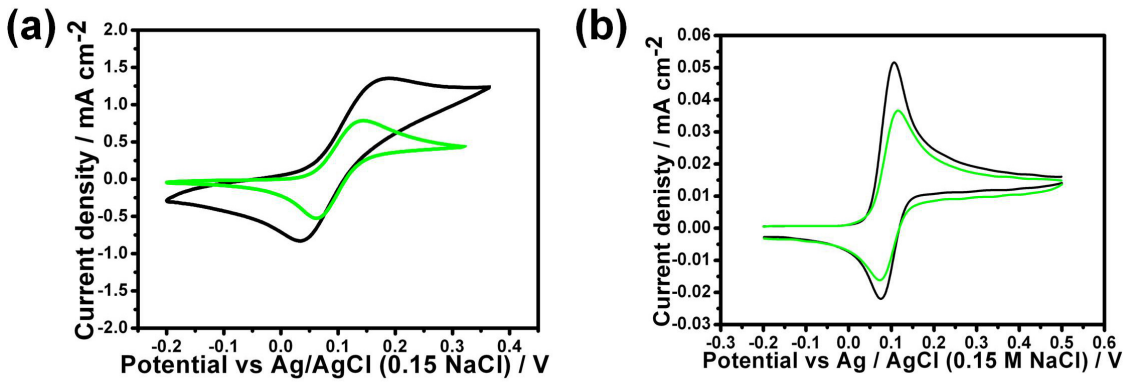

Figure 6. 6 CVs of (a) 1 mM (b) 0.1 mM DA in 0.15 M PBS, pH 7.2, at 0.1 V s^{-1} run after leaving solution in contact with SPI-1 grade basal plane surface for 0 minutes (black) and 30 minutes (green).

The same experiments were carried out at 0.1 mM DA (Figure 6. 6(b)). Over the course of an hour the electrode does become blocked but in a much lower extent as with 1 mM DA. The I_p decreases from 3.56 μA to 2.5 μA and the ΔE_p increases from 31 mV to 41 mV over the course of 30 minutes. This indicates that it is the spontaneous oxidation of DA that is the predominant cause of the observations in Figure 6. 6(a), and that any contribution from the surface deactivation over time is negligible compared to the affects of the dopaminergic compounds blocking the electrodes surface. This data also shows that at lower concentrations the time frame in which electrochemical measurements must be carried out on basal plane HOPG is no longer as critical, but in order to obtain reversible electrochemistry, CV's should be reordered within 30 minutes of set-up.

6.5 *IN-SITU* AFM

To study how the surface fouls over time and as a function of potential cycling, in-situ AFM was carried out whilst performing the electrochemical studies. The surface of SPI-1 grade basal plane HOPG was first imaged in a solution 0.1 mM DA (0.15 M PBS, pH 7.2) with a freshly cleaved SPI-1 grade HOPG and after a potential cycle. Figure 6. 7 shows topographical and phase images for; (a) when the sample was immersed in solution ca. 30 minutes with no electrochemical measurement performed; (b) after 5 potential cycles was recorded between the potential range -0.2 to 0.6 V at 0.1 V s-1. Figure 6. 7(a) shows that within 30 minutes fouling of the surface has already occurred, in which isolated islands can be seen to have formed across the HOPG surface and mainly on the basal plane. From performing one CV these islands most likely become bigger and begin to coalesce. Even though there appears to be complete coverage of the surface from performing 5 potential cycles, there doesn't seem to be significant distortion of the CVs, the ΔEp only increases from ~38 mV to ~ 50 mV. Correlating CVs (Figure 6.4a) show that after 5 CVs electrochemical oxidation still takes place. There are two possible explanations for this, firstly, the melanin-like film may not inhibit ET kinetics but facilitate it and as it builds up the kinetics become slower. A study carried out by McCreery and co-workers[10] showed that adsorption of quinone-like products including DA, promotes its absorption and catalyse ET to DA molecules in solution. As the melanin-like compound, formed from the polymerisation of dopaminergic compounds, the quinone-like species theoretically could act as an electron relay to DA molecules in solution. The second possible explanation is that the film does not completely cover the surface and that pin-holes maybe present which allow flux.

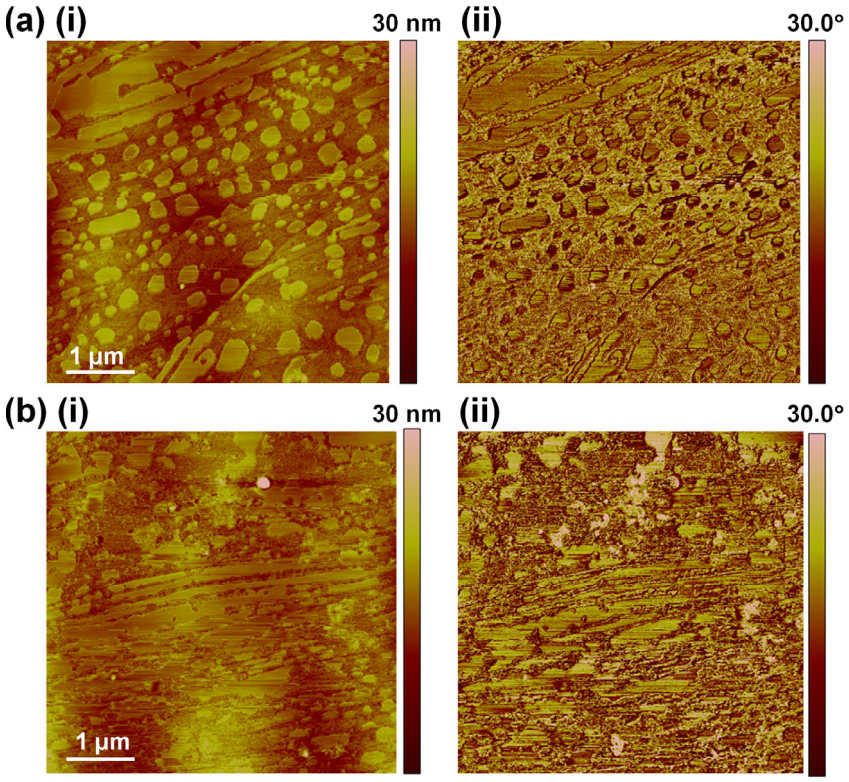

Figure 6. 7 A 5 × 5 µm *in-situ* AFM imaging of SPI-1 HOPG in 0.1 mM DA in 0.15 M PBS, pH 7.2, (a) within 30 minutes of adding DA solution; (b) after applying 1 potential cycle between -0.2 to 0.6 V at 0.1 V s^{-1}.

These *in-situ* experiments were initially attempted with 1 mM DA but was found to foul the surface at a such a high degree within 30 minutes that it was impossible to study the build up of the film as a function of time and potential cycling (note it takes *ca.* < 30 minutes to capture one image).

6.6 INTERFERENCE STUDY

As a major problem encountered when attempting to detect DA is the oxidative interference by coexisting species, such as AA, the detection of DA was investigated in the presence of AA. First CVs were run with just AA in order to establish the potential at which it oxidizes. Figure 6. 8(a) shows the CVs for repetitive cycling in 0.5 mM AA (0.15 M PBS, pH 7.2) at 100 mV s^{-1}, on ZYA grade HOPG. The oxidation of ascorbic acid involves an irreversible two-electron transfer process, therefore no peak is seen when the potential sweep is reversed. As seen with the oxidation of DA at high concentrations, with each successive potential cycling of AA a large decrease in I_p is observed, indicating a fouling of the surface by the AA oxidative products. The experiment was repeated with the addition of 0.1 mM DA on a freshly prepared surface, Figure 6. 8(b), the resulting voltammogram shows two distinctly clear peaks which can be identified as AA (I) and DA (II). As already observed, during potential

cycling the I_p for AA peak rapidly decreases, but surprisingly, no change in the I_p (forward and reverse) and ΔE_p for DA oxidation is seen. This is shown more clearly in Figure 6. 8(c) where a plot of $I_{p(actual)}/I_{p(initial)}$ against number of cycles is shown. It can be seen that after performing ten consecutive cycles, the AA signal has almost completed deteriorated but the DA signal remains relatively constant. The decay in the AA signal clearly indicates a blocking of the surface that leads to the inhibition of further AA oxidation, but as there is no change in the observed oxidation for DA. The data suggests the possibility of a film formation which posses a negative, they by excluding AA but supporting DA electrochemistry.

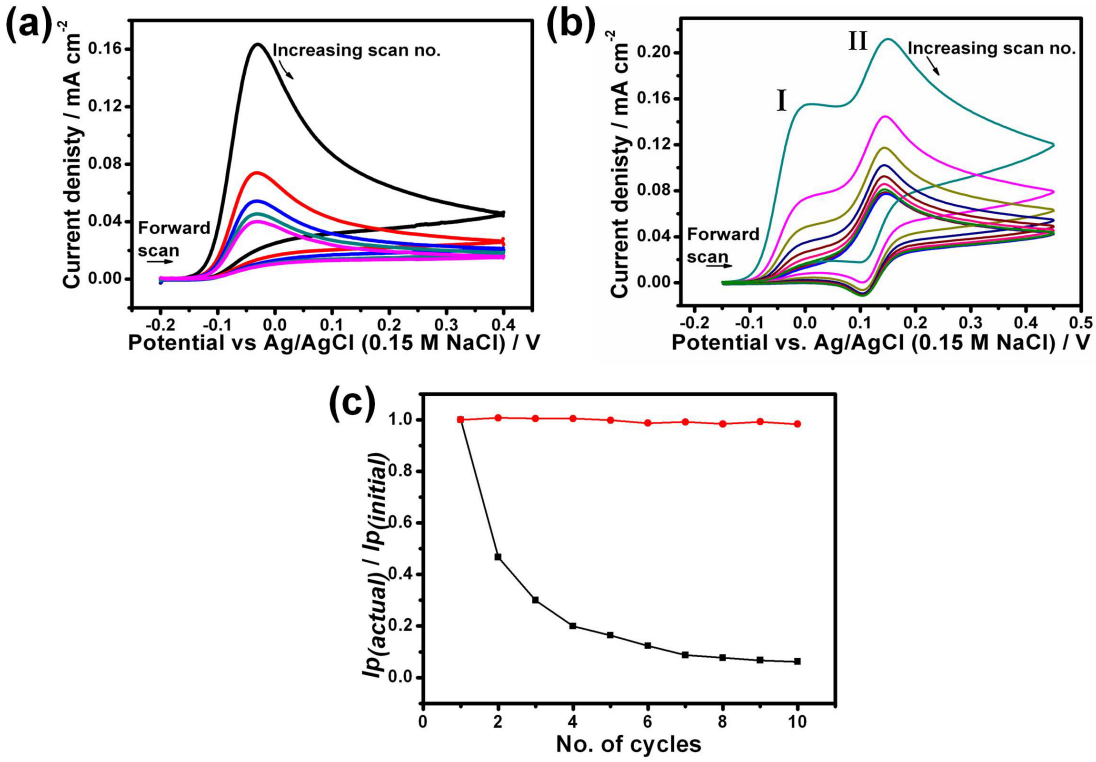

Figure 6. 8 CVs of the repetitive cycling for the oxidation of (a) 0.5 mM AA and (b) 0.5 mM AA and 0.1 mM DA in 0.15 M PBS, pH 7.2, at 0.1 V s^{-1} on ZYA grade basal plane HOPG, run at 5 second intervals. (c) A plot comparing the change in peak current for the successive cycling of AA (black) in the presence of DA(red), extracted from (b).

To investigate the possibility of a film forming, *in-situ* AFM was carried out freshly cleaved SPI-1 grade basal plane HOPG in a solution 0.5 mM AA (0.1 M PBS, pH 7.2) after having performed one potential cycle between the range -0.2 to 0.6 V at 0.1 V s^{-1}. Figure 6. 9(a) shows 2 × 2 μm topographical and phase images which shows of evidences for adsorbed species across basal and edge plane sites of the HOPG surface. An enhancement of a smaller section (Figure 6. 9(b)) shows there to be a continuous film. Due to the to the molecular nature of the AA this film would undoubtedly posses an overall negative charge hence enabling the oxidation of DA to proceed whilst inhibiting AA oxidation.

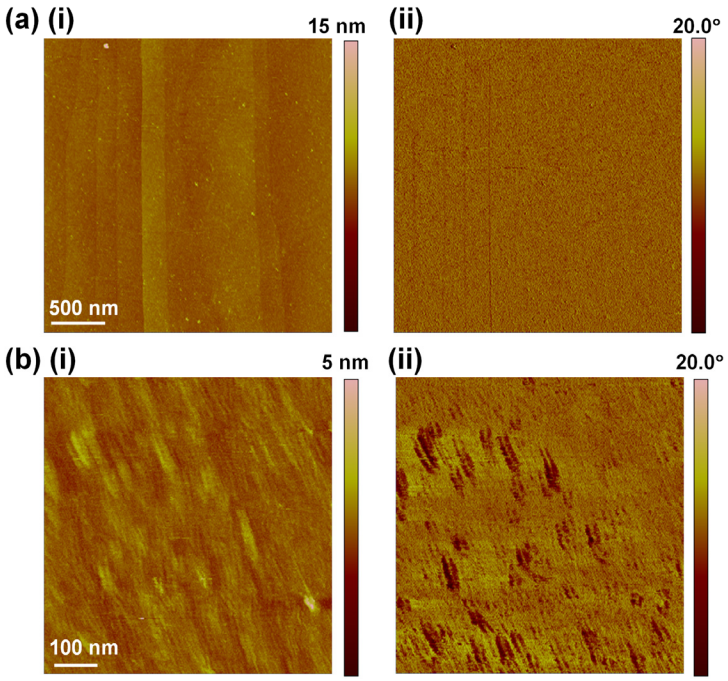

Figure 6. 9 (a) 2 × 2 µm and (b) 500 × 500 nm i*n-situ* AFM imaging of SPI-1 HOPG in 0.5 mM AA in 0.15 M PBS, pH 7.2, after applying 1 potential cycle between -0.2 to 0.6 V at 0.1 V s^{-1}.

6.7 CONCLUSIONS

In this study the electrochemical response of DA at various carbon electrodes has been compared. The data presented herein shows for the first time show the freshly prepared and unmodified basal plane of HOPG to provide ideal reversible voltammetry for DA oxidation. A comparison of DA electrochemistry on basal plane against edge plane HOPG clearly shows that the basal plane HOPG provides lower detection limits, with the most superior grade (ZYA), which possess the lowest step density, providing the lowest detection limits compared to the other basal plane grades (SPI-1 and ZYH). Hence, the unmodified basal plane surface provides reversible electrochemistry for the oxidation of DA (at concentrations below 0.1 mM) compared to the 4 other carbon based electrodes studied herein. At concentrations above 0.1 mM, the unmodified basal plane of HOPG is the most susceptible to blocking by dopaminergic products, however, this is of no consequence as the physiological concentration of DA is < 1 µM. Electrochemical *in-situ* data indicated the film, which forms from dopaminergic products, must either facilitate ET or possess pinholes that enable electrochemical redox to take place. It has also been shown that not only can the signal between AA and DA be easily resolved, without the prerequisite of surface modification, but also that the AA forms a thin negatively charged film that selectively excludes anions, such as AA.

6.8 REFERENCES

1. Wu, K.,J. Fei,S. Hu, *Anal Biochem,* **2003,** *318,* 100-106.
2. Zhao, Y.,Y. Gao,D. Zhan,H. Liu,Q. Zhao,Y. Kou,Y. Shao,M. Li,Q. Zhuang,Z. Zhu, *Talanta,* **2005,** *66,* 51-57.
3. Chen, S.-M.,K.-T. Peng, *J. Electroanal. Chem.,* **2003,** *547,* 179-189.
4. Zhao, H.,Y. Z. Zhang,Z. B. Yuan, *Analyst,* **2001,** *126,* 358-360.
5. Hou, S.,N. Zheng,H. Feng,X. Li,Z. Yuan, *Anal. Biochem.,* **2008,** *381,* 179-184.
6. Bernsmann, F.,V. Ball,F. Addiego,A. Ponche,M. Michel,J. J. Gracio,V. Toniazzo,D. Ruch, *Langmuir,* **2011**.
7. Hawley, M. D.,S. V. Tatawawadi,S. Piekarski,R. N. Adams, *J. Am. Chem. Soc.,* **1967,** *89,* 447-450.
8. Lane, R. F.,A. T. Hubbard, *Anal. Chem.,* **1976,** *48,* 1287-1293.
9. Alwarappan, S.,K. S. A. Butcher,D. K. Y. Wong, *Sensor. Actuat. B,* **2007,** *128,* 299-305.
10. DuVall, S. H.,R. L. McCreery, *J. Am. Chem. Soc.,* **2000,** *122,* 6759-6764.
11. McCreery, R. L., *Chem. Rev,* **2008,** *108,* 2646-2687.
12. Bath, B. D.,H. B. Martin,R. M. Wightman,M. R. Anderson, *Langmuir,* **2001,** *17,* 7032-7039.
13. Bath, B. D.,D. J. Michael,B. J. Trafton,J. D. Joseph,P. L. Runnels,R. M. Wightman, *Anal. Chem.,* **2000,** *72,* 5994-6002.
14. DuVall, S. H.,R. L. McCreery, *Anal. Chem.,* **1999,** *71,* 4594-4602.
15. Rubianes, M. D.,A. S. Arribas,E. Bermejo,M. Chicharro,A. Zapardiel,G. Rivas, *Sensor. Actuat. B,* **2010,** *144,* 274-279.
16. Rubianes, M. D.,G. A. Rivas, *Anal. Chim. Acta,* **2001,** *440,* 99-108.
17. Li, Y.,M. Liu,C. Xiang,Q. Xie,S. Yao, *Thin Solid Films,* **2006,** *497,* 270-278.
18. Wen, X. L.,Y. H. Jia,Z. L. Liu, *Talanta,* **1999,** *50,* 1027-1033.
19. Kachoosangi, R. T.,R. G. Compton, *Anal. Bioanal. Chem.,* **2007,** *387,* 2793-2800.
20. Jacobs, C. B.,T. L. Vickrey,B. J. Venton, *Analyst,* **2011,** *136,* 3557-3565.
21. Zachek, M. K.,A. Hermans,R. M. Wightman,G. S. McCarty, *J. Electroanal. Chem.,* **2008,** *614,* 113-120.
22. Swain, G. M.,M. Hupert,A. Muck,R. Wang,J. Stotter,Z. Cvackova,S. Haymond,Y. Show, *Diamond Relat. Mater.,* **2003,** *12,* 1940-1949.
23. Fujishima, A.,D. Shin,D. A. Tryk,A. Merkoci,J. Wang, *Electroanal.,* **2005,** *17,* 305-311.
24. Rao, T. N.,A. Fujishima, *Diamond Relat. Mater.,* **2000,** *9,* 384-389.
25. Banks, C. E.,R. G. Compton, *The Analyst,* **2005,** *130,* 1232-1239.
26. Trouillon, R.,D. O'Hare, *Electrochim. Acta,* **2010,** *55,* 6586-6595.
27. Venton, B. J.,R. M. Wightman, *Anal. Chem.,* **2003,** *75,* 414a-421a.
28. Kurniawan, F.,V. Tsakova,V. M. Mirsky, *J. Nanosci. Nanotechnol.,* **2009,** *9,* 2407-2412.
29. Niu, L. L.,M. W. Shao,S. Wang,L. Lu,H. Z. Gao,J. Wang, *J. Mater. Sci.,* **2008,** *43,* 1510-1514.
30. Wang, J. X.,M. X. Li,Z. J. Shi,N. Q. Li,Z. N. Gu, *Electroanal.,* **2002,** *14,* 225-230.
31. Codognoto, L.,E. Winter,J. A. Paschoal,H. B. Suffredini,M. F. Cabral,S. A. Machado,S. Rath, *Talanta,* **2007,** *72,* 427-433.
32. Lin, X. Q.,J. M. Gong, *Anal. Chim. Acta,* **2004,** *507,* 255-261.
33. Nagy, G.,G. A. Gerhardt,A. F. Oke,M. E. Rice,R. N. Adams,M. N. Szentirmay,C. R. Martin, *J. Electroanal. Chem.,* **1985,** *188,* 85-94.
34. Zen, J. M.,G. Ilangovan,J. J. Jou, *Anal. Chem.,* **1999,** *71,* 2797-2805.
35. Milczarek, G.,A. Ciszewski, *Electroanal.,* **2004,** *16,* 1977-1983.
36. Kang, T.-F.,G.-L. Shen,R.-Q. Yu, *Anal. Chim. Acta,* **1997,** *356,* 245-251.

37. Roy, P. R.,T. Okajima,T. Ohsaka, *Bioelectrochemistry,* **2003,** *59,* 11-19.
38. Jin, G. Y.,Y. H. Zhang,W. X. Cheng, *Sensor. Actuat. B,* **2005,** *107,* 528-534.
39. Bowling, R.,R. T. Packard,R. L. McCreery, *Langmuir,* **1989,** *5,* 683-688.
40. McCreery, R. L., *Electroanalytical Chemistry*. Dekker: NY, 1991; Vol. 17, p 221-374.
41. Banks, C. E.,R. G. Compton, *Anal. Sci.,* **2005,** *21,* 1263-1268.
42. Ji, X.,C. E. Banks,A. Crossley,R. G. Compton, *ChemPhysChem,* **2006,** *7,* 1337-1344.
43. Bowling, R. J.,R. T. Packard,R. L. McCreery, *J. Am. Chem. Soc.,* **1989,** *111,* 1217-1223.
44. Kneten, K. R.,R. L. McCreery, *Anal. Chem.,* **1992,** *64,* 2518-2524.
45. Lai, S. C. S.,A. N. Patel,K. McKelvey,P. R. Unwin, *Angew. Chem. Int. Ed.,* **2012,** *51,* 5405-5408.
46. Rath, S.,E. Winter,L. Codognoto, *Electrochim. Acta,* **2006,** *51,* 1282-1288.
47. Morris, S.,B. R. Mcmahon, *Physiol. Zool.,* **1989,** *62,* 654-667.
48. Yokoyama, H.,H. Kuroiwa,R. Yano,T. Araki, *Neurol. Sci.,* **2008,** *29,* 293-301.
49. Berman, S. B.,T. G. Hastings, *J Neurochem,* **1997,** *69,* 1185-1195.
50. Carter, J. E.,J. H. Johnson,D. M. Baaske, Dopamine Hydrochloride. In *Analytical Profiles of Drug Substances*, Klaus, F., Ed. Academic Press: 1982; Vol. 11, pp 257-272.

CHAPTER 7: MACROSCOPIC AND MICROSCOPIC ELECTROCHEMISTRY OF ANTHRAQUINONE-2,6-DISULFONATE AT HIGHLY ORDERED PYROLYTIC GRAPHITE: BASAL PLANE VS. EDGE PLANE ACTIVITY

The adsorption of the quinone, anthraquinone-2,6-disulfonate (2,6-AQDS), has been widely considered to be a marker of the active sites on carbon surfaces and used to track the step defect coverage on graphite surfaces. Using macroscopic voltammetry, the adsorption of 2,6-AQDS was investigated on a range of surfaces differing greatly in step defect density. Complemented with tapping mode atomic force microscopy (AFM) and *ex-situ* AFM data, it is shown in this chapter that for surfaces ranging in step defect by a magnitude of 1-3 orders, a negligible variation in the adsorption of 2,6-AQDS is observed. With the use of nanoscopic high resolution scanning electrochemical cell microscopy (SECCM), reactive patterning was carried out with complementary AFM, enabling for the first time, a definitive and direct correlation to be made between the electroactivity and surface site. This powerful electrochemical imaging technique shows uniform adsorption of a quinone on basal plane graphite vs. the step edge at a nanoscale and provides unequivocal evidence for the presence of high activity at the basal surface of HOPG. It is concluded herein that no correlation exists between the step defect density of graphite surfaces and the observed adsorption coverage of 2,6-AQDS.

7.1 INTRODUCTION

Surface modifications have also been used as a measure for the quality of a carbon electrode surface.[1-3] For example, it has been suggested that the adsorption of specific redox active organic molecules, such as quinones, can be used as a direct measure of the percentage of electrochemically active sites present on a surface.[1] Under acid conditions, quinones have been shown to spontaneously adsorb on to carbon surfaces, and are able to undergo a single step 2-H^+, 2-e^- reduction.[4-7] Quinone adsorption has been widely studied on a range of electrode materials have been widely studied on a range of electrode materials,[8-10] including basal plane HOPG,[11-12] an electrode material whose local electrochemical activity is the subject of recent debate.[13-19]

In an early study, McCreery et al used different surfaces of basal plane HOPG that were predetermined to vary in fractional defect density to show the double layer capacitance ($C°$),

the electron transfer kinetics ($k°$) for the redox couple ferri/ferrocyanide, and Γ_{obs} for anthraquinone-2,6-disulfonate (2,6-AQDS) was higher for surfaces with greater step defect densities.[20] An attempt to correlate $C°$ and $k°$ to the Γ_{obs} of 2,6-AQDS was later attempted,[2] and based on their previous study which showed rougher surfaces posses higher $C°$ and $k°$ for ferri/ferrocyanide, an indirect relationship was made between the step defect density to Γ_{obs} 2,6-AQDS. In a follow-up study, a direct correlation between the step defect density of basal plane HOPG and the Γ_{obs} 2,6-AQDS was shown.[17] However, the data for which the correlation was made (Figure 4 in McCreery *et al Langmuir*, 10, 1994, pp 4307) consisted of 5 data points that cover a range less than that of the typical uncertainty in the step density, which is quoted as being as high as ± 45%. Inconsideration of this, it would be impossible to make a correlation of any kind.

Nonetheless, the conclusion was drawn that the Γ_{obs} 2,6-AQDS, $C°$ and the $k°$ for ferri/ferrocyanide are all markers for the presence of step defects. Although, it has since been shown that the ferri/ferrocyanide couple is particularly problematic on the basal surface of graphite.[21-22] Higher Γ_{obs} for quinones (50 times) on GC and edge plane HOPG compared to that of basal plane HOPG advocated a link to step defect density and quinone adsorption.[2] Thus, it was proposed that either quinones do not adsorb onto the basal plane of HOPG, or that adsorbed material does not undergo electron transfer with the basal surface itself, rendering it undetectable through voltammetric experiments. The authors also observed that the adsorption coverage on basal plane HOPG exceeded the area of edge plane sites by a factor of 30. Multilayer formation and intercalation mechanisms were ruled out, and this discrepancy was put down to adsorption taking place on basal plane sites up to a few nm away from step edge defects, as a result of a perturbation in the local electronic properties of the basal surface as a result of the step defect.[17] Recent STS and STM studies have shown the local DOS to be higher at the step edges of graphite surfaces, which decays over the space of a few nanometres into the basal plane.[23-25] The observation of a higher local DOS has since been shown to exist only at zigzag step edges and not at the armchair step edges. In turn, armchair step edges have also been shown to be the higher proportion of step edges present on graphite as well as longer in length compared to zigzag step edges.[24-25] Furthermore, this affect is considered to have a negligible effect on the overall DOS over large surfaces, where terraces are wider than 10 nm. [23, 26]

Swain *et al* also investigated the adsorption of 2,6-ADQS and proposed a correlation between surfaces with carbon-oxygen functionalities and adsorption coverage, suggesting that the functional groups promote strong dipole-dipole and ion-dipole interactions.[3] The authors also observed apparent multilayer absorption on GC but determined that the

adsorbed molecules must orient in an end-on fashion so they are perpendicular to the electrode surface rather than in the flat orientation proposed by others, hence increasing packing area and the surface coverage. They also reported that ~40% of the adsorbed species could be removed simply by rinsing, indicating weak interactions between adsorbed species and the electrode surface. Zhang and Anson reported that the 2,6-AQDS first adsorbs in a flat orientation but then undergoes reorganisation over time, eventually rearranging itself in an end-on arrangement and that the adsorption was a strong and irreversible process.[12]

In-situ scanning force microscopy (SFM) carried out by McDermott *et al* to investigate 2,6-AQDS adsorption found surface coverage determined by voltammetry did not correlate with that observed by SFM. Voltammetry carried out indicated *ca.* 17% monolayer adsorption, whereas SFM images indicated *ca.* 90% of the surface was covered by multilayers of 2,6-AQDS, with a high density of pinhole defects accounting for the remainder of the surface.[27] The authors concluded that 2,6-AQDS adsorption takes place indiscriminately towards the basal-plane and step-edge sites and that only the absorbents at the step-edges were electroactive, hence the electrode response corresponding to only a partially covered electrode. Compton and co-workers observed two voltammetric peaks on their basal plane samples, a large adsorption peak occurring around -0.4V, which was identical to that observed on their edge plane samples, and a smaller adsorption peak occurring at -0.2 V, which they deduced must be due to adsorption on basal-plane sites.[28] From their findings, the authors concluded that the ET on basal plane is not negligible but 2-3 orders of magnitude slower than the edge plane.

In light of studies presented so far, this chapter aims to revisit this theory by carrying out a thorough investigation into the adsorption of 2,6-AQDS and its relationship with the step defect density of graphite surfaces. Within this chapter a range of techniques including voltammetry, *ex-situ* AFM and SECCM is used to probe the basal plane surface of HOPG at the nanoscale.

7.2 RESULTS AND DISCUSSION

7.2.1 Macroscale studies

The adsorption (as detected by voltammetry) of 2,6-AQDS from 10 μM in 0.1M $HClO_4$ was first examined on the three grades of HOPG, SPI-1; ZYA; and AM at a macroscale using the Teflon cell arrangement. Figure 7. 1 shows representative CVs for the reduction and oxidation of the adsorbed 2,6-AQDS on: SPI-1 (red); ZYA (blue); and HOPG (AM) (black) samples. For each HOPG sample, the reduction and oxidation waves occur at the same

potential; where the width of the cathodic peak at half-wave height is ~ 50 mV, close to the theoretical value of 90.6/n mV,[29] where n is the number of electrons transferred per redox event (i.e. n=2), highly indicative of a surface bound electroactive species.[29] The observed surface coverage for the adsorbed species (Γ_{obs}) was calculated for each sample, as done in previous studies,[3, 17] using the charge for the reduction wave (Q), obtained via peak integration, and a molecular area of 126 Å^2 for 2,6-AQDS (assuming species adsorbs in a flat orientation).[2] Note, for all HOPG samples, the time frame for which the maximum observed surface coverage takes place was explored, where each CV was recorded within ca. 10 seconds of addition of 2,6-AQDS and after waiting for up to 1 hour. With no observable change in voltammetry, it was concluded that the maximum adsorption must occur within in the 10 second timeframe for the initial CV.

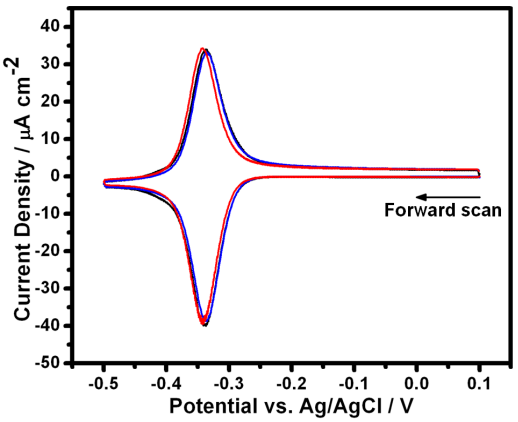

Figure 7. 1 CVs for the reduction of adsorbed 2,6-AQDS (10 μM) in 0.1 M $HClO_4$, at 0.1 Vs^{-1}, on three grades of HOPG: SPI-1 (Black), ZYA (red), and HOPG (AM) (blue); run using a Teflon cell.

The range of Γ_{obs} values obtained for each grade of HOPG along with the mean is shown in Figure 7. 2(a). For 10 repeats, all performed on freshly prepared surfaces, the following Γ_{obs} were obtained: 34.1 ± 11.3% for SPI-1 grade; 37.3 ± 5.6% for ZYA grade; and 41.2 ± 13.5% for HOPG (AM). Although greater adsorption is observed for HOPG (AM), when taking into account the errors associated with each sample set, it is clear all three grades provide similar Γ_{obs}. The step-edge coverage for the three grades of HOPG were analyzed using AFM, Figure 7. 2(b) shows the range of defect density for each grade along with the mean values. It can be seen that the defect density varies greatly between the samples: mechanically cleaved HOPG (AM) was found to possess the lowest (range of 0.006 - 0.48%) followed by ZYA (range of 0.03 - 1%); SPI-1 showed a wider range of defect density as well as a highest percentage coverage (range of 0.5 - 3.4%). HOPG (AM) and ZYA samples were shown to predominantly reveal monolayer and bilayer steps; whereas SPI-1 was found to show a wide range of multilayer steps. As SPI-1 has been shown to exhibit a greater coverage of surface defects, 1-3 orders of magnitude greater than HOPG (AM), and based on the current 2,6-

AQDS adsorption literature, the Γ_{obs} for 2,6-AQDS on HOPG (AM) would be expected to be significantly lower than that observed for SPI-1 grade HOPG. However, the data presented shows no significant variation in the Γ_{obs} exists between the different grades although a significant variation in the defect densities does exists. *In-situ* AFM measurements were performed on samples immediately after 2,6-AQDS adsorption and subsequent voltammetric detection, in an attempt to directly correlate Γ_{obs} with step edge density. However, the 2,6-AQDS layer that formed appeared to be thicker than a single monolayer, effectively masking the step edges and preventing an accurate correlation from being drawn.

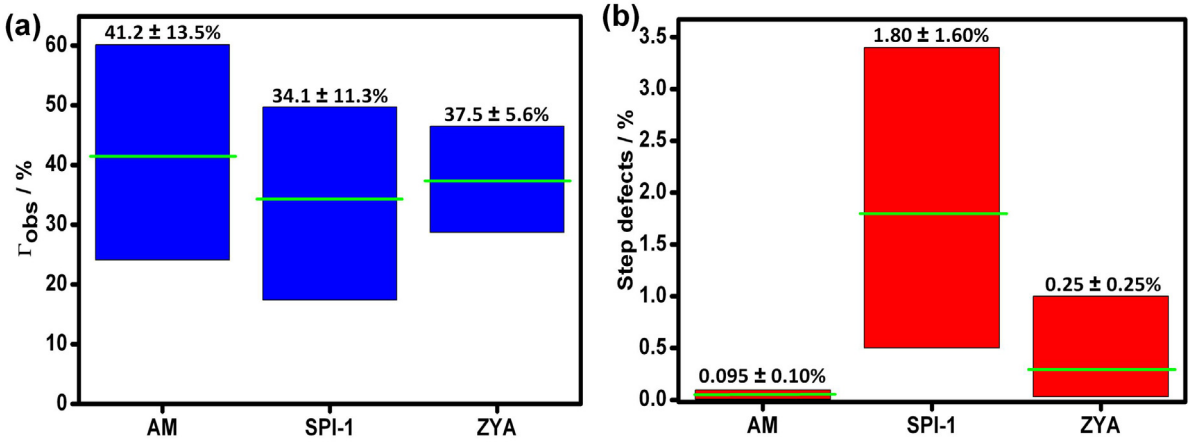

Figure 7. 2(a) The range of the observed surface coverage of 2,6-AQDS (10 μM) in 0.1 M $HClO_4$, at 0.1 Vs^{-1},on different grades of freshly cleaved HOPG: AM; SPI-1; and ZYA, run using a Teflon cell. The mean for each data set is marked (green line) and noted with the sd. (N = 10). (b) The range of the fractional distribution of step defects on three grades of basal plane HOPG: SPI-1; ZYA; AM. The mean for each data set is marked (green line) and noted with the sd. (N = 10).

The stability of adsorbed 2,6-AQDS on HOPG was explored, where the surface of ZYA grade HOPG was first 'pre-treated' with 2,6-AQDS by running a single CV with 10 μM 2,6-AQDS (0.1 M $HClO_4$) before replacing the solution with just the supporting electrolyte (0.1 M $HClO_4$) or 0.2 mM $FcTMA^+$ (0.1 M $HClO_4$); successive potential cycling was then carried out. Figure 7. 3(a) shows 5 consecutive CVs, run at 2 second intervals, with 0.1 M $HClO_4$ on pre-treated ZYA grade HOPG. It can be seen that the peak current (i_p) at -0.1 V readily decreases with each successive cycle, indicating easy desorption of the surface bound 2,6-AQDS species; most likely a result of diffusion of species back into bulk solution. Figure 7. 3(b) shows the effect of potential cycling on the pre-treated surface with the outer-sphere redox mediator, 0.2 mM $FcTMA^+$ (0.1 M $HClO_4$) between -0.3 V and 0.8 V at 0.1 V s^{-1}. As observed from Figure 7. 3(a), the i_p for 2,6-AQDS adsorption decreases as a function of potential cycle; conversely, an increase in i_p for the oxidation of $FcTMA^+$ is observed. With continuous potential cycling, the adsorption peak for 2,6-AQDS slowly deteriorates eventually becoming unobservable. At the same time, the i_p for $FcTMA^+$ oxidation reaches a maximum of 2.85 μA,

and is identical to the CV for the oxidation of 0.2 mM $FcTMA^+$ (in 0.1 M $HClO_4$ at 0.1 V s^{-1}) on a freshly cleaved untreated ZYA grade HOPG (Figure 7. 3(c)). The maximum i_p (2.85 μA) is in close agreement to the theoretical i_p of 2.90 μA for the oxidation of this species with a 3 mm diameter disc electrode; as determined from the Randles-Sevcik equation (Chapter 1, Equation 1.3).[29] This data suggests desorption of the film readily takes place, though it cannot be discerned whether complete desorption takes place to reveal a bare electrode surface or whether partial desorption occurs to which small areas of the bare HOPG surface are revealed allowing overlap of the diffusion field.

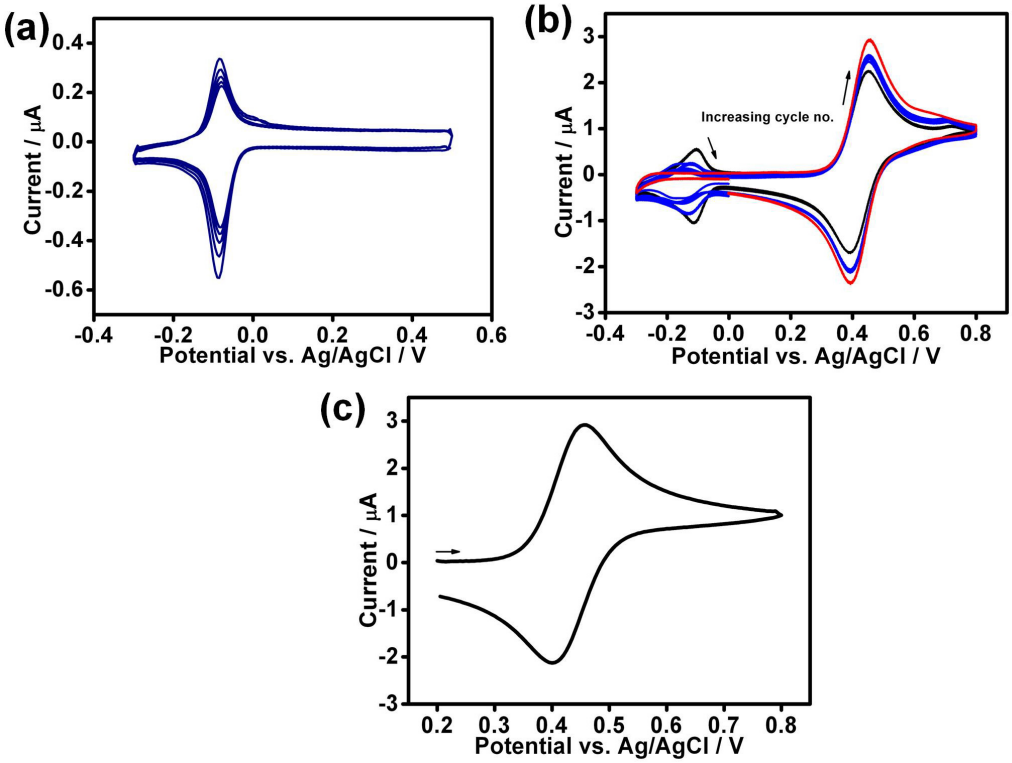

Figure 7. 3 CVs for the potential cycling in (a) 0.1 M $HClO_4$, and (b) 0.2 mM $FcTMA^+$ in 0.1 M $HClO_4$, after running one CV in 10 μM 2,6-AQDS in 0.1 M $HClO_4$. All CVs were performed on ZYA grade HOPG using a Teflon cell at 0.1 Vs^{-1}.

Analysis of the initial CV (black) for the oxidation of 0.2 mM $FcTMA^+$ (Figure 3(b)) indicates the electrochemically active working area to be 70% less than that calculated from the final CV (red). A comparison of this against the reference CV (Figure 7. 3(c)) confirms 30% of the surface area is electrochemically blocked by 2,6-AQDS adsorption. However, in Figure 7. 3(b) the initial CV for 2,6-AQDS adsorption (black) shows the initial Γ_{obs} to be 13%. In order for adsorbed areas to affect the electrochemical current, the surface must contain a mixture of pinholes and large blocked areas that are sparsely distributed. The data shows the electrochemically observed surface coverage of adsorbed 2,6-AQDS is less than and the

actual amount of adsorbed 2,6-AQDS that blocks electrochemically active areas on the basal surface of HOPG.

In-situ and *ex-situ* AFM imaging was carried out with 2,6-AQDS on HOPG in order to study the adsorption on a large scale and to confirm the extent of 2,6-AQDS coverage from applying a single CV. Both *in-situ* and *ex-situ* imaging showed a full surface coverage, however as *ex-situ* imaging was found to provide clearer and higher quality images these are presented. Figure 4 shows a 5 × 5 μm AFM image of the surface of ZYA grade HOPG after having performed voltammetry, the coverage of 2,6-AQDS is greater than 90%; whereas the complementary CV indicates a Γ_{obs} of 36%. The adsorption appears to be relatively uniform across the basal area and over the steps; the image shows no evidence of preferential adsorption on or around the areas of the steps. This is consistent with the observations by McDermott et al,[27] where the electrochemical data indicated monolayer partial surface coverage which was inconsistent with the SFM imaging which clearly showed multilayer adsorption.

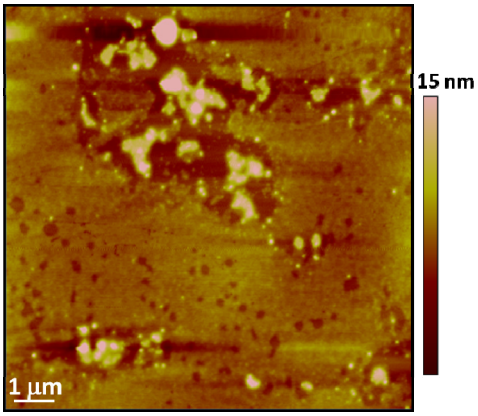

Figure 7. 4 *Ex-situ* AFM image for the adsorption of 10 μM 2,6-AQDS in 0.1 M $HClO_4$ on ZYA grade HOPG.

7.2.2 Nanoscale studies

To determine definitively whether, or not, 2,6-AQDS electroactivity correlated to the presence of step edge defects, SECCM was employed to carryout line-patterning; using the adsorption of 2,6-AQDS as a place marker for the location of the electrochemical reaction that can be related to the electrochemical response. The SECCM line-patterning was carried out with an effective surface bias of -0.4 V (V_s + ½V_{bias}) vs. Ag/AgCl; a potential well past the i_p of 100 μM 2,6-AQDS adsorption, as determined by voltammetry. A representative CV obtained using the SECCM set-up for the adsorption of 100 μM 2,6-AQDS in 0.1 M $HClO_4$, at 0.1 Vs^{-1} is shown in Figure 7. 5.

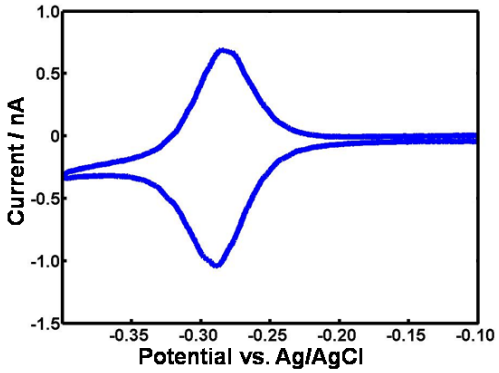

Figure 7. 5 A representative CV for the adsorption of 100 μM 2,6-AQDS in 0.1 M $HClO_4$, at 0.1 Vs^{-1}, on HOPG (AM) obtained using SECCM using a pipet *ca.* 1 μM in diameter.

The line-patterning was carried out with SECCM by moving the HOPG (AM) to create a square-spiral line-pattern. SEM imaging was performed to confirm SECCM patterning, Figure 7. 6(a) shows a 85 μm SEM image in which a continuous line pattern forming a square spiral shape can be seen. The simultaneously obtained SECCM maps are presented in Figure 7. 6 showing: (b) topography; (c) surface activity; (d) AC conductance current used as the feedback set-point; and (e) DC conductance current. The topography map shows the sample to possess a small tilt of ~0.5° across the surface.

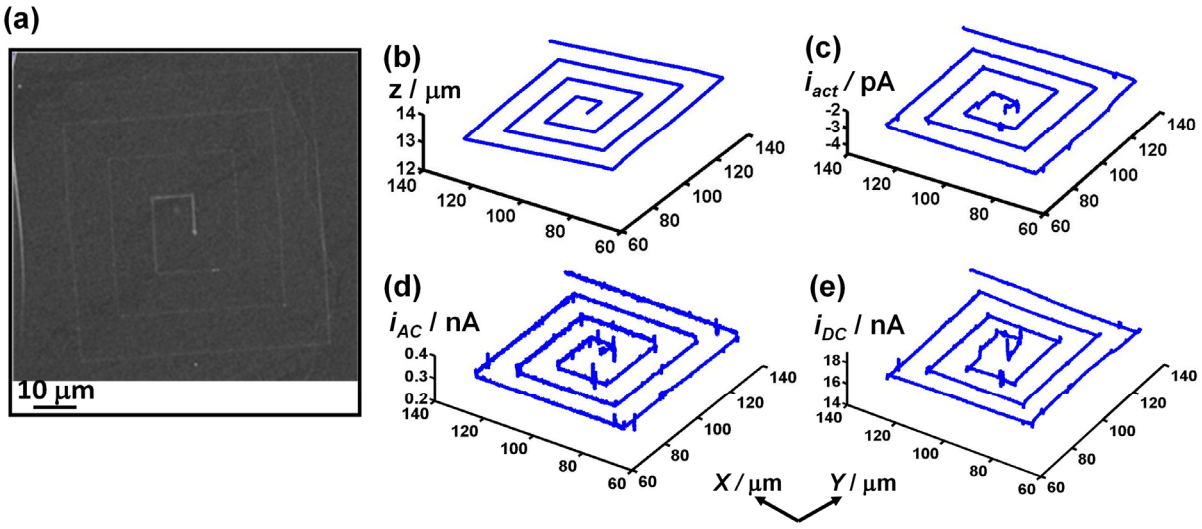

Figure 7. 6(a) A SEM image showing the deposited 2,6-AQDS line pattern on basal plane HOPG (AM). SECCM maps for: (b) topography; (c) surface activity; (d) AC component of conductance current used as feedback set point and (e) DC component of conductance current for the adsorption of 100 μM 2,6-AQDS during line patterning obtained with a 0.4 V bias between the pipet and substrate.

The SECCM surface activity map shows constant and continuous currents and where the electroactivity is essentially constant around 3.25 ± 0.10 pA (1 σ) over the entire probed area indicating uniform electroactivity of 2,6-AQDS throughout the patterning. If there was a

notable difference in the electroactivity of 2,6-AQDS at the basal plane vs. the edge plane, it would be expected that two peak distribution would be observed or a larger spread in surface activity. Small disturbances present in the surface activity map and in the corresponding AC feedback current and DC conductance current are due to small disturbances in the droplet size and surface interaction where the meniscus encounters multilayer or monolayer steps, nonetheless, these features are not significant.

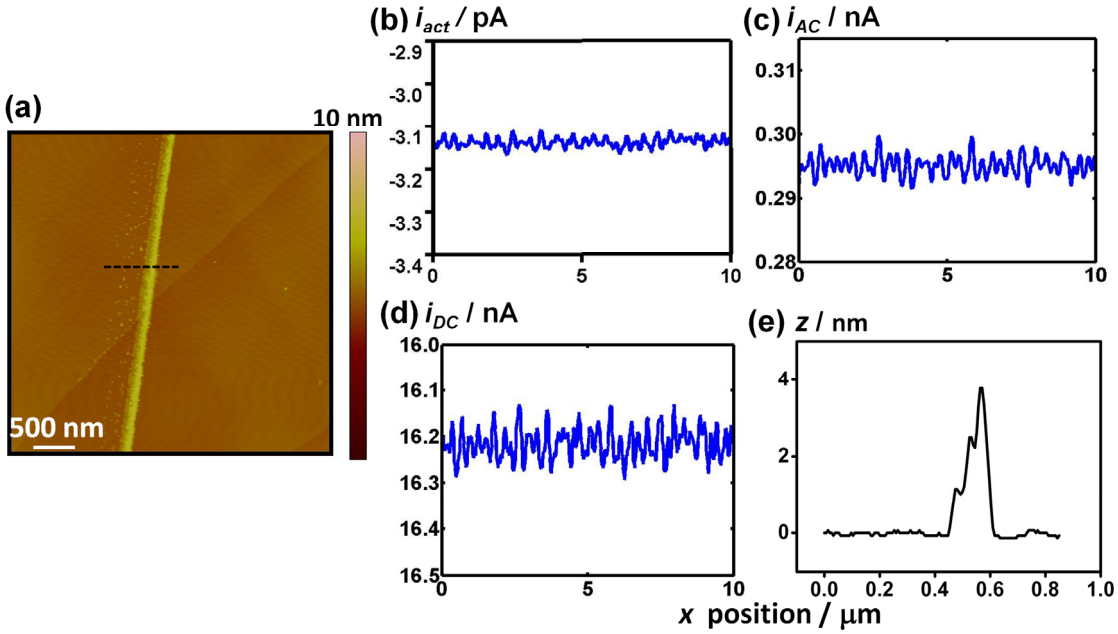

Figure 7. 7 (a) 3.3 × 3.3 μm AFM image showing a section of the pattern, along with the corresponding SECCM maps for: (b) topography; (c) surface activity; (d) AC component of conductance current used as feedback set point and (e) DC component of conductance current. (e) AFM cross section of area marked in figure (a).

AFM characterisation was also carried out on various sections of the line-pattern. Figure 7. 7(a) shows a 3.3 × 3.3 μm AFM image of the line-pattern in which the line of adsorbed 2,6-AQDS travels from a basal terrace over a step edge and onto another basal terrace. The corresponding SECCM maps are also shown in Figure 7. 7 for: (b) surface activity; (c) AC feedback current; (d) DC conductance current and (e) a cross section of the deposited line. The AFM cross-section shows the 2,6-AQDS line to be ~170 nm in width, which is the equivalent to the diameter of one of the pipet barrels. Next to the deposited line there is evidence of 2,6-AQDS particle adsorption from the second pipet barrel, which suggests that the 2,6-AQDS adsorption took place through just one of the pipet barrels rather than through both barrels, as observed in previous SECCM patterning.[22] This is most likely due to the large potential bias applied between the two QRCEs creating a large electric field across the two barrels, influencing the overall mass transport of species down the two barrels, as

explained in a simulation study.[30] Both barrels experience diffusion of species towards the electrodes surface but due to the electric field higher migration of negatively charged species, towards the electrodes surface, takes place under the barrel experiencing the lower potential but away from the electrodes surface under the barrel experiencing the higher potential. This leads to an asymmetry in the overall mass transport of species down the pipet and creates a compression of the concentration gradient under the barrel experiencing a lower potential; hence, a higher rate of adsorption/deposition is observed from one barrel compared to the other. A diagram depicting this effect is shown in Figure 7. 8.

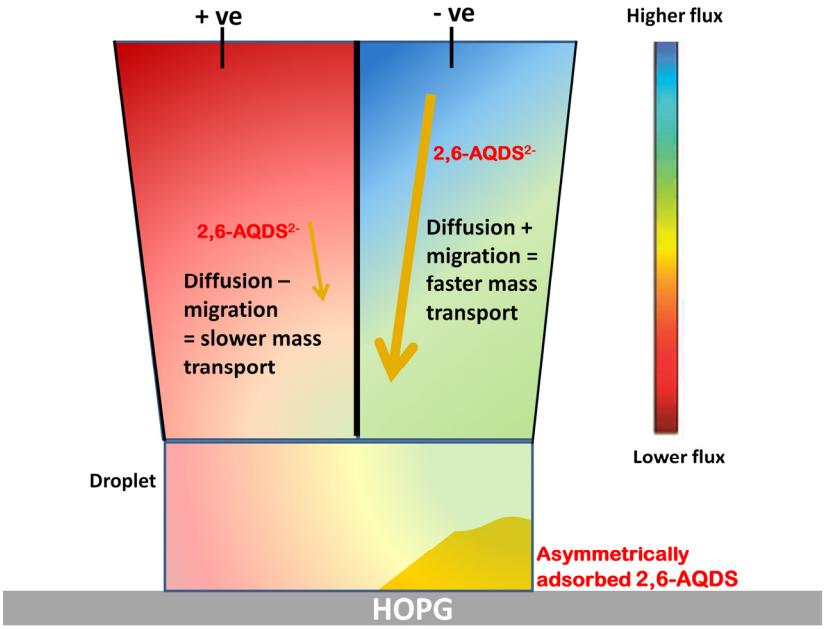

Figure 7. 8 Diagram describing the asymmetrical mass transport of species in the SECCM pipet.

As the SECCM patterning was carried out at a scan rate of 1 μm s^{-1} using a ~400 nm tip, the maximum contact time between the meniscus and the substrate equates to ~ 0.4 s. Macroscale scale voltammetry experiments showed maximum adsorption of 2,6-AQDS is observed on a time scale of 10 seconds, it is therefore clear that the adsorption process was not driven in the data presented in Figure 7. 6 and Figure 7. 7. The effect of increasing the adsorption time was explored by carrying out the same patterning experiment under the same conditions outlined above but at a slower scan rate of 0.2 μm s^{-1} with a tip size of ~800 nm, which corresponds to a maximum contact time between the meniscus and the substrate of 4 s. Figure 7. 9 shows (a) 10 × 10 μm AFM image of a section of the line-pattern with the corresponding SECCM maps (b) surface activity; (c) AC feedback current; (d) DC conductance current and (e) a cross section of the deposited line. It is clear from the AFM image that greater adsorption has occurred. The AFM cross-section shows the 2,6-AQDS line to be ~750 nm in width, equivalent to the diameter of the pipet, and up to 70 nm in

height. It is evident that at slower scan rates higher adsorption takes place and from both barrels.

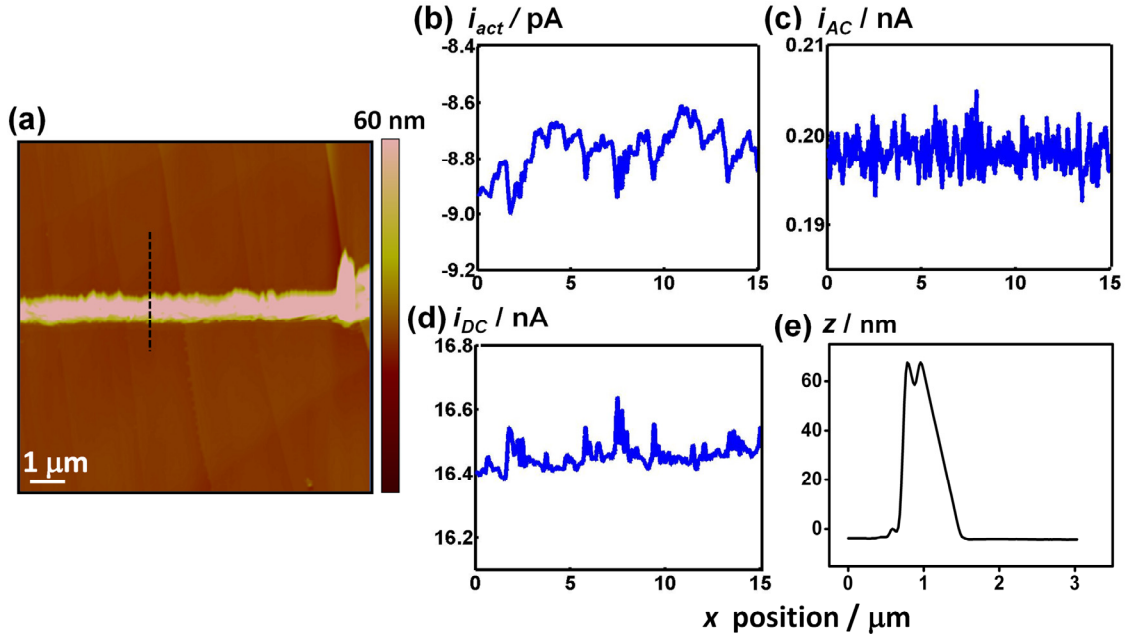

Figure 7. 9(a) 10 × 10 μm AFM image showing a section of the pattern, along with the corresponding SECCM maps for: (b) topography; (c) surface activity; (d) AC component of conductance current used as feedback set point and (e) DC component of conductance current. (e) AFM cross section of area marked in figure (a). For the adsorption of 100 μM 2,6-AQDS obtained with a 0.4 V bias between the pipet and substrate at a scan rate of 0.2 μm s^{-1}.

7.3 CONCLUSIONS

Several methods have been employed with the aim of determining for certain whether, or not, there is a correlation between the observed 2,6-AQDS adsorption and the step defect coverage present on basal plane HOPG. Macroscale voltammetry, presented herein, shows the observed 2,6-AQDS adsorption to be independent of the defect density present. Not only has the observed coverage and the actual coverage been shown to differ greatly but no evidence was found that could indicate a preferential adsorption of 2,6-AQDS at or around step defects. Nanoscale SECCM was employed to show unequivocally that, contrary to what has been proposed in the past literature, the adsorbed 2,6-AQDS material adsorbs and undergoes electron transfer at the basal plane. The data presented herein shows indisputably that 2,6-AQDS adsorption is not an indicator of the step defects present and that there is no correlation with the observed 2,6-AQDS adsorption coverage and step defect coverage present on basal plane HOPG.

7.4 REFERENCES

1. McCreery, R. L.,K. K. Cline,C. A. McDermott,M. T. McDermott, *Colloids Surf., A,* **1994,** *93,* 211-219.
2. McDermott, M. T.,K. Kneten,R. L. McCreery, *J. Phys. Chem.,* **1992,** *96,* 3124-3130.
3. Xu, J.,Q. Chen,G. M. Swain, *Anal Chem,* **1998,** *70,* 3146-3154.
4. Forster, R. J., *Langmuir,* **1995,** *11,* 2247-2255.
5. Liu, Y.,M. S. Freund, *Langmuir,* **2000,** *16,* 283-286.
6. Forster, R. J., *Anal. Chem.,* **1996,** *68,* 3143-3150.
7. Guin, P. S.,S. Das,P. C. Mandal, *International Journal of Electrochemistry,* **2011,** *2011,* 1-22.
8. He, P. X.,R. M. Crooks,L. R. Faulkner, *J. Phys. Chem.,* **1990,** *94,* 1135-1141.
9. Soriaga, M. P.,A. T. Hubbard, *J. Am. Chem. Soc.,* **1982,** *104,* 2735-2742.
10. Han, S. W.,S. W. Joo,T. H. Ha,Y. Kim,K. Kim, *J. Phys. Chem. B,* **2000,** *104,* 11987-11995.
11. Kano, K.,B. Uno, *Anal. Chem.,* **1993,** *65,* 1088-1093.
12. Zhang, J.,F. C. Anson, *J. Electroanal. Chem.,* **1992,** *331,* 945-957.
13. Edwards, M. A.,P. Bertoncello,P. R. Unwin, *J. Phys. Chem. C,* **2009,** *113,* 9218-9223.
14. McCreery, R. L.,M. T. McDermott, *Anal Chem,* **2012,** *84,* 2602-2605.
15. Lee, C.-Y.,S.-X. Guo,A. M. Bond,K. B. Oldham, *J. Electroanal. Chem.,* **2008,** *615,* 1-11.
16. Bowler, R.,T. J. Davies,M. E. Hyde,R. G. Compton, *Anal. Chem.,* **2005,** *77,* 1916-1919.
17. McDermott, M. T.,R. L. McCreery, *Langmuir,* **1994,** *10,* 4307-4314.
18. Davies, T. J.,R. R. Moore,C. E. Banks,R. G. Compton, *J. Electroanal. Chem.,* **2004,** *574,* 123-152.
19. Bradbury, C. R.,L. Kuster,D. J. Fermín, *J. Electroanal. Chem.,* **2010,** *646,* 114-123.
20. Robinson, R. S.,K. Sternitzke,M. T. Mcdermott,R. L. McCreery, *J. Electrochem. Soc.,* **1991,** *138,* 2412-2418.
21. Pharr, C. M.,P. R. Griffiths, *Anal. Chem.,* **1997,** *69,* 4673-4679.
22. Lai, S. C. S.,A. N. Patel,K. McKelvey,P. R. Unwin, *Angew. Chem. Int. Ed.,* **2012,** *51,* 5405-5408.
23. Niimi, Y.,T. Matsui,H. Kambara,K. Tagami,M. Tsukada,H. Fukuyama, *Phys. Rev. B.,* **2006,** *73*.
24. Kobayashi, Y.,K. Fukui,T. Enoki,K. Kusakabe, *Phys. Rev. B.,* **2006,** *73*.
25. Kobayashi, Y.,K. Kusakabe,K. Fukui,T. Enoki, *Physica E-Low-Dimensional Systems & Nanostructures,* **2006,** *34,* 678-681.
26. Nakada, K.,M. Fujita,G. Dresselhaus,M. S. Dresselhaus, *Physical review. B, Condensed matter,* **1996,** *54,* 17954-17961.
27. Ta, T. C.,V. Kanda,M. T. McDermott, *J. Phys. Chem. B,* **1999,** *103,* 1295-1302.
28. Neumann, C. C.,C. Batchelor-McAuley,C. Downing,R. G. Compton, *Chemistry,* **2011,** *17,* 7320-7326.
29. Bard, A. J.,L. R. Faulkner, *Electrochemical methods : fundamentals and applications*. 2nd ed.; John Wiley & Sons: 2001.
30. Snowden, M. E.,A. G. Güell,S. C. S. Lai,K. McKelvey,N. Ebejer,M. A. O'Connell,A. W. Colburn,P. R. Unwin, *Anal. Chem.,* **2012,** *84,* 2483-2491.

CHAPTER 8: ELECTROCHEMICAL DETECTION AND ANALYSIS OF SEROTONIN ON POLYCRYSTALLINE BORON DOPED DIAMOND (PBDD)

Oxygen-terminated pBDD with *in-situ* electrochemical AFM was used to study the state of the electrode surface and, for the first time, visualise the topographical changes associated with electrode fouling during the electrochemical oxidation of 5-HT. The surface of oxygen terminated pBDD was found to be highly susceptible to blocking by 5-HT by-products under conditions of continuous potential cycling. *in-situ* electrochemical AFM clearly evidences the formation of a thick film of 5-HT by-products block the surface from extensive cycling, the film readily desorbs or dissolves off the electrode surface. Using various voltammetry techniques, such as performing voltammetry at fast scan rates and through the inclusion of a preconditioning step, the degree to which the electrode is blocked was found to be significantly minimised. With the use of metal electro-deposition and various outer-sphere redox mediators, as well as with C-AFM, the electrochemical properties of films formed during 5-HT oxidation were identified as being charged and permeable / porous in nature. It is shown herein, the film is able to act as a charge excluder facilitating the electrochemistry of negatively charged species and limiting the electrochemistry of positively charged species to the pin holes in the film.

8.1 INTRODUCTION

Serotonin, also known as 5-hydroxytryptamine (5-HT), is an electrochemically oxidisable neurotransmitter, which plays a key role in numerous physiological processes, such as depression, thermoregulation, liver regeneration, cardiovascular function and irritable bowel syndrome.[1-3] As 5-HT can be oxidised electrochemically with an onset potential of *ca.* 0.4 vs. Ag/AgCl (at physiological pH),[2, 4-5] detection and monitoring of 5-HT levels using electrochemical techniques has received considerable attention. Early research into the oxidation process of 5-HT found it to involve a two-electron two-proton transfer mechanism, during which reactive side-products and dimers are formed at the electrode surface. These reactive products have been reported to adsorb onto the electrode surface forming an insoluble polymer-like by-product.[6-9]

The electrochemical blocking of electrodes during 5-HT oxidation is reported to be irreversible and the polymeric by-products are believed to have electrically insulating

properties.[10-12] However, no direct measurement on the electrical conductivity of the by-products have been reported. The properties of the polymer film which forms during oxidation is not entirely known; however similar melanin-like films have been shown to display a resistance towards charge and mass transfer.[13] As outlined in Figure 8. 1, one can hypothesise that the 5-HT oxidative products could polymerise to form a film of at least four different morphologies: (a) a continuous film that completely blocks electron transfer; (b) a continuous but porous film that allows diffusion of species towards the electrode surface; (c) as nucleated particles that only partially block the electrode surface; or (d) the film that forms can be electrically conducting.

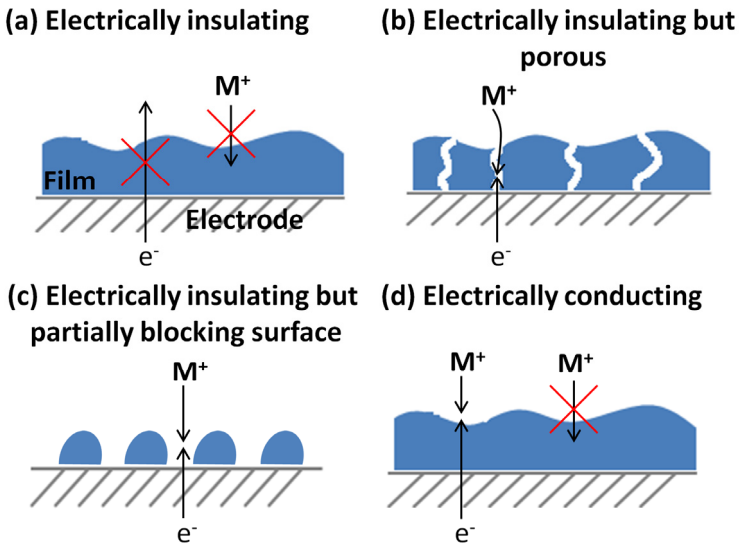

Figure 8. 1 Diagrams showing different scenarios for how the 5-HT oxidative products could polymerise on the electrode surface and affect electrochemical reactions. (a) Full coverage of the electrodes surface occurs where the insulating film prevents electron transfer and is impermeable to the redox couple. (b) The electrically insulating film is porous allowing tunnelling of redox couple to the electrode surface where electron transfer can take place. (c) The insulating film form as particles, partially blocking the electrode surface. (d) Full coverage of the electrode surface occurs with an impermeable film that is conducting, allowing electron transfer to take place.

When studying the electrochemistry of neurotransmitters, it is advantageous to use carbon-based electrodes due to their biocompatibility[14] and, hence, the potential for *in-vivo* applications.[9, 12, 15] The use of carbon-based electrodes is also advantageous due to the low cost, availability, chemical stability and wide potential window compared to metal electrodes. Research into the detection of 5-HT has employed carbon fibre electrodes,[16-17] glassy carbon (GC),[18-19] highly ordered pyrolytic graphite (HOPG), [20]carbon nanotubes (CNT) [5, 21] and polycrystalline boron doped diamond (pBDD).[22-23]

The use of conducting diamond electrode is of particular interest, due to the superior properties the electrode possesses over more traditional carbon and metal electrodes, including a wide solvent window, robustness and a resistance to surface fouling.[24-26] Organic molecules have a tendency to irreversibly adsorb on the more commonly employed sp^2 containing carbon electrodes, such as carbon fibre, glassy carbon and graphite, and thus can be readily and irreversibly become passivated, impairing further electrochemical detection.[11, 14, 27-29] As high quality conductive diamond electrodes are sp^3 in nature, adhesion of biomolecules and/or organic molecules does not take place as easily, leading to an increased resistance to fouling, which could be highly advantageous in the detection of neurotransmitters. The surface termination of diamond is also considered to affect the tendency of diamond electrodes towards fouling; in particular minimising oxygen-containing functional groups present at the surface are believed to be of benefit in inhibiting fouling.[9, 22, 30-31] On the other hand, oxygen-terminated surfaces are more stable and easier to prepare compared to hydrogen-terminated surfaces.[32-34]

The use of fast scan voltammetry and preconditioning steps also reduces electrode fouling. For example, by carrying out fast scan voltammetry, the side-reactions that take place can be outrun, driving the oxidation of 5-HT but at the same time minimising the formation of fouling products.[11-12] Fouling can be further reduced by carrying out preconditioning steps, e.g. by holding the electrode at high anodic/cathodic potentials between voltammetric scans. [11-12]

Various techniques can be used to characterise the electrochemical properties of films and the effect they have on the electron transfer kinetics of an electrode. Inner and outer-sphere redox couples have been used in the past to study the effect on electron transfer of surfaces modified with films of aromatic organic compounds on the diffusion and electron transfer kinetics.[27, 29, 35] Conducting AFM (C-AFM) has been used to characterise quantitatively the conductivity of thin films on electrodes.[36-38]

In this chapter oxygen-terminated pBDD is used with *in-situ* electrochemical AFM to study the state of the electrode surface and, for the first time, visualise the topographical changes associated with electrode fouling during the electrochemical oxidation of 5-HT. Various techniques for preventing/minimising electrode fouling are investigated as well as the electrochemical properties of films formed during 5-HT oxidation using metal electro-deposition and various outer-sphere redox mediators, as well as with C-AFM.

8.2 ELECTROCHEMICAL MEASUREMENTS

It is has been well established that, during the oxidation of 5-HT, by-products are formed at the electrode surface which lead to the irreversible blocking of electrochemical activity.[9] This process has not been examined in detail at pBDD and so to investigate the extent of this fouling on pBDD consecutive CVs were recorded. Figure 8. 2 shows CVs carried out at 30-second intervals for the oxidation of 0.5 mM 5-HT in supporting electrolyte at 0.1 V s^{-1}. A noticeable decrease in the peak current of ca. 13% is observed after the first cycle, which further decreases with each cycle until a constant response is observed (Figure 8. 2). This behaviour is synonymous with fouling of the electrode surface. After 20 cycles, the peak current decreases by over ca. ~ 40% compared to the initial scan. Furthermore, a clear shift positive in the peak current and the onset potential for each successive CV is observed, indicating increasing kinetic resistance.

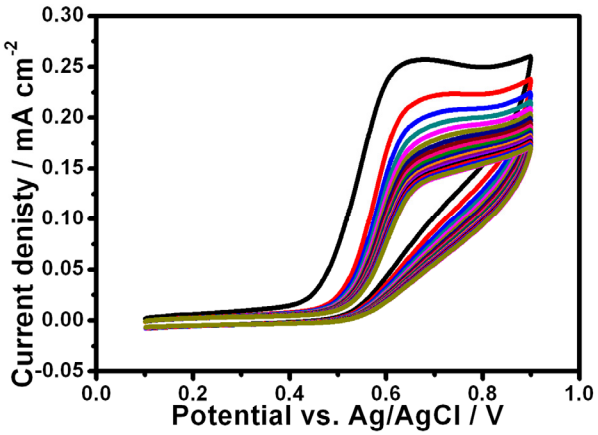

Figure 8. 2 CVs for the repetitive cycling for the oxidation of 0.5 mM 5-HT on pBDD.

Various electrochemical procedures were explored that might minimise this fouling effect. The first was the inclusion of an electrochemical preconditioning step between each repetitive cycle, where the working electrode was held at -1.0 V for 30 seconds. In the second procedure, after scanning to +0.8 V to oxidise 5-HT, the potential was scanned back to -0.6 V rather than +0.1 V (as was the case for the data in Figure 8. 2). By applying such cathodic potentials, we can consider that the amount of oxidation products at the electrode surface might be diminished. Finally, faster scan voltammetry was used, which might reduce the extent of electrode blocking by turning over the redox couple at a rate faster than the competing polymerisation reaction. The CVs were recorded at 1 V s^{-1}, comparing with and without an electrochemical preconditioning step between the cycles. The results of these procedures are summarised in Figure 8. 3, where the forward peak current normalised to the peak current of the first scan for each of these procedures has been plotted.

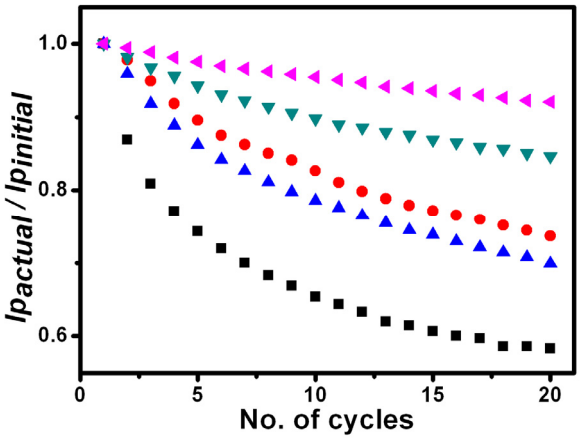

Figure 8. 3 A plot showing the change in peak current for repetitive cycling experiments with pBDD in 0.5 mM 5-HT where different techniques were used to prevent surface fouling where employed. (a) cycling at 30 sec intervals at 0.1 V s^{-1} with no preventative technique employed(■); (b) an electrochemical preconditioning step was employed where the electrode is held at -1 V for 30 sec between each cycle run at 0.1 V s^{-1} (●); (c) cycling at 30 sec intervals between a wider potential window of -0.6 V to 0.8 V run at 0.1 V s^{-1} (▲); cycling at 30 sec intervals at a faster scan rate of 1 V s^{-1} (▼); (d)cycling at 30 sec intervals at a faster scan rate of 1 V s^{-1} with an electrochemical preconditioning step where the electrode is hold at -1 V for 30 sec between each cycle (◀).

Each procedure was found to reduce the extent of electrode fouling compared to the data in Figure 8. 2, but to different extents. Scanning to a more cathodic potential or preconditioning the electrode at a cathodic potential, appears to decrease the overall blocking effect presumably by driving any adsorbed species from the surface. Performing voltammetry at a faster scan rate also significantly reduced the extent to which the electrode surface was blocked: after performing 20 cycles there is only *ca.* ~ 10% decrease in the observed peak current (Figure 8. 3). This is due to competition between the rate at which side-reactions take place that block the electrode and the electrochemical redox process for 5-HT. Scanning faster drives the oxidation/reduction of 5-HT, outrunning the rate at which fouling products adsorb and polymerise on the electrode surface. When a preconditioning step was included between each cycle, a further improvement in the extent of fouling was observed, where the peak current decreased by *ca.* ~ 5% after performing 20 voltammetric cycles. These investigations show that fouling of the pBDD surface with 5-HT by-products can be significantly reduced and controlled.

8.3 IN-SITU ELECTROCHEMICAL AFM

In order to elucidate the fouling process in more detail, the surface of the electrode was studied using *in-situ* electrochemical AFM whilst performing the electrochemical studies. Figure 8. 4 shows images of the pBDD surface: (a) before potential cycling; (b) after 5 cycles;

(c) after 10 cycles; (d) after 20 cycles; in 0.5 mM 5-HT at 0.1 V s^{-1}. After 5 cycles the presence of a film is hardly observable in the height image, however, after 10 cycles the formation of a film can be seen distinctly. After 20 cycles, the entire surface appears to be completely covered by a film.

An enhanced AFM image of the film suggests it could be formed by the coalescence of particles. The thickness of the film was estimated by re-engaging on the surface in contact mode and 'scratching' through the film, as shown in Figure 8. 4 (f). Thicknesses of 5.0 ± 0.5 nm (low) and 8.0 ± 0.1 nm (high) were in the differently doped grain areas, after 20 potential cycles. Cross-sections taken on the same area (marked in Figure 8. 4(a)) show the build of the film as a function of cycling, where a greater growth of the film by ~3 nm is clearly evident on a lower-lying grain (by ~0.5 nm). As the working electrode is polycrystalline, the sample contains different grains, some of which contain more boron content than others and therefore are more conducting.[39] The *in-situ* data shows faster growth of the film on the more conducting grains (as confirmed by FE-SEM).[39] During *in-situ* imaging some parts of the film were found to 'disappear' after re-imaging (Figure 8. 5), evidencing for either desorption or dissolution of the film.

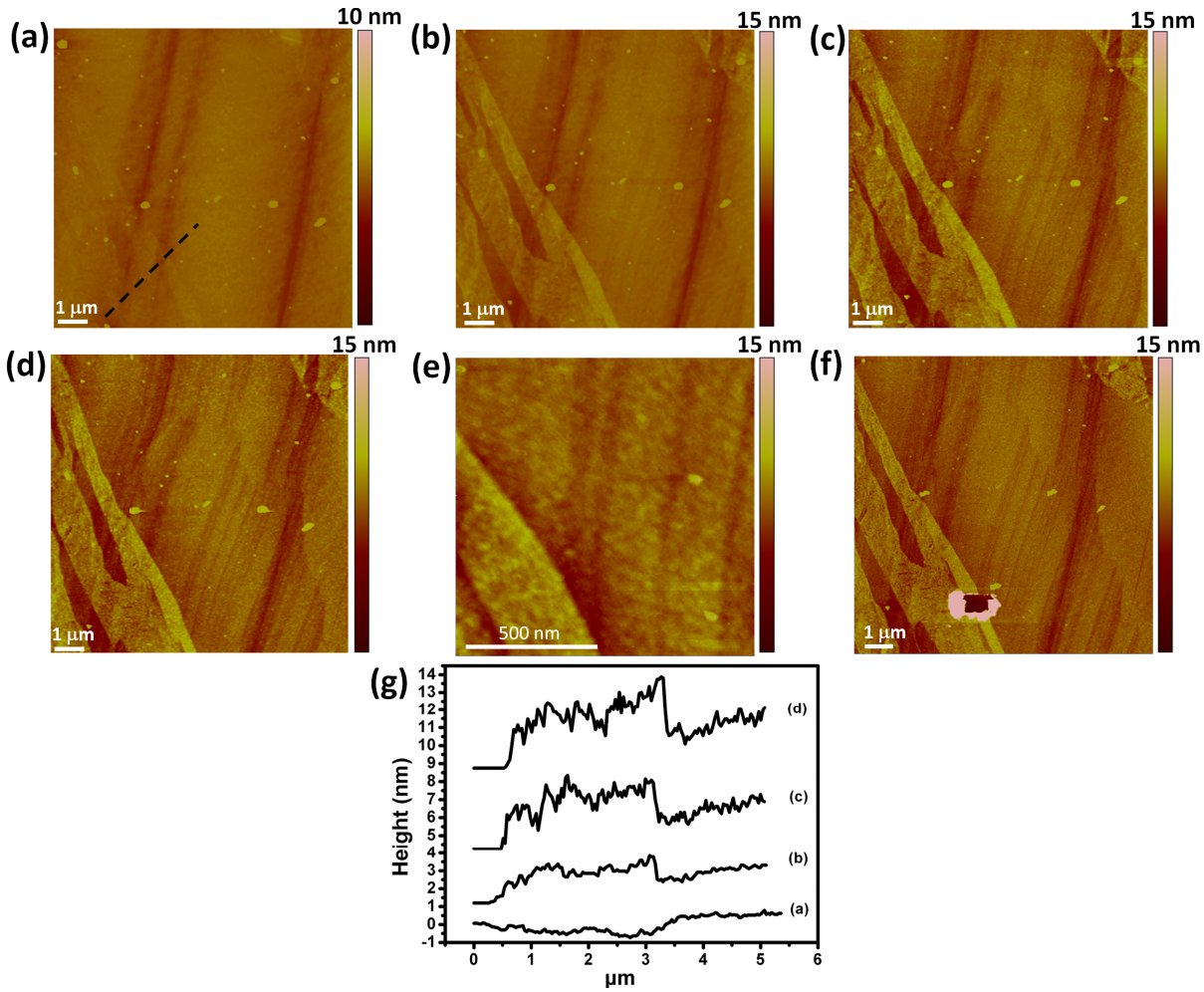

Figure 8. 4 10 × 10 μm *in-situ* AFM images of the pBDD surface in 0.5 mM 5-HT where the electrodes potential was cycled at 30 second intervals. (a) before potential cycling; (b) after 5 potential cycles; (c) after 10 potential cycles and (d) after 20 potential cycles between 0.2 V and 1 V at 0.1 V s^{-1}. (e) A 500 x 500 nm zoom of (d). (f) After scratching through a small part of the film by engaging in contact mode AFM whilst still in *in-situ.* (g) Cross sections of the area marked in (a) for each *in-situ* image to show the growth of the film as a function of potential cycling.

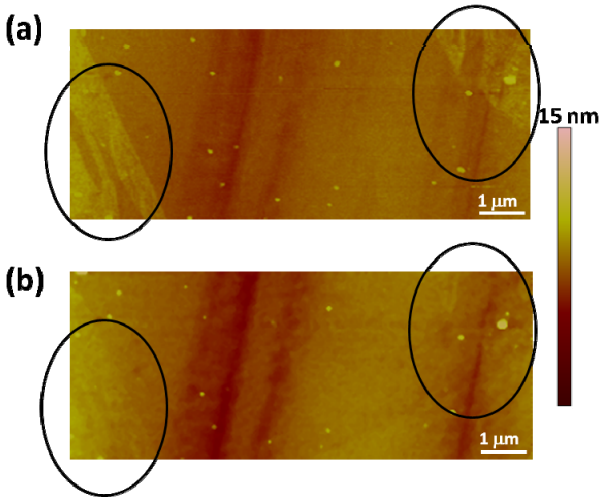

Figure 8. 5 10 × 4 µm in-situ AFM images of the pBDD surface in 0.5 mM 5-HT where (a) 5 potential cycles had been carried out and (b) site immediately re-imaged without any further electrochemistry applied.

The *in-situ* electrochemical studies were repeated for the various electrochemical procedures aimed at minimising fouling, as outlined above. Figure 8. 6 shows *in-situ* data for when the electrode was preconditioned between each cycle by holding the potential at -1 V for 30 seconds. Figure 8. 7 shows *in-situ* data for when the electrode was cycled at a faster scan rate of 1 V s^{-1}. For both procedures *in-situ* imaging was carried out: (a) before potential cycling; (b) after 5 cycles; (c) after 10 cycles; (d) after 20 cycles; and (e) after 30 cycles in 0.5 mM 5-HT. For these studies (Figure 8. 6 and Figure 8. 7), complete surface blocking was not evident after 20 cycles as seen for Figure 8. 3 so further cycling of the electrodes potential was performed until no change in the voltammetry was observable. In both case a film can still be seen to grow on the electrode surface in layers that form over another, as seen before in Figure 8. 5, but the extent to which the film forms is reduced, as indicated by CV data (Figure 8. 3). In Figure 8. 7, where the electrode was cycled at a faster scan rate of 1 V s^{-1}, the presence of a film is hardly noticeable after 20 potential cycles and only just evident after 30. The thicknesses of the film was obtained for both electrochemical procedures by scratching into the film: Figure 8. 6(f) shows the film to be 4.0 ± 0.3 nm (low) and 6.5 ± 0.2 nm (high); and Figure 8. 7(f) shows the film to 3.7 ± 0.2 nm (low) and 5.6 ± 0.2 nm (high). Cross sections for both procedures (Figure 8. 6(g) and Figure 8. 7(g)) show a slower growth in the film on the lower-lying grain compared to Figure 8. 4(g). The *in-situ* studies visually show the electrochemical procedures reduce the extent to which the electrode surface is blocked.

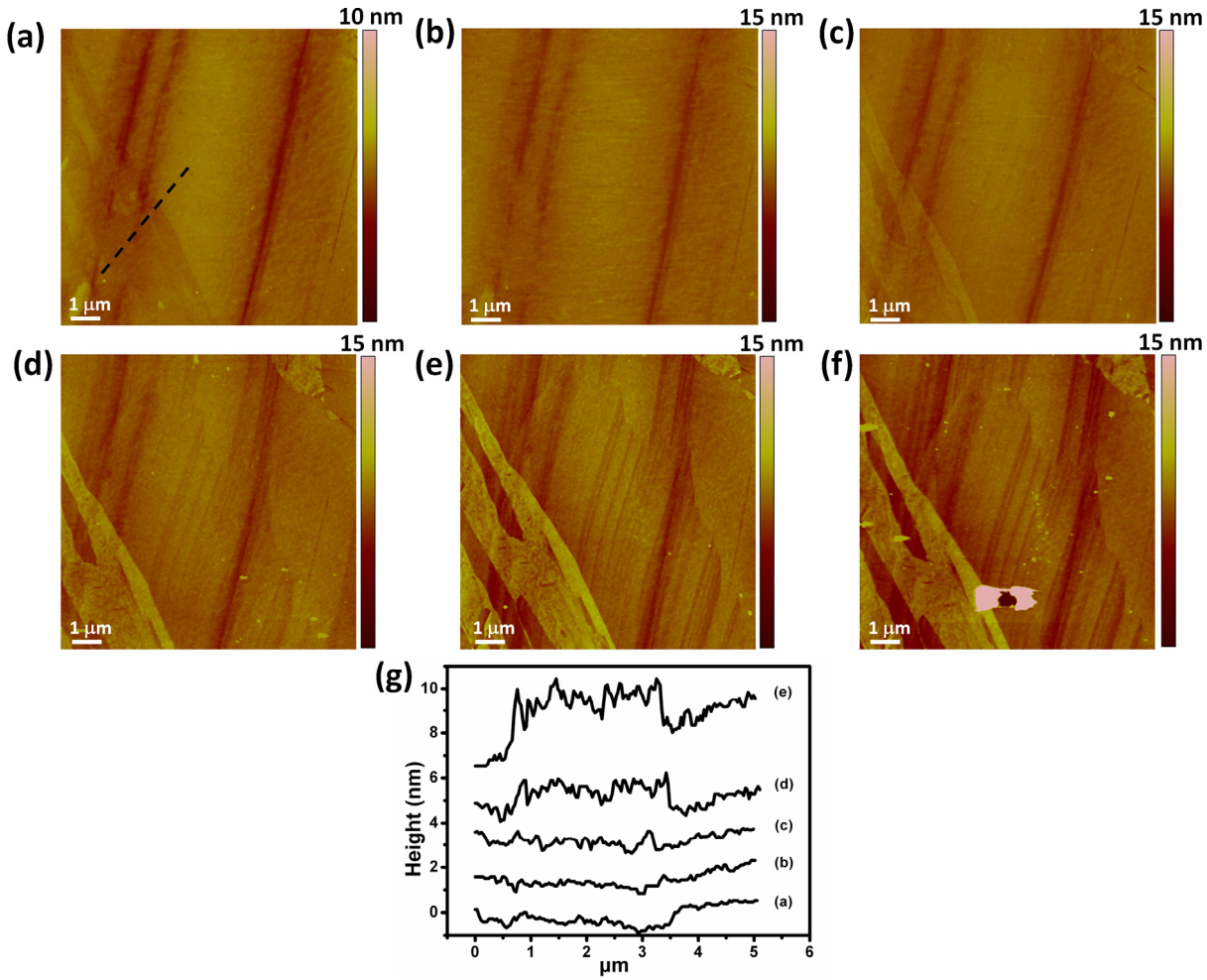

Figure 8. 6 10 × 10 μm *in-situ* AFM images of the pBDD surface in 0.5 mM 5-HT where the electrode is held at -1 V for 30 sec between each cycle. (a) before potential cycling; (b) after 5 potential cycles; (c) after 10 potential cycles; (d) after 20 potential cycles and (e) after 30 potential cycles, over a potential window of 0.2 V and 1 V at 0.1 V s^{-1}. (f) After scratching through a small part of the film by engaging in contact mode AFM whilst still in *in-situ.* (g) Cross sections of the area marked in (a) for each in-situ image to show the growth of the film as a function of potential cycling.

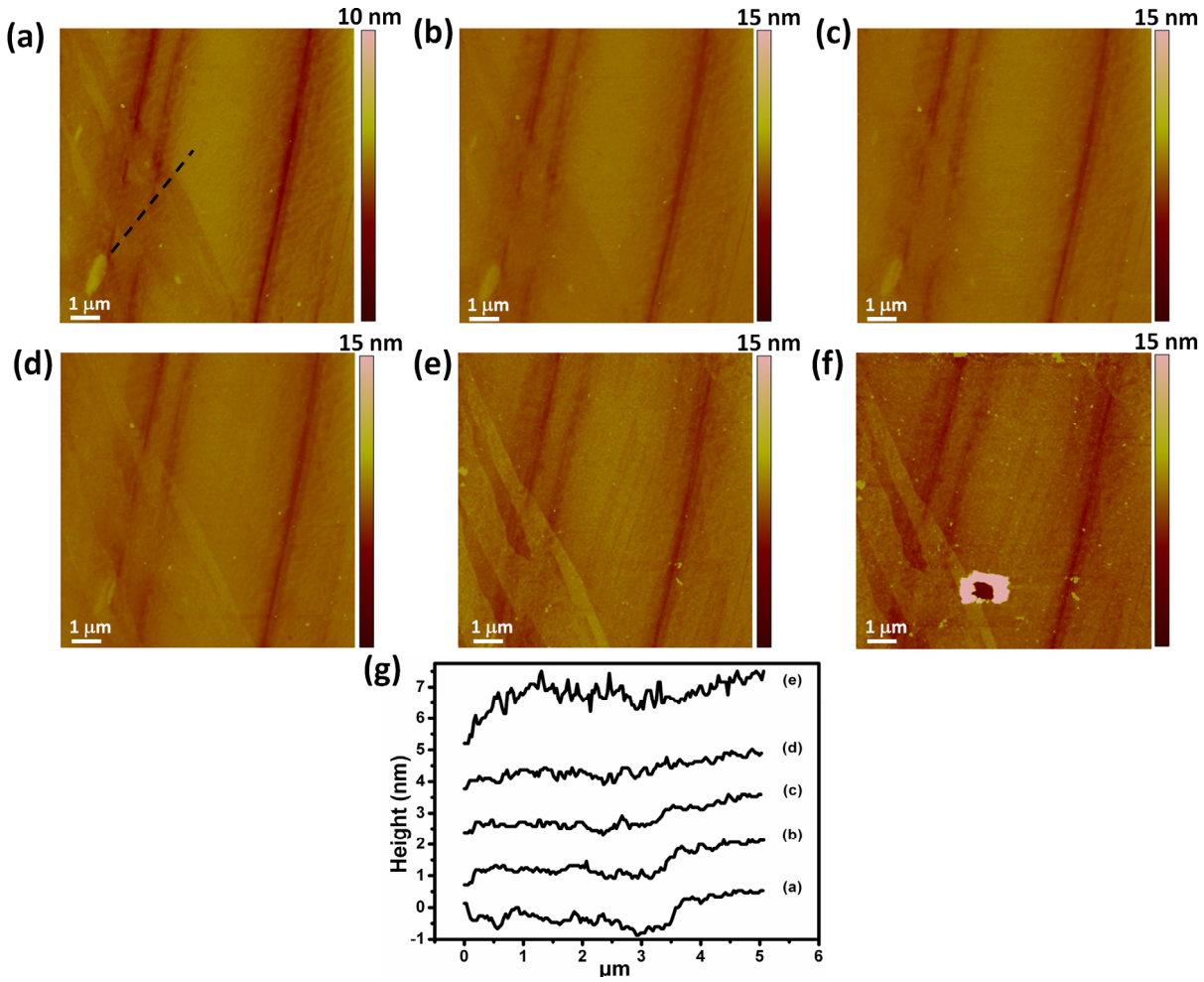

Figure 8. 7 10 × 10 μm *in-situ* AFM images of the pBDD surface in 0.5 mM 5-HT where the electrode was cycled at 30 second intervals at a faster scan rate of 1 V s^{-1}. (a) before potential cycling; (b) after 5 potential cycles; (c) after 10 potential cycles; (d) after 20 potential cycles and (e) after 30 potential cycles, over a potential window of 0.2 V and 1 V. (f) After scratching through a small part of the film by engaging in contact mode AFM whilst still in *in-situ.* (g) Cross sections of the area marked in (a) for each *in-situ* image to show the growth of the film as a function of potential cycling.

8.4 FILM STABILITY AND GRAVITATIONAL EFFECTS

The stability of the "fouling" film on the pBDD surface was investigated by cycling the electrode, until no change was observed in the voltammetry (25 cycles with no pre-treatments), and then leaving it at open circuit for 1 minute before performing another cycle. Figure 8. 8(a) shows that after severely blocking the pBDD electrode (facing down) but then waiting 60 seconds, the recorded CV shows an astonishing *ca.* ~99% recovery in the observed peak current and CV profile. The data indicates the adsorbed products fouling the electrode must either rapidly desorbs from the surface or dissolves back into bulk solution (or possibly both).

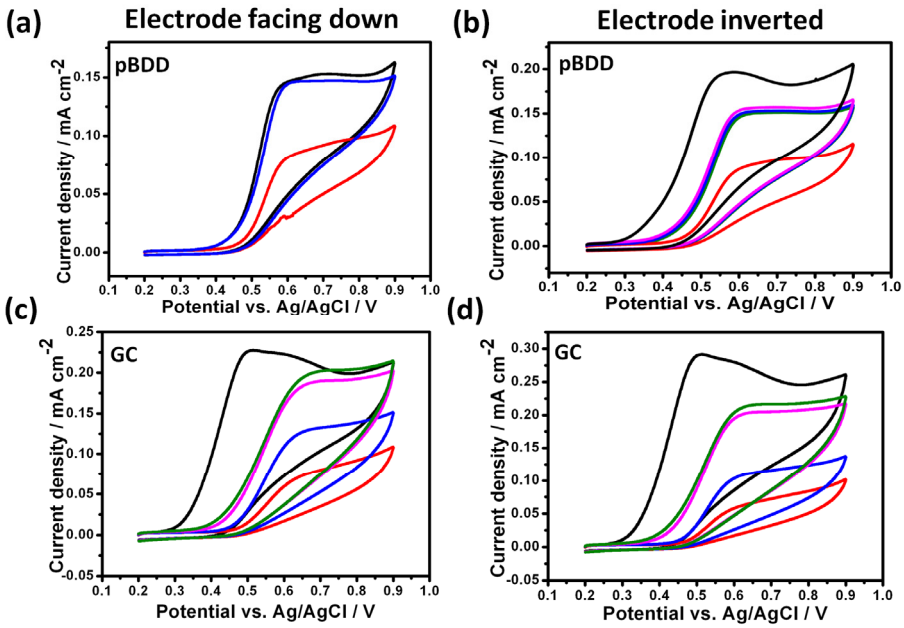

Figure 8. 8 Voltammograms run in a solution of 0.5 mM 5-HT where the electrode, either pBDD or GC was facing down or inverted to face up, where a CV was recorded: immediately after immersing a clean electrode (black); after 20 potential cycles (red); after having completely blocked the electrode by carrying out 20 potential cycles and then waiting 1 minute (blue), 10 minutes (pink), and 30 minutes (green). All CVs run at 0.1 V s^{-1}.

To see if the desorption was an affect of gravity or related to the properties of the electrode, the same experiment was performed but with the electrode inverted (i.e. electrode facing up) and mounted inside a cell that can hold at least 10 mL solution. Figure 8. 8(b) shows that when inverted, the pBDD electrode becomes more blocked than when the electrode is facing down, but when left for 60 seconds before performing another cycle, the electrode makes a *ca.* ~ 80% recovery in the observed peak current. Even after waiting for 30 minutes full recovery of the electrodes signal was not possible, indicating both the electrode material and electrode orientation has a large effect on the rate at which the desorption/dissolution of the fouling products occurs. Note, these observation are not directly comparable to the *in-situ* electrochemical AFM experiments as the imaging was carried out in a set-up where a small amount of solution was present above the electrode surface creating a saturated environment, unfavourable towards dissolution.

These experiments were also carried out using a glassy carbon (GC) electrode, where the electrode was orientated to face downwards (Figure 8(c)) and inverted to face upwards (Figure 8. 8(d)). Figure 8. 8(c) and Figure 8. 8(d) both show that the electrodes signal could not be fully recovered. When the pBDD was oriented to face downwards a ~99% recovery in the electrodes current was observed; however for GC, even after waiting 30 minutes only ~90% of the current signal was recovered. Figure 8. 8(d) shows after waiting 30 minutes at

least ~77% of the electrodes current signal was recovered, which is only slightly less than that observed for pBDD. This shows there are gravitational effects on the desorption/dissolution of the film and that the surface properties of the electrode material also play apart. As discussed in the Introduction, within literature it has been seen that irreversible blocking occurs on sp^2 carbon electrodes, which includes GC,[11, 14, 22] and that the surface of conducting diamond is reported by many to resistant towards adsorption due to the sp^3 carbon structure.[22, 29, 31] Although adsorption is observed here, it is readily reversed, unlike for GC.

8.5 EFFECT OF FILM PROPERTIES ON ELECTRON TRANSFER

In the literature the films formed are often referred to as insulating.[10-12] To probe whether this is the case or not, the effect the film has on electron transfer were investigated by electrodepositing Ag from a solution containing 1 mM $AgNO_3$ in 1 M KNO_3 by applying a potential of -0.2 V vs. Ag/AgCl for 60 seconds with a clean pBDD electrode (Figure 8. 9) and on a pBDD electrode containing the 5-HT film (grown by running 20 CVs, Figure 8. 10). The FE-SEM images show that on a clean surface of pBDD the Ag particles have preferentially deposited on the higher doped grains, where ET is more facile, as seen previously.[40-41] This is expected for the heterogeneously doped BDD electrode surface where the conductivity of the grains varies.[39-41] In the presence of the 5-HT film, a much more uniform deposition is observed. Figure 8. 9 shows that the particles no longer preferentially decorate the higher doped grains, as shown by the in-lens FE-SEM image (Figure 8. 9(b)) that enables the visualisation of grains with different boron dopant levels. The lighter grains are of higher conductivity. It can be seen that the Ag nanoparticles have now deposited uniformly across the surface independent of the boron uptake of the grains. This is an indication that the film may create a 'mask' to the underlying substrate, allowing electron transfer to take place but creating a homogenous electrode surface or that the film possess pinholes, creating sites for which electron transfer is possible.

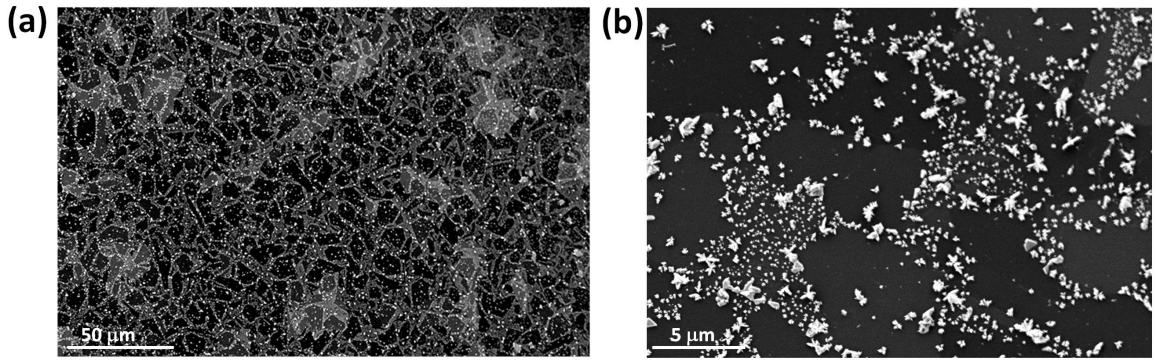

Figure 8. 9 FE-SEM 250 μm (a) secondary lens and (b) in-lens image and a 30 μm secondary lens enhanced image (c) showing the deposition of 1 mM $AgNO_3$ in 1 M KNO_3 by applying a potential of -0.2 V vs. Ag/AgCl for 60 seconds on a pBDD surface with a 5-HT film first deposited by running 20 repetitive CVs in 0.5 mM 5-HT at 0.1 V s^{-1}.

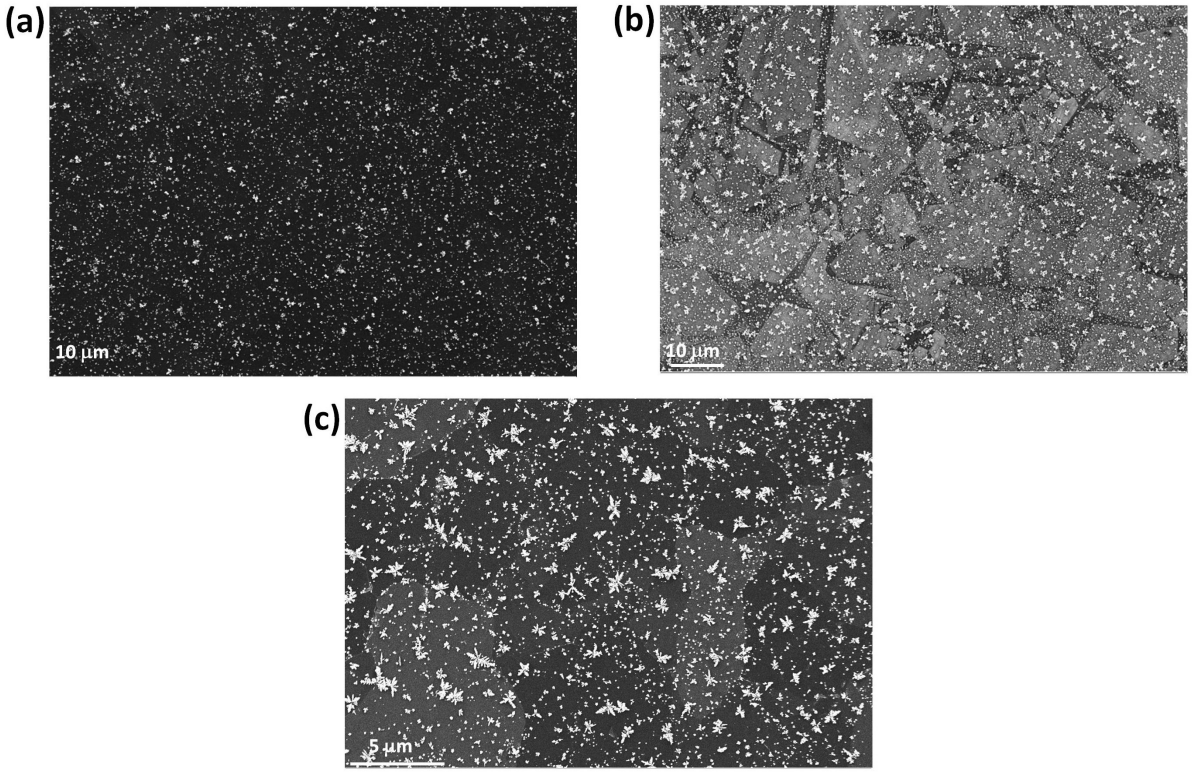

Figure 8. 10 FE-SEM 250 μm (a) secondary lens and (b) in-lens image and a 30 μm secondary lens enhanced image (c) showing the deposition of 1 mM $AgNO_3$ in 1 M KNO_3 by applying a potential of -0.2 V vs. Ag/AgCl for 60 seconds on a pBDD surface with a 5-HT film first deposited by running 20 repetitive CVs in 0.5 mM 5-HT at 0.1 V s^{-1}.

8.6 EFFECT ON VARIOUS MEDIATORS

After completely blocking the pBDD surface by running 20 - 30 potential cycles with 0.5 mM 5-HT, the electrode was immersed into various solutions containing different mediators of

different charges in order to investigate the charge state of the film, see Table 1. In the case of $Fc(CH_3OH)^0$ a decrease in peak current and an increase in ΔE_p is observed, which indicates partial blocking of the electrode. For $FcTMA^{+/2+}$ the CVs shows a more enhanced affect, Figure 8. 11(a), after 30 cycles in 5-HT the CV for $FcTMA^{+/2+}$ begins to resemble a steady state response, which is indicative of a partially blocked electrode with a large coverage of widely spread 'microscopic active sites'.[42]

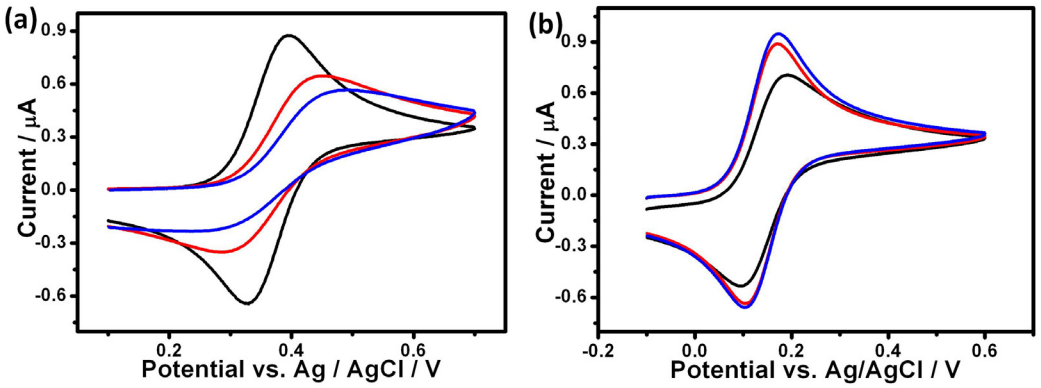

Figure 8. 11 CVs for (a) the oxidation of 1 mM $FcTMA^+$ and (b) 1 mM $Fe(CN_6)^{4-}$ run with: a clean pBDD electrode surface (black); after blocking electrode by running 20 (red) and 30 (blue) potential cycles in 0.5 mM 5-HT at 0.1 V s^{-1}.

This is this observation is further enhanced when the pH is increased from 5 to 8.8. For $Fe(CHOOH)^{-/0}$ an improvement in the voltammetry was observed, where the peak current increased and ΔE_p become more reversible (Table 8.1). This observation become more pronounced for $Fe(CN_6)^{4-/3-}$, which provides quasi-reversible voltammetry on bare pBDD, however, when the electrode has been modified with the 5-HT film, voltammetry becomes more reversible and the peak current increases, Figure 8. 11(b), the observation is further enhanced when the pH is decreased from 5 to 3. This data suggests that the film blocks electrochemistry for positively charged mediators but promotes the electrochemistry for negatively charged mediators and that the higher the charge on the mediator the greater affect. The observation fits in with previous studies, which identified the fouling by-products and suggested they possess positive charges,[7-8] hence, if the film formed possess a charge it would be expected to be an overall positive charge.

Table 8. 1 Outline of the affect of the 5-HT film on the electrochemistry of different redox mediators varying in charge.

Mediator	Initial		After 20 cycles		After 30 cycles	
	ΔE_p (mV)	I_p (µA)	ΔE_p (mV)	I_p (µA)	ΔE_p (mV)	I_p (µA)
$FcTMA^+$	62	0.855	165	0.597	n/a	0.484
Ferrocyanide	96	0.700	69	0.848	68	0.900
Ferrocene methanol	82	0.810	140	0.606	159	0.604
Ferrocene monocarboxylic acid	78	0.324	73	0.377	-	-

8.7 ELECTRICAL PROPERTIES OF THE FILM

To determine the film was insulating, C-AFM was carried out to map the conductivity of clean pBDD and pBDD with the 5-HT film, grown by SECCM patterning. Using a conductive AFM tip, a potential of 0.5 V was applied to the electrode surface, with a 1 MΩ resistor in series. Figure 8. 12(a) shows the topography (i) and conductivity (ii) map in which the deposited 'S' shape of oxidised 5-HT is clearly visible. *i*-V curves were taken on areas marked in Figure (ai) on the clean pBDD surface (1) and on the deposited film (2) and is shown in Figure 8. 12(b). The local resistance (*R*) values were extracted at regions of low bias (*i.e.* 0.1 V), on the pBDD surface (curve 1) R = 1.2 MΩ. A cross section of the conductivity map, marked in Figure (aii), shows the zero current is measured over the film, clearly showing the film is insulating.

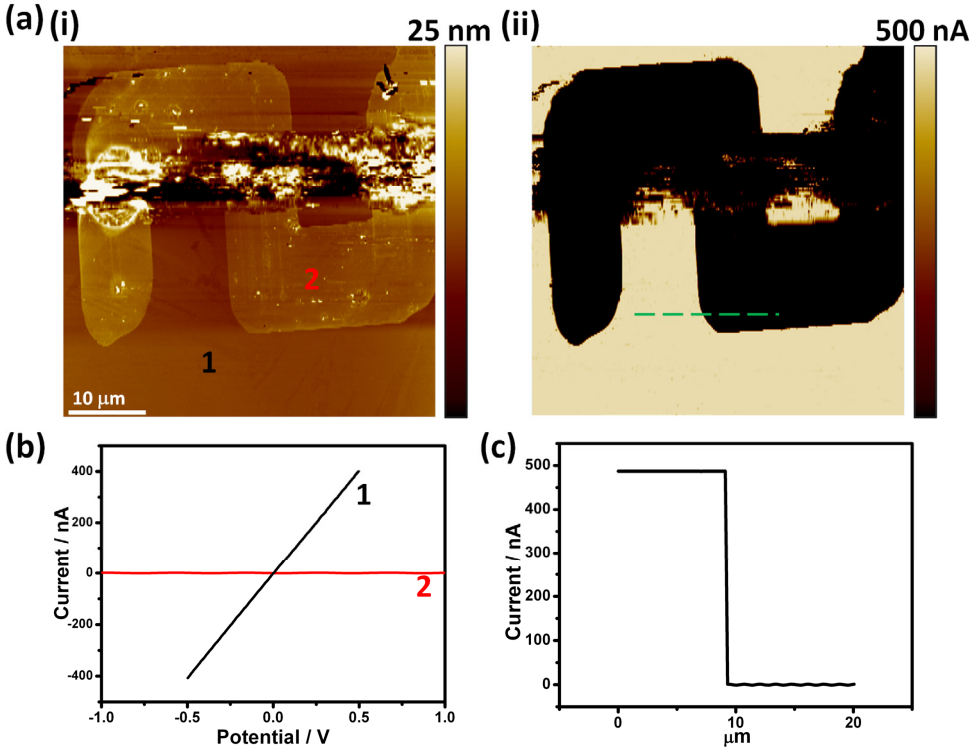

Figure 8. 12(a) Simultaneously recorded 45 × 45 µm topography (i) and conductivity (ii) maps of pBDD surface after pattern deposition of 0.5 mM 5-HT. (b) C-AFM i-V curves recorded in locations 1 and 2 marked on (ai). (c) Cross section of the of conductivity map of area marked in green on (aii).

8.8 CONCLUSIONS

The surface of oxygen terminated pBDD is highly susceptible to blocking by 5-HT by-products under conditions of continuous potential cycling. It is clear, however, that although a thick film of 5-HT by-products block the surface from extensive cycling, the film readily desorbs or dissolves off the electrode surface. The degree to which the electrode is blocked can be significantly minimised by performing voltammetry at fast scan rates and through the inclusion of a preconditioning step, the degree of blocking is further minimised. The 5-HT film which forms must be charged and permeable / porous in nature, enabling it to act as a charge excluder facilitating the electrochemistry of negatively charged species and limiting the electrochemistry of positively charged species to the pin holes in the film.

8.9 REFERENCES

1. Berger, M.,J. A. Gray,B. L. Roth, *Annu. Rev. Med.,* **2009,** *60,* 355-366.
2. Sun, Y. X.,J. J. Fei,J. Hou,Q. Zhang,Y. L. Liu,B. A. Hu, *Microchimica Acta,* **2009,** *165,* 373-379.
3. Patel, B. A., *Analyst,* **2008,** *133,* 516-524.
4. Wu, K.,J. Fei,S. Hu, *Anal Biochem,* **2003,** *318,* 100-106.
5. Güell, A. G.,K. E. Meadows,P. R. Unwin,J. V. Macpherson, *Phys. Chem. Chem. Phys.,* **2010,** *12,* 10108-10114.
6. Wrona, M. Z.,D. Lemordant,L. Lin,C. L. Blank,G. Dryhurst, *J. Med. Chem.,* **1986,** *29,* 499-505.
7. Wrona, M. Z.,G. Dryhurst, *J. Org. Chem.,* **1987,** *52,* 2817-2825.
8. Wrona, M. Z.,G. Dryhurst, *Bioorg. Chem.,* **1990,** *18,* 291-317.
9. Hashemi, P.,E. C. Dankoski,J. Petrovic,R. B. Keithley,R. M. Wightman, *Anal. Chem.,* **2009,** *81,* 9462-9471.
10. Hoyer, B.,N. Jensen, *Electrochem. Commun.,* **2006,** *8,* 323-328.
11. Jackson, B. P.,S. M. Dietz,R. M. Wightman, *Anal. Chem.,* **1995,** *67,* 1115-1120.
12. Swamy, B. E.,B. J. Venton, *Analyst,* **2007,** *132,* 876-884.
13. Ball, V., *Colloid Surface A,* **2010,** *363,* 92-97.
14. McCreery, R. L., *Chem. Rev,* **2008,** *108,* 2646-2687.
15. Njagi, J.,M. Ball,M. Best,K. N. Wallace,S. Andreescu, *Anal. Chem.,* **2010,** *82,* 1822-1830.
16. Crespi, F.,K. Martin,C. Marsden, *Neuroscience,* **1988,** *27,* 885-896.
17. Bertrand, P. P., *Neurogastroent. Motil.,* **2004,** *16,* 511-514.
18. Li, Y. X.,X. Huang,Y. L. Chen,L. Wang,X. Q. Lin, *Microchimica Acta,* **2009,** *164,* 107-112.
19. Wu, K.,J. Fei,S. Hu, *Anal. Biochem.,* **2003,** *318,* 100-106.
20. Kachoosangi, R. T.,R. G. Compton, *Anal. Bioanal. Chem.,* **2007,** *387,* 2793-2800.
21. Wang, Z. H.,Q. L. Liang,Y. M. Wang,G. A. Luo, *J. Electroanal. Chem.,* **2003,** *540,* 129-134.
22. Sarada, B. V.,T. N. Rao,D. A. Tryk,A. Fujishima, *Anal. Chem.,* **2000,** *72,* 1632-1638.
23. Singh, Y. S.,L. E. Sawarynski,H. M. Michael,R. E. Ferrell,M. A. Murphey-Corb,G. M. Swain,B. A. Patel,A. M. Andrews, *ACS Chem. Neurosci.,* **2010,** *1,* 49-64.
24. Compton, R. G.,J. S. Foord,F. Marken, *Electroanal.,* **2003,** *15,* 1349-1363.
25. Pleskov, Y. V., *Russ. J. Electrochem.,* **2002,** *38,* 1275-1291.
26. Hutton, L.,M. E. Newton,P. R. Unwin,J. V. Macpherson, *Anal. Chem.,* **2009,** *81,* 1023-1032.
27. Trouillon, R.,Z. Combs,B. A. Patel,D. O'Hare, *Electrochem. Commun.,* **2009,** *11,* 1409-1413.
28. Zhao, H.,X. C. Bian,J. J. Galligan,G. M. Swain, *Diamond Relat. Mater.,* **2010,** *19,* 182-185.
29. Trouillon, R.,D. O'Hare, *Electrochim. Acta,* **2010,** *55,* 6586-6595.
30. Xu, J.,Q. Chen,G. M. Swain, *Anal. Chem.,* **1998,** *70,* 3146-3154.
31. Patel, B. A.,X. Bian,V. Quaiserova-Mocko,J. J. Galligan,G. M. Swain, *Analyst,* **2007,** *132,* 41-47.
32. Yano, T.,D. A. Tryk,K. Hashimoto,A. Fujishima, *J. Electrochem. Soc.,* **1998,** *145,* 1870-1876.
33. Yagi, I.,H. Notsu,T. Kondo,D. A. Tryk,A. Fujishima, *J. Electroanal. Chem.,* **1999,** *473,* 173-178.
34. Yano, T.,E. Popa,D. A. Tryk,K. Hashimoto,A. Fujishima, *J. Electrochem. Soc.,* **1999,** *146,* 1081-1087.

35. Tammeveski, K.,R. Reilson,M. Kullapere, *Electroanal.,* **2010,** *22,* 513-518.
36. Klein, D. L.,P. L. Mceuen, *Appl. Phys. Lett.,* **1995,** *66,* 2478-2480.
37. Olbrich, A.,B. Ebersberger,C. Boit, *Appl. Phys. Lett.,* **1998,** *73,* 3114-3116.
38. Yang, H.,T. J. Shin,M. M. Ling,K. Cho,C. Y. Ryu,Z. Bao, *J. Am. Chem. Soc.,* **2005,** *127,* 11542-11543.
39. Wilson, N. R.,S. L. Clewes,M. E. Newton,P. R. Unwin,J. V. Macpherson, *J. Phys. Chem. B,* **2006,** *110,* 5639-5646.
40. Colley, A. L.,C. G. Williams,U. D'Haenens Johansson,M. E. Newton,P. R. Unwin,N. R. Wilson,J. V. Macpherson, *Anal. Chem.,* **2006,** *78,* 2539-2548.
41. O'Mullane, A. P.,A. K. Neufeld,A. R. Harris,A. M. Bond, *Langmuir,* **2006,** *22,* 10499-10505.
42. Amatore, C.,J. M. Saveant,D. Tessier, *J. Electroanal. Chem.,* **1983,** *147,* 39-51.

CHAPTER 9: ULTRA-THIN LANGMUIR-SCHAEFER FILMS OF NAFION AND GLUCOSE OXIDASE FOR THE AMPEROMETRIC DETECTION OF GLUCOSE

An easy method for the development of ultra thin films for a sensitive amperometric glucose biosensor is described in this chapter. Using Nafion as the immobiliser for glucose oxidase (GOx), glutaraldehyde (GA) and bovine serum albumin (BSA), ultra thin biofilms were prepared using the Langmuir−Schaefer (LS) technique and transferred on two different carbon electrodes, namely, glassy carbon and polycrystalline boron doped diamond (pBDD). The performance of the two biosensors was highly dependent on the number of layers transferred, as the films showed greater adhesion for pBDD surfaces; when fewer layers were transferred (< 20), pBDD showed superior performance with greater sensitivity. At layers greater than 30, both biosensor show high sensitivity, displaying a linear response between up to 50 mM glucose, with detection limits of down to 60 μM. These films are demonstrated to be highly reproducible with a long shelve life.

9.1 INTRODUCTION

The electrochemical glucose biosensor, which utilises glucose oxidase (GOx) as a the recognition element, is one of the most frequently used analytical devices and the most widely studied in literature.[1-7] Compared to other methods of detecting glucose, electrochemical methods are advantageous in offering rapid detection, high sensitivity, low cost and reliability.[8-14] GOx is at the heart of the glucose biosensor due to detecting glucose specifically, and showing high durability, and its strong activity over a broad range of pH values while leaving a low cost.[15-16] Current research on biosensors focuses on developing systems that provide high stability and functionality of the enzyme for in-vitro and in-vivo measurements.[17-18]

The oxidation of glucose by oxygen is a two-electron transfer process, outlined in equation 9.1 and 9.2.[19] The enzymatic process involves the reduction of a flavin group (FAD), which is buried within the enzyme, to $FADH_2$. Reoxidation of $FADH_2$ by oxygen leads to the regeneration of the enzyme and formation of hydrogen peroxide.[14, 19-20]

$$\mathrm{Glucose} + \mathrm{O_2} \xrightarrow{\mathrm{GOx}} \mathrm{Gluconicacid} + \mathrm{H_2O_2} \qquad \textbf{Equation 9. 1}$$

$$2\mathrm{H^+} + \mathrm{O_2} + 2\mathrm{e^-} \rightarrow \mathrm{H_2O_2} \qquad \textbf{Equation 9. 2}$$

The first generation of biosensors were based on the production and detection of hydrogen peroxide with use of oxygen as a co-substrate.[21] The principle of the second-generation biosensors was to eliminate the use of oxygen as the co-substrate. As most enzymes have their active site deeply embedded within the protein structure, spatial separation means direct ET with the electrode is usually impossible. Therefore, a mediator is required to shuttle electrons between the enzyme and electrode surface.[14, 22-23] Figure 9. 1 outline the basic principles of the three different generations of enzyme sensor.

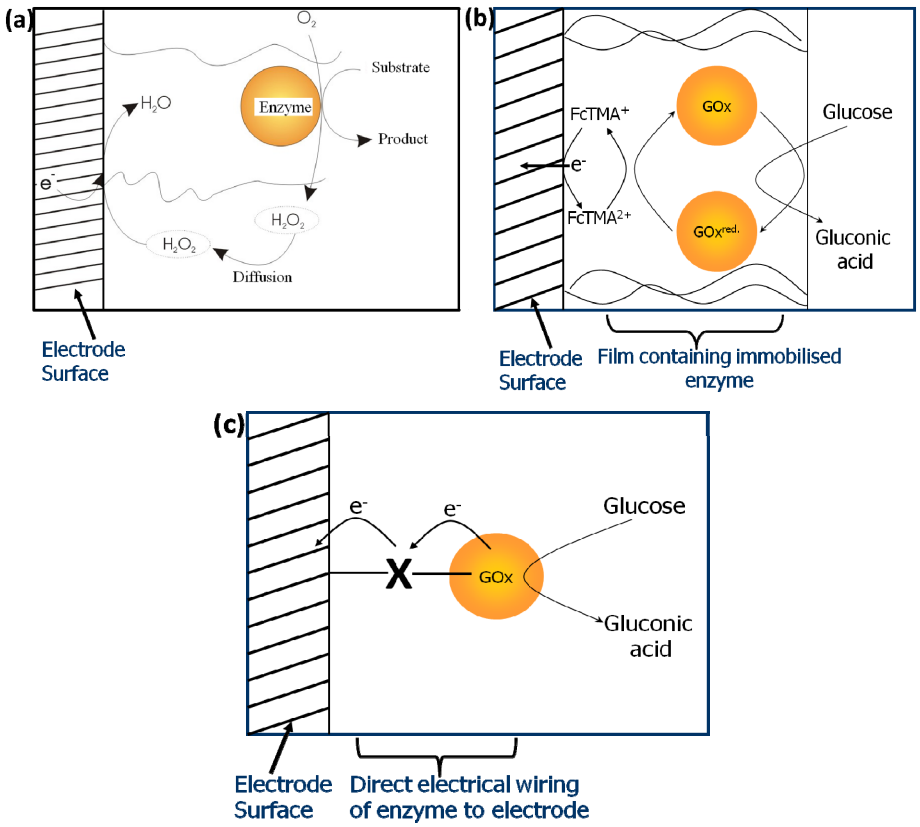

Figure 9. 1 A schematic for the basic principle of: (a) first generation; (b) second generation and (c) third generation enzyme biosensor.

An ideal mediator should provide: (1) rapid reaction with the enzyme, (2) reversible ET kinetics, (3) low redox potential for regeneration, (4) maintain sufficient chemical stability in both its oxidised and reduced forms, and (5) be free from toxicity.[24-25] There are a wide range of mediators employed in research (and in practical devices), these include Prussian blue,[26-27] quinines,[28-29] methyl viologen[30-31] as well as ferrocene and its derivatives,[2, 32] which are a very popular class of mediators as they have a wide redox potential range which is pH-independent and the derivatives are easy to make. Electroactive polymers are mediators, which can also act as an immobiliser; they include conducting polymers, e.g. polypyrole and redox polymers, e.g. polyvinylferrocene.[33-35]

The enzyme in a biosensor can either be in solution[2] or immobilised on the electrode surface. Immobilisation of the enzyme has benefits as it leads to increased stability of the enzyme structure and function and allow for repeatable use of the biosensor.[18, 25] Various methods have been developed for the immobilisation of enzymes: electrochemical copolymerisation e.g. with an electroactive polymer;[36-37] microencapsulation e.g. in a matrix such as sol-gel;[21, 38] entrapment e.g. behind a membrane such as cellulose acetate;[12, 39] electrostatic layer-by-layer assembly e.g. through the consecutive adsorption of polyanions and polycations such as poly(vinylsulfonate)[40-41] and poly(allylamine hydrochloride);[42-43] cross-linking e.g. using a bifunctional agent such as glutaraldehyde and bovine serum albumin,[44-45] and covalent bonding e.g. to a nylon membrane, such as polyamide.[46-47] Chemical immobilisation of the enzyme has the advantage of providing more stability, thereby greatly enhancing the lifetime of the biosensor by months in comparison to the other techniques which typically last 0-4 weeks.[46, 48-49] Langmuir techniques are an interesting method for creating modified surfaces and immobilising proteins, such as the enzyme GOx, as it allows for the transfer of ultra-thin films in which the thickness of the film, its density and the orientation of the molecules can be controlled.[50-54]

Within this chapter it is described the fabrication of a glucose analysis system that incorporates glutaraldehyde, bovine serum albumin, glucose oxidase, Nafion and a ferrocene based mediator. Thin films by sub-Nafion Langmuir-Schaefer technique have proved effective for the deposition of a variety of Nafion composites, including conducting polymers,[55-56] metal nanoparticles[57-58] and redox-active cationic species.[59-60] Herein, it is shown the ultrathin films (described above) provides a fast response with high sensitivity on pBDD and GC electrodes, with the former providing the highest effect.

9.2 FABRICATION OF LANGMUIR-SCHAEFER BIOFILMS

The subphase for the Langmuir trough was 0.1 M aqueous KNO_3. Using a Wilhemy balance, the surface pressure was measured within an accuracy of ± 0.1 mN m^{-1}. After 5 minutes of having added the Nafion/GA/BSA/GOx mixture onto the subphase, compression of the floating films began. Based on the Langmuir isotherm obtained, a surface pressure of 25 mN m^{-1} was established and maintained (Figure 9. 2). A layer of the film was transferred onto the electrode surface by bringing the electrode surface down towards the film until contact was made. The electrode was removed vertically and allowed to dry before the subsequent addition of another layer. Once a desired number of layers had been transferred, the electrode was stored in a solution of 0.1 mM $FcTMA^+$ (0.1 M PBS, pH 7.2) for at least 24 hours at room temperature (*ca.* 20-25°C).

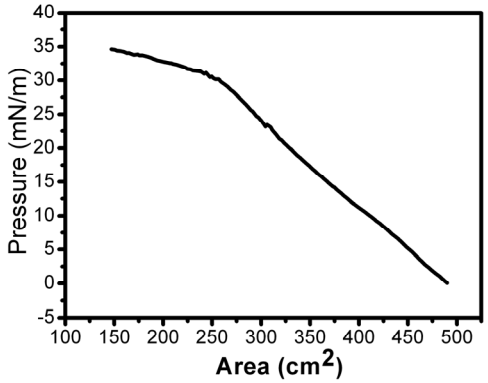

Figure 9. 2 A typical Langmuir isotherm for a Nafion/GA/BSA/GOx mixture.

9.2 VERIFICATION OF CATALYTIC ACTIVITY

Using the LS technique, 10 layers of the biofilm (Nafion/GA/BSA/GOx) were transferred onto the surfaces of GC and pBDD electrodes. The enzymatic activity of these biosensors were confirmed by recording CVs (1 mV s^{-1}). Figure 2 shows the CVs obtained for the GC-based biosensor (Figure 9. 3(a)) and the pBDD based biosensor (Figure 9. 3(b)) in a solution of PBS (black) and then the generation of a catalytic peak upon the addition of 10 mM glucose to the solution (red). The observed enhancement of the forward oxidation signal is classic behaviour for a catalytic reaction where the enzymes continuous regeneration causes a cycling of the enzymatic reaction.[8, 61] This confirms the successful immobilisation of GOx and fabrication of a glucose biosensor.

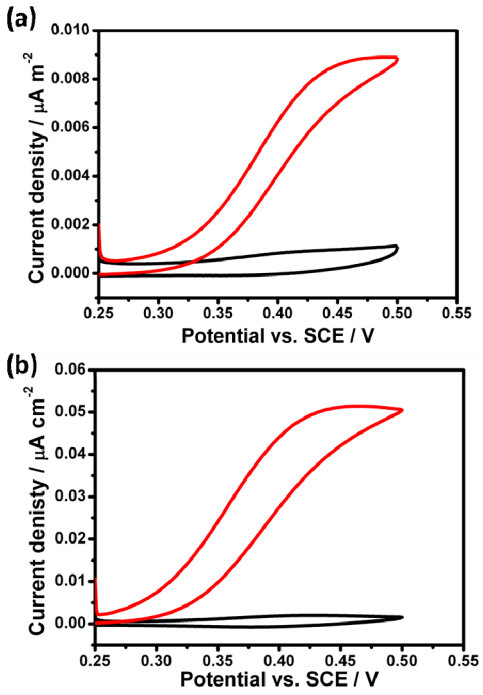

Figure 9. 3 CV's for the oxidation of 10 mM glucose in 0.15 M PBS, pH 7.2, at 1 mV s^{-1} using (a) GC biosensor with 10 layers and (b) BDD biosensor with 10 layers, against a CV of the background electrolyte.

9.3 OPTIMISATION OF BIOSENSOR

The effect of the number of LS layers was determined by further fabricating biosensors where 20, 30 and 50 layers of the biofilm were transferred onto GC and pBDD surfaces. As the normal physiological range for blood glucose is 4.4 - 6.6 mM, an ideal glucose sensor should be sensitive between 1-10 mM,[14] therefore the performance of biosensors were tested for glucose concentrations range 0.1 – 10 mM. Figure 9. 4 shows linear relationship of the stationary current against glucose concentration for all fabricated biosensors in which the R^2 ranges between 0.98 - 0.99 for 3a and 0.97 - 0.99 for 3b. For electrodes of 10 layers, the catalytic response reached saturation at glucose concentrations ≥ 20 mM, whereas for electrodes of layers ≥ 20, saturation was reached at concentrations ≥ 50 mM. All electrodes were able to detect to at least 0.1 mM except for the GC-based sensor of 10 layers, which could not detect concentrations < 1 mM. Figure 9. 4 also shows an increase in current as the number of layers is increased, which is expected as this leads to an overall increase in enzyme concentration.

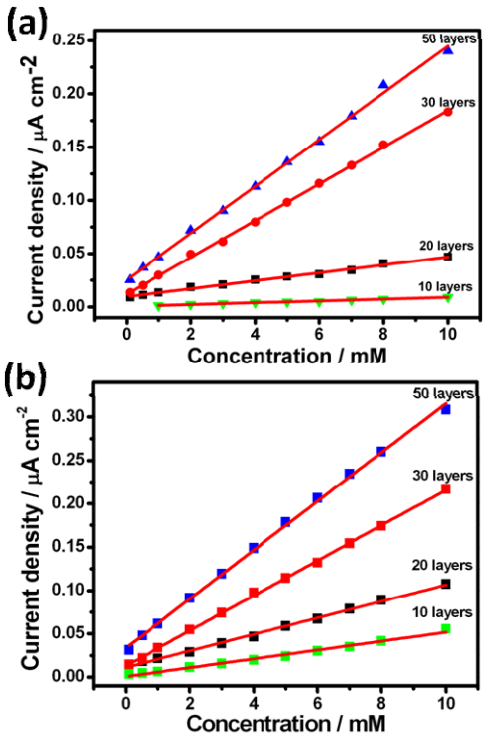

Figure 9. 4 Calibration curves for the amperometric response of glucose against concentration, ranging between 0.1 – 10 mM, in which the number of layers adsorbed is varied, (a) GC and (b) BDD. The number of layers investigated are 10, 20, 30 and 50.

Comparing the activity of pBDD with GC based biosensors it is evident that when the number of transferred layers 10 or 20, pBDD appears to provide a superior response but at layers greater than 20 the two electrode materials show similar performance. This is likely to be due to a difference in adhesion of the first few layers on the pBDD surface compared to the GC, with the former proving better. Therefore, although 10 or 20 layers were transferred on to both pBDD and GC, it's likely fewer layers actually adhered onto the GC surface hence a thinner film and a lower activity. Figure 9. 5 which compares the activity of a 30 layer pBDD biosensor against a 30 layer GC biosensor, the difference in activity is less pronounced but the pBDD-based sensor still provides slightly higher currents.

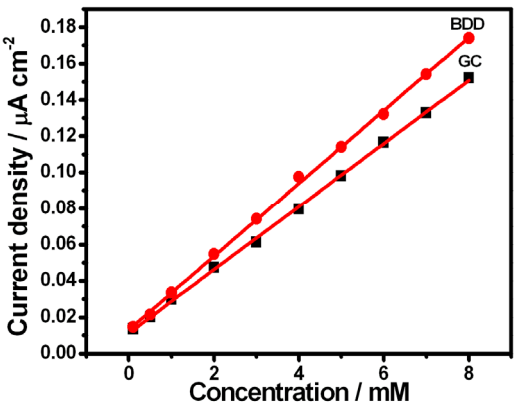

Figure 9. 5 Calibration curves for the amperometric response of glucose against concentration ranging between 0.1 to 10 mM for 30 layers of Nafion/GA/BSA/GOx adsorbed on to BDD and GC.

The performance of these electrodes was also explored in blood substitute. Figure 9. 6(a) shows the CVs of GC (i) and pBDD (ii) based biosensors in blood substitute and when spiked with 1 mM glucose. Figure 9. 6(b) shows the response from pBDD and GC at a range of glucose concentrations of 1 - 8 mM in the same blood substitute medium. When comparing the signals obtained from solutions containing glucose in PBS, although a decrease in sensitivity is observed, both electrodes maintain a linear response with a difference of < 1 μA cm^{-2} between the two electrode materials.

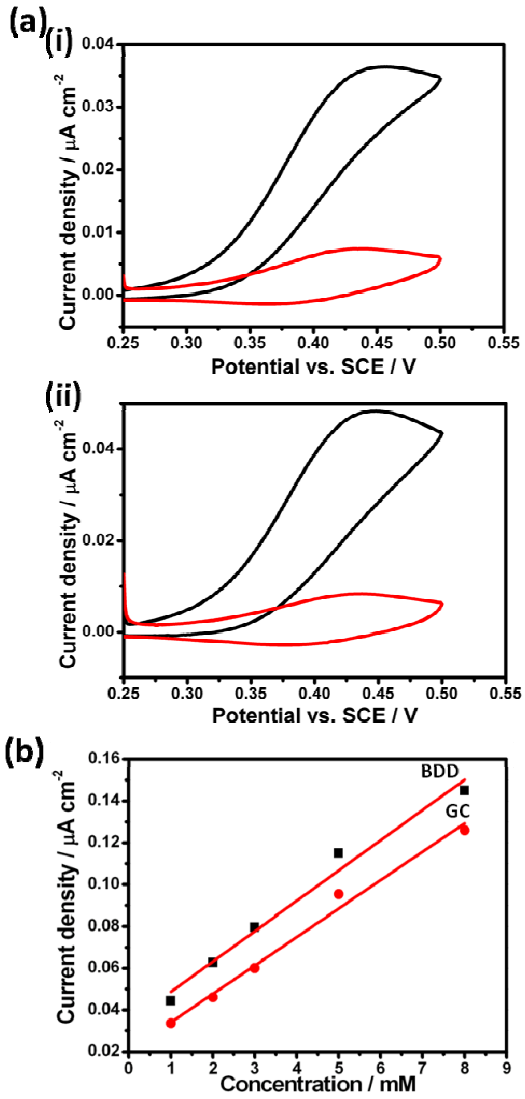

Figure 9. 6 (a) CV's for the oxidation of 1 mM glucose in blood substitute, at 1 mV s^{-1} using (i) GC biosensor with 30 layers and (ii) BDD biosensor with 30 layers, against a CV of blood substitute without any glucose. (b) Calibration curves for the biosensor response from GC and BDD in blood substitute spiked with concentrations of glucose varying between 1 – 8 mM.

9.4 MICHAELIS-MENTEN KINETICS, SENSITIVITY AND DETECTION LIMITS

Enzyme kinetics can be determined using the Michaelis-Menten equation:

Equation 9. 3

where V is the rate of conversion (in this case oxidation peak current), V_{max} is the maximum rate of conversion where the enzyme reaches saturation, [S] is the substrate (glucose) concentration, and K_m is the Michaelis constant. The K_m values indicate the substrate concentration at $½V_{max}$ and indicates the enzymes affinity for the substrate. A low K_m means the enzyme has a high affinity for the substrate and therefore will approach V_{max} at lower [S].

The K_m of a particular system can be determined using a modified version of the Michaelis-Menten equation, in the form of as the Lineweaver-Burk equation, that enables ready calculation of both the K_m and V_{max}.

$$\frac{1}{V} = \frac{K_m}{V_{max}} . \frac{1}{[S]} + \frac{1}{V_{max}}$$ **Equation 9. 4**

A plot of *1/V* versus *1/*[*S*] produces a straight line in which the gradient is used to determine the K_m (Figure 9. 7). The Lineweaver-Burk plot was used to calculate the K_m for each of the fabricated biosensors, the values were found to range between 20 – 28.6 mM (see Table 9. 1). A comparison of K_m values obtained from GC based biosensors against pBDD based biosensors shows that there is no apparent advantage of using one material over the other, for GC the values range between 21.03 to 28.68 mM, and for pBDD, 20 to 27.66 mM. The K_m values are high, this means the enzymes reach saturation at high [*S*], which is useful as it provides a wide concentration range in which to do analysis. In a system where the analyte is being detected by an enzyme, it is essential for the K_m to be greater than the physiological substrate concentration in order for the limiting factor to be [*S*], and so that the rate of reaction increases linearly with [*S*].[61-62] The K_m for the GOx when free in solution is 33 mM - 100 mM, which is higher than that for the immobilised enzymes indicating that there is a loss in bioactivity upon immobilisation. This phenomenon is commonly observed and can be attributed to a couple of possible causes; steric hindrance of the active site and/or small changes to the enzymes tertiary structure which can be caused by covalent linking to other molecules such as the BSA, GA or Nafion.[63-64] As the enzymatic activity of the biosensors is still relatively high, the loss can seen to be inconsequential.

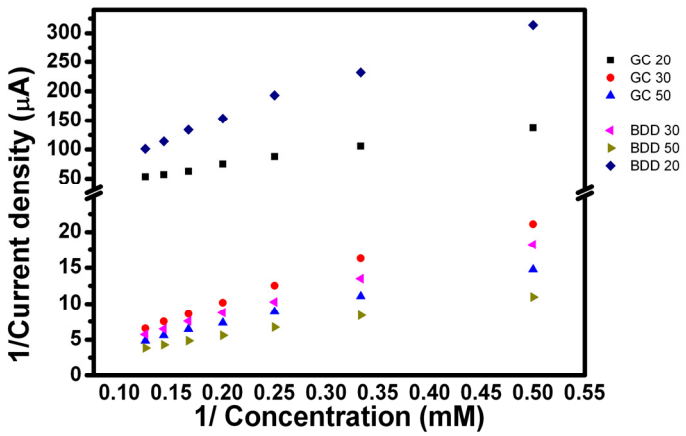

Figure 9. 7 Lineweaver-Burk plot for pBDD and GC biosensors.

The limit of detection (L.O.D.) and the limit of quantification (L.O.Q.) were found for all fabricated biosensors and is reported in Table 1. These values were defined from:

$$L.O.D. = \overline{\mu} + (3\sigma) \quad \textbf{Equation 9. 5}$$

$$L.O.Q. = 10\sigma \quad \textbf{Equation 9. 6}$$

where μ is the mean value for the background currents measured without glucose and σ is the standard deviation of the measurements. For the biosensors fabricated on GC, the L.O.D. ranged from 70 to 76 μM and for those fabricated on pBDD, the L.O.D. was found to range from 28 to 33 μM. This shows that due to the lower background currents provided by pBDD, it is possible to detect glucose at lower concentrations than for GC. Similar observation is seen when comparing the L.O.Q., for pBDD biosensors it ranges from 0.06 to 0.1 mM whereas for GC it ranges between 0.13 to 0.20 mM.

Table 9. 1 Statistical analysis of linear data obtained from the fabricated biosensors showing, R^2, K_m, L.O.D and L.O.Q for each linear calibration curve as well as the surface coverage of the mediator $FcTMA^+$ in each biosensor.

	R^2	K_m (mM)	L.O.D. (mM)	L.O.Q . (mM)	Surface coverage Γ/ (10^{-12}) mol cm^{-2}
GC-20 layers	**0.972**	**28.6**	**0.075**	**0.20**	**0.14**
GC-30 layers	**0.998**	**21.0**	**0.070**	**0.13**	**0.47**
GC-50 layers	**0.995**	**27.6**	**0.076**	**0.14**	**0.88**
BDD-20 layers	**0.989**	**24.8**	**0.033**	**0.10**	**0.81**
BDD-30 layers	**0.997**	**27.6**	**0.028**	**0.06**	**1.01**
BDD- 50 layers	**0.998**	**20.0**	**0.033**	**0.06**	**1.66**

Using CV measurements taken in just the background electrolyte, the surface coverage of $FcTMA^+$, Γ, can be determined. By integrating the anodic peak current, a charge (*Q)* is obtained which is then substituted into the following equation:[52, 65]

$$\Gamma = \frac{Q}{nFA} \quad \textbf{Equation 9. 7}$$

where *n* is the number of electrons transferred (1 in this case), *F* is the Faraday constant (96486 C mol^{-1}) and *A* is the geometric area of the working electrode (cm^2). The values obtained can be found in Table 9. 1.

9.5 REPEATABILITY, STORAGE, STABILITY

The repeatability of using the Langmuir technique to create these functionalised electrodes was studied and is shown in Figure 9. 8(a). Three separate electrodes were fabricated with 20 layers adsorbed onto the surface and the amperometric response tested between 0.1 - 10 mM. The data shows this method of producing thin film biosensors is highly reproducible.

The longevity of the biosensors, which were stored at room temperature (~ 19 °C) in a solution of PBS with $FcTMA^+$, at pH 7, was tested over a 10 week period. Figure 7b shows the change in response for a pBDD and a GC based biosensor of 20 layers as a percentage decrease. The activity of the biosensors reduced over a 10 week period but still maintained high activity.

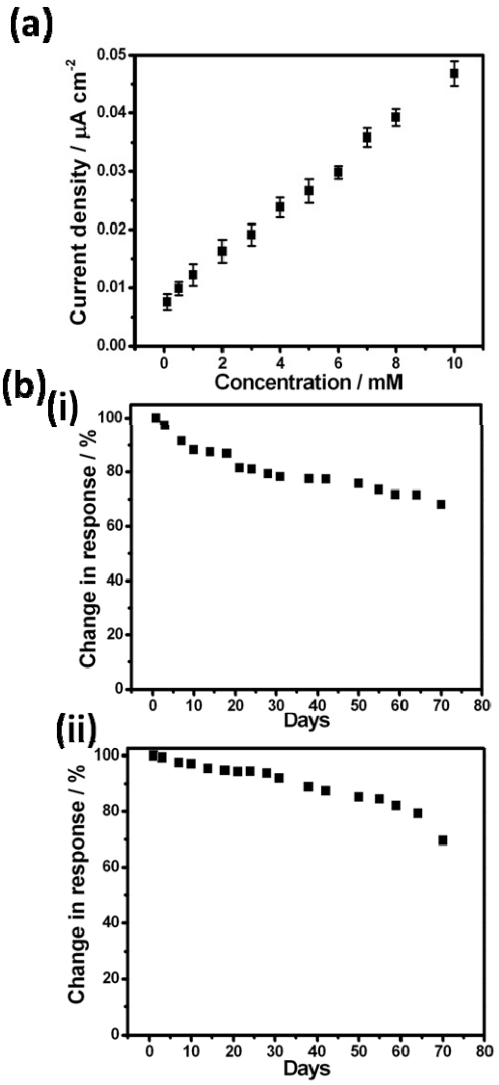

Figure 9. 8 (a) Reproducibility of Nafion/GA/BSA/GOx LS films using 10 layer films on pBDD as an example, (b) Stability of (i) GC biosensor with 20 layers and (ii) BDD biosensor with 20 layers, over a 70 day period.

Table 9. 2 summarises the observed changes in response over time. After 21 days all biosensor retained at least 81% activity which reduced to 76% after 42 days and 66% after 70 days.

Table 9. 2 Percentage change in response of each biosensor over a 70 day period.

	Change in response, %					
Day	**BDD 20**	**BDD 30**	**BDD 50**	**GC 20**	**GC 30**	**GC 50**
21	**94.3**	**96.6**	**93.6**	**81.3**	**85.3**	**83.4**
42	**87.4**	**83.4**	**79.8**	**77.3**	**76.2**	**77.4**
70	**69.5**	**74.8**	**66.3**	**68.1**	**66.1**	**67.2**

9.6 CONCLUSION

The successful fabrication of ultrathin Nafion film biosensors has been demonstrated on two electrode substrates, pBDD and GC. Although loss of enzyme activity is evident due to immobilisation, these biosensors have demonstrated to be highly sensitive (60 μM), provide a linear response (up to 50 mM), highly reproducible as well as stable over long periods of time with appropriate storage conditions, especially on pBDD.

9.7 REFERENCES

1. Gregg, B. A.,A. Heller, *Anal. Chem.,* **1990,** *62,* 258-263.
2. Cass, A. E.,G. Davis,G. D. Francis,H. A. Hill,W. J. Aston,I. J. Higgins,E. V. Plotkin,L. D. Scott,A. P. Turner, *Anal Chem,* **1984,** *56,* 667-671.
3. Frew, J. E.,H. A. O. Hill, *Anal. Chem.,* **1987,** *59,* 933A-944A.
4. Jonsson, G.,L. Gorton, *Biosensors,* **1985,** *1,* 355-368.
5. Foulds, N. C.,C. R. Lowe, *J Chem Soc Farad T 1,* **1986,** *82,* 1259-1264.
6. Bartlett, P. N.,R. G. Whitaker, *J. Electroanal. Chem.,* **1987,** *224,* 37-48.
7. Thevenot, D. R.,R. Sternberg,P. R. Coulet,J. Laurent,D. C. Gautheron, *Anal. Chem.,* **1979,** *51,* 96-100.
8. Bernhardt, P. V., *Aust. J. Chem.,* **2006,** *59,* 233.
9. Lu, J.,L. T. Drzal,R. M. Worden,I. Lee, *Chem. Mater.,* **2007,** *19,* 6240-6246.
10. Lim, S. H.,J. Wei,J. Lin,Q. Li,J. Kuayou, *Biosensors & bioelectronics,* **2005,** *20,* 2341-2346.
11. Shan, C.,H. Yang,J. Song,D. Han,A. Ivaska,L. Niu, *Anal Chem,* **2009,** *81,* 2378-2382.
12. Ren, X.,D. Chen,X. Meng,F. Tang,A. Du,L. Zhang, *Colloids and surfaces. B, Biointerfaces,* **2009,** *72,* 188-192.
13. Shan, C.,H. Yang,J. Song,D. Han,A. Ivaska,L. Niu, *Anal. Chem.,* **2009,** *81,* 2378-2382.
14. Wang, J.,J. A. Carlisle, *Diamond Relat. Mater.,* **2006,** *15,* 279-284.
15. Huang, J. D.,Y. Yang,H. B. Shi,Z. Song,Z. X. Zhao,J. Anzai,T. Osa,Q. Chen, *Mat Sci Eng C-Bio S,* **2006,** *26,* 113-117.
16. Ohnuki, H.,T. Saiki,A. Kusakari,H. Endo,M. Ichihara,M. Izumi, *Langmuir,* **2007,** *23,* 4675-4681.
17. Saha, S.,S. K. Arya,S. P. Singh,K. Sreenivas,B. D. Malhotra,V. Gupta, *Biosensors & bioelectronics,* **2009,** *24,* 2040-2045.
18. Grieshaber, D.,R. MacKenzie,J. Voros,E. Reimhult, *Sensors-Basel,* **2008,** *8,* 1400-1458.
19. Bourdillon, C.,C. Demaille,J. Moiroux,J. M. Saveant, *J. Am. Chem. Soc.,* **1993,** *115,* 1-10.
20. Wilson, R.,A. P. F. Turner, *Biosensors & bioelectronics,* **1992,** *7,* 165-185.
21. Wang, J., *Anal. Chim. Acta,* **1999,** *399,* 21-27.
22. Cosnier, S.,S. Da Silva,D. Shan,K. Gorgy, *Bioelectrochemistry,* **2008,** *74,* 47-51.
23. Zhou, M.,Y. Zhai,S. Dong, *Anal. Chem.,* **2009,** *81,* 5603-5613.
24. Ozoemena, K. I.,T. Nyokong, *Electrochim. Acta,* **2006,** *51,* 5131-5136.
25. Katz, E.,A. N. Shipway,I. Wilner, *Encyclopedia of Electrochemistry: Bioelectrochemistry*. Wiley-VCH: Weinheim, 2002.
26. de Mattos, I. L.,L. V. Lukachova,L. Gorton,T. Laurell,A. A. Karyakin, *Talanta,* **2001,** *54,* 963-974.
27. Ricci, F.,A. Amine,C. S. Tuta,A. A. Ciucu,F. Lucarelli,G. Palleschi,D. Moscone, *Anal. Chim. Acta,* **2003,** *485,* 111-120.
28. Piro, B.,V. A. Do,L. A. Le,M. Hedayatullah,M. C. Pham, *J. Electroanal. Chem.,* **2000,** *486,* 133-140.
29. Kaku, T.,H. I. Karan,Y. Okamoto, *Anal Chem,* **1994,** *66,* 1231-1235.
30. Ghica, M. E.,C. M. A. Brett, *Anal. Chim. Acta,* **2005,** *532,* 145-151.
31. Zen, J. M.,C. W. Lo, *Anal Chem,* **1996,** *68,* 2635-2640.
32. Bean, L. S.,L. Y. Heng,B. M. Yamin,M. Ahmad, *Bioelectrochemistry,* **2005,** *65,* 157-162.
33. Hall, E. A. H., *Biosensors*. Open University Press: Milton Keynes, 1990.
34. Shin, M. C.,H. C. Yoon,H. S. Kim, *Anal. Chim. Acta,* **1996,** *329,* 223-230.
35. Nguyen, A. L.,J. H. T. Luong, *Appl. Biochem. Biotechnol.,* **1993,** *43,* 117-132.
36. Vidal, J. C.,E. Garcia-Ruiz,J. R. Castillo, *Microchimica Acta,* **2003,** *143,* 93-111.

37. Karyakin, A. A.,L. V. Lukachova,E. E. Karyakina,A. V. Orlov,G. P. Karpachova, *Anal. Commun.,* **1999,** *36,* 153-156.
38. Li, F.,W. Chen,C. Tang,S. Zhang, *Talanta,* **2009,** *77,* 1304-1308.
39. Rauf, S.,A. Ihsan,K. Akhtar,M. A. Ghauri,M. Rahman,M. A. Anwar,A. M. Khalid, *J Biotechnol,* **2006,** *121,* 351-360.
40. Prabhakar, N.,G. Sumana,K. Arora,H. Singh,B. D. Malhotra, *Electrochim. Acta,* **2008,** *53,* 4344-4350.
41. Hoshi, T.,H. Saiki,J. Anzai, *Talanta,* **2003,** *61,* 363-368.
42. Wang, B.,T. Noguchi,J. Anzai, *Talanta,* **2007,** *72,* 415-418.
43. Ferreira, M.,P. A. Fiorito,O. N. Oliveira, Jr.,S. I. Cordoba de Torresi, *Biosensors & bioelectronics,* **2004,** *19,* 1611-1615.
44. Wu, B.,G. Zhang,S. Shuang,M. M. Choi, *Talanta,* **2004,** *64,* 546-553.
45. Cai, C. X.,K. H. Xue,Y. M. Zhou,H. Yang, *Talanta,* **1997,** *44,* 339-347.
46. Blum, L. J., *Enzyme Microb. Technol.,* **1993,** *15,* 407-411.
47. Gautier, S. M.,L. J. Blum,P. R. Coulet, *Biosensors,* **1989,** *4,* 181-194.
48. Higson, S. P. J.,S. M. Reddy,P. M. Vadgama, *Eng. Sci. Educ. J.,* **1994,** *3,* 41-48.
49. Bowers, L. D.,P. W. Carr, *Immobilized enzymes in analytical and clinical chemistry, chemical analysis, fundamentals and applications*. John Wiley & sons: New York, 1982.
50. Bertoncello, P.,M. K. Ram,A. Notargiacomo,P. Ugo,C. Nicolini, *Phys. Chem. Chem. Phys.,* **2002,** *2,* 4036-4043.
51. Zhang, L.,Q. Lu,M. Liu, *J. Phys. Chem. B,* **2003,** *107,* 2565-2569.
52. Bertoncello, P.,I. Ciani,F. Li,P. R. Unwin, *Langmuir,* **2006,** *22,* 10380-10388.
53. Yasuzawa, M.,M. Hashimoto,S. Fujii,A. Kunugi,T. Nakaya, *Sensor. Actuat. B,* **2000,** *65,* 241-243.
54. Sun, S.,P. Ho-Si,J. Harrison, *Langmuir,* **1991,** *4,* 727.
55. Riul, A.,D. S. dos Santos,K. Wohnrath,R. Di Tommazo,A. C. P. L. F. Carvalho,F. J. Fonseca,O. N. Oliveira,D. M. Taylor,L. H. C. Mattoso, *Langmuir,* **2002,** *18,* 239-245.
56. Bertoncello, P.,A. Notargiacomo,D. J. Riley,M. K. Ram,C. Nicolini, *Electrochem. Commun.,* **2003,** *5,* 787-792.
57. Bertoncello, P.,A. Notargiacomo,C. Nicolini, *Langmuir,* **2005,** *21,* 172-177.
58. Bertoncello, P.,M. Peruffo,P. R. Unwin, *Chem Commun (Camb),* **2007,** 1597-1599.
59. Bertoncello, P.,L. Dennany,R. J. Forster,P. R. Unwin, *Anal Chem,* **2007,** *79,* 7549-7553.
60. Bertoncello, P.,M. Peruffo,F. Li,P. R. Unwin, *Colloid Surface A,* **2008,** *321,* 222-226.
61. Marangoni, A. G., *Enzyme Kinetics: A Modern Approach*. John Wiley & Sons: Hoboken, NJ, USA, 2003.
62. Bender, D. A., *Introduction to nutrition and metabolism*. Taylor & Francis: New York, 2002.
63. Cen, L.,K. G. Neoh,E. T. Kang, *Biosensors & bioelectronics,* **2003,** *18,* 363-374.
64. Caliceti, P.,O. Schiavon,L. Sartore,C. Monfardini,F. M. Veronese, *J. Bioact. Compatible Polym.,* **1993,** *8,* 41-50.
65. Bard, A. J.,L. R. Faulkner, *Electrochemical methods : fundamentals and applications*. 2nd ed.; John Wiley & Sons: 2001.

Chapter 10: Conclusions

Carbon materials have key attributes for analytical and industrial electrochemistry. Several advantageous electrochemical properties compared to metal electrodes make them attractive for a wide range of applications, particularly in bioanalysis (biosensing) and industrial processes (e.g. water purification). Although carbon-based materials have been widely used for electrochemical sensing and analysis since the 1960's, fundamental aspects of their behaviour are unclear especially for the allotrope graphite, where discrepancies in the reported electroactivity at the basal plane of HOPG (Highly Oriented Pyrolytic Graphite) call for a re-evaluation of the electrochemical properties of graphitic materials.

High resolution SECCM was used to map the electrochemical activity of high quality HOPG for the two most studied redox species, $Ru(NH)_6^{3+/2+}$ (on ZYA grade and AM grade HOPG in Chapters 3 and 4), and $Fe(CN)_6^{4-/3-}$ (on ZYA grade in Chapter 3). Direct amperometric imaging was carried out under high mass transport conditions with a spatial resolution of 300 - 400 nm, enabling the basal surface activity, free from any influence of step edges, to be determined for the first time. SECCM has clearly illustrated the ET kinetics on the basal plane of HOPG to be significantly greater (by at least a factor of 10^5) than previously believed. Specifically, these studies have revealed that the basal surface supports very fast electron transfer for both $Ru(NH)_6^{3+/2+}$ and $Fe(CN)_6^{4-/3-}$, although the rate for the $Fe(CN)_6^{4-/3-}$ process was seen to deteriorate during the course if an image.

In Chapter 4, the voltammetric characteristics of the basal surface of HOPG were reconsidered and re-evaluated. Detailed investigations were carried out with $Fe(CN)_6^{4-/3-}$ and $Ru(NH_3)_6^{3+/2+}$, in aqueous solution, at 5 different grades of HOPG: AM; SPI-1; SPI-2; ZYA; and ZYH. Due to the significant difference the freshly cleaved surface of these materials, in terms of step defect densities, surface height ranges and general surface quality, the relationship between surface structure and electrochemical behaviour was successfully investigated. Initial CV characteristics for both $Fe(CN)_6^{4-/3-}$ and $Ru(NH_3)_6^{3+/2+}$ were found to be close to reversible and independent of the HOPG grade. Deterioration in the $Fe(CN)_6^{4-/3-}$ response during the study of time-effects, where the electrode was exposed to solution for extended periods of time or exposed to the natural atmosphere for certain periods of time before use, provides evidence for the deterioration of the electrode kinetics. *In-situ* AFM revealed deposition of material during $Fe(CN)_6^{4-/3-}$ voltammetry, which leads to a decrease in the active electrode area and electron transfer kinetics. Conducting-AFM was used to study the local surface conductivity. The surface conductivity was found to spatially heterogeneous and to deteriorate with time.

The electrochemical oxidation of many neurotransmitters, and related molecules, show the apparently slow kinetics at graphite electrodes and this has led to such processes being assigned as inner-sphere and catalyzed by step edges only. Consequently, carbon electrodes used in neuroscience and on biosensing platforms are often designed to maximize step edges. In Chapter 5, it is shown for the first time that the freshly prepared and unmodified basal plane of HOPG provides ideal reversible voltammetry for DA oxidation. SECCM was modified to carryout reactive patterning with DA, so that the electrochemical response could be related unambiguously to the location on the carbon electrode surface. It was shown show that in the case of the catechol, DA, that the electrochemical reaction is rapid at the basal surface of highly orientated pyrolytic graphite (HOPG), but rapidly poisoned by reaction products of the electro-oxidation process which block the electrode.

In light of these findings (Chapters 3-5), voltammetry was used to re-examine and compare the electrochemical response for the electro-oxidation of DA on the unmodified surfaces of 5 different carbon electrode surfaces: GC, oxygen-terminated pBDD, EPPG, BPPG and three grades of basal plane HOPG (ZYA, SPI-1 and ZYH) (Chapter 6). At high concentrations (≥ 1 mM DA) reversible voltammetry was not observed on any of the electrodes and evidence of significant surface blocking was found for all basal plane graphite surfaces and GC (although the extent varied between each electrode). However, the pBDD and EPPG electrode showed relatively high stability for the oxidation of DA, indicating that these materials would be ideal for detection at high concentrations. At physiological concentrations (≤ 1 μM DA) reversible electrochemistry takes place at the pristine, freshly cleaved, basal plane of HOPG (as shown in Chapter 5) and the effects of surface blocking were no longer evident. However, time-effect studies and *in-situ* AFM indicate that blocking of the surface takes place by dopaminergic products even at 1 μM and that the way in which the film forms at low concentrations does not significantly affect DA electro-oxidation but must either: facilitate ET, supporting electrochemistry by acting as an electron relay to DA molecules; or possess pin-holes allowing a flux of species to the electrode/electrolyte interface. Interestingly, in the presence of a common inferring redox species, AA, the basal plane of HOPG not only provides reversible electro-oxidation for DA but AA forms a thin negatively charged film that selectively excludes AA but allows DA electro-oxidation. Together with the fact this form of carbon material provides the lowest detection limit of DA when using simple voltammetry, the basal plane of HOPG is clearly the most ideal material.

Due to the findings of Chapter 5 and 6, further work considered the adsorption and electrochemistry of 2,6-AQDS (another highly studied quinone) on 3 different grades of

HOPG (AM, SPI-1, and ZYA). As outlined in Chapter 7, it had been proposed that 2,6-AQDS is a marker for step sites on basal plane graphite, but re-evaluation shows that there is, in fact, no correlation between 2,6-AQDS voltammetry and step defect density. Reactive SECCM pattering with, 2,6-AQDS was used to show unambiguously, that uniform electrochemistry takes place across the basal surface and step edges. Chapters 3-7 provide a significant body of evidence that calls for a new model for the electroactivity of basal plane HOPG, with implications for related sp^2 materials.

Chapters 8 and 9 considers pBDD for biological applications. In Chapter 8 pBDD is used to examine the neurotransmitter 5-HT. The surface of the electrode was shown to be highly susceptible to blocking by oxidative by-products under conditions of continuous potential cycling but reversible and controllable with various voltammetry treatment techniques. Using *in-situ* AFM and a range of voltammetric studies, complete coverage of the pBDD surface by a thick film of the oxidative by-products, which readily desorbs or dissolves, was found to form as a result of extensive potential cycling. Further voltammetry and C-AFM were used to reach the conclusion that the film which forms is electrically insulating but must be charged and porous in nature, enabling it to act as a charge excluder, facilitating the electrochemistry of negatively charged redox species and limiting the electrochemistry of positively charged species to the pinholes in the film.

Chapter 9 explored the development of ultra-thin biofilms on pBDD for the enzymatic detection of glucose. In this chapter a method was described of creating biosensors in which Nafion films were used to encapsulate and immobilise enzymes that are extremely stable, with pBDD providing the more optimal surface compared to GC.

In summary, this thesis has significantly advanced knowledge of carbon electrodes and shown how voltammetry needs to be combined with high resolution electrochemical measurements and microscopy in order to resolve complex structure activity issues.